

# REPORT DOCUMENTATION PAGE

AFRL-SR-BL-TR-98-

0596

Public reporting burden for this collection of information is estimated to average 1 hour per response, including the time for reviewing instructions, searching existing data sources, gathering the collection of information. Send comments regarding this burden estimate or any other aspect of this collection of information, including suggestions for reducing the burden, to Washington Headquarters Services, Directorate for Information Operations and Reports, 1215 Jefferson Davis Highway, Suite 1204, Arlington, VA 22202-4302, and to the Office of Management and Budget, Paperwork Reduction Project (0704-0188).

1. AGENCY USE ONLY (Leave blank)		2. REPORT DATE July 1998	3. REPORT TYPE AND DATES COVERED FINAL REPORT 15 Apr 95 - 14 Apr 98
4. TITLE AND SUBTITLE OPTICAL PHASE CORRECTION IN A PLANE SHEAR LAYER USING PARALLEL OPTOELECTRONIC IMAGE PROCESSING, GLOBAL OPTICAL FLOW DIAGNOSTICS			5. FUNDING NUMBERS F49620-95-1-0246
6. AUTHOR(S) MARTIN BROOKE, ARI GLEZER, AND NAN MARIE JOKERST			61102F 2307/BS 2305/DS
7. PERFORMING ORGANIZATION NAME(S) AND ADDRESS(ES) GEORGIA INSTITUTE OF TECHNOLOGY MECHANICAL ENGINEERING ATLANTA, GA 30332-0420			8. PERFORMING ORGANIZATION REPORT NUMBER
9. SPONSORING/MONITORING AGENCY NAME(S) AND ADDRESS(ES) AIR FORCE OFFICE OF SCIENTIFIC RESEARCH (AFOSR) 110 DUNCAN AVENUE ROOM B115 BOLLING AFB DC 20332-8050			10. SPONSORING/MONITORING AGENCY REPORT NUMBER
11. SUPPLEMENTARY NOTES			
12a. DISTRIBUTION AVAILABILITY STATEMENT APPROVED FOR PUBLIC RELEASE, DISTRIBUTION IS UNLIMITED			12b. DISTRIBUTION CODE
13. ABSTRACT (Maximum 200 words) Neural networks that allow aero-optic phase correction to be made using localized measurements without an external probe beam are being developed in an information-rich laboratory environment. The neural networks are trained to relate phase corrections to low-order modal descriptions of a plane shear layer obtained by a proper orthogonal decomposition (POD) applied to index of refraction data. Optical measurements are taken in a plane shear layer between two uniform streams with different temperatures. The training sequence will use actuators to influence the flow, thus providing the networks with a broader operational range. Elements critical to the training include development of a three-dimensionally interconnected high frame rate optoelectronic smart camera, extraction of the velocity field using two scalars, and determination of modal coefficients in a low-order description of the flow. The ultimate objective is to simultaneously determine the three-dimensional index of refraction field and the resulting optical phase front distortion in the plane shear layer, thereby providing real-time correlation between index variation and optical phase shift to the neural networks.			
14. SUBJECT TERMS  DTIC QUALITY INSPECTION			15. NUMBER OF PAGES 118
			16. PRICE CODE
17. SECURITY CLASSIFICATION OF REPORT UNCLASSIFIED	18. SECURITY CLASSIFICATION OF THIS PAGE UNCLASSIFIED	19. SECURITY CLASSIFICATION OF ABSTRACT UNCLASSIFIED	20. LIMITATION OF ABSTRACT

17 AUG 1999

# **NEURAL NETWORK DETERMINATION OF OPTICAL PHASE CORRECTION IN A PLANE SHEAR LAYER USING PARALLEL OPTOELECTRONIC IMAGE PROCESSING AND GLOBAL OPTICAL FLOW DIAGNOSTICS**

**Final Technical Report  
AFOSR GRANT F49620-95-1-0246**

**Martin A. Brooke<sup>1</sup>, Ari Glezer<sup>2</sup>, Nan Marie Jokerst<sup>1</sup>**

**<sup>1</sup>School of Electrical Engineering**

**<sup>2</sup>School of Mechanical Engineering  
Georgia Institute of Technology**

19980831 036

## **OVERVIEW**

Neural networks that allow aero-optic phase correction to be made using localized measurements without an external probe beam are being developed in an information-rich laboratory environment. The neural networks are trained to relate phase corrections to low-order modal descriptions of a plane shear layer obtained by a proper orthogonal decomposition (POD) applied to index of refraction data. Optical measurements are taken in a plane shear layer between two uniform streams with different temperatures. The training sequence will use actuators to influence the flow, thus providing the networks with a broader operational range. Elements critical to the training include development of a three-dimensionally interconnected high frame rate optoelectronic smart camera, extraction of the velocity field using two scalars, and determination of modal coefficients in a low-order description of the flow. The ultimate objective is to simultaneously determine the three-dimensional index of refraction field and the resulting optical phase front distortion in the plane shear layer, thereby providing real-time correlation between index variation and optical phase shift to the neural networks.

## **A. OPTICAL PHASE DISTORTION IN A PLANE SHEAR LAYER**

### **I. TECHNICAL BACKGROUND**

The transmission of light through turbulent shear flows having nonuniform index of refraction and the correction of the resulting optical degradations have been the subject of a number of investigations. The study of aero-optics and atmospheric optics owes much of its importance to its applications in imaging of remote objects through the atmosphere and beam projection and imaging through a wind-induced shear flow in the near field of atmospheric flight vehicles. In many of these applications, a time-dependent distortion of a propagating light beam leads to a reduction in performance of the optical systems that use light beams to transmit or receive optical information through a flowfield.

Aero-optics and atmospheric optics are distinguished largely by the beam diameter, the size of the large-scale structures in the turbulent flow, and the thickness of the turbulent region through which the light propagates. In atmospheric optics, the beam diameter is normally much smaller than the index of refraction scale and the path length through the turbulent region, and statistical treatment of such flows is well established (Tatarskii 1971). In aero-optics applications, the beam diameter can be of the same order (or even much larger) than the thickness of the turbulent region through which the light propagates and statistical treatments of such problems are not likely to be successful.

Approved for public release;  
distribution unlimited.

Often in aero-optics applications, the central problem is adaptive correction of the optical phase aberrations, which requires an understanding of the interaction between the optical distortions and the turbulent flow field. Correction of aero-optic effects in flows where the frequencies associated with optical changes can be orders of magnitude greater than in the atmosphere, has been hampered by lack of time-resolved measurements of the rapidly changing optical wavefronts. Early measurements were limited to time-averaged wavefront distortions in the near-field that were used to estimate far-field effects. As noted by Jumper et al. (1994), in order to capture time-varying optical wavefronts in a typical aero-optic problem, it might be necessary to take measurements at rates of more than 5 kHz, even for relatively low flow velocities. This significantly limits the usefulness of interferograms used in the past to capture the instantaneous optical front distortion of a light beam propagating through a shear flow.

More recently, Jumper et al. (1994) demonstrated the utility of a new wavefront sensor that exploits a small-aperture beam technique for measurement of the optical phase distortion of light beams through a heated, two-dimensional jet (with mean velocity of 7 m/s). The small-aperture beam technique takes advantage of the fact that the optical aberrations are convected with the flow, and involves collecting a time trace of the off-axis displacement of a small-diameter beam as it is traversed through the turbulent flow. The small beam aperture sensor has a bandwidth of 100 kHz and is the fastest wavefront sensor available, largely due to the fact that the number of detectors is two orders of magnitude smaller than required by other wavefront sensors. However, the small-beam aperture sensor can only reconstruct optical wavefronts in the streamwise direction. This technique was later used by Hugo and Jumper (1995) to measure a wavefront aberrated by a compressible shear layer flow produced by two air streams with Mach numbers of 0.8 and 1.1.

The more conventional Hartmann method (Shack 1971) for measuring optical phase distortions was used by McMackin et al. (1994, 1995) to study dynamical behavior of coherent structures in a round low speed air jet (5 m/s). A linear 1-D Hartmann sensor consisted of an array of small cylindrical lenses and a CCD camera that was used to record the intensity pattern for each subaperture. The time-dependent deflection of the focused spots was proportional to the local derivative of the optical wavefront, and was integrated in the streamwise direction to determine the optical phase of a projected light. Unlike the small aperture beam technique, the sensitivity of Hartmann sensors could be controlled because the magnitude of the deflection of focal spots was directly proportional to the focal length of an array of small lenses. McMackin et al. (1994) used the one-dimensional Hartmann sensing technique and dynamic tomographic analysis to infer the relevant flow structures, and computed tomographic reconstructions of the flow field cross sections. The effect of large and small scale coherent structures within these flows on the phase distortion of the propagating light suggested that the capability to influence the evolution of these coherent structures may play a crucial role in the development of methods for real-time phase corrections.

This dissertation describes an experimental investigation of optical effects in a laser sheet propagating through a plane shear layer in a closed-return water facility, where temperature was used as a thermal analog to mixing of two species. The plane mixing layer is a prototypical aero-optic flow, in which high-speed and low-speed fluid with different nominal densities (due to different free stream temperatures) mix. Our approach was to use instantaneous temperature (and thus index of refraction) maps based on the laser induced fluorescence of Rhodamine B and disodium Fluorescein to simultaneously determine optical phase distortions and the evolution of the index of refraction field responsible for the optical distortion in an essentially isopycnic flow. Furthermore, an array of cantilevered piezo-electric flow actuators was developed to directly introduce small scales in the shear layer flow and to mitigate aero-optic effects. The advantage of this approach was that full-field data could be used to develop and train neural networks to predict the evolution of the flow field and to compute optical phase corrections. This was accomplished

by using a low-order description of the flow obtained by a proper orthogonal decomposition technique applied to full-field index of refraction data.

### **I.1. Dynamic Aero-Optic Interactions in Turbulent Shear Flows**

Until recently, the treatment of aero-optics flows has been based on the assumption that the random, statistically homogenous index of refraction variations were advected by an isotropic and homogenous turbulent flow. The failure of traditional statistical methods to fully characterize the temporal and spatial frequencies associated with the aero-optics distortions in turbulent shear flows containing large coherent structures, suggested that the assumption of homogeneity was too limiting. The effect of large coherent vortical structures in a low-speed plane shear layer of two dissimilar gases on optical distortions was investigated experimentally by Chew and Christiansen (1990), who asserted that optical phase distortions could not be accurately predicted by assuming that the turbulent medium is homogeneous. Measured intensity profiles of a large diameter light beam (6.5 cm) propagating through a shear layer exhibited multiple peaks instead of a single Gaussian-like peak with small amplitude fluctuations that would be expected for a homogeneous shear layer, clearly indicating the effect of the large coherent structures on optical distortion. Similar observations were made by Wissler and Roshko (1992) who investigated the distortion of small diameter He-Ne laser beam propagating through the cross stream direction of a low-speed plane turbulent shear layer (high-speed stream velocity 3-10 m/s). They performed experiments in both equal ( $\text{He}/\text{N}_2$ ) and unequal ( $\text{N}_2/\text{He-Ar}$ ) density mixing layers, and found that beam deflections in the streamwise direction are associated with the spanwise coherent vortical structures. Spanwise deflections, which can exceed streamwise deflections, were caused by the appearance of streamwise vortices and exhibited large variations across the span of the flow.

Of particular note is the work of Fourguette and Dimotakis (1995) who discovered the appearance of streaks in Rayleigh-scattering images of a laser sheet propagating through a turbulent jet of ethylene issuing into nitrogen, and conjectured that these streaks may be formed by vortical structures within the flow. A comprehensive review of the recent advances in the study of dynamic aero-optic interactions can be found in Jumper (1997).

As noted by investigators of aero-optic effects (e.g., Chew and Christiansen, 1990), the receptivity of turbulent shear flows to external excitation and its dramatic effects on the evolution of the large vortical structures may provide a powerful tool for the control of optical distortions. The effect of forcing on the evolution of large coherent structures has been the subject of numerous investigations (e.g., Crow and Champagne 1971, Oster and Wygnanski 1982), with particular interest in mixing enhancement (e.g. Roberts 1985).

Nygaard and Glezer (1991) utilized a mosaic of surface heaters mounted on the flow partition to investigate the effect of spanwise periodic excitation on the evolution of spanwise and streamwise vortices in a plane water shear layer. One of the main findings of this investigation was that streamwise vortices could be easily triggered at an arbitrary wavelength by the heater array, and that their appearance leads to a substantial increase in small-scale motions which can be related to the onset of the mixing transition. In a later work in the same facility, Nygaard and Glezer (1994) used a surface heater array to demonstrate that a time-harmonic wavetrain having spanwise nonuniform phase distribution could be used to force complex pairing interactions between the spanwise vortices. These authors showed that development of excitation schemes has progressed to the point where the large coherent structures governing mixing in the plane shear layer can be manipulated with great versatility.

More recently, Wiltse (1993) demonstrated that these schemes can be used to manipulate the large and small-scale vortical structures, leading to mixing enhancement in open and closed-loop control experiments. These experiments were conducted in a closed return water shear layer facility, using a thermal analog to the concentration measurements normally performed in blowdown shear layer facilities. The extent of mixing was inferred from the time-dependent temperature distribution that



was measured using a rake of 31 cold-wire sensors. This approach relied on excitation of large-scale instabilities within the flow where the small scales, which ultimately lead to molecular mixing, are affected indirectly through the classical cascading mechanism.

Wiltse and Glezer (1993) used direct excitation of the small scales within the dissipation range of an air jet to demonstrate the long range interactions between widely disparate scales in the turbulent flow. In these experiments, each of the four shear layer segments of a square jet was forced by a planar bimorph actuator driven at a resonance frequency well within the dissipation range of the base flow. These experiments also showed that the base flow was very sensitive to the addition of low-frequency sidebands to the excitation frequency, leading to the appearance of large scale vortical structures and modification of entrainment and mixing.

One of the objectives of the present work was to investigate the effect of direct small-scale excitation on mixing and aero-optics distortions in a plane shear layer. To that end, planar laser-induced fluorescence of a temperature sensitive fluorescent dye was used to acquire two-dimensional maps of the scalar temperature field. A review of previous work using laser induced fluorescence is presented in the following section.

## **1.2. Laser Induced Fluorescence Measurements**

Laser induced fluorescence (LIF) has proven to be a powerful tool in the study of turbulent flows. Direct measurements of scalar transport in turbulent flows are usually performed in blow-down facilities using measurements of fluorescence intensity of dye mixed with the fluid (typically water). A monochromatic light source is normally used to excite an energy transition in a fluorescent dye, and the resulting fluorescence is captured by an imaging array. A comprehensive review of the laser induced fluorescence is given in Hanson (1988) and Eckbreth (1996).

One of the first studies where the laser induced fluorescence was used for quantitative measurements was performed by Dimotakis et al. (1982). These authors used laser sheet illumination to study the dynamics of round turbulent jets and recorded the fluorescence data by a linear scanning photodiode array, which eliminated the need for the photographic recording of the fluorescence. Later, Koochesfahani and Dimotakis (1986) used laser-induced fluorescence to investigate entrainment and mixing in reacting and a nonreacting shear layers. This work was an extension of the earlier work of Dimotakis et al. (1982). The optical setup consisted of an argon-ion laser with a long focal length lens, and scanning photoarrays which were used to measure the fluorescence intensity along the beam. In the nonreacting case, measurements of the fluorescence intensity provided a direct measure of the dye concentration, and thus of the relative concentration of high- to low-speed fluid in the shear layer. In the reacting experiments, the concentration of the product of the reaction was directly proportional to the fluorescence intensity of the Fluorescein dye premixed with the acid solution.

Most of the early studies that utilized laser induced fluorescence for scalar measurements were not concerned with problems such as laser beam extinction or temperature dependence of the fluorescence. Walker (1986) examined laser induced fluorescence technique in bench tests and in a liquid jet (1 m/s), and considered the beam extinction, laser saturation as well as temperature dependence of disodium Fluorescein which was used for concentration measurements. Bench measurements were performed in a test cell (flask or beaker) and the fluorescent intensity was used to determine a concentration that provided a suitably high intensity without significant self-absorption ("extinction") effects. This technique was used, together with the laser Doppler velocimetry, to perform concentration and velocity measurements in the turbulent submerged water jet.

Sakakibara et al. (1993) used the cross-correlation technique and temperature dependent fluorescence of Rhodamine B to simultaneously measure velocity and temperature fields in a stratified pipe flow. They confirmed that, if the concentration and absorptivity were constant, the

fluorescent intensity of Rhodamine B varied almost linearly with temperature for a range of temperatures between 20 °C and 70 °C, and that the sensitivity of Rhodamine B fluorescence was about 2.5 %/K.

Dahm et al. (1992) and Buch and Dahm (1996) performed a series of experimental investigations into the small-scale structure in turbulent shear flows using highly resolved spatio-temporal laser-induced fluorescence measurements. The jet-fluid mixture fraction was determined from the measured fluorescence intensity of the dye mixed with the fluid, with spatial and temporal resolution that allowed accurate determination of the local instantaneous scalar gradient field. These results were used to show that the scalar gradient vector field for large Schmidt numbers (defined as the ratio of kinematic viscosity to molecular diffusivity) was nearly isotropic, and that the scalar dissipation rate had a shape that was consistent with the layer-like small-scale structures.

An important connection between the structure of a turbulent shear layer flow and various parameters, such as Reynolds number and speed ratio, was made by Karasso and Mungal (1996). They used the planar laser induced fluorescence technique for scalar (concentration) and chemical product measurements in a two-dimensional liquid shear layer (high-speed stream velocity was varied between 0.34 m/s and 1.9 m/s). These results were used to determine the accuracy of the passive scalar measurements and to show that the probability density function for a fully developed, turbulent mixing layer evolves from a non-marching type to a tilted type. Smith and Mungal (1998) studied the mixing in a round air jet normal to a uniform crossflow (jet-to-crossflow velocity ratio was varied from 5 to 25) using planar laser-induced fluorescence of acetone vapor seeded into the jet. Instantaneous images of the scalar concentration field were characterized by distributed regions of high-concentration fluid, and showed deep penetration of the free-stream fluid into the upper edge of the jet.

More recently, Sakakibara and Adrian (1997) used a two-dye approach for the correction of fluorescence-dependent temperature measurements in a natural convection flow over a heated surface within a closed container. Their approach was based on simultaneous measurements of intensity of two fluorescent dyes (Rhodamine B and Rhodamine 110), whose ratio of fluorescent intensities was temperature dependent.

One of the advantages of the laser induced fluorescence technique is that it provides instantaneous two-dimensional scalar measurements, which is particularly useful for the investigation of flows dominated by large scale structures. However, the amount of data produced in such experiments is usually large and unsuitable for direct application in optical phase correction systems where the correction must be performed in real time. Thus, a low-order description of the flow is typically needed in order to reduce the effort required for real-time computation of optical phase corrections. In this work, a reduced order description of the shear layer flow dynamics was based on a proper orthogonal decomposition technique (POD), in which a small set of modes captured a large fraction of the energy in the measured temperature field. A summary of previous work using proper orthogonal decomposition is presented in the next section.

### **I.3. Proper Orthogonal Decomposition**

Although the presence of coherent structures in turbulent flows and their influence on aero-optical distortion have been investigated extensively, the extraction of deterministic features that can be used for correction schemes remains a challenging problem. In contrast to conditional sampling methods that required some arbitrary choice of detection functions and threshold values, Lumley (1967 and 1981) proposed an unbiased technique for identifying coherent structures in a given set of realizations of a turbulent flow field using proper orthogonal decomposition (POD). The most significant aspect of the POD approach is that it can be used to approximate the flow field using time-invariant eigenfunctions multiplied by time-dependent coefficients, thus providing a partial separation of spatial and temporal structure, along with a means for flow reconstruction and approximation.

Early applications of the POD technique in fluid mechanics date back to Payne (1966) who applied the POD method to a wake behind a cylinder, and Bakewell and Lumley (1967) who studied the near-wall region of turbulent pipe flow. This technique has been used by number of researchers to study turbulence, including the numerical simulation of channel flows (Moin 1984, Moin and Moser 1989, Sirovich et al. 1990, and Ball et al. 1991), turbulent jet flow (Glauser and George 1987, and Sirovich et al. 1990), turbulent pipe flow (Herzog 1986), and the plane turbulent mixing layer (Ukeiley and Glauser 1995, and Delville et al. 1989, 1993). An extension of the classical POD method was developed by Glezer et al. (1989) and used to compute modes that efficiently captured a large fraction of the "action" in a forced shear layer. The extended POD can be used in flows that are not necessarily statistically homogeneous and stationary and does not require computation of the second-order correlations.

Berkooz et al. (1993) gave an excellent review of applications of the proper orthogonal decomposition in the analysis of turbulent flows, and compared this technique to statistical and deterministic methods typically used in turbulence studies.

Several authors have suggested that for turbulent flows dominated by energetically dominant coherent structures, it should be possible to develop a low-dimensional model of the flow by using only the most energetic structures (Sirovich 1987, Holmes et al. 1996). These authors suggested that the POD technique could be used as a basis for low-dimensional approximation of the flow dynamics, and proposed the procedure for developing a system of ordinary differential equations which described the evolution of the turbulent flows, such as shear layers, jets, wakes and boundary layers. Aubry et al. (1988) used the proper orthogonal decomposition to expand the instantaneous velocity field in empirical eigenfunctions, and to construct a system of ordinary differential equations suitable for description of the flow dynamics in the wall region of a turbulent boundary layer. The resulting system of 10 ordinary differential equations revealed a rich bifurcation structure and existence of the bursting phenomenon in the pipe flow near the wall.

In a later work, Zhou and Sirovich (1992) considered the dynamics of coherent structures in the wall region of a turbulent channel flow using the proper orthogonal decomposition and Galerkin procedure to derive the dynamical description. The behavior of the resulting low-dimensional model equations included intermittency, quasi-periodicity and chaos. Three-dimensional effects were included in order to provide satisfactory explanation of bursting and ejection events in turbulent boundary layers.

Rajaei et al. (1994) applied the snapshot POD technique to two-dimensional acoustically excited shear layer flow, and found that the first few modes carried a large fraction of the fluctuating energy. Time-dependent coefficients corresponding to those modes exhibited almost perfect sinusoidal oscillations. These authors used a Galerkin projection of the Navier-Stokes equations onto the POD modes to obtain a low-dimensional system, the solution of which described the dynamics of the coherent structures. They found good agreement between the simulated and experimentally determined time coefficients for systems with eight and sixteen POD modes.

## II. EXPERIMENTAL APPARATUS AND TECHNIQUES

### II.1. Experimental Facility

The shear layer facility used in the present research (Figure 1) was described in detail in Nygaard and Glezer (1991) and Wiltse (1993). An external heat exchanger was added in an effort to increase maximum temperature difference between the two streams. Water from the diffuser was simultaneously pumped through a heat exchanger and a 63 kW circulation heater, and then injected back into the low- and high-speed streams using multiple jets in order to increase mixing. The average temperatures of the two streams were kept at  $T_L=17^\circ\text{C}$  and  $T_H=22^\circ\text{C}$  for most

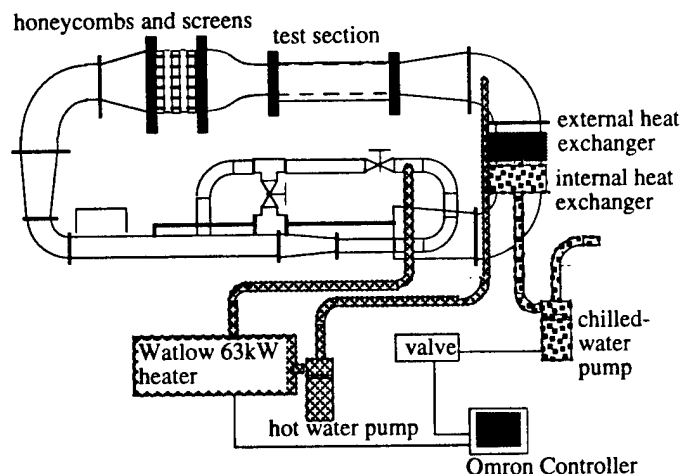


Figure 1. Water shear layer facility

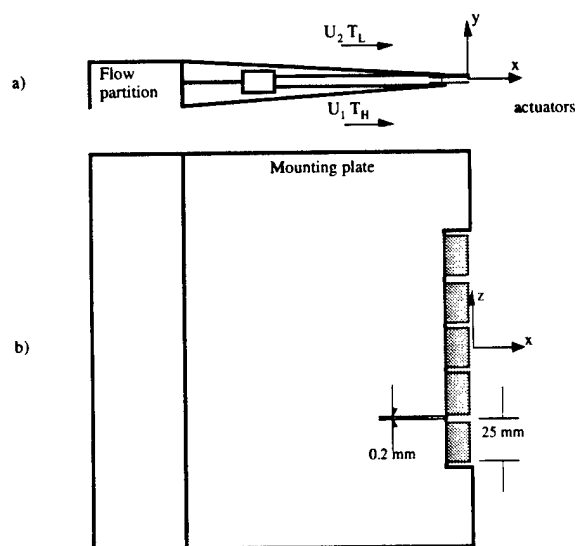


Figure 2. Schematic drawing of the cross stream (a) and span (b) views of flow partition. The span view shows actuators array, which is comprised of five actuator pairs.

## II.2. Laser Induced Fluorescence Technique and Instrumentation

Laser induced fluorescence (LIF) was used to measure temperature distributions in the shear layer by exploiting the temperature-dependent fluorescence of Rhodamine B. The temperature distribution obtained from the Rhodamine B intensity map was distorted due to optical aberrations at the laser sheet caused by sharp density gradients between hot and cold streams. This effect was corrected for by simultaneous measurements of fluorescence of Rhodamine B and disodium Fluorescein, whose fluorescence was only weakly dependent on temperature, with two separate imaging systems. Both Rhodamine B and disodium Fluorescein were water soluble, and their fluorescence was excited using a single multi-line argon ion laser beam.

Rhodamine B was selected for the temperature measurements because of its high temperature sensitivity, and short reaction time required to reach the lowest vibrational level from which the fluorescence occurs (typically less than 10 ns). However, this time was long enough for the absorption and emission orientations to be independent (molecules were randomly spun during this

experiments, but could be varied in a range between 10-35 C°. The temperature of each stream at the entrance of the test section was maintained constant to within  $\pm 0.03^\circ\text{C}$  with two Omron controllers that were used to regulate the amount of chilled water supplied to the heat exchangers and the amount of heat generated by the heater. Temperature in various sections of the facility was measured by RTD temperature sensors, and the free-stream velocities were measured with a Pitot tube connected to a pressure transducer that was calibrated for a velocity range between 0-2 m/s.

The flow partition was made from polyvinyl chloride, and was equipped with a removable stainless steel splitter plate instrumented with an array of piezo-electric actuators. Figure 2 shows a spanwise view of the test section geometry and the trailing edge of the flow partition. The test section windows were modified in order to provide optical access for the laser beam and to minimize the laser beam path through the shear layer. A  $45^\circ$  reflective mirror was placed on one side of the test section in order to prevent reflections. The flow was visualized by using equally-spaced dye-injection ports located on each side of the flow partition.

time) and the fluorescence was independent of direction. This dye has a fluorescence quantum yield (defined as a ratio of photons emitted per photon absorbed) of about 0.4 between 15°C and 30°C.

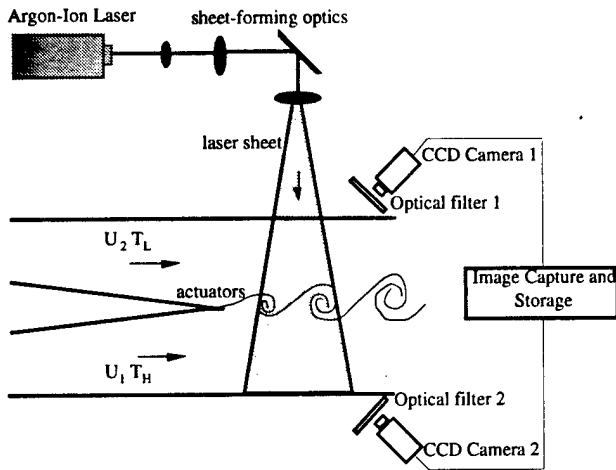


Figure 3. LIF optical setup.

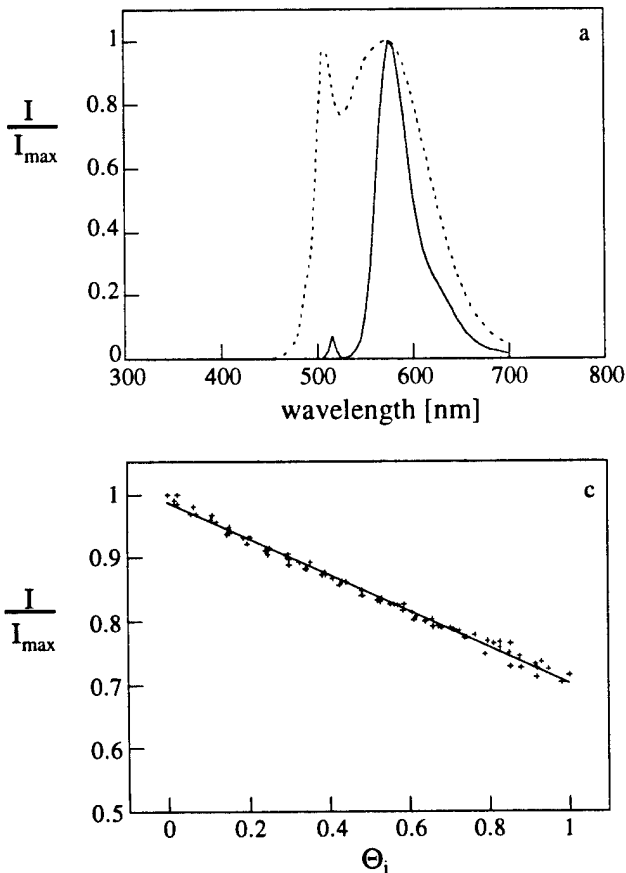


Figure 4. a) Emission spectra Rhodamine B (solid line) and Rhodamine B/Fluorescein (1:1 mass ratio, dashed line). b) Temperature sensitivity of Rhodamine B ( $\Theta_i = 1 - \Theta$ ).

The optical arrangement for fluorescence measurements is shown in Figure 3. The beam of an argon ion laser (Coherent Innova 90 - 5W) was expanded into a sheet with an optical setup (Prenel et al. 1989) that allowed for precise control of the Rayleigh range ( $\pm 8$  cm on either side of the focal point) and the width of the sheet (15 cm at the focal point). The thickness of the laser sheet was estimated to be  $\leq 1$  mm. The temperature distribution in the plane of the laser sheet were measured using a pair of high-speed (128 x 128 pixels, 800 fps) Dalsa CCD cameras, each with a Nikon 50 mm f/1.2 lens, whose gain and offset could be independently controlled using a PCI image capture board with variable scan input and a host laboratory computer (Figure 3). The maximum frame rate of the CCD array was 838 fps (equivalent to temporal resolution of 1.2 ms), but most of the experiments were performed at a lower frame rate in order to acquire data corresponding to the passage of a large number of vortical structures suitable for statistical analysis.

In order to eliminate the effects of the excitation light sheet non-uniformities, reference intensity maps were acquired at the equilibrium state when the temperatures of the two streams were identical. The main reason for the laser sheet non-uniformity was light absorption by the fluorescent dye, which resulted in variations of the laser sheet intensity in the cross-stream direction of the shear layer. This attenuation of the propagating laser sheet could amount to 45% of the intensity difference between the two streams with different temperatures. It is important to note that the pixel output is linearly proportional to the fluorescence intensity received from the measurement volume and thus proportional to the intensity of the excitation light.

The emission spectra of solutions of Rhodamine B and a 1:1 Rhodamine B/Fluorescein mixture of low concentration

in water (50-300  $\mu\text{g/l}$ ) are shown in Figure 4a. Results indicate that Rhodamine B has an absorption peak at around 540 nm and emits in a range between 560-650 nm, with the peak at around 580 nm. It is important to note that the absorption and emission spectral peaks of Rhodamine B water solution are separated by almost 40 nm so that the fluorescence light coming from the measurement volume can be separated from the scattered light with the high pass optical filter. Disodium Fluorescein has an absorption peak at around 485 nm and an emission peak around 515 nm. Fluorescence intensities of Rhodamine B and disodium Fluorescein were simultaneously imaged on camera sensors through a 560-nm high pass filter and a combination of 490-nm high pass filter and 550-nm low pass filter, respectively.

The optical diagnostics system used to calibrate the temperature-dependent fluorescence intensity of Rhodamine B consisted of a multi-line laser beam (wavelengths of 488 and 514 nm) that excited the fluorescence of Rhodamine B solution contained in a small cell (15 cm length, 8 cm width and 3 cm height) with two brass surfaces (top and bottom) whose temperatures ( $T_{\text{top}}=T_{\text{bottom}}=T$ ) were controlled using a Peltier junction and a pair of embedded thermistors. A linear RTD element, coupled with the highly accurate Fluke Thermometer, was used to measure the temperature with an accuracy of 0.02°C. The temperature of the solution was varied between  $T_{\text{Low}}=14^\circ\text{C}$  and  $T_{\text{High}}=26^\circ\text{C}$  and normalized as  $\Theta=(T-T_{\text{Low}})/(\Delta T)$ , where  $\Delta T=T_{\text{High}}-T_{\text{Low}}$ . The fluorescence intensity was measured using the Burr-Brown integrated photodiode (2.29 mm square array) and the amplifier. The excitation beam was independently monitored using a photodetector placed in the laser head, in order to correct for fluctuations of the laser intensity.

The calibration measurements were performed for different concentrations (50-400  $\mu\text{g/l}$ ) and several excitation beam intensities, and the detected intensity was normalized by the intensity at the lowest temperature. The relation between temperature and fluorescence intensity of Rhodamine B shown in Figure 4c was independent of the dye concentration, confirming that the temperature dependence of the fluorescence was not due to dimerization of the dye molecules that tend to aggregate in solutions. The measurements shown in Figure 4c indicate that the fluorescence intensity decreases with increasing temperature of the fluorescent dye solution, with a temperature coefficient of 2.5 %/K (these results were later confirmed in the shear layer facility). A functional relationship between the temperature and the normalized intensity was approximated by a linear least-square method, based on more than 50 measurements.

The Rhodamine B concentration for the temperature measurements in the shear layer facility was selected based on measurements of fluorescence intensity and attenuation of the transmitted light for different dye concentrations. While the attenuation was negligible for very low concentrations ( $<10 \mu\text{g/l}$ ), it became more important for concentrations that were required in order to provide enough fluorescent intensity for the temperature measurements in the shear layer. The optimal concentration was determined by the intersection of the two curves describing the laser beam attenuation and fluorescence intensity dependence on the concentration of Rhodamine B. For the optimal concentration of  $c_{\text{Rh}}=220 \mu\text{g/l}$ , laser sheet propagating through the shear layer test section was attenuated at the rate of 2.5 %/cm, and this rate remained unchanged as long as the dye concentration remained constant.

### II.3. Piezoelectric Actuators

The presence of large coherent structures significantly influences optical effects in the plane shear layer. A question arises as to whether the evolution of the coherent structures can be manipulated in such a way that the optical phase distortion can be predicted or controlled. While entrainment of irrotational fluid in turbulent shear flows is effected by large-scale motions, molecular mixing (and hence reduction of index of refraction gradients) ultimately takes place at the smallest scale. The traditional approach to control of mixing through manipulation of global instability modes of the base flow depends on the classical cascading mechanism to transfer energy from the large coherent structures, whose evolution is being manipulated, to the scales at which molecular mixing occurs. Although the mixing at the smallest scales is coupled to the control of large coherent structures,

more efficient control of mixing might be achieved by direct control of both the large-scale and the small-scale mixing processes.

Mixing enhancement in the shear layer was accomplished by direct excitation of small scales within the dissipation range of the base shear layer flow using an array of cantilevered piezoelectric actuators mounted at the trailing edge of the splitter plate separating the two streams. These actuators must be able to operate at high frequencies (200-300 Hz), in order to apply forcing at frequencies approximately two orders of magnitude higher than the most unstable frequency of the base flow (3-6 Hz). Furthermore, these actuators must be small and able to apply significant disturbances to the flow in order to directly excite small scale motions.

Several test actuators were developed and built in order to determine their frequency response and maximum displacement. The actuators used in this research consisted of a 0.28 mm thick piece of a lead-zirconate-titanate (PZT) ceramic (15 mm long and 24 mm wide) bonded to a 0.13 mm thick stainless steel blade that was 25 mm long and 25 mm wide. When the voltage (15-50  $V_{rms}$ ) is applied across the piezo-ceramic surface of the cantilevered actuator, the cantilever oscillates with a resonance frequency that can be determined from the analysis of the beam dynamics. Furthermore, these actuators require significantly less power (typically 1-3 mW) than conventional mechanical actuators or surface-mounted film heaters. The advantage of this approach, first developed by Wiltse and Glezer (1993) and later applied by Jacobson (1995), is that the small strain in the piezoelectric material produced by an applied voltage results in a large tip deflection.

An array of piezoelectric actuators (Figure 2) consisted of 5 pairs centered around the middle plane in the spanwise direction and separated by narrow gaps (0.1 mm). The PZT material was coated with two layers of a copolymerized Astroseal coating made by EPD Technology Corporation in order to electrically insulate piezo-ceramics from the surrounding water. Each pair of piezoelectric actuators was wired through the splitter partition to individual AC power amplifiers, each capable of providing up to 80  $V_{rms}$ . The actuators were operated in phase with each other for different frequencies, and the resonant frequency was estimated from the flow visualization of a wake behind the blade. The resonant frequency in water varied from about 220 up to 250 Hz, due to slight differences between actuators.

Each actuator pair produced a zero mass flux jet that was synthesized from the surrounding fluid and was comprised of a train of small-scale vortex pairs. A vortex pair was formed when the actuator blades were deflected toward each other during one-half of the driving cycle and the fluid contained between them was ejected out. During the second half of the cycle, the actuators were deflected away from each other and surrounding fluid was drawn into the space between the actuators.

The flow around an actuator pair driven at a constant amplitude was visualized using a colored dye and an argon-ion laser sheet, and the measurements were taken with a high-speed CCD camera array (image size was 8 mm square) at 838 fps. The dye was introduced upstream of the actuator pair, along the span of the splitter plate, and the free stream velocities were held constant at low speeds ( $U_1=U_2=9$  cm/s) in order to remove the dye from the field of view. The laser sheet was oriented in the x-y plane.

A sequence of 8 consecutive images of the actuator flow disturbance (separated by 1.2 msec) in Figures 5a-h (spatial resolution was 60  $\mu m$ ) shows vortex pairs formed near the trailing edges of the actuator pair blades. The vortices have diameters of about 0.5 mm, and are formed at the resonant frequency of the piezoelectric actuator blades. The vortical structure becomes visible about 0.5 mm downstream from the cantilever blade tip, and remains coherent for a few millimeters downstream. The vortex pairs are originally centered at  $y=\pm 0.8$  mm (where  $y=0$  is at the geometrical center of the shear layer), but they are displaced in the cross-stream direction farther downstream at a spreading angle of about  $10^\circ$ .

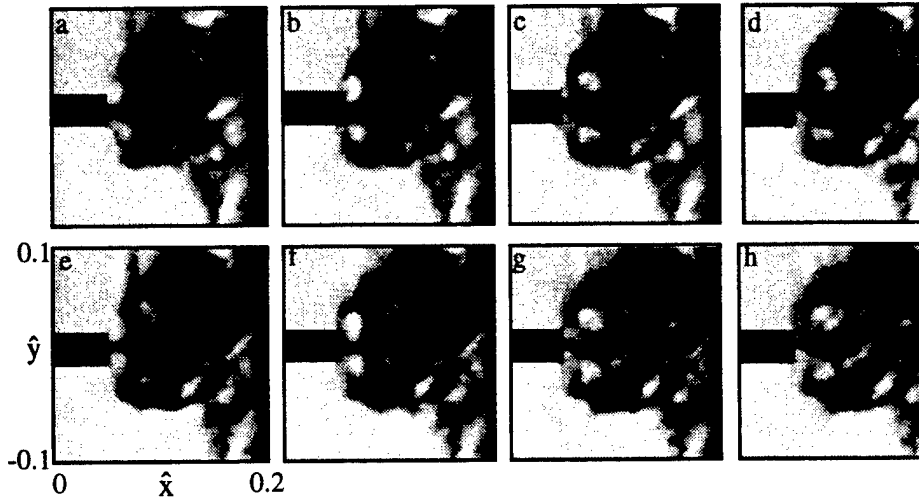


**Figure 5.** Instantaneous actuator flow field visualization,  $f=225$  Hz. Sequence of 8 consecutive frames separated by 1.2 msec (a-i).

the actuator, where  $\lambda_{K-H}=5.0$  cm is the wavelength of the initial instability for the shear layer with free stream velocities  $U_2=24$  cm/s and  $U_1=9$  cm/s. The intensity measurements were taken at 838

The fact that the vortex pairs are generated at the forcing frequency indicates that the intensity measurement should fluctuate at the same frequency close to the actuator blade tip. Figures 6a-c show normalized intensity power spectra indicating the flow fluctuations at  $y=0$ ,  $z=0$ , and  $\hat{x}=x/\lambda_{K-H}=0.1, 0.11$  and  $0.5$  away from

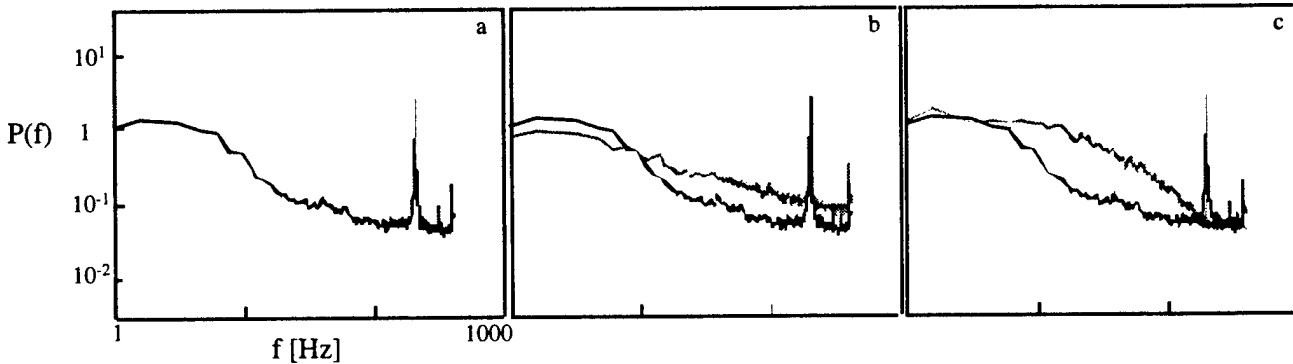


**Figure 6.** Normalized power spectra indicating flow fluctuations at the centerline at  $z=0$  cm and  $x/l_{K-H}=0.1$  (a),  $0.11$  (b) and  $0.5$  (c) for the 24:9 shear layer.

fps, and 30 sequences, each with 2400 image, were taken at each location. In order to smooth the spectrum and reduce the variance, the sequences were divided into overlapping sub-sets of 1024 frames and the power spectrum was calculated for each sub-set and then averaged. The resulting frequency resolution for the data presented in Figure 6a-c was less than 1 Hz.

At the first streamwise position  $\hat{x}=0.1$ , a sharp peak is evident at the forcing frequency, together with a weaker peak at the first harmonics of the forcing frequency. The spectrum for the first streamwise position, where the spectral peak at the forcing frequency is strongest, is plotted as a reference case for all streamwise positions shown in Figures 6b-c. Notice that the spectral peak at the forcing frequency rapidly decays with the streamwise distance, indicating that the flow fluctuations at this frequency are very dissipative. At the second streamwise position ( $\hat{x}=0.11$ ), more than half of the energy contained at the forcing frequency at  $\hat{x}=0.1$  was dissipated, as indicated by the decrease of the spectral peak and the corresponding increase in energy contained at other scales. Farther downstream ( $\hat{x}=0.5$ ), the spectral peak at the forcing frequency is barely visible, and there is a significant increase in energy at almost all scales.

The spatial distributions of the spectral components (normalized with the maximum value) at the forcing frequency and the first harmonics are shown in Figures 7a-c, together with streamwise



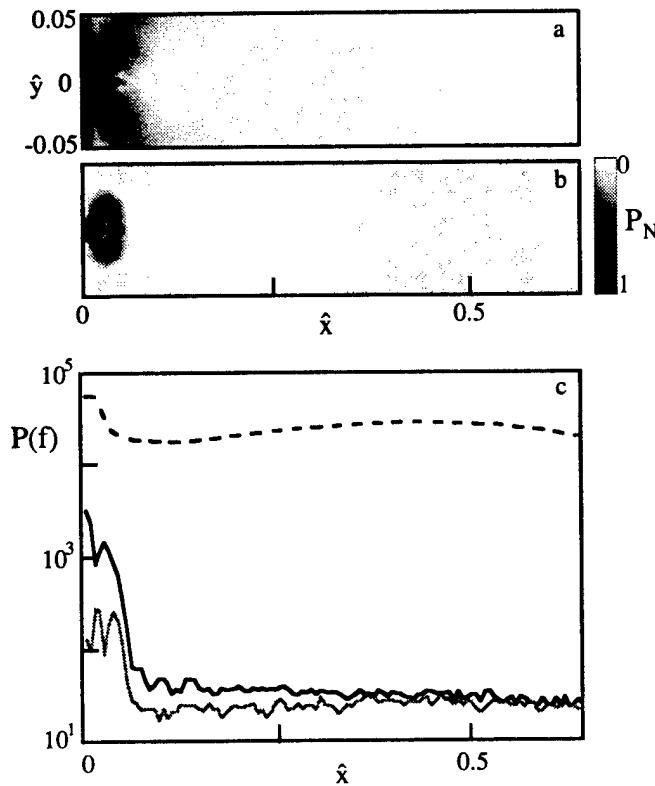


**Figure 7.** Spatial distributions of the spectral components (normalized with the maximum value) at the forcing frequency (a) and its first harmonic (b) for the 24:9 shear layer (logarithmic scale), (c) Streamwise variations of the spectral components at the forcing frequency (black line), first harmonic (gray line), and the mean intensity (dotted line).

distributions at the centerline of the jet. It is clear from Figure 7a that the spectral peak at the forcing frequency has two maxima at spatial locations where the vortex pair is the strongest. It is also evident that the flow fluctuations are localized to a narrow region around the actuator and are practically undetectable at any cross-stream elevation at  $\hat{x}=0.18$ . That the flow disturbance at the forcing frequency is weak and localized around the actuator is an indication of the essentially steady nature of the actuator flow disturbance. The streamwise dependence of the spectral peaks at the forcing frequency and its first harmonic (Figure 7c) show that the maximum of the spectral peak at the forcing frequency corresponds to the minimum of the first harmonics, and vice versa. It is noteworthy that the mean centerline intensity decreases during this interaction, after which the energy content at the forcing frequency and its first harmonic becomes negligible.

The actuators' mean and fluctuating temperature disturbances were measured in the shear layer using the LIF technique described earlier, for the free-stream velocities  $U_2=24$  cm/s and  $U_1=9$  cm/s. Henceforth, we will

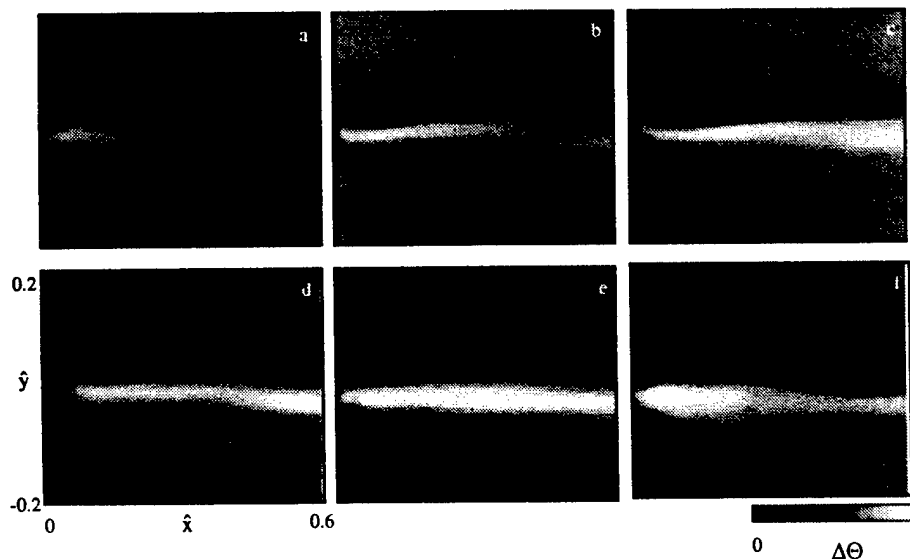


**Figure 8.** Actuator mean temperature disturbance in the x-y plane for a typical actuator operated at different forcing amplitudes  $V_N$  (normalized by  $45 V_{rms}$ ).  $V_N = 0.45$  (a), 0.55 (b), 0.66 (c), 0.77 (d), 0.88 (e), and 1.0 (f) for the 24:9 shear layer.

refer to this as a 24:9 shear layer, and to shear layers with  $U_2=36$  cm/s and  $U_1=12$  cm/s, and  $U_2=42$  cm/s and  $U_1=14$  cm/s as 36:12 and 42:14 shear layers, respectively. A non-dimensional temperature is defined as  $\Theta=(T-T_L)/\Delta T$ , where  $T_L$  is the temperature in the high speed stream, and  $\Delta T=T_H-T_L$  is the temperature difference between the two streams. Figures 8a-f show the two dimensional mean temperature disturbance in the x-y plane for a typical actuator operated at different forcing amplitudes. The actuator amplitude,  $V_N$ , was normalized by the amplitude of 45  $V_{rms}$  (used in most experiments), and the mean temperature disturbance,  $\Delta\Theta=\Theta_{for}-\Theta_{unf}$ , was defined as the difference between the measured non-dimensional mean temperatures for the forced and unforced flow. The spatial and temporal resolutions of the measurements were 210  $\mu m$  (image size was 2.7 cm square) and 2.5 msec (400 fps), respectively, and the data shown in Figures 8a-f were averaged over 2400 successive frames (corresponding to 10 sec of the flow). The trailing edge of the actuator blade was aligned with  $\hat{x}=0$ , and its cross-stream elevation is  $\hat{y}=y/\lambda_{K-H}=0$  mm. The bright and dark regions correspond to positive and negative disturbances, respectively, where the positive disturbance indicates a decrease in the mean temperature with forcing.

At low forcing amplitudes, the influence of the forcing is weak and is confined to the region around the actuator tip (Figure 8a). The streamwise region of the forcing is significantly expanded with increased forcing amplitude. The temperature disturbance map in Figure 8b shows a strong concentration of negative disturbance away from the blade in the high-speed free stream (cold stream in the upper half of the image), and positive disturbance away from the blade in the low-speed free stream (warm stream in the bottom part of the image). Between these two well-defined regions with concentrated disturbance, there is a closed region where the temperature disturbance is much weaker. Video imaging of the flow indicates that the fluid within this region is recirculating in the clockwise orientation. This region extends 1-2 cm downstream, depending on the forcing

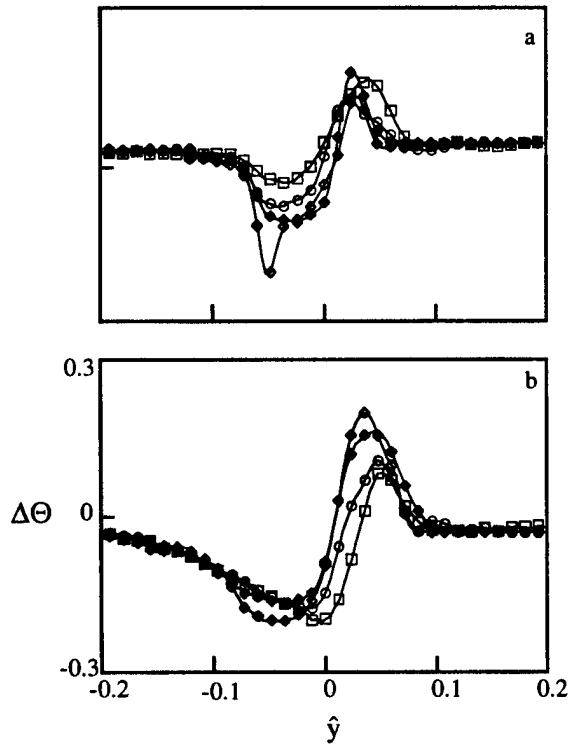


**Figure 9.** Cross-stream distribution of the average temperature disturbance  $V_N = 0.66$  (a) and 1.0 (b), at  $x/\lambda_{K-H} = 0.1$  (○), 0.25 (□), 0.4 (△) and 0.55 (◇) for the 24:9 shear

amplitude, and remains closed for  $V_N < 0.6$ . With further increases in the forcing amplitude, the closed region opens on its downstream end and two well-defined layers of positive and negative disturbance are formed. The cross-stream distribution of the temperature disturbance normalized with the mean temperature of the unforced flow is shown in Figure 9a-b to illustrate the increase in the transverse extent of the actuator disturbance. Note that the cross-stream profile taken at  $V_N = 0.66$  (Figure 9b) and  $\hat{x} = 0.1$  has a slight slope discontinuity associated with the closed region near the actuator blade. The peak temperature disturbance  $\Delta\Theta$  and the cross-stream region of influence are 0.15 and 7.6 mm at  $\hat{x} = 0.1$ , and 0.09 and 9.3 mm at  $\hat{x} = 0.55$ . Also note that the maximum  $\Delta\Theta = 0.25$  for  $V_N = 1.0$  (Figure 9b) at  $\hat{x} = 0.1$ , indicating a very strong temperature disturbance which remains significant farther downstream ( $\Delta\Theta = 0.12$  at  $\hat{x} = 0.55$ ).

As mentioned above, the strength of the vortex pairs and the extent of the actuator flow disturbance can be controlled by varying the amplitude of the forcing signal. The average actuator temperature

disturbance over the field of view (2.7 cm square) is defined as

$$\Delta\Theta_{avg} = \frac{1}{N_p} \sum_{j=1}^{N_p} \sqrt{\Delta\Theta_j^2} \quad (1)$$

where  $N_p$  is the total number of pixels in the image. Figure 10 shows the average temperature disturbance as a function of the actuator forcing amplitude.

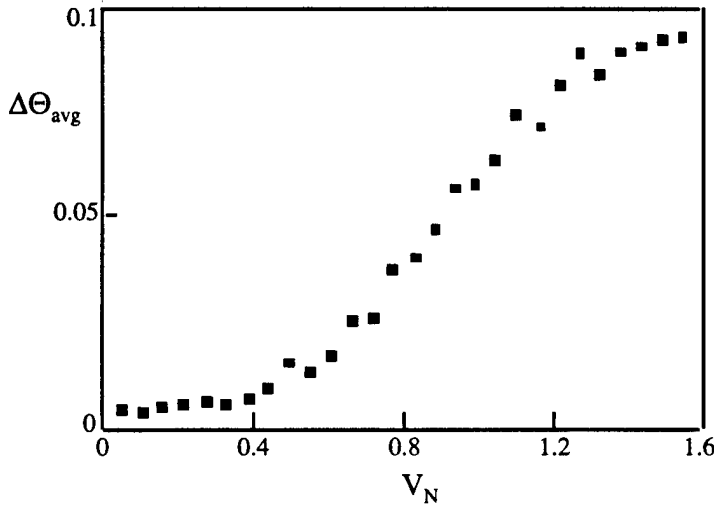


**Figure 10.** Average actuator temperature disturbance as a function of the actuator forcing amplitude for the 24:9 shear layer.

The actuator disturbance is very weak for  $V_N$  values below 0.4. In a region  $0.5 < V_N < 1.2$ , the temperature disturbance is increased almost linearly, and then continues to increase reaching the value  $\Delta\Theta_{avg}=0.065$  at  $V_N=1.0$ . In the present experiments, most measurements were taken with actuators operated at  $V_N=1.0$  (45  $V_{rms}$ ). Although the higher voltages provide stronger flow disturbance, prolonged operation at voltages higher than 45 V can cause leaks in the insulation around the piezo-ceramic elements.

It was also instructive to estimate the time response of the flow after the actuators are turned on or off. Measurements of the actuators' step response were performed for each case for  $V_N=1.0$  for the 24:9 shear layer. The phase-averaged data was calculated from 200 sequences consisting of 500 frames capturing the transition from the unforced flow to the fully forced flow and vice versa. The mean temperature disturbance,  $\Delta\Theta$ , was defined as the difference between the phase-averaged temperature field for each frame and the undisturbed temperature field (that is, first (on) or last (off) frame in the sequence). The times are nondimensionalized as  $t^*=t/t_r$ , where  $t_r = 110$  msec is the nominal time it takes for a fluid particle in the high-speed stream to travel across the field of view.

Time traces of the average temperature disturbance (Eq.1) normalized with its maximum value for the step-on and step-off cases are shown in Figure 11. Results for the step-on case indicate that the actuator flow disturbance becomes essentially steady for  $t^*>4$ . It is noteworthy that the flow remains unchanged during the first two fly-over times ( $t_r$ ), after which the temperature disturbance changes very rapidly until it reaches a steady state level. Similarly, when the actuator is turned off the flow becomes approximately steady for  $t^*>6$ . Note that it takes longer for the flow to return to the unforced conditions, and at  $t^*=6$  the flow is still slightly perturbed. Jacobson (1995) measured similar response times for cantilevered actuators and confirmed that

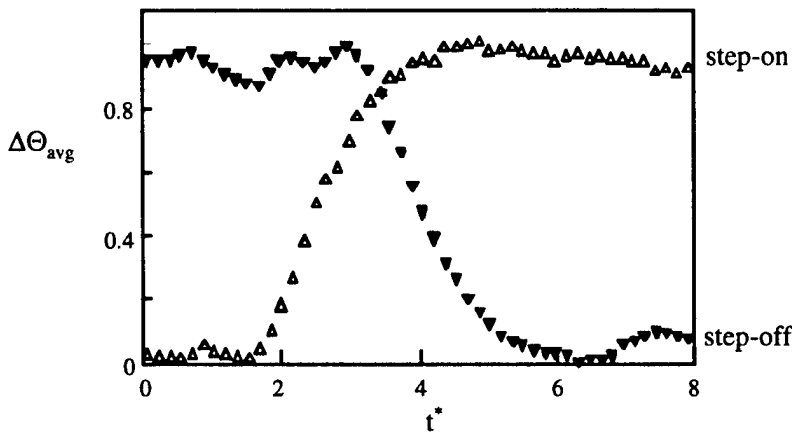


**Figure 11.** Time traces of the average temperature disturbance for the step-on ( ) and step-off ( ) for the 24:9 shear layer.

measured similar response times for cantilevered actuators and confirmed that

this kind of actuator was fast enough for control applications in a boundary layer flow.

## II.4. Experimental Conditions

Table 1 summarizes the flow conditions for which results were reported. Measurements were taken at several streamwise positions ( $0 < \hat{x} < 5.7$ ), over a range of Reynolds numbers [ $Re_\delta = (\Delta U \delta / \nu)$ , where  $\Delta U = U_2 - U_1$ , and  $\delta$  is the cross-stream extent of the shear layer] covering the mixing transition. The Reynolds number was controlled by changing the free stream velocities ( $4 \times 10^3 \leq Re_\delta \leq 1.9 \times 10^4$ ), and at each position a sequence containing 100-200 cycles (4000-6000 successive frames) of the base flow was captured and used to extract instantaneous 2-D temperature (and thus index of refraction) maps. Temperatures of the two streams were  $T_H = 22^\circ\text{C}$  and  $T_L = 17^\circ\text{C}$ , and they were nondimensionalized as  $\Theta = (T - T_L) / \Delta T$ , where  $T_L$  is the temperature in the high speed stream, and  $\Delta T$  is the temperature difference between the two streams. The measured region was approximately 6 cm in both the streamwise and the transverse directions, and was larger than the local shear layer thickness. The temporal and spatial resolutions were determined by the CCD array frame rate and the magnification ratio, and were held constant at  $\Delta t = 4.5$  msec and  $\Delta x = 0.45$  mm for all cases in Table 1.

Selected cases from the unforced shear layer were examined under three different forcing conditions: high-frequency forcing at the resonance frequency ( $f_H = 225$  Hz, actuator tip displacement 1 mm) of the piezoelectric actuators (HF), low-frequency forcing ( $f_L = 3$  Hz and 4.5 Hz) within the unstable range of the shear layer (LF), and the combination of the two (HF+LF). The level of the high-frequency forcing was quantified in terms of the momentum ratio  $J_{ac} = [U_j^2 h] / [U_c^2 \delta_{2.5}]$ , where  $h$  is the width of the actuator pair,  $\delta_{2.5}$  is the cross-stream extent of the shear layer at  $\hat{x} = 2.5$ ,  $U_c$  is the convective velocity of the shear layer, and  $U_j$  is the average velocity of the jet produced by a piezoelectric array (estimated from the step-on experiment and flow visualization). For the results reported in this dissertation, the estimated momentum ratio  $J_{ac}$  was between 0.025 and 0.075. A low-frequency forcing was achieved by using a time-harmonic forcing of the driving pump, which resulted in 5% fluctuations around the mean velocity in the shear layer, and was synchronized with the CCD camera image acquisition sequence to provide phase-locked information.

$U_j$ [cm/s]	$x$ [cm]	Unforced $Re_\delta$	$\Delta t$ [msec]	Forcing conditions
24	8-23	4200-7200	4.5	Unforced, HF, LF and HF+LF
36	8-23	6900-17000	4.5	Unforced, HF, LF and HF+LF
42	8-23	7100-19000	4.5	Unforced, HF, LF and HF+LF

### II.4.1. Resolution and signal-to-noise ratio

In the present experiments, temperature was used as a thermal analog to the concentration measurements normally performed in blowdown shear layer facilities. The two free streams were maintained at different constant temperatures ( $\Delta T = 5^\circ\text{C}$ ), and the extent of mixing was inferred from the time-dependent temperature distribution in the shear layer. The corresponding relevant parameter for mixing of temperature was the Prandtl number,  $Pr$ , which is defined as a ratio of kinematic viscosity and thermal diffusivity (Prandtl number is about 7 in water, and about 1 in air). For the mixing of chemical species, the corresponding relevant parameter is the Schmidt number,  $Sc$ , which is about 1 in air, but is three orders of magnitude larger in water. Thus, experiments that utilize temperature as a passive scalar for measurements in water are more comparable to mixing in air than are those involving mixing of species in water.

Scalar mixing measurements can be severely affected by their inability to resolve the finest spatial and temporal fluctuations which control the mixing process. The smallest diffusion (Batchelor) scale can be approximated by (Karasso and Mungal 1996)

$$\lambda_B \approx \delta \text{Re}^{-0.75} \text{Sc}^{-0.5} \quad (2)$$

where  $\delta(x)$  is the cross-stream extent of the shear layer,  $\text{Re}$  is the Reynolds number based on  $\delta(x)$  and the free-stream velocity difference, and the Schmidt number should be replaced by the Prandtl number for the temperature measurements. The smallest diffusion scale is related to the smallest velocity scale (Kolmogorov microscale)  $\eta$  through the ratio  $\eta/\lambda_B = \text{Sc}^{3/4}$  (Tennekes and Lumley 1972). For mixing of species in water, the smallest diffusion scale can be two orders of magnitude smaller than the smallest velocity scale (typically,  $\text{Sc} \sim 2000$  and  $\lambda_B \sim 1\text{-}10 \mu\text{m}$ ). In contrast, for mixing of temperature in water the smallest diffusion and velocity scales are of the same order and related through the ratio  $\eta/\lambda_B = \text{Pr}^{3/4} \sim 4.3$ .

In the present experiments, the smallest diffusion scale was estimated to be about  $50 \mu\text{m}$ , and the corresponding temperature diffusion scale advection time was estimated to be on the order of  $1 \text{ ms}$ . The relative resolution of the temperature measurements, defined as a ratio of the measuring probe largest dimension and the smallest diffusion scale, was between 4.1 and 9.0. Since the measuring probe volume was larger than the smallest diffusion scale in the flow, the temperature measurements produced average values of the true temperature field within the probe volume.

The signal-to-noise ratio of the LIF measurements was related to the optical setup's ability to accurately capture the fluorescence images. In this work, the signal-to-noise ratio (SNR) was maximized by maximizing the fluorescence intensity that was received from the measuring volume. The spatial noise was estimated using the method described by Moffat (1988) and Farina et al. (1994), in which averaging consecutive images of the undisturbed temperature field removes most of the temporal noise. The overall noise was estimated to be  $\pm 0.07^\circ\text{C}$ , and the worst-case estimate of the absolute accuracy was about  $\pm 0.15^\circ\text{C}$  (based on twice the standard deviation with 95% confidence interval). Typical SNR values in the shear layer experiments, determined from the estimated spatial noise, ranged from 60 to 80, with higher values occurring for lower temperatures (higher fluorescence intensity).

### III. LIF MEASUREMENTS OF OPTICAL DISTORTIONS

An important objective of the present research has been the investigation of the effects of the spanwise and streamwise vortices in a plane shear layer on the optical distortion of a laser sheet which propagated through the shear layer cross section. The approach was to use simultaneous measurements of intensity and temperature by exploiting the fluorescence of disodium Fluorescein and the temperature-dependent fluorescence of Rhodamine B. These results are presented in this chapter.

#### III.1. Optical Distortions in the Unforced Shear Layer

##### III.1.1 Optical Distortions in the x-y Plane

Cross-stream distribution of the fluorescence intensity of Rhodamine B in a frame from a sequence taken at 220 fps is shown in Figure 12a. The free-stream velocities are 24 and 9 cm/s, and the corresponding free-stream temperatures are  $17^\circ\text{C}$  and  $22^\circ\text{C}$ . The field of view measures  $4.5 \times 4.5 \text{ cm}$  (spatial resolution is approximately  $300 \mu\text{m}$ ) and begins 8 cm downstream from the flow partition (approximately  $1.6 \lambda_{K-H}$ ). The laser sheet propagates from top (the cold stream) to bottom. Because intensity decreases with temperature, high intensity regions correspond to low temperatures. This streamwise domain is upstream from the onset of (natural) mixing transition (the Reynolds number based on the width of the shear layer is 4100), and is marked by a sharp interfacial temperature gradient between the two streams. The characteristic transit time within a field of view is 270 msec and is longer than the exposure time of the CCD array (4.5 msec). Also

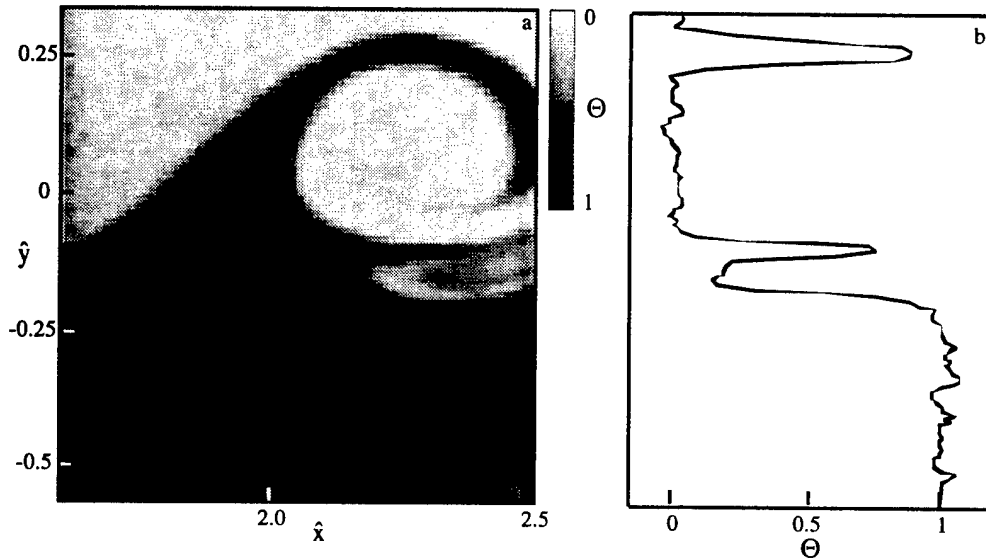


**Figure 12.** Digitized image of the Rhodamine B fluorescence distribution in the shear layer (a), and one-dimensional cross stream temperature distribution at  $x/\lambda_{K-H}=2.3$  (b) for the 24:9 unforced shear layer.

shown in Figure 12b is a cross-stream intensity distribution at  $\hat{x}=2.3$  showing the uniform intensity in the free streams and the sharp change at the interface. It is evident that the mixing in this low Reynolds number flow occurs within a thin interface (measuring  $\approx 0.1 \lambda_{K-H}$ ) separating the hot and cold streams. It is also clear that the spanwise vortex contains a large excess of high-speed fluid entrained from the cold stream.

A sequence of successive frames of the intensity field (Figure 13) during the roll-up of a spanwise vortex reveals that an important feature of the optical transmission through the shear layer is the

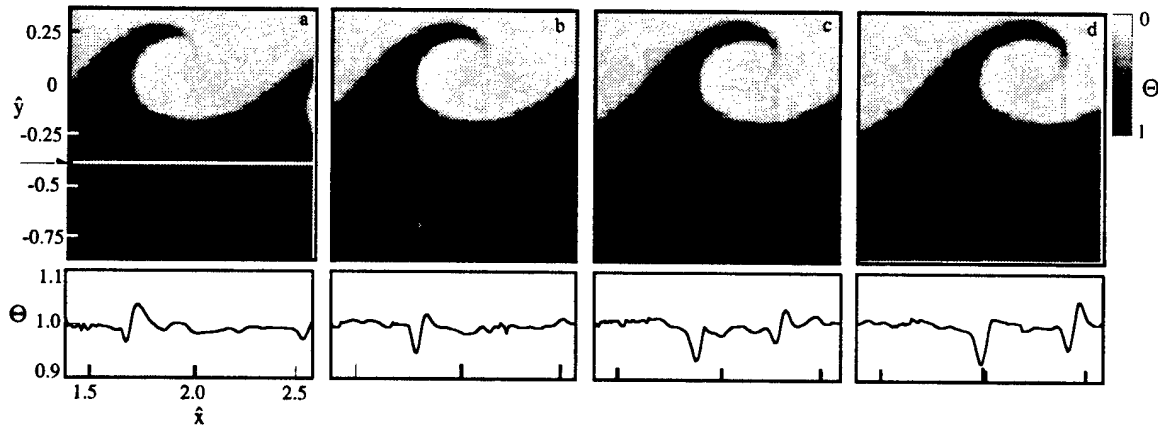


**Figure 13.** Optical distortion: four consecutive frames showing optical streak advection by a propagating vortical structure for the 24:9 shear layer.

appearance of vertical streaks in the laser sheet as it propagates across the interface between the two streams. It is evident from Figure 13 that streaks originate from regions of the flow where the angle between the local temperature (or index of refraction) gradients and the wave vector of the incident light is large. The most noticeable optical distortion is associated with the trailing edge of

the spanwise vortical structure. Figure 13 demonstrates that a new streak appears as the roll-up of the spanwise vortex progresses and the angle between the normal to the interface and the incident ray increases. It is also clear that the streaks are advected with the vortex.

Figure 14 is a magnified view of the spanwise vortex and the accompanying optical distortion. A given ray within the sheet is refracted at a cumulative angle that depends on local index of refraction gradients ( $\nabla n$ ) in its path ( $L$ ),

$$\delta\theta = \int_0^L \frac{(\nabla n)_\perp}{n} ds \quad (3)$$

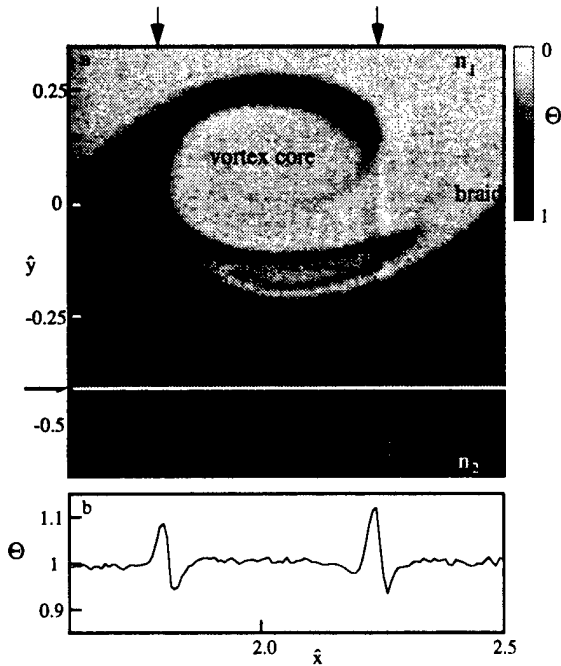


**Figure 14.** Magnified view of the spanwise vortex (a) and the accompanying optical distortion (b) for the 24:9 shear layer.

The optical distortion appears to form as a result of two different scenarios that are indicated by tracing two rays from the top of the image. The first (to the right) is the result of total internal reflection at the interface where the critical angle of incidence for which the angle of refraction is  $90^\circ$  is given by  $\theta_c = \sin^{-1}(n_2/n_1)$  (approximately  $88.5^\circ$  for the present experiments). For angles of incidence larger than the critical angle, some rays experience total reflection, and, as a result, a low-intensity streak is formed in the sheet and the refracted rays concentrate to form an adjacent high-intensity streak on the right, as demonstrated by a horizontal trace of the intensity distribution across the image that is plotted below the frame. The large positive and negative peaks of the streamwise intensity distribution correspond to upstream and downstream deflections of the laser beam. For the second ray (to the left), total internal reflection is not possible because the rays propagate from the hot stream into the cold stream and thus  $n_2 < n_1$ . The formation of a low-intensity streak at this interface is due

to the fact that a ray having a large angle of incidence with the interface between two streams must refract at larger angles. As the angle of incidence approaches  $90^\circ$ , refraction effects become significant enough to cause formation of the low-intensity streak that is comparable to one for the first ray.

The mechanism for the generation of optical distortions described above suggests that the strongest optical distortions in the x-y plane are associated with the leading and trailing edges of the spanwise vortices, where the angle between the local temperature gradients and the direction of the light propagation is large. The spatial separation of the vortices (frequency of the initial instability) within the field of view determines how many rays within the laser sheet will encounter large index-of-refraction gradients associated with the core of the vortical structures (marked on Figure 14). It is clearly advantageous to increase the spacing between spanwise structures so that most of the incoming light passes through the braid region (Figure 14) which connects two adjacent vortices, where the optical distortions are weaker. One way to accomplish this would be to apply a periodic upstream disturbance at a frequency lower than the fundamental frequency of the shear layer instability. Through the manipulation of the global Kelvin-Helmoltz instability modes (spanwise vortices) of the base flow it may be possible to affect the spacing and the growth rate of

the spanwise vortical structures and, depending on the size of the field of view, provide less optical distortion by synchronizing the optical transmission to coincide with the braid region.

The effect of the spanwise vortices is most apparent in time traces of the Strehl ratio,  $St$ , which is defined as a ratio of the aberrated beam intensity to the ideal beam intensity at a particular cross-stream elevation within the low-speed stream (with the mean subtracted). In the present work, the ideal beam intensity at a given streamwise location is assumed to be equal to the time-averaged intensity at the same location. Figures 15a-b show typical portions of time traces of the Strehl ratio

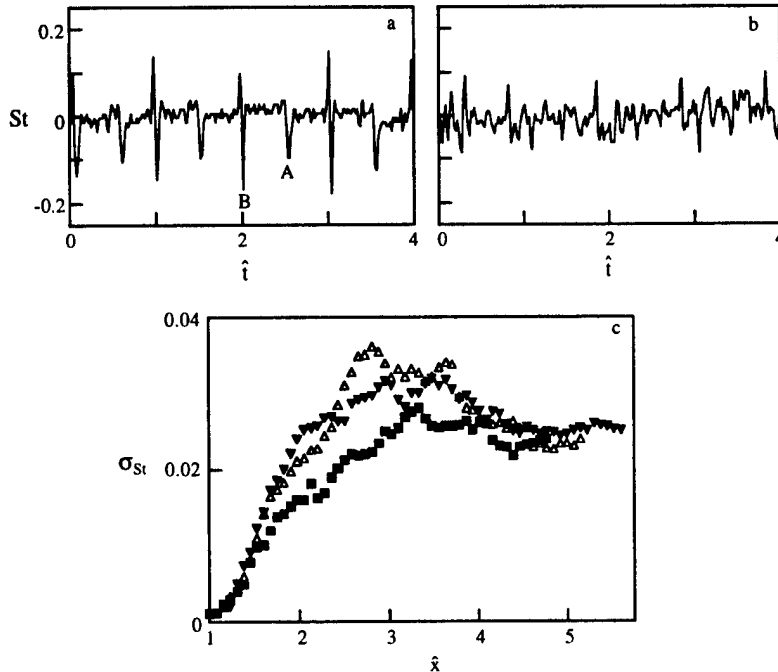


**Figure 15.** Time trace of the Strehl ratio, unforced 24:9 shear layer,  $x/\lambda_{K-H}=2.8$  (a) and 4.6 (b), (c) r.m.s. Strehl ratio for 24:9 (○), 36:12 (△) and 42:14 (□) shear layers (c).

at  $\hat{y}=-0.5$  (within the low-speed stream) for the 24:9 shear layer, at two different streamwise positions,  $\hat{x} = 2.8$  and 4.6. The time is nondimensionalized with the period of the initial (Kelvin-Helmholtz) instability  $T_{K-H}$  (where  $T_{K-H} = 0.3$  sec). The most striking feature of the time trace is the existence of pairs of nominally time-periodic peaks that correspond to the passage of the spanwise vortices. Each pair is comprised of a smaller peak (marked A) followed by a larger peak (marked B) 150 msec later. The peak ("A") is associated with the passage of the leading edge of the

spanwise vortex where the optical distortion is caused by total internal reflection of the laser light. The second peak ("B") corresponds to the trailing edge of the spanwise vortex, where the distortion is caused by the refraction effects, and thus there is an increase in the intensity followed by a comparable decrease. Between these two peaks the fluctuations in the Strehl ratio are small when the light propagates through the braid region.

Farther downstream the effect of the spanwise vortices is less noticeable but still present. While the leading edge distortion is somewhat obscured by random small-scale variations of the signal, the peak caused by the trailing edge of the vortex is still very pronounced. This suggests that the index of refraction field near the leading edge is relatively uniform because the hot and cold fluids are better mixed near the high-speed side, and that the gradients associated with the trailing edge near the low-speed side of the shear layer are still present. Occasionally, the basic periodicity of the Strehl ratio is interrupted, ostensibly as a result of the appearance of secondary vortical structures (i.e., streamwise vortices, Bernal and Roshko 1985).

The variance (r.m.s value) of the Strehl ratio is defined as:



$$\sigma_{St} = \frac{1}{N_t} \sum_{i=1}^{N_t} \sqrt{(St_i - St_{av})^2} \quad (4)$$

where  $St_{av}$  represents the time-averaged Strehl ratio and  $N_t$  is number of time steps (frames). Figure 15c shows  $\sigma_{St}$  as a function of streamwise position for the 24:9, 36:12 and 42:14 shear layers. For  $\hat{x} < 2.2$ , the spanwise vortices are in the early stages of their evolution and the mixedness is low, so that the resulting r.m.s. optical distortion is relatively small. As the roll-up of the vortical structure progresses farther downstream, the r.m.s. optical distortion increases and reaches a maximum value mid-way through the transition region. As the mixing transition develops farther downstream, the length scale and temperature gradients become smaller and the r.m.s. distortion of a laser beam decreases from the peak value.

Another method of determining the spatial and temporal characteristics of aberrated wavefronts passing through a turbulent flow, based on the Fourier technique, was proposed by Malley et al. (1990). This approach was used in the present experiment to determine spectral content of the Strehl ratio time trace at a fixed cross-stream location ( $\hat{y} = -0.5$ ) for the 24:9, 36:12, and 42:14

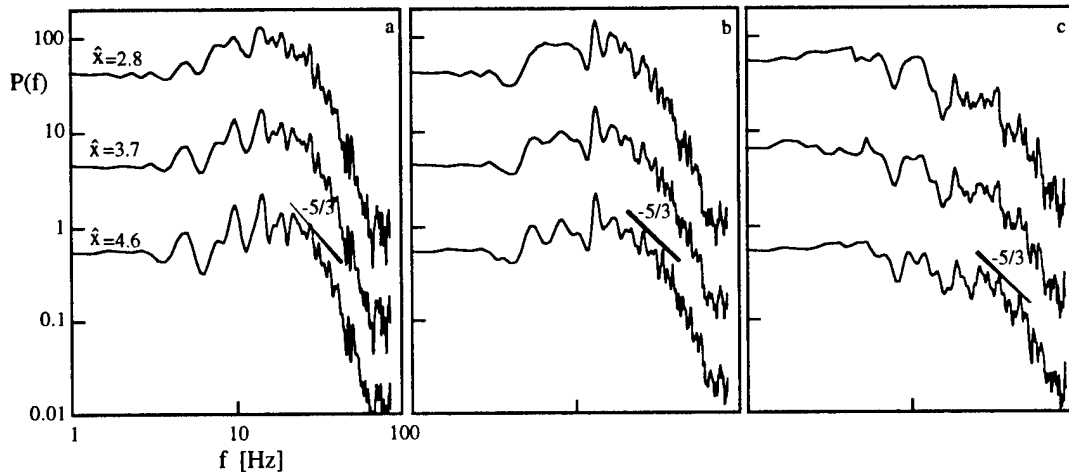


**Figure 16.** Power spectra of the intensity changes due to optical distortions: 24:9 (a), 36:12 (b) and 42:14 (c) unforced shear layers. The spectra for  $x/\lambda_{KH} = 3.7$  and 4.6 are displaced vertically by two and four decades, respectively.

shear layers at  $\hat{x} = 2.8, 3.7$  and 4.6 (Figures 16a-c). The intensity measurements are sampled at 220 fps (2400 frames), and the frequency resolution is 0.5 Hz. It is evident that most of the energy is confined to frequencies below 30 Hz, with a strong peak at the passage frequency of the spanwise vortices and its higher harmonics. The spectral peaks at the first and second harmonics result from passage of the leading and trailing edges of the vortices. Farther downstream, the peaks are less noticeable and broader and the total energy associated with optical distortions decreases.

Figure 17 shows the spatio-temporal distribution of the optical aberrations for the 24:9, 36:12, and 42:14 shear layers for  $2.0 \leq \hat{x} \leq 3.0$ , and  $3.8 \leq \hat{x} \leq 4.8$ . These images are generated from the instantaneous 2-D maps of the index of refraction field using the intensity time trace (normalized with the mean intensity) for all streamwise positions at the cross-stream elevation  $\hat{y} = -0.5$  (i.e. within the low-speed stream). At this cross-stream elevation the temperature of the low-speed stream is uniform and there is no mixing. Thus, the streamwise intensity distribution at this cross-stream elevation is associated with the optical distortions that are accumulated in the laser sheet as it

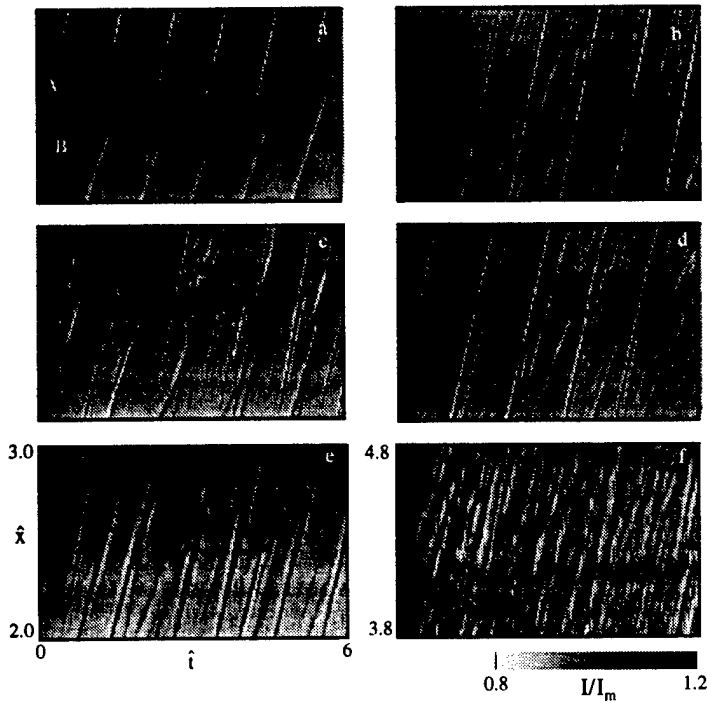


**Figure 17.** maps of optical aberrations: 24:9 (a-b), 36:12(c-d), and 42:14 (e-f) unforced shear layers.

propagates through the shear layer. The streamwise intensity measurements resemble the wavefront slope measurements performed by McMackin et al. (1994) using Hartmann sensors, at least in the region where the optical distortions are strong.

The most dominant feature of these images is a pair of spatially-periodic trajectories associated with the spanwise vortices (most noticeable in Figure 17a for the 24:9 shear layer). The slopes of the trajectories remains constant throughout the streamwise region of measurements and can be used to deduce the convective velocity of the vortices. The slope corresponding to the first trajectory (marked B in Figure 17a for the 24:9 shear layer) is approximately equal to 12 cm/s and is directly related to the

convective speed of the trailing edge of the vortical structure. The second trajectory (marked A in Figure 17a for the 24:9 shear layer) appears later with the slope of 20 cm/s and is associated with the leading edge of the spanwise vortex. The same structural form, dominated by pairs of trajectories with different slopes, persists farther downstream, as evidenced in Figure 17b where the second trajectory now extends throughout the streamwise domain.

These results have significant implications for the validity of the convection hypothesis typically used to determine the optical path length from measurements of beam deflection (Jumper and Hugo 1992). It is generally assumed that the vortical structures propagate with a characteristic velocity that is same throughout the shear layer. If that was the case, the trajectories A and B in Figure 17a would have the same slope and the leading and trailing edges of the vortical structure would convect with the same speed. The fact that the slopes are different suggests that the high-speed part of the shear layer moves at a different speed than the low-speed part. The ratio of the convective velocities associated with the leading and trailing edges of the spanwise structures is approximately equal to 1.4, which compares well to results of Jimenez et al. (1985). These authors used the laser induced fluorescence images of Bernal (1981) and concluded that the upper and lower parts of the shear layer have different convective velocities.

### III.1.2 Optical Distortions in the y-z Plane

The present measurements are primarily restricted to the cross-stream plane  $\hat{z}=z/\lambda_{K-H}=0$ . To the light beam propagating through the shear layer the flow appears frozen, and the optical distortions are determined by the non-homogeneous index of refraction field defined by the instantaneous spatial location of spanwise and streamwise vortices. The depth of field of the optical setup ( $> 6$  cm) is much larger (four orders of magnitude) than the beam deflection out of the x-y plane and thus, imaging in this plane is insensitive to out-of-plane optical distortions. However, it is clear that the presence of spanwise nonuniformities, which arise from streamwise vortical structures, has a significant effect on optical distortions of the laser sheet out of the plane  $\hat{z}=0$ . In order to assess these effects, the laser sheet was aligned with the y-z plane at a given streamwise position, and a sequence of 7200 successive images (corresponding to the passage of 100-150 vortical

structures) was acquired for 24:9 and 36:12 shear layers. The fluorescence intensity distribution was imaged on a CCD sensor array through the same optical system described in Chapter II with the viewing angle of approximately  $50^\circ$ . The field of view was 6 cm in the spanwise direction (spatial resolution was approximately  $450\text{ }\mu\text{m}$ ), and 9 cm in the cross-stream direction (spatial resolution  $700\text{ }\mu\text{m}$ ).

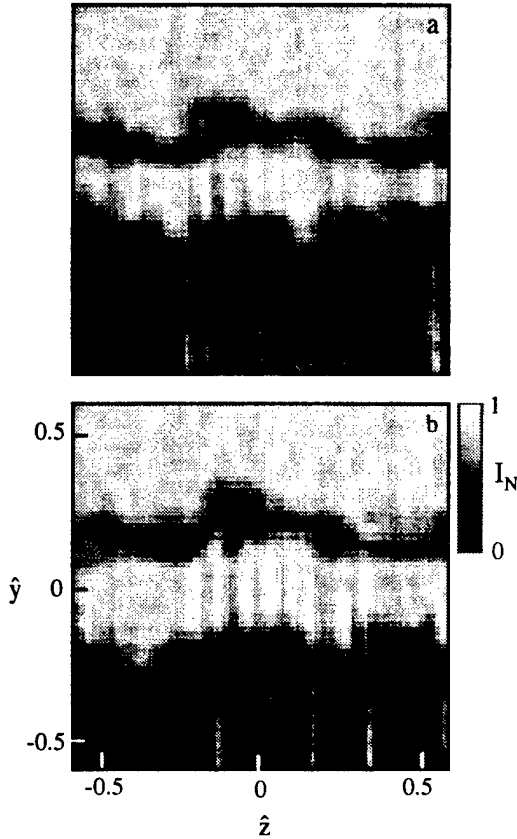


**Figure 18.** Spanwise view of the shear layer. Unforced flow, 24:9 (a) and 36:12 (b) shear layers,  $x/\lambda_{K-H}=2.8$

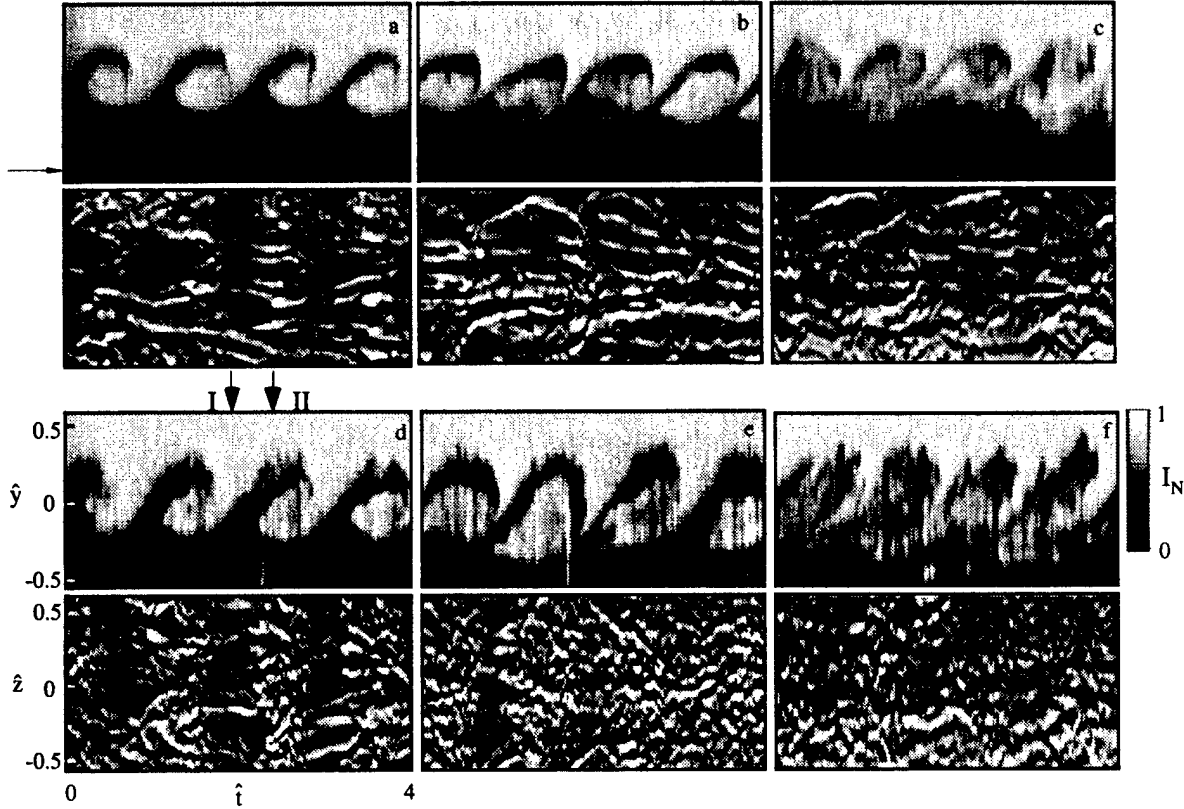
Two typical frames for the 24:9 and 36:12 shear layers are shown in Figures 18a-b [ $I_N=(I-I_{\min})/\Delta I$ ]. The flow comes toward the observer, the light propagates from top to bottom and the image is centered at  $\hat{z}=0$  cm. These two frames correspond to a streamwise cut through the core of the spanwise vortical structures, and the "wavy" structures noticeable at the interface between the two streams are attributable to the streamwise vortices. Each frame can be treated as the transverse section of a 3-D volume, with two spatial coordinates  $y$  and  $z$ , and time. A 3-D data cube can now be used to extract 2-D slices in the spanwise and transverse directions, carrying information about the location of the vortical structures and their influence on optical distortions.

Figure 19 is comprised of two composites acquired for the 24:9 and 36:12 shear layers at  $\hat{x}=2.8, 3.7$ , and  $4.6$ . Each composite includes a  $\hat{z}-\hat{t}$  plane at the cross-stream elevation  $\hat{y}=-0.5$  (i.e., within the low-speed stream), and a  $\hat{y}-\hat{t}$  plane at the spanwise location  $\hat{z}=0$ . The  $\hat{z}-\hat{t}$  plane cut reveals the optical distortion signature in the spanwise direction and can be used to visualize the effects of the streamwise vortical structures on the deflection of a laser light. The  $\hat{y}-\hat{t}$  plane cut corresponds to a two-dimensional projection of the shear layer with the view along the axes of the spanwise structures as they are advected past the sensor

array. The extent of the optical phase distortion, represented by the change in intensity, is most apparent in the  $\hat{z}-\hat{t}$  plane, where the shear layer is viewed from the low-speed side, looking upstream, and the flow (time) runs from left to right. The naturally occurring streamwise vortices in the braid region leave their optical signature in the  $\hat{y}-\hat{t}$  plane in the form of low- and high-intensity streaks that connect the spanwise vortices and cause their slight spanwise distortion (most noticeable in Figure 19a). For the 36:12 shear layer at  $\hat{x}=2.8$ , the upstream and downstream edges of the primary vortices are well defined by sharp intensity gradients in the  $\hat{y}-\hat{t}$  plane. It is also noteworthy that the optical distortion is localized, except for the streaks caused by the streamwise vortices, to the core of the spanwise vortices and that the extent of distortion is more or less uniform across the span. Farther downstream and especially in the transition region (Figure 19c for the 36:12 shear layer), the optical distortion is more uniformly distributed in the  $\hat{y}-\hat{t}$  plane due to the growth of the spanwise vortices and the accompanying increase in the small-scale motion.

Figures 20a-d show the Strehl ratio time traces at  $\hat{y}=-0.5$  and  $\hat{z}=0$  for the 24:9 and 36:12 shear layers at  $\hat{x}=2.8$  and  $4.6$ . Again, the Strehl ratio is defined as a ratio of the aberrated beam intensity to the mean beam intensity at a particular spanwise position, and is related to the optical distortions in the  $\hat{y}-\hat{t}$  plane at a particular streamwise position. These results indicate that the time trace of the

optical distortions in the  $\hat{y}$ - $\hat{t}$  plane does not display characteristic periodic peaks that were prominent in the time traces of the optical distortions in the  $\hat{x}$ - $\hat{y}$  plane (Figure 15). This is due to the fact that the streamwise vortices, which are causing optical distortions in the  $\hat{y}$ - $\hat{z}$  plane, are not convected in the spanwise direction.



**Figure 19.** Optical distortions in the spanwise plane:  $z$ - $t$  plane cut through the low-speed stream at  $y/\lambda_{KH} = -0.5$  and  $y$ - $t$  plane cut at  $z=0$  for the unforced 24:9 (top) and 36:12 (bottom) shear layers at  $x/\lambda_{KH} = 2.8$  (a), 3.7 (b), and 4.6 (c).

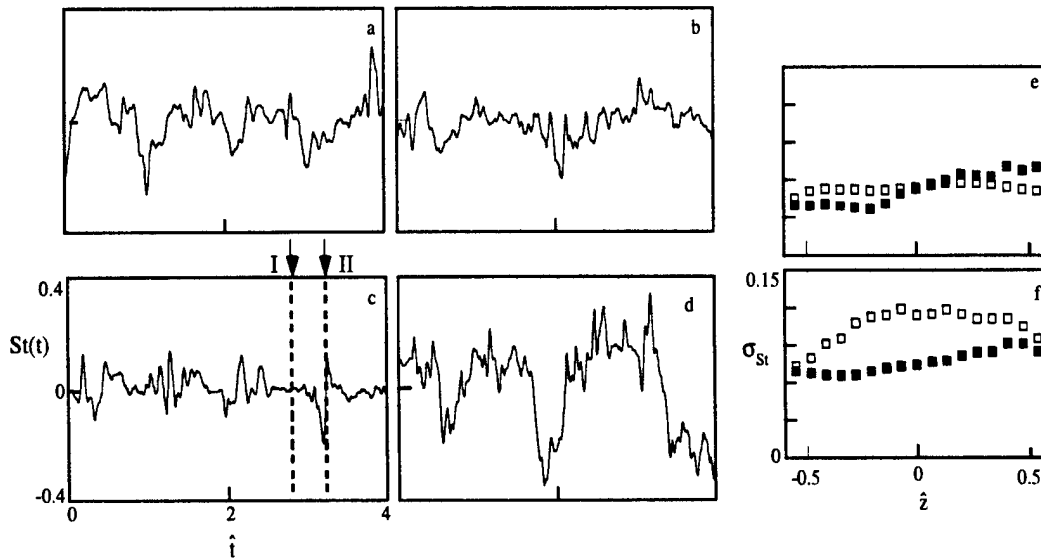


**Figure 20.** Strehl ratio time traces at  $z=0$  and  $x/\lambda_{KH} = 2.8$  and 4.6 for 24:9 (a,b) and 36:12 shear layers (c,d).  $\sigma_{St}$  for the unforced flow, 24:9 ( ) and 36:12 ( ) shear layers at  $x/\lambda_{KH} = 2.8$  (e) and 4.6 (f).

At the first streamwise position ( $\hat{x}=2.8$ ), the time traces of optical distortions display long intervals with relatively little distortion, followed by a positive or negative peak whose magnitude is typically 10-15% of the mean intensity at that spanwise position (Figure 20c). Intervals of the weak optical distortions correspond to the passage of a laser sheet through the braid region that connects adjacent spanwise vortices (indicated by tracing a ray I in Figures 19a and 20c). The peaks of the optical distortions coincide with the passage of a laser sheet through the core of the spanwise vortex, and is indicated by tracing a second ray to the right (marked by II in Figures 19a and 20c). At the third streamwise position ( $\hat{x}=4.6$ ), the intervals with weak distortions are shorter and less frequent, and the optical distortions in the  $\hat{y}$ - $\hat{z}$  plane grow stronger exceeding the distortions in the  $\hat{x}$ - $\hat{y}$  plane (Figure 20d). The maximum change in the laser intensity due to optical distortions in the  $\hat{y}$ - $\hat{z}$  plane reaches occasionally 40% of the reference mean intensity at  $\hat{z}=0$  cm.

Figures 20e and f show the spanwise profile of the r.m.s. values of the optical distortions for the 24:9 (closed symbols) and 36:12 (open symbols) shear layers. At the first streamwise position ( $\hat{x}=2.8$ ), the average r.m.s. distortion is between 3-5% of the mean intensity at that position. The fact that the r.m.s. distortions are not uniform across the span implies the existence of streamwise vortices that have preferential spanwise locations. At the third streamwise position ( $\hat{x}=4.6$ ), the r.m.s. distortions are stronger (8-11% of the mean intensity), and the spanwise variations are more pronounced, especially for the higher free-stream velocities.

It is of interest to consider how the optical distortions depend on phase during one cycle of the base flow, and what is the most optimal time interval for the optical transmission. Figures 21a-f show the spanwise views of the shear layer at six time intervals (20 msec) during the passage of a spanwise vortex (passage period was approximately 0.19 sec), for the 36:12 shear layer at  $\hat{x}=2.8$ .

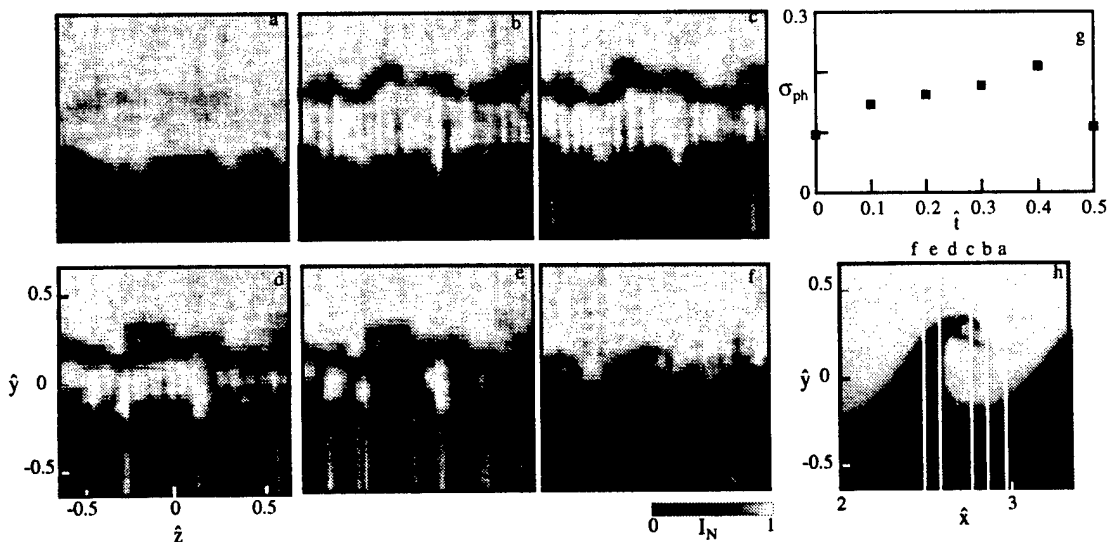


**Figure 21.** Spanwise views for the unforced 36:12 shear layer for six time intervals separated by 20 ms (a-f), r.m.s. Strehl ratio averaged across the span (g), and the spanwise vortex indicating time intervals (h).

The image corresponding to the time interval for which the laser beam propagates through the braid region (marked by *a* in Figure 21h) of the spanwise coherent structure is shown first. It is obvious that during this time interval the light encounters a relatively uniform index of refraction field and the resulting average r.m.s. distortion is less than 10% of the mean intensity (averaged for all spanwise positions). At this time, the flow in the shear layer is reasonably uniform in the spanwise direction and the streamwise vortices are creating only slight optical distortions. During

the next phase (indicated by *b* in Figure 21h), the core of the spanwise vortex appears in the image and the light now encounters two interfaces with sharp streamwise gradients of the index of refraction. The first interface, corresponding to the leading edge of the primary vortex, is relatively thin and, although reasonably two-dimensional, is characterized by waviness (caused by the streamwise vortices) in the spanwise direction. The spanwise non-uniformity results in stronger optical distortions (15% of the mean intensity) at this time, as shown in Figure 21g, where the r.m.s. optical distortion averaged across the span is plotted as a function of the phase. The optical distortion continues to grow with the advection of the spanwise vortex, and reaches its peak at the instant in time when the light propagates through the trailing edge of the primary vortex (marked by *e* in Figure 21h). As soon as the spanwise vortex completely passes the streamwise location at which the light enters the shear layer (indicated by *f* in Figure 21h), the optical distortion decreases sharply to the original level.

### III.2. Correction of Optical Effects

It is important to note that the instantaneous maps of Rhodamine B fluorescence intensity, such as shown in Figure 12, do not lead to correct temperature distributions due to optical distortions in the laser sheet caused by sharp density gradients between hot and cold streams (high and low intensity streaks in Figure 12a). In order to eliminate the effects of the deflections and fluctuations of the exciting laser light, a novel correction technique was developed based on simultaneous measurements of fluorescence of Rhodamine B and disodium Fluorescein, whose fluorescence is only weakly dependent on temperature ( $\sim 0.2\%$ /°C). Thus, instantaneous maps of the fluorescent intensity of disodium Fluorescein were only weakly affected by temperature, while capturing the optical effects caused by the index of refraction gradients associated with nonuniform temperature. A similar approach to the correction of fluorescence-dependent temperature measurements has also been used by Sakakibara and Adrian (1997) in a natural convection flow over a heated surface within a closed container.

The correction was performed by noting that the local instantaneous temperature  $T(x,y)$  is related to emitted fluorescence intensities through the temperature calibration function, and by assuming that the change in the disodium Fluorescein intensity due to the temperature was negligible when compared to Rhodamine B,

$$T(x,y) = f_{\text{calib}} \{ [I_{\text{Rh}}(x,y) - I_{\text{Rh ref}}(x,y)] - c_F [I_{\text{Fl}}(x,y) - I_{\text{Fl ref}}(x,y)] \} \quad (5)$$

where  $I_{\text{Rh}}$  and  $I_{\text{Fl}}$  were local fluorescence intensities of Rhodamine B and disodium Fluorescein,  $I_{\text{Rh ref}}$  and  $I_{\text{Fl ref}}$  were reference intensities taken when the temperatures of two streams were identical,  $f_{\text{calib}}$  was the calibration function determined from the Rhodamine B calibration and the free stream temperature measurements and  $c_F$  was a scaling constant. It was clearly beneficial to keep the Fluorescein concentration as low as possible in order to minimize the attenuation effects and increase the temperature resolution ( $c_{\text{Fl}} \sim 120 \mu\text{g/l}$ ). However, this resulted in unequal fluorescence intensities received by two CCD cameras that were used to simultaneously measure fluorescence of Rhodamine B and disodium Fluorescein. This necessitated the use of the scaling factor  $c_F$  in Eq. (5) that was defined as the ratio of the r.m.s. Strehl values at  $\hat{x}=2.5$  determined from the Rhodamine B and disodium Fluorescein intensity maps,  $c_F = (\sigma_{\text{St}})_{\text{Rh}} / (\sigma_{\text{St}})_{\text{Fl}}$  (typically between 1.0 and 1.4).

The performance of the correction technique was first evaluated for the 24:9 shear layer at  $\hat{x}=1.8$ -3.0, and results are shown in Figure 22. Three maps shown in Figure 22 are the original Rhodamine B fluorescence intensity map, disodium Fluorescein map and the corrected temperature map computed from the Eq. (5) using the results of the simultaneous measurements. The original Rhodamine B map shows characteristic bright and dark regions that map the temperature field, interlaced with the streaks of high and low intensity caused by the deflection of the incoming light. The most striking feature of the Fluorescein intensity map, shown in the middle, is almost complete absence of temperature gradients that are very prominent in the Rhodamine B intensity map. However, comparison between optical distortions in the Rhodamine B and Fluorescein maps

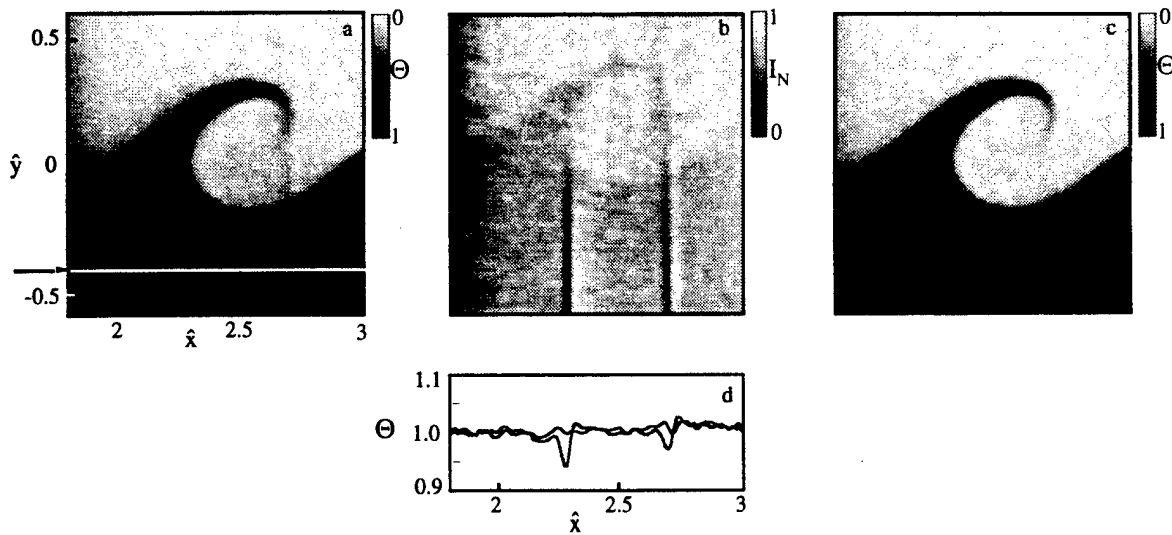


**Figure 22.** Two-dye temperature correction scheme, unforced flow, 24:9 shear layer. (a) Rhodamine B intensity map; (b) Fluorescein intensity map; (c) corrected temperature map; (d) 1-D streamwise intensity distribution: uncorrected (gray line) and corrected (black line).

reveals that the high and low intensity streaks are equally pronounced and located at identical spatial locations. The change in intensity across the streak is not identical for two maps and this effect is accounted for through the scaling factor in Eq. (5). That the 2-dye correction technique successfully removes optical distortion effects is evident from the corrected temperature map, shown in Figure 22c. Note that the high and low intensity bands have been almost completely removed, exposing the correct temperature gradients that were originally not separable from the index of refraction effects.

The effectiveness of the correction technique is further demonstrated using a one-dimensional temperature distribution in the streamwise direction at the cross-stream elevation  $\hat{y} = -0.4$  (i.e., within the low-speed stream) for both the original Rhodamine B map and the corrected temperature map (Figure 22d). Attention is drawn to almost complete removal of peaks and valleys that are signatures of the optical distortions of the incoming excitation light. The corrected streamwise

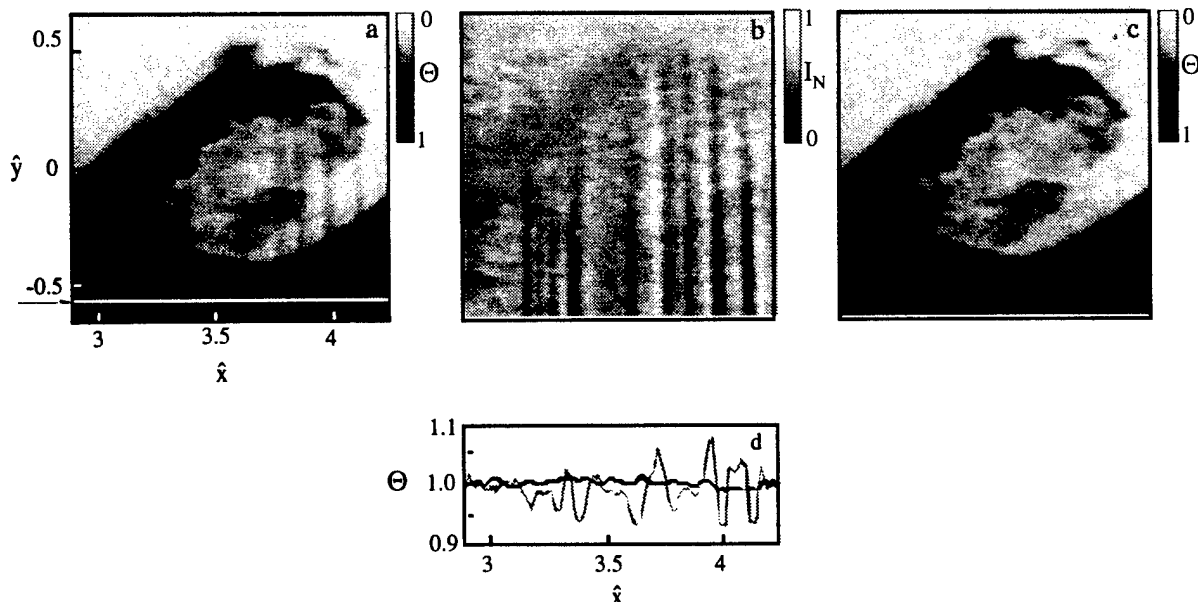


**Figure 23.** Two-dye temperature correction scheme, unforced flow, 36:12 shear layer. (a) Rhodamine B intensity map; (b) Fluorescein intensity map; (c) corrected temperature map; (d) 1-D streamwise intensity distribution: uncorrected (gray line) and corrected (black line).

temperature distribution in the hot stream is relatively uniform when compared to the original Rhodamine B distribution, which shows intensity variations corresponding to temperature variations of the order of 5-8% of the variation between the two streams. Figure 23 shows the original and corrected temperature maps for the 36:12 shear layer at  $\hat{x}=2.8-4.3$ . It is noteworthy that the high and low intensity streaks are more numerous in this case, as indicated by the one-dimensional temperature distribution in the streamwise direction (Figure 23d). Despite that, the corrected temperature map shown in Figure 23c is free of optical distortions and the streamwise temperature distribution indicates uniform temperature in the hot stream.

After being tested, the correction technique was later used to extract correct temperature (and thus, index of refraction) maps for different flow conditions and the corrected maps were used to quantify optical distortions and mixing in the shear layer.

Once the corrected temperature (and index of refraction) field is computed, the optical wavefront of the light propagating through the shear layer can be directly determined from the ray-tracing equation

$$\frac{d}{ds}(n\hat{\tau}) = \nabla n \quad (6)$$

where  $\hat{\tau}$  is the unit-vector in the direction of the light propagation,  $s$  is the propagation length, and  $n$  is the index of refraction field of the medium (Jumper and Hugo 1992). The index of refraction is related to the temperature through a quadratic approximation  $n(x,y)=k_1+k_2T(x,y)+k_3T^2(x,y)$ , determined by a least-square fit ( $k_1=1.334$ ,  $k_2=-1.3549 \times 10^{-5}$ ,  $k_3=-1.9038 \times 10^{-6}$ ) to experimental data (Weast and Selby 1966). When light is transmitted through an aberrated index of refraction field, the initially planar wavefront is distorted and the light rays, always normal to the wavefront, emerge from the flow field with different cumulative bending angles  $\delta\theta$  corresponding to index of

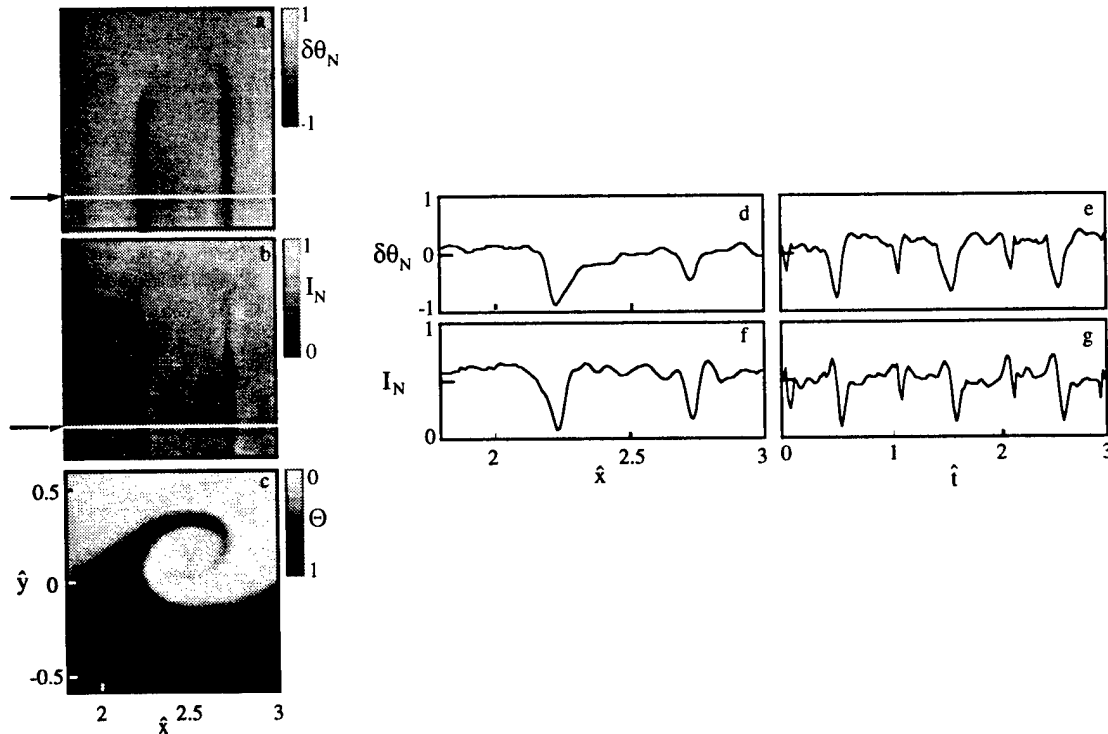


**Figure 24.** Integrated optical distortion, unforced flow, 24:9 shear layer. The optical phase angle (a), and the corresponding Fluorescein intensity, and temperature maps (b,c). Spatial dependence of  $\delta\theta_N$  and  $I_N$  is shown in d and f. Temporal dependence at  $x_{k-H}=2.5$  is shown in e and g



refraction gradients encountered along the path. This cumulative bending angle  $\delta\theta$  at a given streamwise location was determined from Eq. (3), where the index of refraction gradients are computed using second-order central difference approximations. The optical phase angle determined from the 2-D temperature measurements is associated only with distortions in the imaging plane ( $x$ - $y$ ), because the imaging is insensitive to the out-of-plane distortions due to the depth of field of the optical setup. The angle  $\delta\theta$  is the derivative of the wavefront in the streamwise direction and can be used to compute the average and the r.m.s. values of the bending angle.

Figure 24 shows a raster image of the bending angle  $\delta\theta_N = \delta\theta / \Delta(\delta\theta)$  (a), and the corresponding Fluorescein intensity  $I_N = (I - I_{\min}) / \Delta I$  (Figure 24b) used to determine the corrected temperature field (Figure 24c) from the fluorescence intensity map of Rhodamine B for the 24:9 shear layer. The integration of Eq. (3) starts at the top of the image where the laser sheet with a uniform wavefront enters a shear layer through which it propagates in the cross-stream direction toward the bottom part of the image. As light propagates through the shear layer, the wavefront is locally distorted and the optical phase angle is determined by the angle between the index of refraction gradient and the direction of the light propagation (Figure 14). For the 24:9 shear layer presented in Figure 24, the optical phase distortion results from a single large deflection of the light beams that encounter the spanwise vortex, and the rest of the image is practically distortion-free.

It is evident from Figures 24d and f, showing the streamwise distribution of the bending angle and the normalized intensity for the cross-stream elevation  $\hat{y} = -0.4$  (within the low-speed stream), that the characteristic peaks associated with the optical distortions are similar in shape and occur at the same streamwise position. Examples of the time traces of the integrated and experimental data for the same cross-stream position and a fixed streamwise location  $\hat{x} = 2.5$  are shown in Figures 24e and g. The most visible feature of the integrated phase time trace is the reproduction of the periodic peaks corresponding to the passage of the spanwise coherent structures.

Once the time history of the bending angle  $\delta\theta$  was determined, the average bending angle was calculated from:

$$\delta\bar{\theta} = \frac{1}{N_t} \sum_{i=1}^{N_t} \delta\theta_i \quad (7)$$

where  $N_t$  was the number of samples. In addition to that, the average phase angle [also called the mean bore sight error (Jumper and Hugo, 1992)] was used to determine the r.m.s. variance of the instantaneous bending angle:

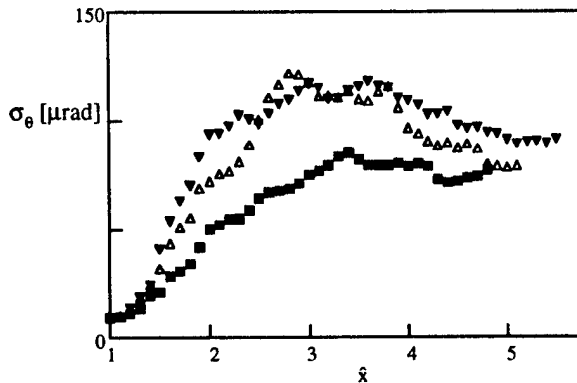


Figure 25. Streamwise dependence of the optical phase variance for the unforced 24:9 ( ), 36:12 ( ), and 42:14 ( ) shear layers.

$$\sigma_{\theta}(x) = \frac{1}{N_t} \sum_{i=1}^{N_t} \sqrt{(\delta\theta_i(x) - \delta\bar{\theta})^2} \quad (8)$$

Figure 25 shows the streamwise dependence of the optical phase variance for the 24:9, 36:12, and 42:14 shear layers. These results indicate that  $\sigma_{\theta}$  is between 50-100  $\mu\text{rad}$ , where the higher values correspond to higher velocities in the test section. It is also evident that  $\sigma_{\theta}$  varies with the streamwise positions in a similar fashion as the r.m.s. of the Strehl ratio (Figure 15c). At the lower speeds in the test section, the variation of the r.m.s. fluctuations is relatively mild (15-25  $\mu\text{rad}$ ) with the maximum  $\sigma_{\theta}$  of 75  $\mu\text{rad}$  at  $x/\lambda_{K-H}$

$\approx 3.5$ . The r.m.s. fluctuations increase to approximately  $50 \mu\text{rad}$  for the higher speeds, and the maximum magnitude of  $\sigma_\theta$  ( $125 \mu\text{rad}$ ) occurs closer upstream at  $\hat{x}=3.25$ . It is interesting that, once the flow undergoes small-scale transition, the variance of the optical phase angle approaches some asymptotic value that appears to be independent of the free-stream velocities. This is in good agreement with findings of Wissler et al. (1992) which indicate that the peak optical distortion occurs relatively early in the mixing transition region, after which it decreases to some value that may change only slowly (if at all) farther downstream.

### III.3. Optical Distortions in the Forced Shear Layer

As mentioned in section III.1.1., the most prominent optical effects within the plane shear layer were associated with the rollup and advection of the spanwise vortices. Specifically, pairs of high- and low-intensity streaks were formed in intensity maps of the transmitted light when the angle between the local index of refraction gradient and the wave vector of the incident light was large. The intensity variation within these streaks depended on the length scale and magnitude of the index of refraction gradient. Thus, it might be expected that optical effects of the interface between the two streams could be mitigated by direct excitation of small-scale motions within the dissipation range of the base flow having characteristic scales one to two orders of magnitude smaller than the wavelength of the primary (Kelvin-Helmholtz) instability.

In the present experiments, an array of piezo-electric actuators mounted at the trailing edge of the splitter plate (described in Chapter II) was used to directly excite small-scale motions within shear layer flow. Actuators were operated at their resonance frequency of 225 Hz, and the optical distortion in the x-y and y-z planes was measured using the LIF technique described in Chapter II.

Figure 26 shows the time trace of the Strehl ratio for the forced flow for the 24:9, 36:12, and 42:14 shear layers (at  $\hat{x}=2.8$  and 4.6), where the Strehl ratio for the unforced flow (gray lines) is reproduced for reference. Also shown in the same figure (Figures 26 c, f, and i) are the r.m.s.

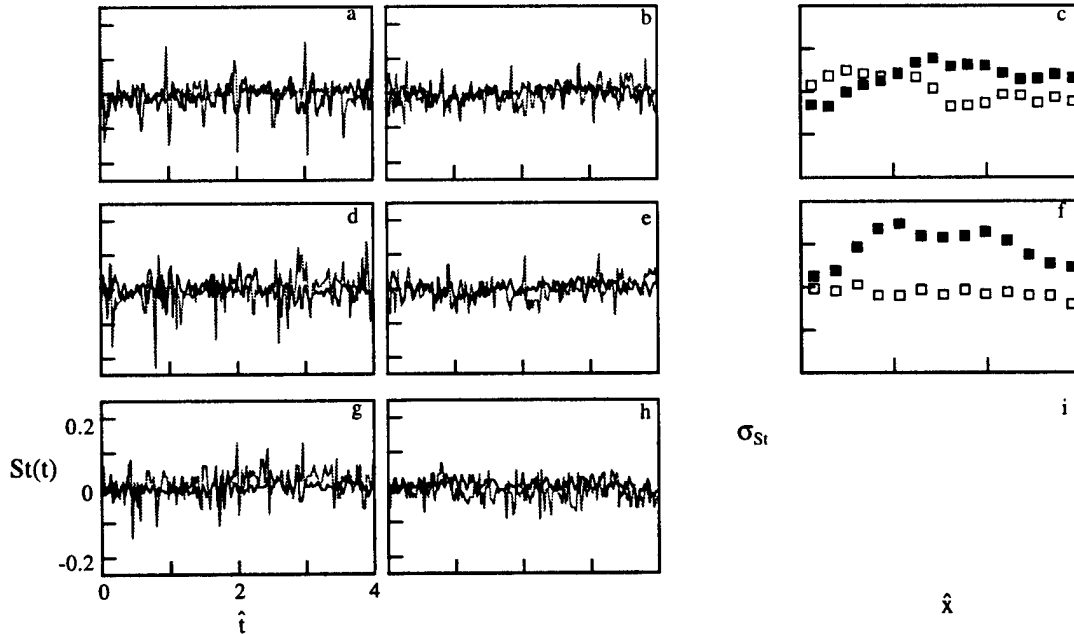


**Figure 26.** Strehl ratio time traces at  $x/\lambda_{K-H}=2.8$  and 4.6, and  $\sigma_{St}$  for 24:9 (a-c), 36:12 (d-f), and 42:14 (g-i) forced shear layers ( $f=225$  Hz). Unforced  $St$  (gray lines) and  $\sigma_{St}$  (closed symbols) are reproduced for reference

values of the Strehl ratio plotted as a function of streamwise position for the unforced and forced flow (the unforced flow distribution is reproduced for reference). The most striking effect of direct small-scale excitation is the absence of periodic peaks associated with the large coherent structures

in the unforced flow (Figure 15a,b). While the maximum fluctuation of the Strehl ratio for the unforced flow is almost 30% of the mean light intensity at some streamwise locations, it is reduced with forcing to less than 10%. Although the number of streaks is somewhat increased at the first streamwise location for the 24:9 shear layer (Figure 26a), they are much weaker in magnitude. Farther downstream, the peaks in the time trace for the forced flow are still much weaker and occur with a frequency similar to that of the unforced flow.

The r.m.s. Strehl ratio  $\sigma_{st}$  for the forced 24:9 shear layer (open symbols in Figure 26c) is 20-30% lower than in the unforced flow throughout most of the streamwise domain, and the effect of the high-frequency excitation persists far downstream. The reduction of the r.m.s. optical distortion is even more pronounced for the higher speeds (the 36:12 and 42:14 shear layers), as shown in Figure 26f and 26i. Notice that  $\sigma_{st}$  for the unforced flow is always larger than in the forced flow. The average  $\sigma_{st}$  (spatially averaged in the streamwise direction) is used as a global measure of the optical quality of the unforced and forced shear layer. The ratio of the average  $\sigma_{st}$  for the unforced flow to that for the forced flow is 1.25, 1.51, and 1.9 in the 24:9, 36:12, and 42:14 shear layers, respectively, indicating that the average optical quality of the shear layer is typically improved by more than 20%. It is interesting to note that the r.m.s. Strehl ratio for the forced flow remains practically unchanged throughout the streamwise measurement domain, indicating that the temperature (and thus, index of refraction) gradients at different streamwise positions are similar.

Another way of determining the influence of the high-frequency forcing on optical distortion is based on the spatio-temporal distribution of the aberrated wavefront generated from the instantaneous 2-D maps of the index of refraction field, using the intensity time trace for all streamwise positions at the cross-stream elevation  $\hat{y} = -0.4$ . As mentioned before (Figure 17), the streamwise intensity measurements resemble the wavefront slope measurements made with Hartmann sensors, and are characterized, in the unforced case, by a pair of spatially-periodic trajectories associated with the large spanwise structures. Figure 27 shows the spatio-temporal distribution of the optical aberrations for the 24:9, 36:12 and 42:14 shear layers at the same streamwise positions as in Figure 17. As shown in Figures 27, the spatio-temporal profile of the optical distortion is drastically changed when the flow is forced at the high frequency. Notice that most of the features in the image of the forced flow appear to be uncorrelated with each other, for all streamwise locations and velocity ratios. Furthermore, the periodic trajectories associated with the trailing and leading edges of the spanwise vortices (noticeable in Figure 27c) are much weaker than the similar trajectories in the unforced flow (Figure 17c). Farther downstream in the 42:14 shear layer (Figure 27f), the spatio-temporal image of the forced flow is diffused and seemingly featureless.

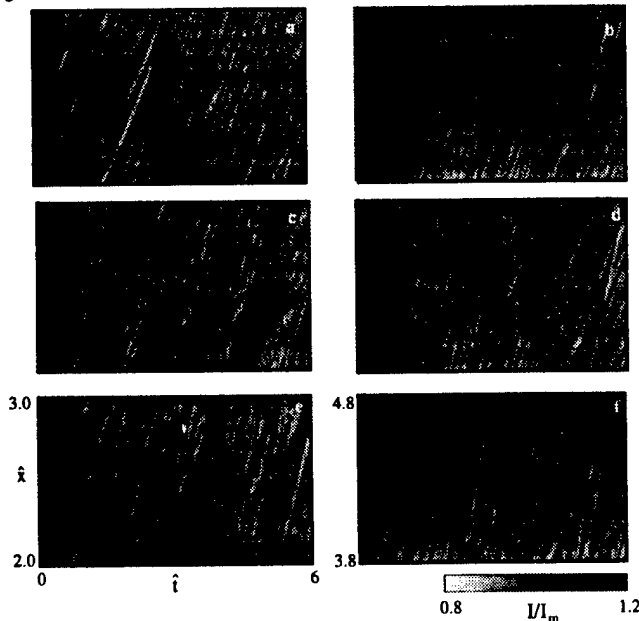


Figure 27. maps of optical aberrations: 24:9 (a-b), 36:12(c-d), and 42:14 (e-f) forced shear layers ( $f=225$  Hz).

A two-dimensional spatio-temporal profile provides an indication of the index of refraction gradient through which the light propagates, and appears to be much more homogeneous in the forced flow. Some clues about the integral length scales in the flow and the magnitude of the index of

refraction gradients can be obtained from the time-averaged covariance function at the fixed streamwise position,

$$\text{cov}_T(y_1, y_2) = \frac{1}{N_t} \sum_{i=1}^{N_t} (T(y_1, t_i) - \bar{T}(y_1))(T(y_2, t_i) - \bar{T}(y_2)) \quad (9)$$

where  $N_t$  is the number of samples (frames),  $T(y, t)$  denotes the instantaneous temperature at the spatial location  $y$ , and  $\bar{T}(y)$  is the time averaged temperature at the same spatial location. As noted by Hugo and Jumper (1995), the covariance function is normally used in linking equations through which the r.m.s. values of the optical phase distortion are related to the density fluctuations along the direction of light propagation. A 1-D profile at  $y_2=0$  (normalized by the root-mean square values of the temperature fluctuations) is denoted by  $\rho_{\text{cov}}$ , and can be interpreted as the covariance coefficient distribution of the temperature data, while the cross-stream width of the covariance function provides a measure of the average size of the coherent structures in the flow.

Figure 28 shows the covariance function, averaged over 2400 frames and normalized [ $\text{cov}_N = \text{cov}_T / \max(\text{cov}_T)$ ], for the unforced and the forced flow for the 24:9 shear layer (at  $\hat{x}=2.8$  and 4.6), and

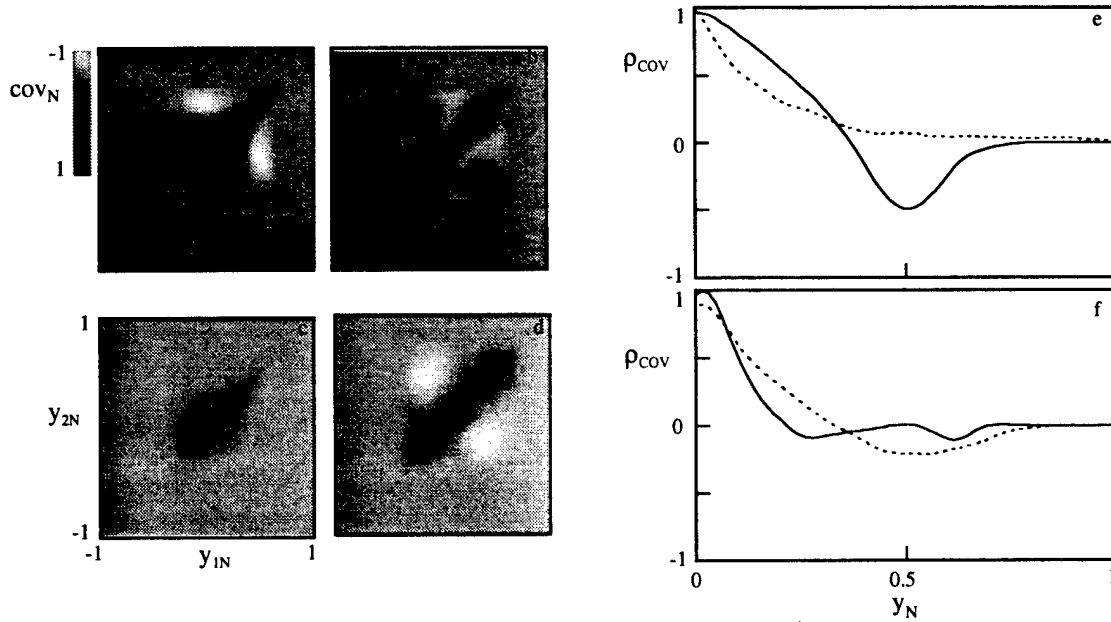


**Figure 28.** Temperature covariance function normalized with the maximum value [ $\text{cov}_N = (\text{cov}_T / \max(\text{cov}_T))$ ] at  $x/\lambda_{K-H} = 2.8$  and 4.6 for the unforced (a, b), and forced (c, d) 24:9 shear layer ( $f=225$  Hz). A 1-D covariance distribution  $\rho_{\text{cov}}$  at  $y_{2N} = 0$  and  $x/\lambda_{K-H} = 2.8$  and 4.6 (e, f) for the unforced (solid lines), and forced flow (dashed lines).

a 1-D distribution  $\rho_{\text{cov}}$  taken at  $y_N = y/y_{\text{max}} = 0$  (centerline of the shear layer). The images of the covariance function are symmetric with respect to the diagonal  $y_{1N} = y_{2N}$ , and indicate the relative correlation of the temperature fluctuations at different cross-stream elevations at fixed streamwise position (the center of the shear layer is approximately in the middle of these images). The dark and bright regions correspond to positive and negative values of the covariance, respectively.

In the unforced flow at  $\hat{x}=2.8$  (Figure 28a), the correlation region is 2.5 cm wide in the cross-stream direction, and is biased toward the high-speed side of the shear layer ( $y_N > 0$ ), where the spanwise vortices pass at the natural frequency. Furthermore, the covariance function has a significant negative peak (bright region) at  $y_{1N}=0.5$  and  $y_{2N}=0$  indicating that the temperature fluctuations at these two cross-stream elevations are out of phase with respect to each other (also evident in Figure 28e). Farther downstream (Figure 28b), the region over which the temperature

data are correlated is 3.5 cm in the cross-stream direction and spreads deeper into the low-speed stream as the primary vortices grow.

The influence of direct small-scale excitation on the length scales and coherence region is shown in Figures 28c-d, for the flow conditions used in the unforced case. One first notes that the spatial region over which the temperature field is correlated is reduced by forcing. The cross-stream extent of the correlation function for the forced flow at  $\hat{x}=2.8$  and 4.6 is 2 cm and 2.9 cm, respectively. At the first streamwise position, the correlation region is localized to a narrow band around the center of the shear layer where very intense mixing takes place, and the covariance coefficient distribution (dashed line in Figure 28e) rapidly decays with cross-stream distance. Farther downstream, the vortical instability is more noticeable, and the covariance function spreads in the cross-stream direction almost as much as in the unforced case.

A classical statistical analysis of turbulence was used to obtain the integral length scale over which the temperature fluctuations are correlated (Hinze 1975),

$$\Lambda(y_2) = \int_0^{\infty} \frac{\text{cov}_T(y_1, y_2)}{T_1' T_2'} dy_1 \quad (10)$$

where  $T'(y, t) = T(y, t) - T(y)$ , and the integral scale  $\Lambda(y_2)$  is computed along the direction of light propagation. In the case of isotropic turbulence, the integral scale defined this way has been accepted as a valid representation of the dominant length scale in the flow (Tennekes and Lumley 1972). For temporally periodic flows, where the covariance function can become negative, length scales computed from Eq. (10) can be negative. Thus, Eq. (10) is typically integrated only to the first zero crossing (Hugo and Jumper, 1995). The integral scale for the forced flow at  $\hat{x}=2.8$  is estimated to be 4.1 mm, and is almost 40 % smaller than the unforced flow scale (6.4 mm). Also note that the slope of the covariance coefficient at the origin ( $y_{2N}=y_{1N}$ ) is very sharp for the forced flow case (Figure 28e), indicating that the dissipation microscale for the temperature fluctuations, defined by the curvature of the covariance coefficient at the origin (Hinze 1975), is smaller than in the unforced flow.

Results presented so far indicate that the instantaneous and time-averaged optical distortions are reduced throughout the shear layer when the flow is forced at the high frequency. It is also clear that reduction of optical distortions by high-frequency forcing is directly related to the change in the index of refraction gradient in the shear layer. In order to explain these effects, the temperature correction technique described in Section 3.2 is used to extract the correct temperature and index of refraction fields, and these results are used to investigate index of refraction gradients and the characteristic lengths scales for different flow conditions.

Figure 29 shows the index of refraction field [ $n_N = (n - n_{\min})/\Delta n$ ], derivatives in the x [ $(n_x)_N = (n_x - n_{x\min})/\Delta n_x$ ] and y [ $(n_y)_N = (n_y - n_{y\min})/\Delta n_y$ ] direction, and the index gradient for the unforced 24:9 (a-d), 36:12 (e-h) and 42:14 (i-l) shear layers at  $\hat{x}=2.0-3.0$ . The dark and bright regions in Figures 29b, f and j are associated with strong positive and negative rates of change in the direction normal to the direction of light propagation. The largest negative values of  $n_x$  are located in the braid region that connects two adjacent spanwise vortices, and the largest positive values of  $n_x$  are associated with the leading and trailing edges of the vortex. Furthermore, the values of  $n_y$  (Figures 29c, g and k) at the leading and trailing edges of the vortex are much smaller than  $n_x$  values and the index gradient vector at those locations (Figures 29d, h and l) is pointing in x direction (normal to the direction of light propagation). As mentioned in Section 2.1, the strongest optical distortion occurs when the angle between the index of refraction gradients and the direction of the light propagation is large. Clearly, light is distorted even when this angle is small, but the distortion (bending angle) is much smaller. The magnitude of the optical distortion also depends on length scales in y direction over which the  $\ln_x$  is large. Based on that observation, it is clear that the optical distortion caused by the gradient field should be stronger around the leading and trailing edges of the vortex, where the incidence angle is almost 90° and the interface length in y direction

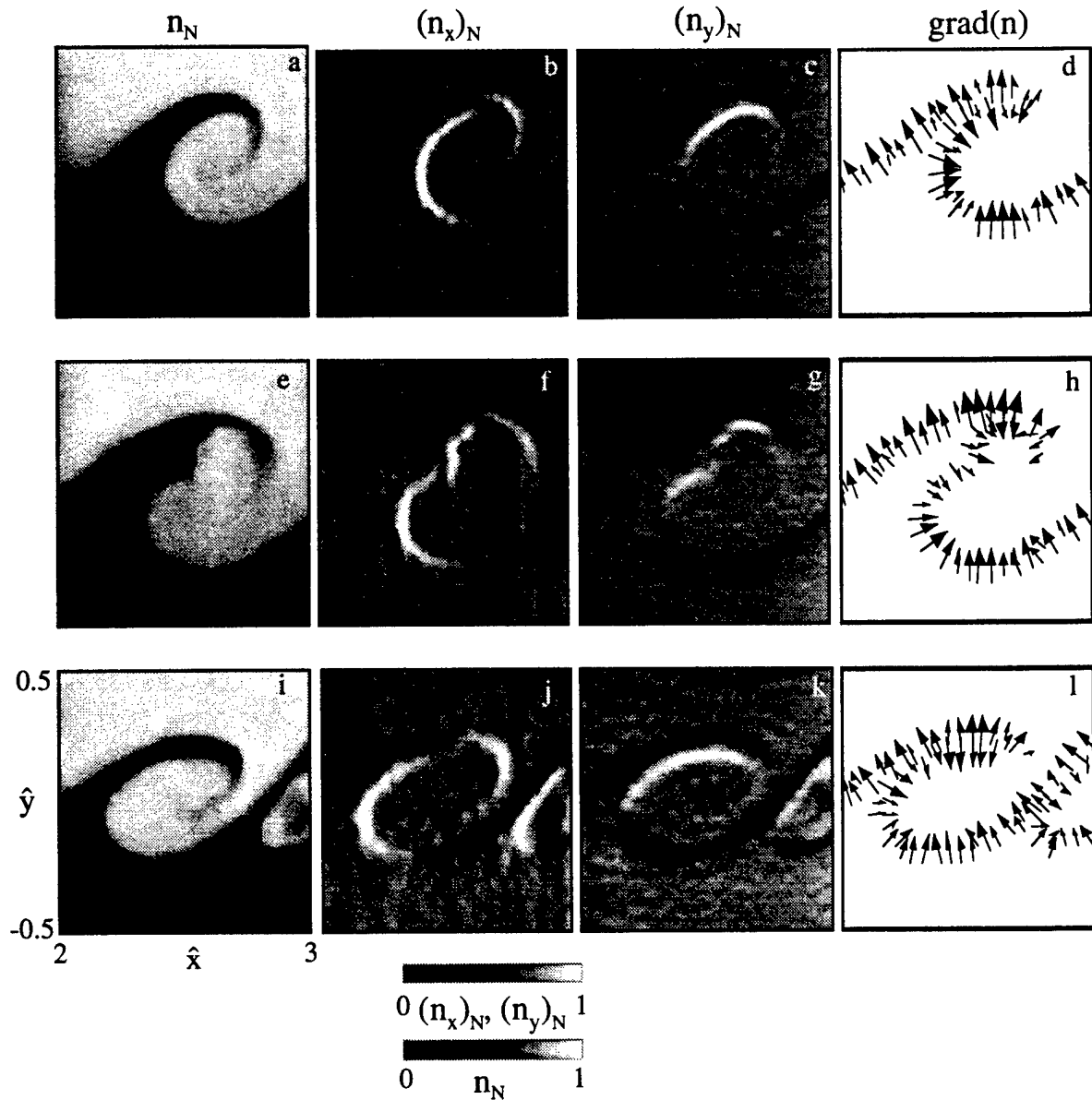


**Figure 29.** Index of refraction [ $n_N = n/\max(n)$ ], magnitude of the index derivative in x [ $(n_x)_N = n_x/\max(n_x)$ ] and y [ $(n_y)_N = n_y/\max(n_y)$ ] directions, and the index gradient for the unforced 24:9 (a-d), 36:12 (e-h), and 42:14 (i-l) shear layers.

is 8-10 mm, than in the braid region where the angle of incidence is typically less than  $45^\circ$  and the interface length is less than 2 mm.

Figures 30a-l show the index of refraction field, derivatives in the x and y direction and the index gradient for the forced ( $f=225$  Hz) 24:9, 36:12 and 42:14 shear layers. The most striking feature of the instantaneous  $n_x$  field for the forced flow (Figure 30b, f and j) is the drastic reduction in the magnitude of the index gradient and the corresponding length scales throughout the flow. For the forced 24:9 shear layer (Figure 30b), the largest  $n_x$  values are 40% smaller than in the unforced flow. Furthermore, the maximum length scale is reduced from 9 mm in the unforced flow to 2 mm in the forced flow. This effect is most evident for the low speed flow (24:9 shear layer), but is also very pronounced for the 36:12 and 42:14 shear layers, shown in Figures 30f and j. While the primary vortex is still prominent for these two cases, the small scales have diffused the interface

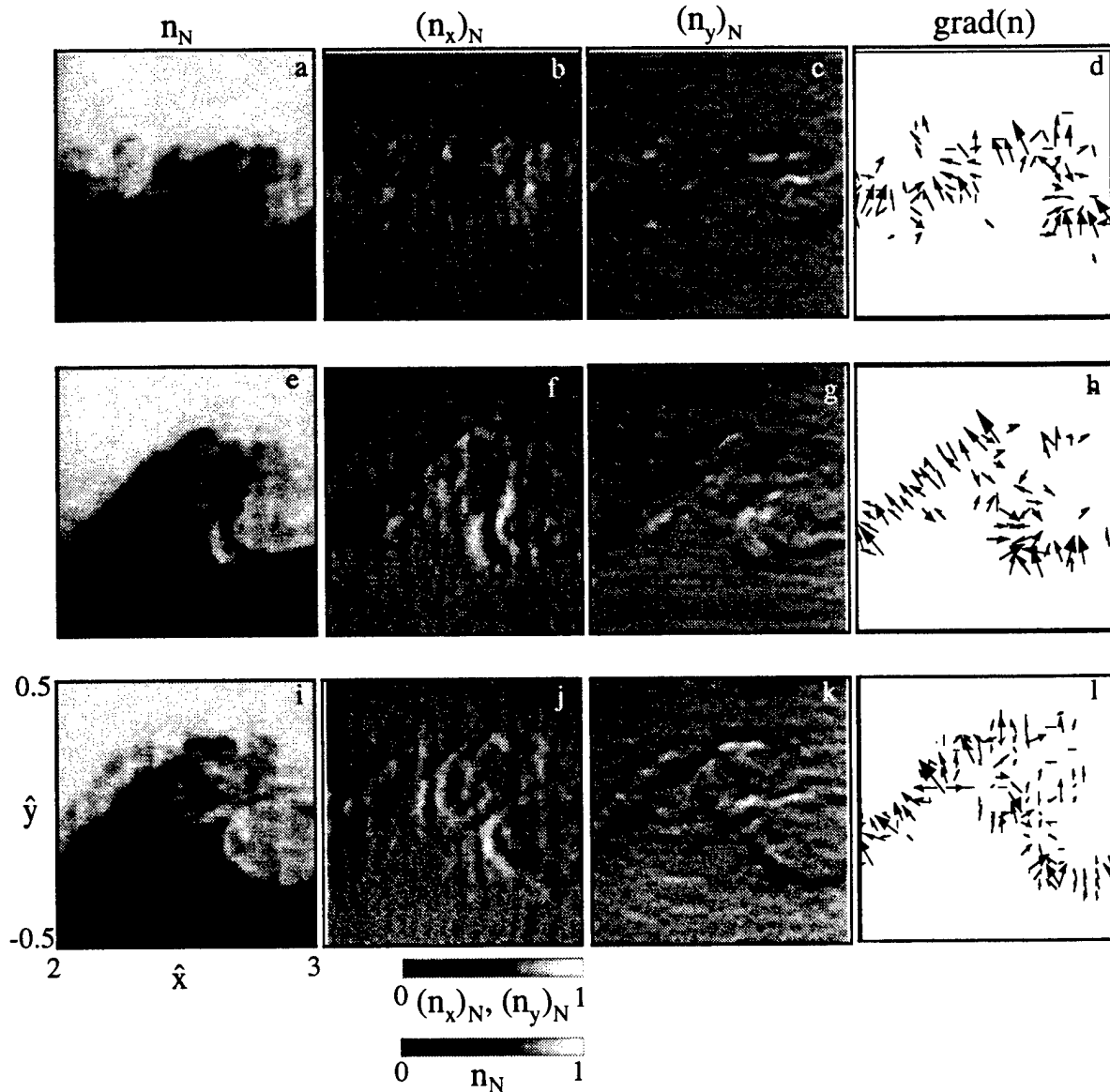


**Figure 30.** Index of refraction,  $n_N = n/\max(n)$ , magnitude of the index derivative in x [ $(n_x)_N = n_x/\max(n_x)$ ] and y [ $(n_y)_N = n_y/\max(n_y)$ ] directions, and the index gradient for the forced ( $f=225$  Hz) 24:9 (a-d), 36:12 (e-h), and 42:14 (i-l) shear layers.

between the two streams in such a way that the maximum length scale is reduced from 8 and 7 mm in the unforced flow in the 36:12 and 42:14 shear layers, respectively, to less than 2 mm in the forced flow. It should also be noted that the r.m.s.  $\sigma_\theta$  (calculated from the corrected temperature maps as described in Section 3.2.) is reduced by more than 30%, from about 72  $\mu\text{rad}$  for the unforced flow to 50  $\mu\text{rad}$  for the forced flow.

Based on observations presented above, it is clear that the net effect of high-frequency excitation on the shear layer optical quality is a result of a combined reduction of the index of refraction gradient and the length scales over which the gradient acts. However, the relative importance of the diffusion zone thickness and shape of the interface on optical distortions is unclear. In order to separately analyze effects of the diffusion zone thickness and interfacial geometry, we developed idealized models of the shear layer. As a first step, we use a typical temperature map from the unforced 24:9 shear layer (such as one shown in Figure 29a) and the correction technique

described in Chapter 3.2. to compute a typical index of refraction map. This map was then used to generate an idealized index of refraction map using a threshold procedure

$$\begin{aligned} n_i(x,y) &= n_1(x,y) & \text{if } n(x,y) > (n_m + n_T) \\ &= n_2(x,y) & \text{if } n(x,y) < (n_m - n_T) \\ &= n(x,y) & \text{otherwise} \end{aligned} \quad (11)$$

where  $n_i(x,y)$  is the idealized index of refraction map,  $n(x,y)$  is the original index of refraction map (determined from the temperature map),  $n_1$  and  $n_2$  are the index of refraction magnitudes in the high- and low-speed streams,  $n_m$  is the average index of refraction [ $n_m = (n_1 + n_2)/2$ ], and  $n_T$  is the threshold value. This procedure makes use of the fact that the diffusion zone thickness of the idealized shear layer is determined by the threshold parameter  $n_T$ . The corresponding bending angle  $\delta\theta$  was computed using Eq. (3), as described in Chapter 3.2.1.

The effect of the diffusion zone thickness,  $\delta_D$ , on optical distortions was investigated using five idealized index of refraction maps with  $\delta_D = 0.5$  mm, 1 mm, 2 mm, 3 mm, and 5 mm (Figures 31a-e). The lowest  $\delta_D$  value is limited by the spatial resolution of the original temperature map, i.e., the magnitude of the index of refraction in Figure 31a changes from  $n_1$  to  $n_2$  across one pixel width.

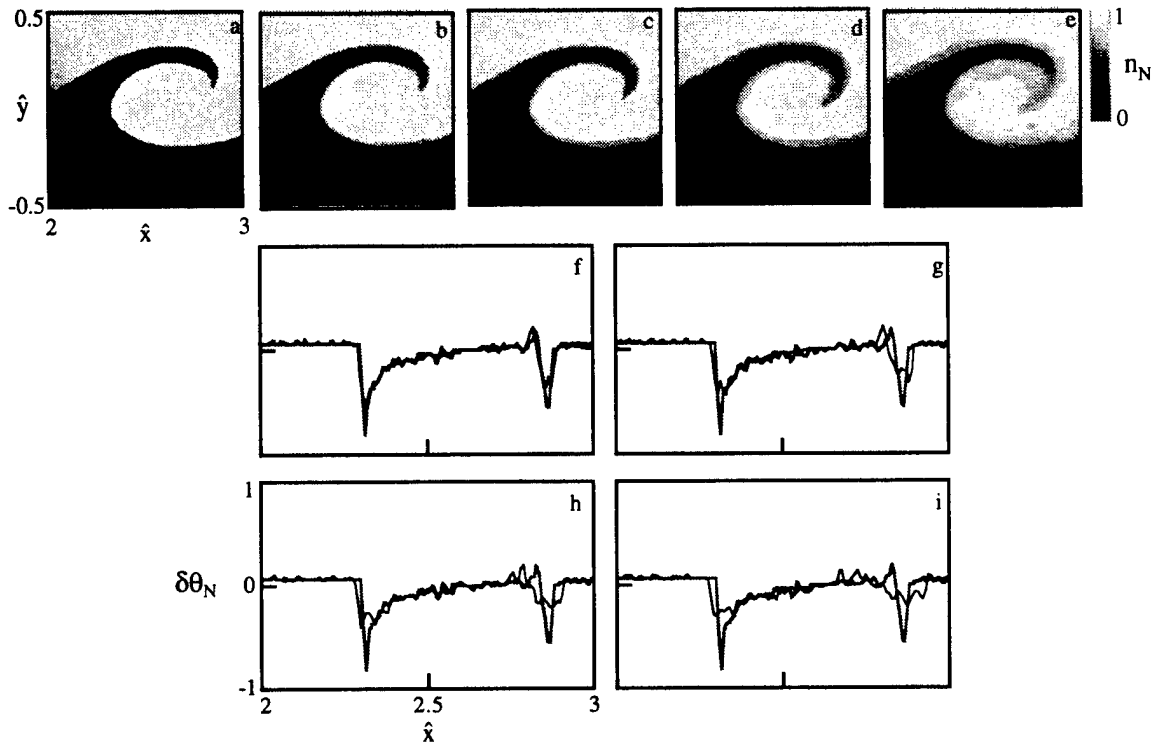


**Figure 31.** The effect of diffusion on optical distortion: interface with diffusion thickness  $\delta_D = 0.5$  mm (a), 1 mm (b), 2 mm (c), 3 mm (d), and 5 mm (e). The corresponding optical distortions for cases b-e (black lines) are shown in (f-i). The optical distortion for case a (gray line) is reproduced for each case

As the diffusion zone thickness increases, the magnitude of the index of refraction gradient decreases (Figures 31b-e). The corresponding normalized bending angles for the index of refraction maps are shown in Figures 31f-i, where the result for  $\delta_D = 0.5$  mm (Figure 31a) is plotted gray and reproduced for each case. As mentioned in the discussion of Figure 24, the optical distortions in a typical 24:9 shear layer result primarily from large deflections of the light rays that



encounter the leading and trailing edges of the spanwise vortex. These deflections produce sharp peaks in the distribution of the bending angle  $\delta\theta$  for the  $\delta_D=0.5$  mm case (gray lines in Figures 31f-i). The light rays propagating through other regions of the spanwise vortex (braid and core region) are also deflected but at much smaller bending angle (notice small positive and negative offset in distributions of  $\delta\theta_N$ ). Results presented in Figures 31f-i suggest that:

- 1) The magnitude of the peak deflections (caused by the leading and trailing edges) decreases as the diffusion zone thickness increases. The maximum beam deflection for the shear layers with  $\delta_D=1$  mm, 2 mm, 3 mm, and 5 mm is reduced by 36%, 45%, 51%, and 63%, respectively, when compared to the maximum deflection for the shear layer with  $\delta_D=0.5$  mm.
- 2) The number of small peaks increases as the diffusion zone thickness increases. However, the peak deflections are still caused by the leading and trailing edges of the spanwise vortex.
- 3) The r.m.s. optical distortion decreases as the diffusion zone thickness increases. For the shear layers with  $\delta_D=1$  mm, 2 mm, 3 mm, and 5 mm, the r.m.s. optical distortion is reduced by 10%, 15%, 21%, and 29%, respectively, compared to the shear layer with  $\delta_D=0.5$  mm.

The effect of the interfacial geometry (shape of the interface separating the two streams) is analyzed using an idealized model of the shear layer, shown in Figure 31a. The idealized (unforced) interface between the two streams for the shear layer with  $\delta_D=0.5$  mm is shown in Figure 32a, and

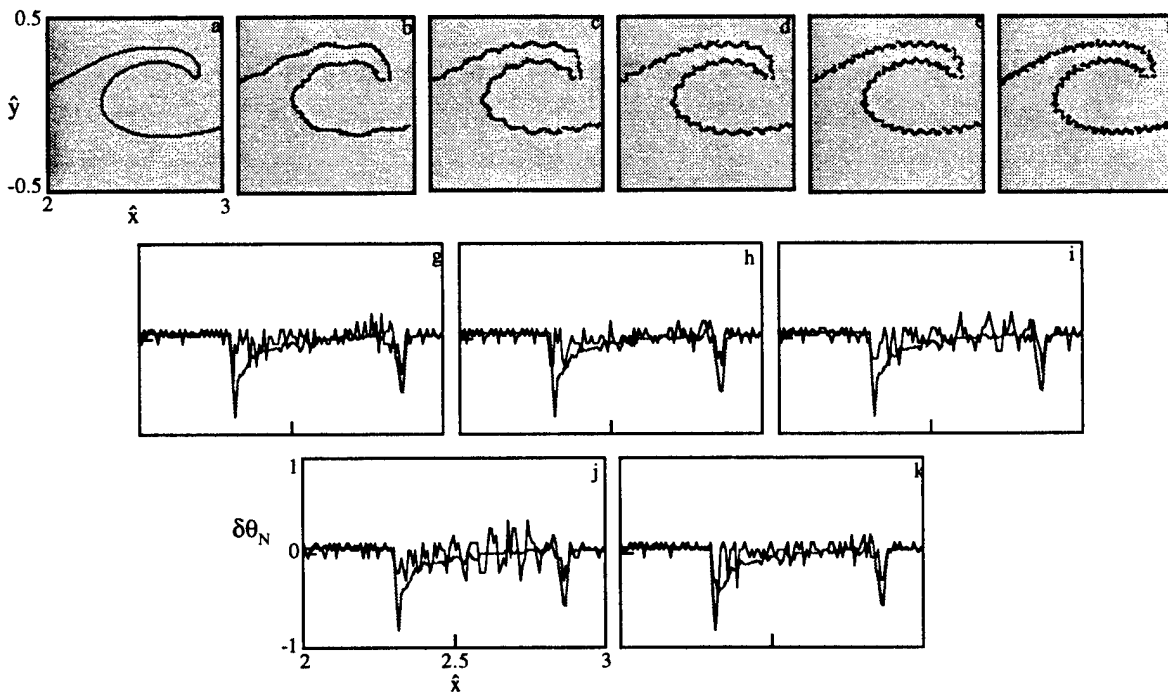


**Figure 32.** The effect of the interface geometry on optical distortions ( $\delta_D=0.5$  mm): unforced interface (a), and interface perturbed with a periodic disturbance with a wavelength of  $0.3 \lambda_{K-H}$  (b),  $0.15 \lambda_{K-H}$  (c),  $0.1 \lambda_{K-H}$  (d),  $0.07 \lambda_{K-H}$  (e), and  $0.06 \lambda_{K-H}$  (f). The corresponding optical distortions for cases b-f (black lines) and case a (gray line) are shown in (g-k). The peak-to-peak disturbance amplitude is 5% of the interface cross-stream extent

the corresponding optical distortion is shown in Figures 32g-k (gray lines). This interface is then perturbed with a periodic disturbance, and the resulting optical distortion was compared to one caused by the idealized (unforced) interface. Figures 32b-f show the perturbed interfaces with the disturbance wavelengths of  $0.3 \lambda_{K-H}$ ,  $0.15 \lambda_{K-H}$ ,  $0.1 \lambda_{K-H}$ ,  $0.07 \lambda_{K-H}$ , and  $0.06 \lambda_{K-H}$ . The peak-to-peak disturbance amplitude is 5% of the interface cross-stream extent. The corresponding results for the normalized bending angle  $\delta\theta$  are shown in Figures 32g-k, where the result for the unforced interface (gray lines) is reproduced for reference. Since the diffusion zone thickness remains

unchanged for all cases presented in Figure 32, we are comparing optical distortions that are caused by changes in the interfacial geometry due to a periodic disturbance.

When the interface is perturbed with the disturbance wavelength of  $0.3 \lambda_{K-H}$  (Figure 32g), the maximum and r.m.s. values of the optical distortion are reduced by 46% and 29%, respectively, when compared to distortions for the idealized (unforced) interface (gray line). Although the perturbation of the interface results in a dramatic reduction of the peak distortions caused by the edges of the vortical structure, it also produces a number of smaller peaks. As the wavelength of the disturbance increases (Figures 32h-k), the number of smaller peaks in the distribution of the distortion also increases. However, both the maximum and r.m.s. values of the optical distortion remain smaller than values computed for the idealized (unforced) interface. The reduction of the peak distortions remains practically unchanged with the change of the disturbance wavelength: 55%, 48%, 47% and 46% for the  $0.15 \lambda_{K-H}$ ,  $0.1 \lambda_{K-H}$ ,  $0.07 \lambda_{K-H}$ , and  $0.06 \lambda_{K-H}$  wavelengths, respectively. The r.m.s. optical distortion is reduced by 38%, 31%, 17%, and 32%, respectively, when compared to the distortion for the unforced interface. Notice that the interface perturbed with the wavelength  $0.07 \lambda_{K-H}$  causes pronounced distortions in the region around the core of the vortical structure. Figure 32e indicates that the interface perturbed this way has several sharp peaks where the angle between the index gradient and the direction of the light propagation is large, which results in large deflection of the incoming light.

Figures 33a-k show the idealized interfaces and the corresponding optical distortion for the same disturbance wavelength as in Figure 32 but with the peak-to-peak disturbance amplitude of 10% of

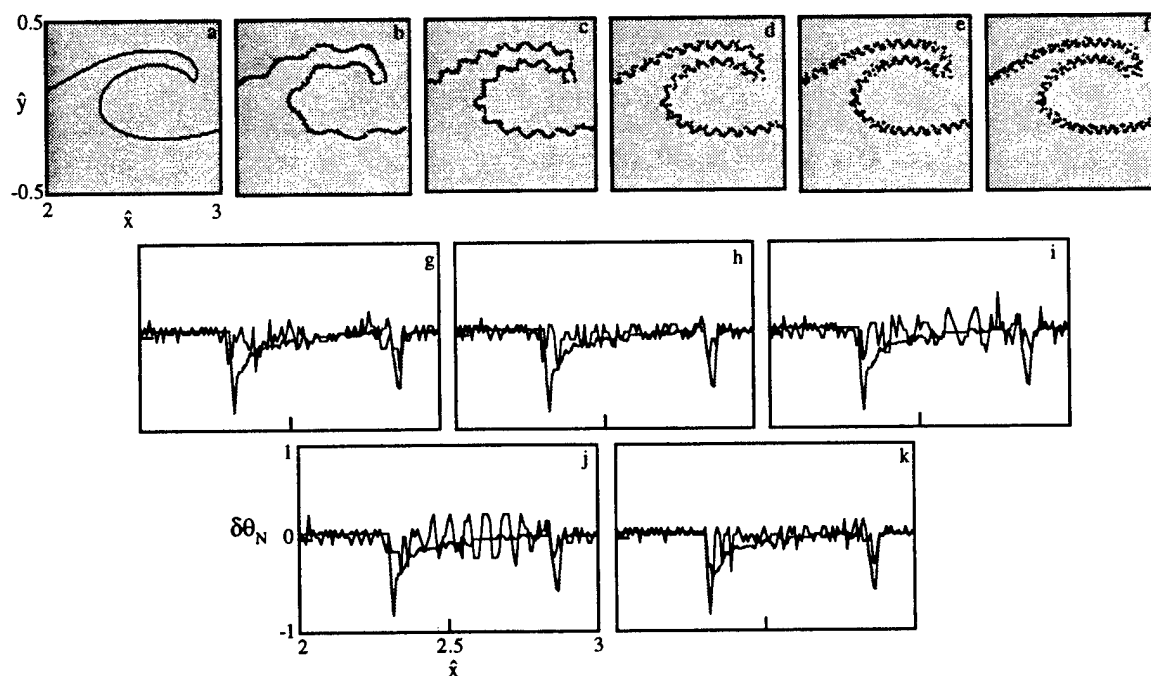


**Figure 33.** The effect of the interface geometry on optical distortions ( $\delta_D=0.5$  mm): unforced interface (a), and interface perturbed with a periodic disturbance with a wavelength of  $0.3 \lambda_{K-H}$  (b),  $0.15 \lambda_{K-H}$  (c),  $0.1 \lambda_{K-H}$  (d),  $0.07 \lambda_{K-H}$  (e), and  $0.06 \lambda_{K-H}$  (f). The corresponding optical distortions for cases b-f (black lines) and case a (gray line) are shown in (g-k). The peak-to-peak disturbance amplitude is 10% of the interface cross-stream extent.

the interface cross-stream extent. The maximum distortion values are reduced by 54%, 55%, 48%, 47%, and 46% for the disturbance wavelengths  $0.3 \lambda_{K-H}$ ,  $0.15 \lambda_{K-H}$ ,  $0.1 \lambda_{K-H}$ ,  $0.07 \lambda_{K-H}$ , and  $0.06 \lambda_{K-H}$ , respectively. The r.m.s. distortion is reduced by 31%, 38%, 22%, 10%, and 32% for

the same wavelengths. It appears that the interface perturbed with the wavelength  $0.15 \lambda_{K-H}$  provides optimal reduction of optical distortions in terms of peak and r.m.s. values.

It is also of interest to consider distortion of a light sheet that propagates through an idealized interface perturbed with a random disturbance. Again, the idealized index of refraction map for the shear layer with  $\delta_D = 0.5$  mm was used as a reference to which the random disturbance is added, and the corresponding bending angle was computed using Eq. (3). Figures 34a-i show the idealized interfaces and resulting distortions for the random perturbation with disturbance levels of 9%, 18%, 27%, and 36% of the mean value. The corresponding maximum distortion values are reduced by 29%, 31%, 37%, and 26% when compared to maximum distortion for the idealized (unforced) interface. On the other hand, the r.m.s. optical distortion was actually increased by 1%, 8%, 15%, and 23% for the same disturbance levels. This is mainly due to the fact that the diffusion thickness is kept constant at  $\delta_D = 0.5$  mm for all cases. As the disturbance level increases the interface appears thicker but the index of refraction gradient remains strong, causing optical distortions.

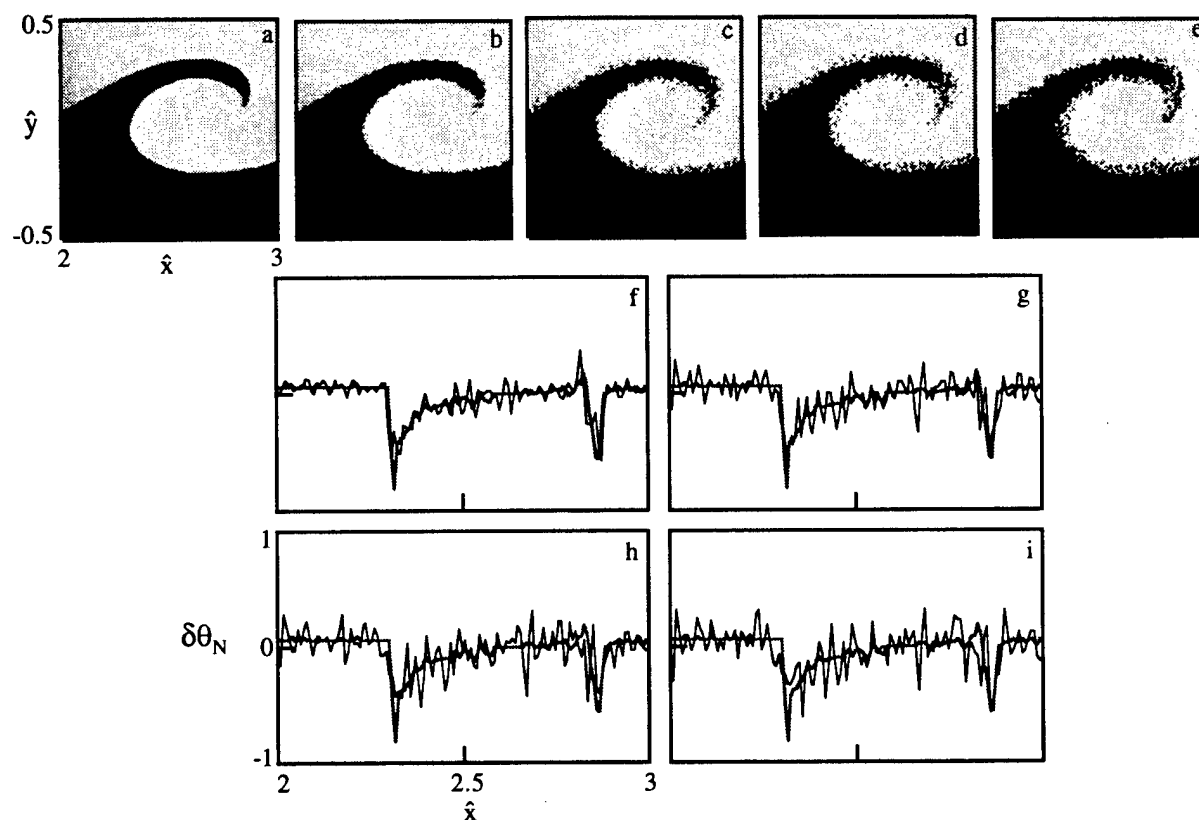


**Figure 34.** The effect of the interface geometry on optical distortion ( $\delta_D = 0.5$  mm): undisturbed interface (a), and randomly disturbed interface with disturbance levels of 9% (b), 18% (c), 27% (d), and 36% (e) of the mean value. The corresponding optical distortions for cases b-e (black lines) are shown in (f-i). The optical distortion for case a (gray line) is reproduced for each case.

As mentioned above, the optical distortion in the spanwise direction can be even stronger than the distortion in the streamwise direction caused by the spanwise coherent structures. The effect of high-frequency excitation on beam deflection in the spanwise direction is shown in Figures 35a-g for the 24:9 and 36:12 shear layers and streamwise positions that correspond to the unforced case

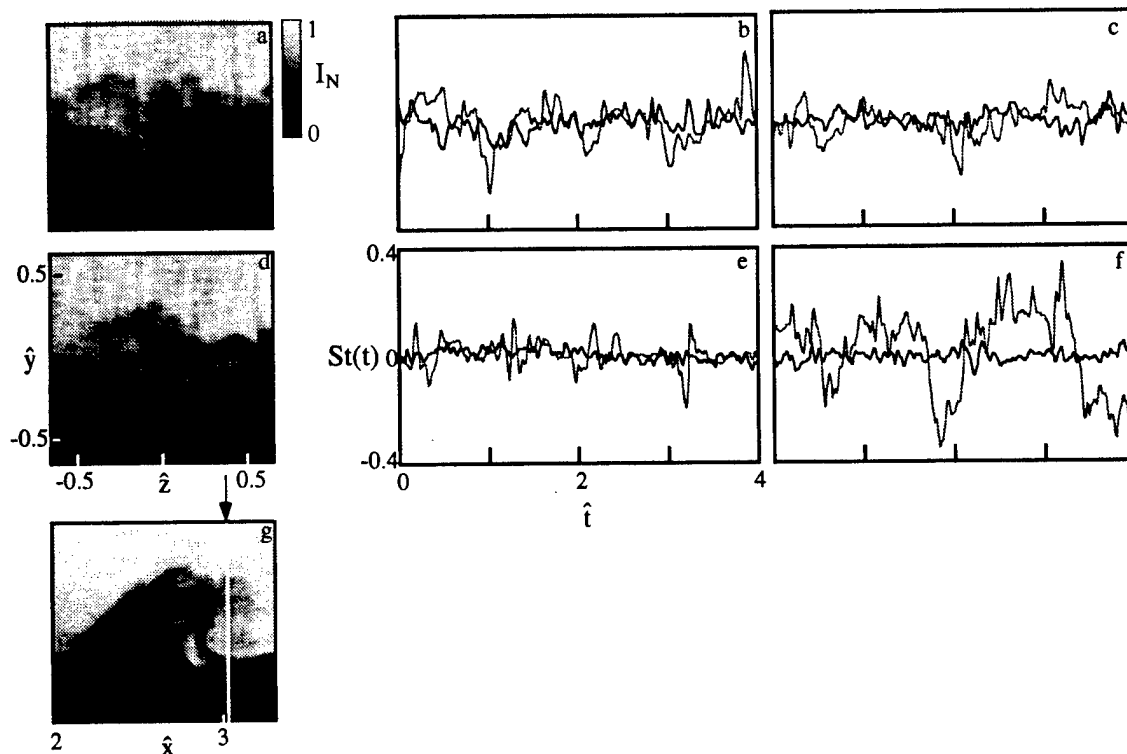


**Figure 35.** Instantaneous intensity field (a, d) and a time trace of the Strehl ratio for the forced ( $f=225$  Hz) 24:9 and 36:12 shear layers at  $\hat{x}/\lambda_{KH}=2.8$  (b, c) and 4.6 (e, f). A typical x-y image (g) of the spanwise vortex indicating the x-location (I-I) for y-z images.

(Figure 20). Each composite includes the instantaneous intensity field (a, d) and a time trace of the Strehl ratio at  $\hat{x}=2.8$  (b, e) and 4.6 (c, f), where the unforced flow results (gray lines) are reproduced for reference. Also shown in Figure 35g is a typical instantaneous x-y view of the shear layer, showing the spanwise vortex and the streamwise location of Figures 35a,d. In general, the interface between the two streams appears to be much more diffused in the forced flow. Furthermore, the interface corresponding to the tip of the primary vortex, that is evident in the unforced flow, is masked by the small scale turbulence in the forced flow. While the spanwise distortion in the unforced flow (Figure 20) occasionally reaches 40% of the reference intensity, the peak distortions for the forced flow are always much smaller (less than 10%), and their time traces are free of occasional large deflections characteristic of the unforced flow. This effect is particularly striking for the higher free-stream velocities (36:12 shear layer), as shown in Figures 35c and f.

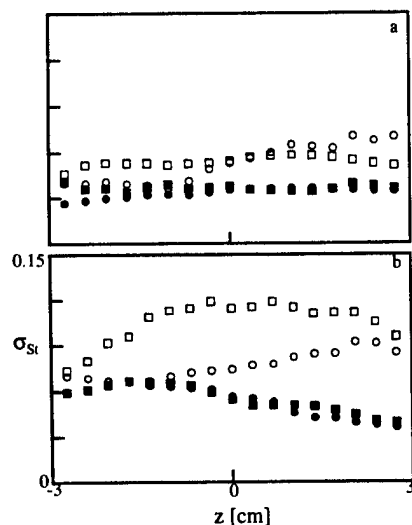


**Figure 36.** Spanwise  $\sigma_{St}$  for 24:9 (○) and 36:12 (□) shear layers at  $\hat{x}/\lambda_{KH} = 2.8$  (a) and 4.6 (b) for the forced flow ( $f=225$  Hz). Open symbols indicate unforced  $\sigma_{St}$ .

The r.m.s. Strehl ratio  $\sigma_{St}(z)$  in the spanwise direction for the forced 24:9 and 36:12 shear layers at  $\hat{x}=2.8$  and 4.6 is shown in Figures 36a-b, where the unforced profiles (open symbols) are reproduced for

reference. It is clear that the optical distortion is always much weaker when the flow is forced at the high frequency. This is particularly evident at  $\hat{x}=2.8$  (Figure 36b), where the streamwise structures are larger and better defined. The average r.m.s. distortion in the forced flow is reduced between 40% and 50% with respect to that in the unforced flow, depending on the flow velocities and the streamwise location. While the optical distortions varied with the spanwise direction in the unforced flow (due to the preferential locations of the streamwise vortices) the variations for the forced flow are much less noticeable, indicating that the high-frequency forcing is very effective in suppression of the organized streamwise structures.

Figures 37a-f show the  $\hat{y}-\hat{t}$  and  $\hat{z}-\hat{t}$  plane cuts of the forced ( $f=225$  Hz) 24:9 (a-c) and 36:12 (d-f) shear layers that correspond to time-frozen pictures of the shear layer and a corresponding optical distortion in the spanwise direction, respectively. These results are directly comparable to the unforced results in Figure 19. It is evident that the optical distortion in the  $\hat{z}-\hat{t}$  plane is relatively unchanged during a time interval corresponding to four periods of the initial instability. Furthermore, the optical distortion is not localized to the core and cusp regions of the spanwise vortices and the streaks caused by the streamwise vortices are imperceptible.

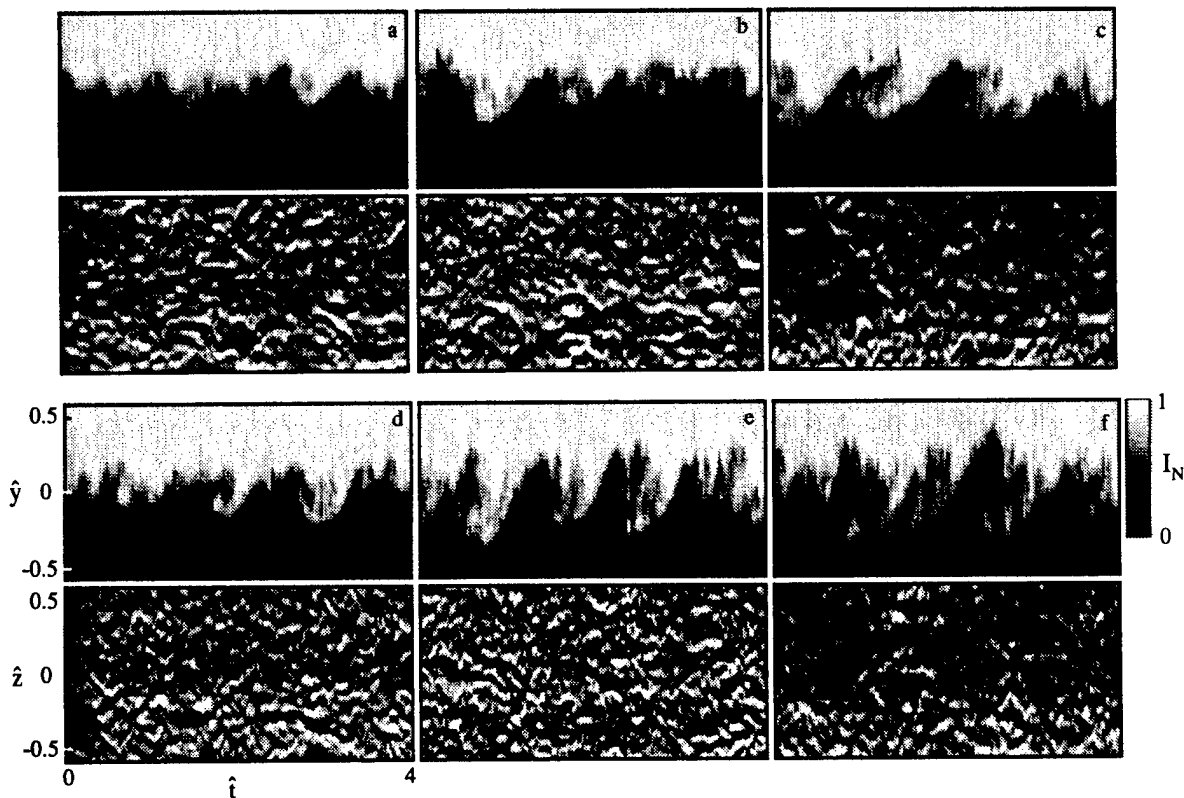


**Figure 37.** Optical distortions in the spanwise plane for the 24:9 (a-c) and 36:12 (d-f) forced ( $f=225$  Hz) shear layers:  $z$ - $t$  plane cut through the low-speed stream at  $x/\lambda_{K-H}=-0.5$  and  $y$ - $t$  plane cut at  $z=0$  and  $x/\lambda_{K-H}=2.8$  (a, d), 3.7 (b, e), and 4.6 (c, f).

While the optical distortions in the spanwise direction in the unforced flow strongly depend on the particular phase (as shown in Figure 21), this dependence is significantly reduced when the high-frequency excitation is applied. Figures 38a-f show the spanwise views of the forced 24:9 shear layer for six time steps separated by 20 ms corresponding to one passage of the spanwise coherent structure, and the corresponding variation of the r.m.s. distortion for different phases. Not only is the r.m.s. distortion always smaller for the forced flow, but it is also practically constant throughout the cycle.

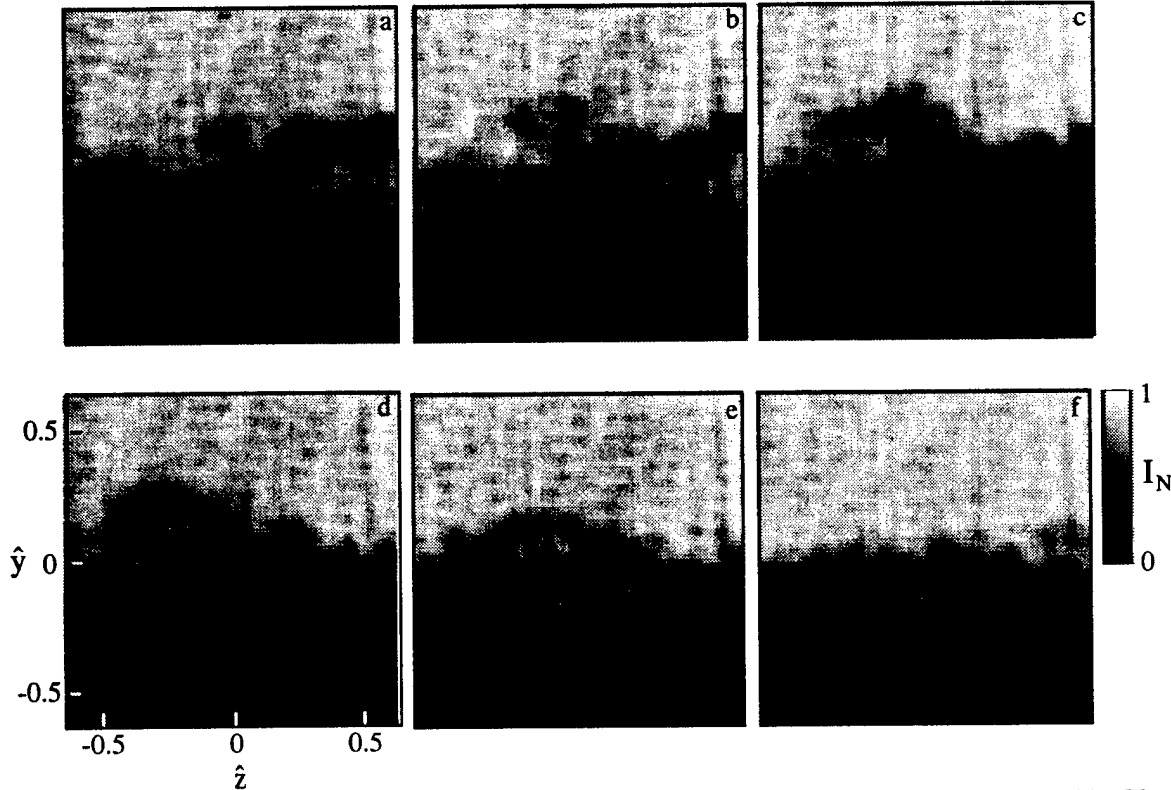


**Figure 38.** Spanwise view of the forced ( $f=225$  Hz) 36:12 shear layer for six time intervals separated by 20 ms in one cycle of the base flow (a-f).

#### IV. LIF MEASUREMENTS OF THERMAL MIXING

In the present experiments, the instantaneous 2-D temperature distributions were obtained using simultaneous measurements of laser-induced fluorescence of Rhodamine B and disodium Fluorescein. The extent of mixing in unforced and forced shear layer flows was inferred from the history of the temperature distribution. The effect of the direct small-scale excitation on mixing and aero-optics distortions in the shear layer is discussed in the following section.

##### IV.1. Mixing in the Unforced Shear Layer

The instantaneous images of the temperature field in the cross-section of the shear layer were obtained using the planar laser induced fluorescence technique. The time history of the instantaneous temperature field at a given streamwise station can be used to augment the spatial image which is limited by the magnification and size of the imaging sensor.

Figures 39-41a-c show time plots of cross-stream intensity maps taken in the 24:9, 36:12, and 42:14 unforced shear layers at  $x/\lambda_{K-H}=2.8$ , 3.7, and 4.6, respectively. The sequence taken in the 24:9 shear layer (Figures 39a-c) contains a train of nearly periodic, well defined eddies that remain coherent at all streamwise positions. The time-averaged cross-stream temperature distribution, shown to the left of each sequence, exhibits pronounced slope discontinuity on the high speed side of the shear layer, and then increases almost linearly. As pointed out by Wiltse (1993), the slope discontinuity is a result of the rollup of the spanwise vortices and the absence of mixing at this streamwise location. At the second streamwise station in the 24:9 shear layer ( $x/\lambda_{K-H}=3.7$ ), the spanwise vortices are larger compared to the first streamwise station, and the slope discontinuity in the time-averaged cross-stream temperature distribution is even more pronounced. As the flow

develops toward turbulent transition farther downstream ( $x/\lambda_{K-H}=4.6$ ) the slope discontinuity becomes less noticeable but is still visible, suggesting that fluid within the vortex core is rolled into orderly layers.

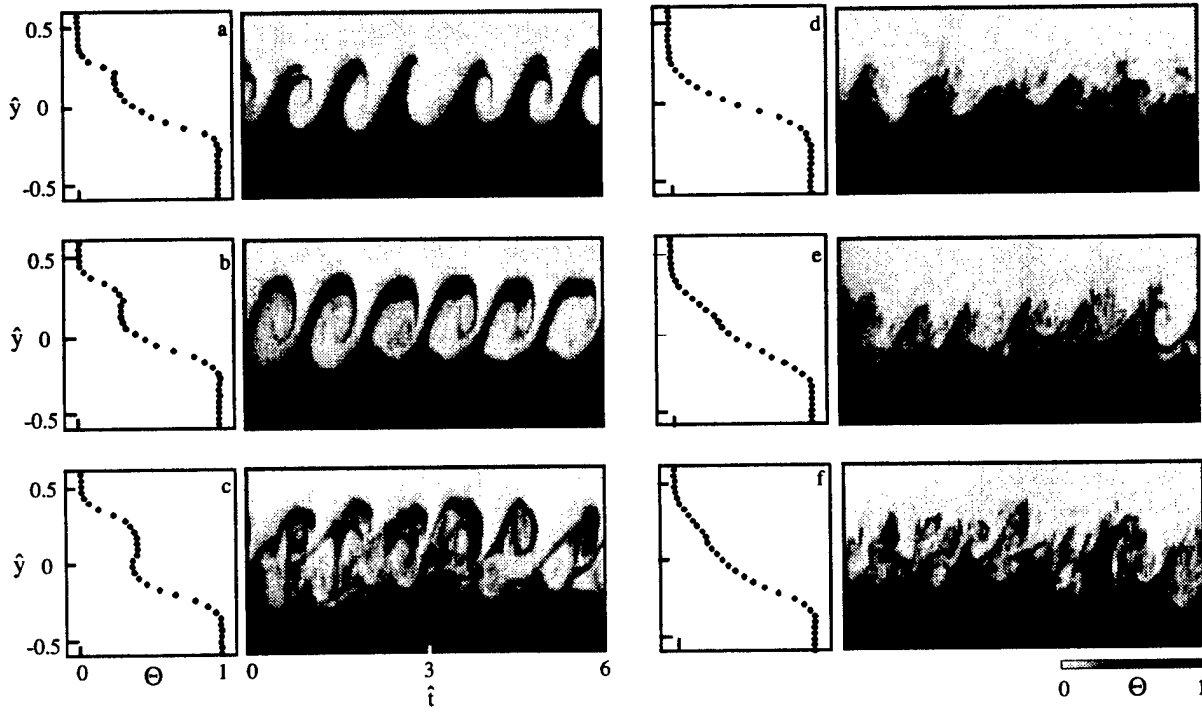


**Figure 39.** Temperature-time plots and mean cross-stream temperature distribution. Unforced (a-c) and forced (d-f) 24:9 shear layer at  $x/\lambda_{K-H}=2.8$  (a, d), 3.7 (b, e), and 4.6 (c, f).

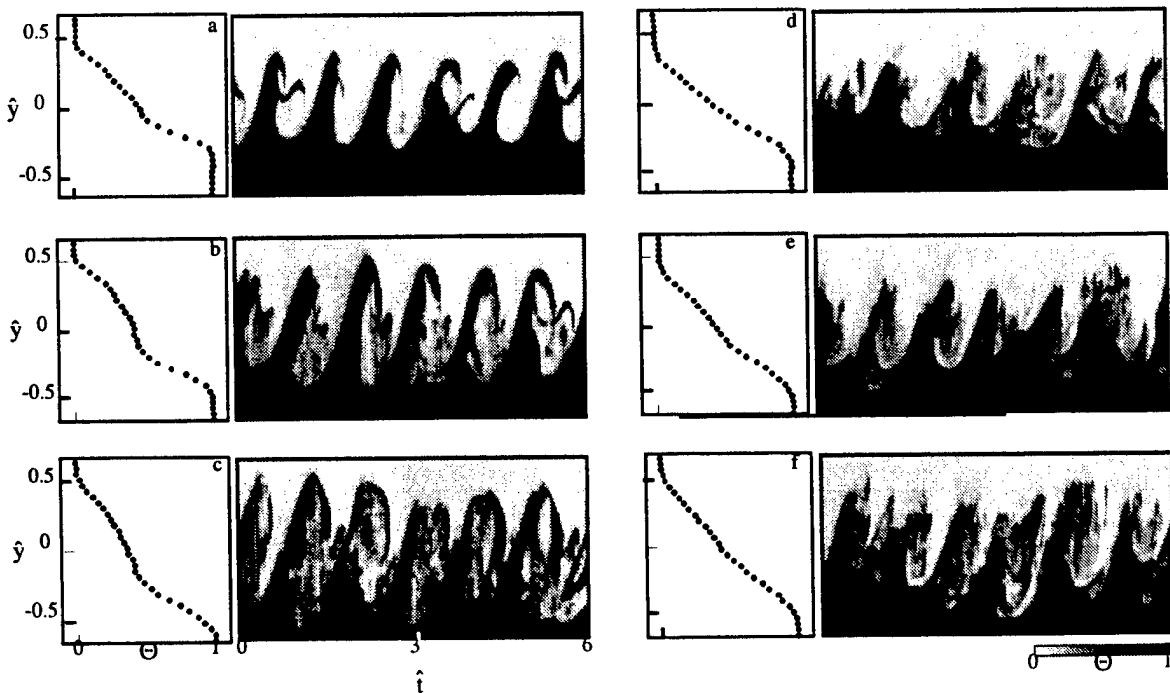


**Figure 40.** Temperature-time plots and mean cross-stream temperature distribution. Unforced (a-c) and forced (d-f) 36:12 shear layer at  $x/\lambda_{K-H}=2.8$  (a, d), 3.7 (b, e), and 4.6 (c, f).

The sequence taken for the 36:12 shear layer (Figures 40a-c) is more complex and dominated by large vortical structures. Previous work (Koochesfahani 1984) indicates that the mixing transition in the unforced shear layer flow occurs at  $Re_\delta = 6000-17000$ , where the Reynolds number is based on the local cross-stream extent of the shear layer and the velocity difference. It appears that by the third streamwise position ( $x/\lambda_{K-H}=4.6$ ,  $Re_\delta=11,000$ ) the flow has undergone a turbulent transition with significant increase in mixing (this increase will be discussed later in terms of performance measures). The cross-stream temperature distribution has a distinct region around the geometrical center of the shear layer where the slope of the temperature profile is steeper than in the regions closer to free-stream conditions. This effect is more pronounced farther downstream where the mixing is more intense and the temperature distribution is even steeper in the central region. Another notable feature of the cross-stream temperature distribution is that the steepest temperature variation occurs near the low-speed edge of the shear layer, suggesting that the temperature field is better mixed near the high-speed side.

Figures 41a-c show time plots and time-averaged cross-stream temperature distributions for the unforced 42:14 shear layer. At  $x/\lambda_{K-H}=2.8$ , the frequency of the initial instability is higher than for the first two cases (7 Hz), but the flow is still reasonably simple. Like the  $T(y)$  profile in Figure 40a, the mean temperature profile also shows a slope discontinuity at this streamwise station. At the second streamwise station  $x/\lambda_{K-H}=3.7$ , the slope discontinuity in  $T(y)$  is much less noticeable and the flow is in the transition stage ( $Re_\delta=14,000$ ). Farther downstream at  $x/\lambda_{K-H}=4.6$ , the slope discontinuity in  $T(y)$  is imperceptible and the temperature increases smoothly (almost linearly) from  $T_L$  to  $T_H$ .

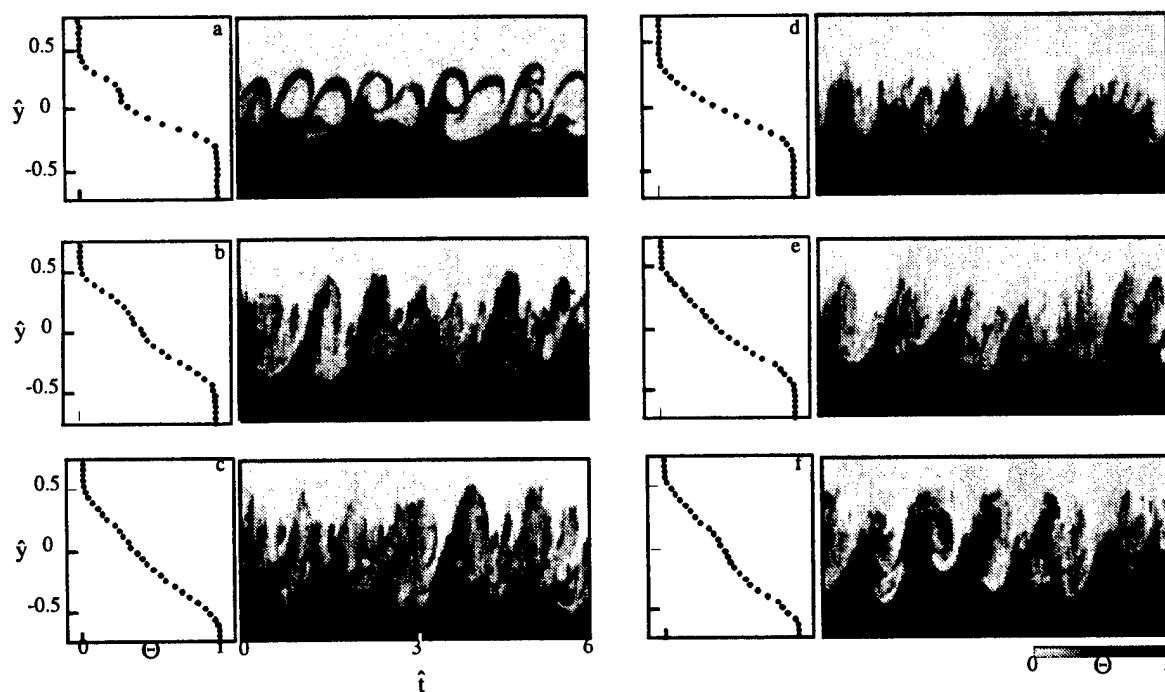


**Figure 41.** Temperature-time plots and mean cross-stream temperature distribution. Unforced (a-c) and forced (d-f) 42:14 shear layer at  $x/\lambda_{K-H} = 2.8$  (a, d), 3.7 (b, e), and 4.6 (c, f).

#### IV.2. Mixing in the Forced Shear Layer

The effect of direct small-scale excitation on mixing and optical distortion in the shear layer is determined from LIF temperature measurements. As indicated above, direct excitation of small-scale motions is accomplished using an array of piezoelectric actuators mounted at the trailing edge of the splitter partition, and operated at the resonant frequency of 225 Hz. The spatial resolution is 0.45 mm and measurements are taken for the 24:9, 36:12, and 42:14 shear layers at the same three



streamwise stations as in Figures 39-41a-c. The corresponding local Reynolds numbers are in the range  $4000 < Re_\delta < 18000$ , where  $Re_\delta$  is based on the cross-stream extent of the shear layer.

Both the instantaneous and mean temperature distributions in the shear layer are affected by the high-frequency forcing. Figures 39d-f show time plots of the cross-stream intensity maps for the forced 24:9 shear layer at  $x/\lambda_{K-H}=2.8$ , 3.7, and 4.6 (these figures are directly comparable to Figures 39a-c). As a result of forcing, the initial instability of the unforced shear layer is suppressed at the first streamwise station (Figure 39d), and the spanwise vortices are almost undetectable. Furthermore, the interface between the two streams, which is sharp and well-defined in the unforced flow, is convoluted and diffuse in the forced flow. This indicates that the high-frequency excitation leads to the appearance of small-scale structures and mixing enhancement. Because of that, the slope discontinuity evident in the mean temperature profiles for the unforced flow is not noticeable in the  $T(y)$  profile for the forced flow (shown to the left in Figure 39d). It is noteworthy that the mean temperature varies almost linearly across the shear layer and that the cross-stream extent of the shear layer at  $x/\lambda_{K-H}=2.8$  is slightly reduced by forcing.

At  $x/\lambda_{K-H}=3.7$ , a slight slope discontinuity is evident in the  $T(y)$  profile, indicating the reappearance of spanwise vortices. The slope of the mean temperature profile changes across the shear layer and is steeper around the center than in regions closer to the free stream conditions. At the last streamwise station  $x/\lambda_{K-H}=4.6$ , the spanwise vortices are more noticeable in the time plot, but the slope discontinuity in the  $T(y)$  profile is almost imperceptible. This suggests that fluid within the core of the spanwise vortex is not rolled into orderly layers as in the unforced flow.

Two sequences taken for the 36:12 and 42:14 shear layers are shown in Figures 40d-f and 41d-f (these figures are comparable to the unforced flow in Figures 40a-c and 40a-c). Again, external excitation causes a significant change in the appearance of the shear layer. At the first streamwise station, both flows are still dominated by vortical structures, but the interface between the two streams is diffuse. Furthermore, the  $T(y)$  profile for the forced flow is not as steep in the central region as for the unforced flow, and the slope discontinuity is less noticeable. Once the flow undergoes turbulent transition ( $x/\lambda_{K-H}=4.6$ ), both the time plots and  $T(y)$  profiles for the unforced and forced flow are very similar.

The effect of direct small-scale excitation on the spectral content of the shear layer flow was investigated using a 2-D Fourier Transform of the temperature-time plots shown in Figures 39-41. We introduce spectral amplitudes defined by:

$$P_{\Sigma f}(k_y) = \sum_{i=1}^{M_f} P(f_i, k_y) \quad (12)$$

$$P_{\Sigma k_y}(f) = \sum_{i=1}^{M_y} P(f, k_{y_i})$$

where  $M_f$  and  $M_y$  denote the number of temporal and cross-stream wavenumbers used in the summation,  $P(f, k_y)$  is the 2-D spectral amplitude,  $f$  is the frequency, and  $k_y=1/\lambda_y$  is the wavenumber in the cross-stream direction.

Figures 42a-f show spectral amplitudes for the 24:9, 36:12, and 42:14 unforced (gray lines) and forced (black lines) shear layers, at  $x/\lambda_{K-H}=2.8$ . A comparison of the unforced and forced flow spectral amplitudes  $P_{\Sigma f}(k_y)$  (Figures 42a, c, and e) reveals that the amplitude of spectral components at low wavenumbers in the forced flow is lower than in the unforced flow. On the other hand, in the 24:9 shear layer (Figure 42a) the amplitude of spectral components at all wavenumbers above  $k_y \approx 1 \text{ cm}^{-1}$  in the forced flow is higher than in the unforced flow. Similarly, for the 36:12 and 42:14 shear layers the amplitude of spectral components for the forced flow is increased (compared to the unforced flow) at all wavenumbers above  $k_y \approx 2 \text{ cm}^{-1}$ .

The natural frequency of the shear layer and its higher harmonics are evident in the spectral amplitude  $r_{\Sigma k_y(j)}$  of the unforced flow for all velocity ratios (Figures 42b, d, and f). Other researchers (Tennekes and Lumley 1972, Batchelor 1958) have found that the temperature spectrum varies as  $f^{5/3}$  in the inertial (equilibrium) range in which negligible viscous dissipation occurs. Batchelor (1958) recognized that the scalar quantity spectrum ceases to vary with  $-5/3$  slope near the region where viscosity effects become dominant (dissipation range). If the Prandtl number is high enough there is a part of the spectrum where temperature fluctuations are not yet dissipated by conduction, but their scales are progressively reduced. Batchelor (1958) predicted that the temperature spectrum varies with  $-1$  slope in this region. In the present experiments, the inertial subrange is estimated to be  $8 \text{ Hz} < f < 70 \text{ Hz}$ .

Figures 42b also show the spectral amplitude (black lines) for the forced 24:9 shear layer. The most noticeable feature in the forced spectra is the decrease in the magnitude of spectral components with frequencies near the natural frequency of the shear layer instability. This is another indication that the Kelvin-Helmholtz instability of the shear layer is suppressed at this streamwise location. Although the peak at the forcing frequency is undetectable this far from the actuator blade, the effect of the high-frequency excitation is evidenced in a substantial and broad-band increase in the magnitude of small and large scale motions. Despite the fact that the shear layer flow is forced at 225 Hz, the power in spectral components at all frequencies above 15 Hz is higher than in the unforced flow. Furthermore, the reduction of the power in spectral components

at low frequencies (around the natural frequency) suggests that the high-frequency forcing induces coupling between small and large scales, accelerating energy transfer from large to small scales (Wiltse 1988).

Figures 42d and f show the forced (black lines) and unforced (gray lines) spectral amplitudes for the 36:12 and 42:14 shear layers. The fundamental instability of the shear layer is not as strongly suppressed for these velocity ratios, as evidenced by peaks at the natural frequency and its higher harmonics. We note the decrease in magnitude of spectral components around the natural frequency and at higher harmonics of the natural frequency in the 36:12 and 42:14 shear layers. Similarly to the forced 24:9 shear layer, the power in spectral components at all frequencies above 20 Hz is higher than in the unforced flow.

The effect of the direct small-scale excitation on the instantaneous and mean temperature distributions in the shear layer was quantified by using a performance measure  $pm$ , an integral performance measure  $PM$ , and the probability density function  $pdf$ :

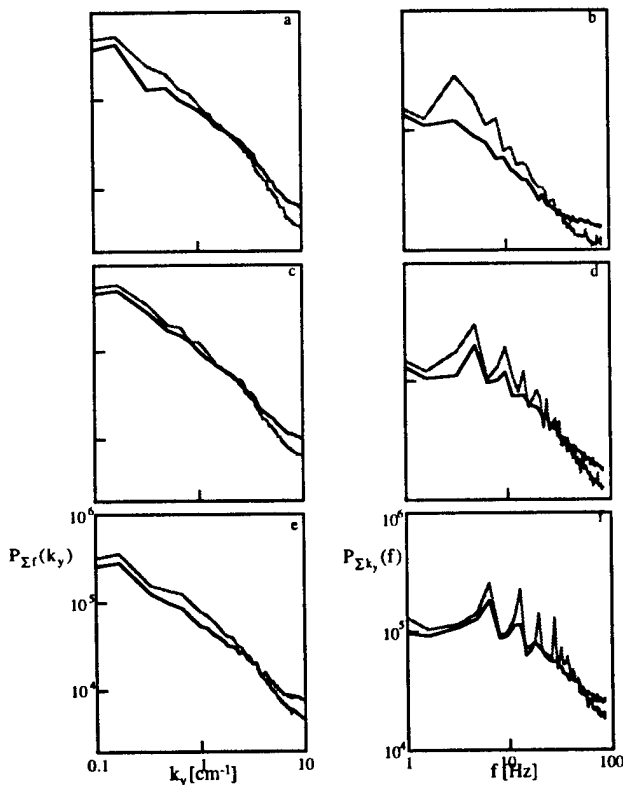


Figure 42. Spectral amplitudes of temperature-time maps for the 24:9 (a, b), 36:12 (c, d), and 42:14 (e, f) shear layers for the unforced (gray line) and forced ( $f=225 \text{ Hz}$ ) flow (black line) measured at  $x/\lambda_{K-H}=2.8$ : (a, c, and e), and (b, d, and f).

$$pm(x, y, t) = \frac{(T_H - T(x, y, t))(T(x, y, t) - T_L)}{(T_H - T_L)^2} \quad (13)$$

$$PM(x, t) = \int_{-y_0}^{y_0} pm(x, y, t) dy \quad (14)$$

$$P(T_L < T < T_H) = \int_{T_L}^{T_H} pdf(T, x, y) dT \quad (15)$$

where  $T(x, y, t)$  was the instantaneous temperature field obtained from the LIF measurements, and  $T_L$  and  $T_H$  were the free-stream temperatures.

The instantaneous performance measure  $pm(x, y, t)$  is a local measure of mixedness in the two streams, and is equal to zero when the measured temperature is equal to one of the free stream temperatures. Figures 43-45 show gray scale raster plots of  $pm(x, y, t)$  for the 24:9, 36:12, and 42:14 shear layers for the unforced and forced flows. In addition to high-frequency forcing with piezo-electric actuators at  $f_H=225$  Hz (Figures 43-45b), the flow was also forced at the lower frequency  $f_L=3$  Hz in order to introduce a clear phase reference (Figure 43-45c), and at the combination of low ( $f=3$  Hz) and high ( $f=225$  Hz) frequency forcing (Figures 43-45d).

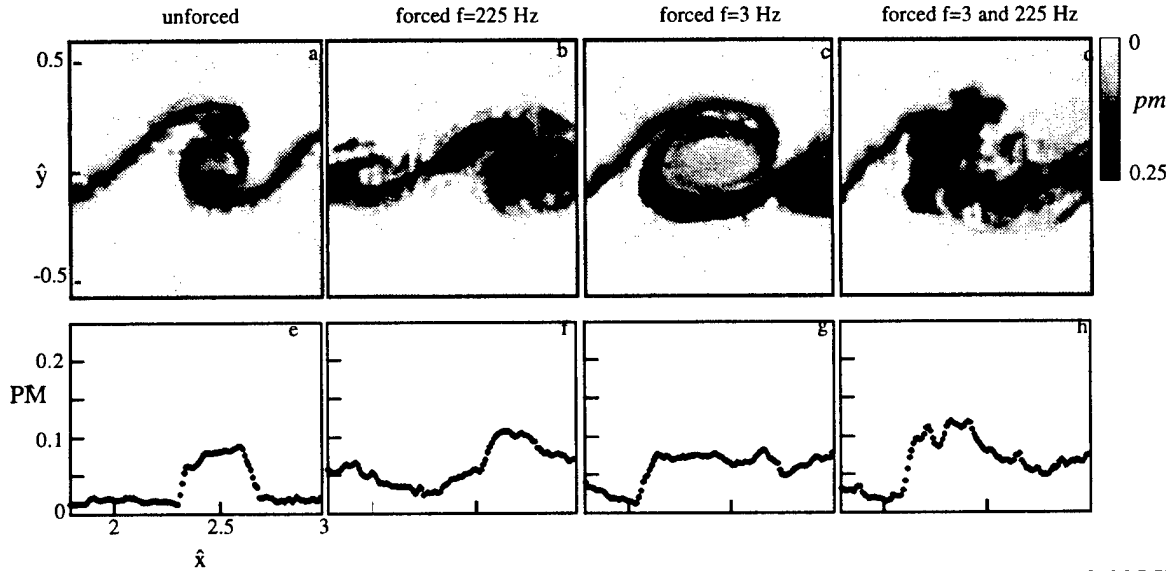


**Figure 43.**  $pm(x, y, t)$  and  $PM_{K-H}$  for the 24:9 shear layer for the unforced (a, e) and forced flow at  $f=225$  Hz (b, f),  $f=3$  Hz (c, g) and the combination  $f=225+3$  Hz (d, h).

Figures 43-45a for the unforced flow show that the amount of mixed fluid is very low for the unforced flow, and that the mixing is localized to a narrow region around the interface between the two streams. When the flow is forced at the high frequency (Figures 43-45b), the amount of mixed fluid within the core of the spanwise vortex is significantly increased. The relative increase in the amount of mixed fluid is demonstrated in plots of the integral performance measure  $\hat{PM}(x, t) = PM(x, t) / \lambda_{K-H}$  across the flow field shown below the instantaneous images for the same instant in time. Forcing at the high frequency  $f=225$  Hz leads to an average increase of 25-35% over the unforced case. Figures 43-45c-d show  $pm(x, y, t)$  for low frequency forcing, and a combination of low and high frequency forcing, respectively. It is clear that the effects of the low frequency forcing on mixing in the shear layer, although significant (average  $\hat{PM}$  increases by 15-20%), are caused mainly by the early rollup of the primary vortex and subsequent growth of the shear layer in the cross-stream direction. In contrast, the high-frequency forcing suppresses growth of the primary vortices at this streamwise station, and the mixing is increased because of

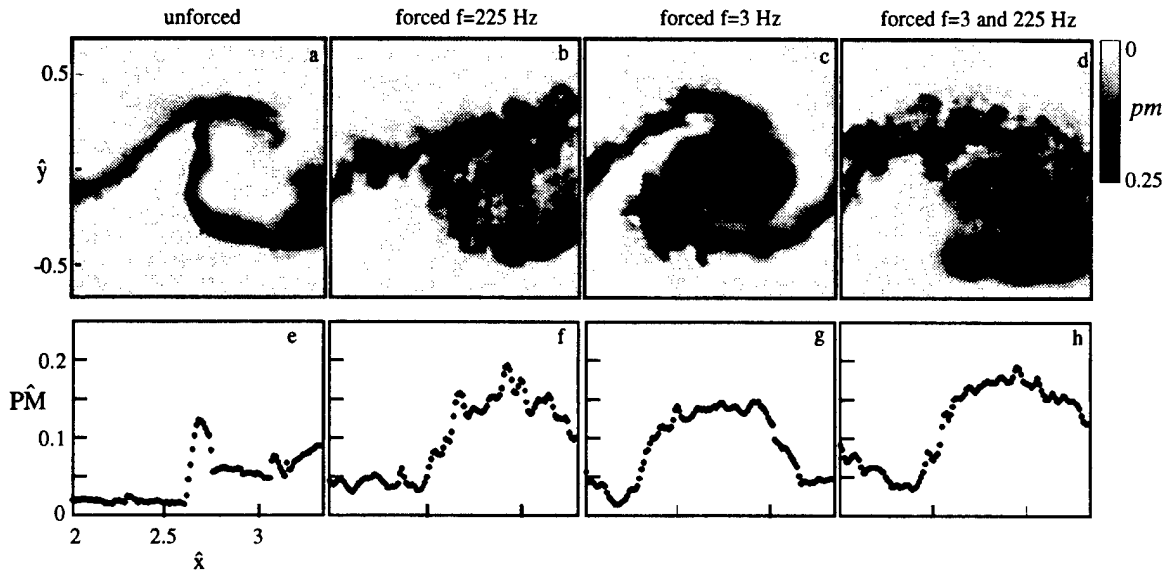


**Figure 44.**  $pm(x,y,t)$  and  $PM_{K-H}$  for the 36:12 shear layer for the unforced (a, e) and forced flow at  $f=225$  Hz (b, f),  $f=3$  Hz (c, g) and the combination  $f=225+3$  Hz (d, h).

the direct introduction of the small scales. Notice that the patches of unmixed fluid within the vortex core visible in Figures 43-45c for the low frequency forcing are less noticeable when the combination of low- and high-frequency forcing is applied (Figure 43-45d). The average integral performance measure for the combination of low and high frequency forcing is increased by 40-60% when compared to the unforced case.

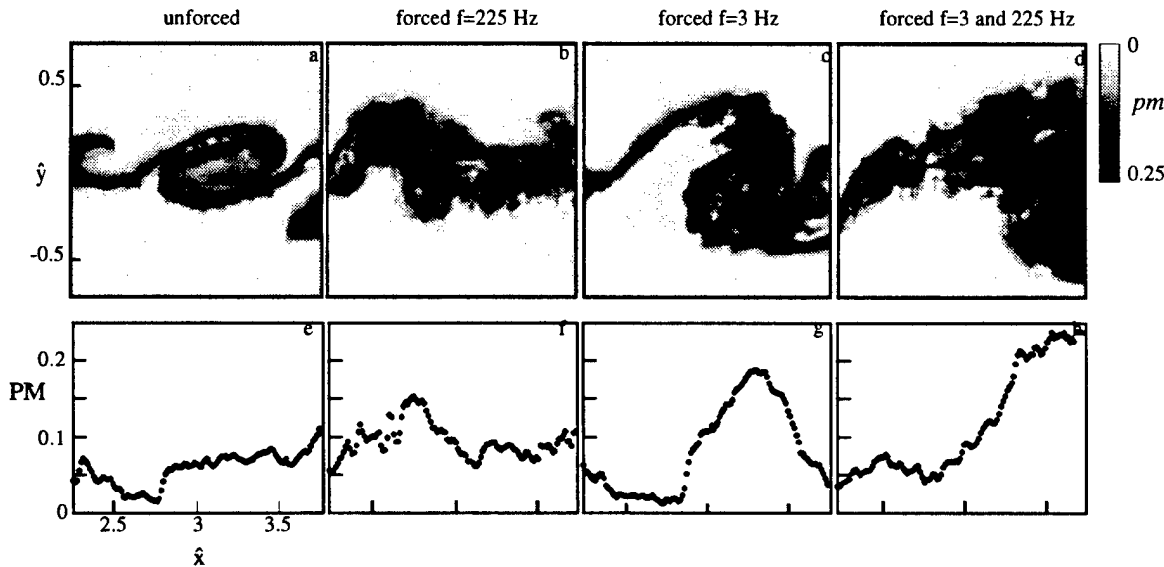


**Figure 45.**  $pm(x,y,t)$  and  $PM/\lambda_{K-H}$  for the 42:14 shear layer for the unforced (a, e) and forced flow at  $f=225$  Hz (b, f),  $f=3$  Hz (c, g) and the combination  $f=225+3$  Hz (d, h).

Figures 46-48 show the average performance measure  $pm(x,y)$  for the unforced and high-frequency (225 Hz) forced 24:9, 36:12, and 42:14 shear layers, together with the time-averaged integral performance measure  $PM(x)$ , obtained from Eq. (14). The time-average cross-stream performance measure distributions  $pm(y)$  at  $x/\lambda_{K-H}=2.8, 3.7$ , and  $4.6$  are shown to the left of each sequence. The temperature measurements were taken separately for partially overlapping regions by traversing the CCD camera in the streamwise direction (images are taken at 220 fps, and the

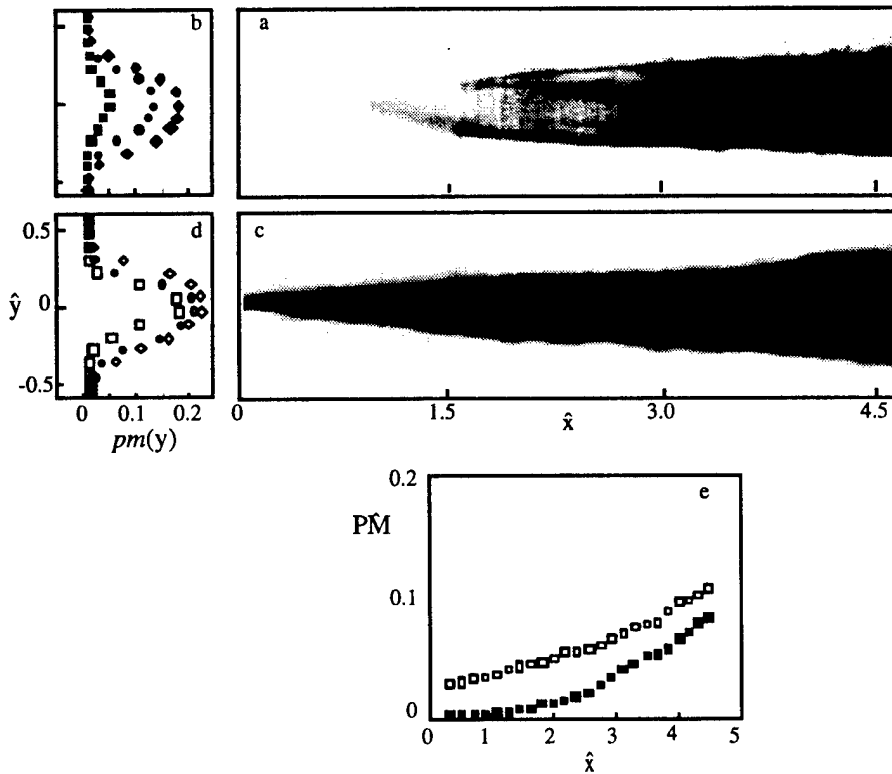


**Figure 46.** Average 2-D performance measure  $pm(x,y)$  and 1-D cross-stream distribution  $pm(y)$  [at  $x/\lambda_{K-H}=2.8$  ( ),  $3.7$  ( ), and  $4.6$  ( )] for the 24:9 shear layers for the unforced (a, b) and forced ( $f=225$  Hz) flow (c, d). The integral performance measure (e) for the unforced (closed symbols) and forced (open symbols) flow

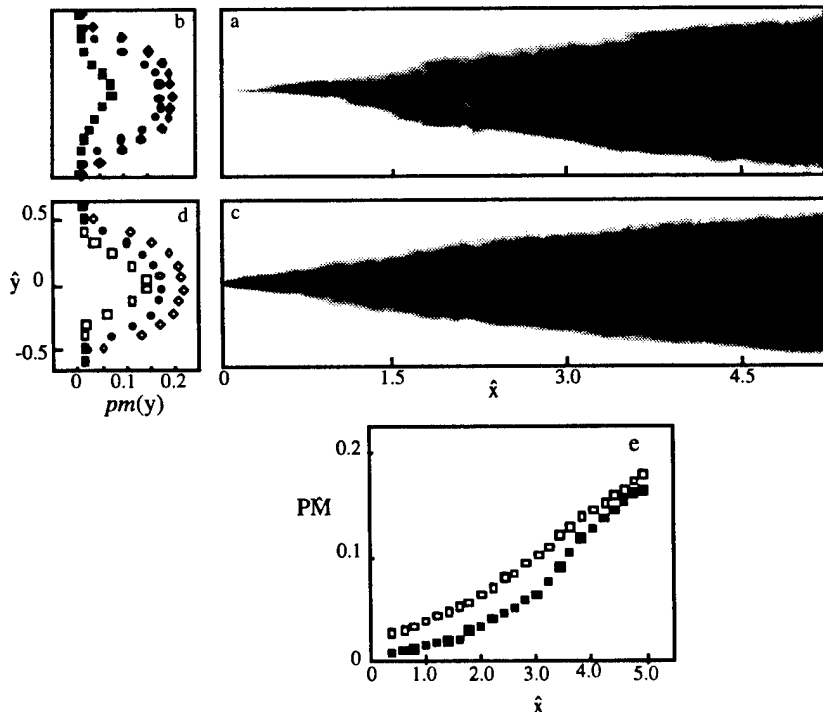


**Figure 47.** Average 2-D performance measure  $pm(x,y)$  and 1-D cross-stream distribution  $pm(y)$  [at  $x/\lambda_{K-H}=2.8$  ( ),  $3.7$  ( ), and  $4.6$  ( )] for the 36:12 shear layers for the unforced (a, b) and forced ( $f=225$  Hz) flow (c, d). The integral performance measure (e) for the unforced (closed symbols) and forced (open

field of view is 6 cm square). The corrected temperature distributions corresponding to individual positions were combined in a composite array and the mean flow parameters were calculated by averaging over 150 cycles of the base flow.

The time-averaged performance measure for the unforced 24:9 shear layer (Figure 46a) indicates that there is virtually no mixing for  $0 \leq x/\lambda_{K-H} \leq 2$ , and that mixing remains weak for most of the streamwise domain. The integral performance measure  $PM$ , shown in Figure 46e (closed symbols), remains relatively weak for  $0 < x/\lambda_{K-H} < 3.5$ , but almost doubles between  $x/\lambda_{K-H}=3.5$  and  $4.6$ . It is also evident from the time-averaged cross-stream distributions  $pm(y)$  at  $x/\lambda_{K-H}=2.8$ ,  $3.7$ , and  $4.6$  (shown to the left) that the region with intense mixing (high  $pm$  values) spreads in the cross-stream direction farther downstream. A reference thickness of the shear layer,  $\delta$ , is determined from the time-average cross stream temperature profile  $T(y)$  at each streamwise station by assuming that the edges of the shear layer correspond to cross-stream locations in the layer where the time-averaged temperature has reached 99% of the mean free-stream temperature.

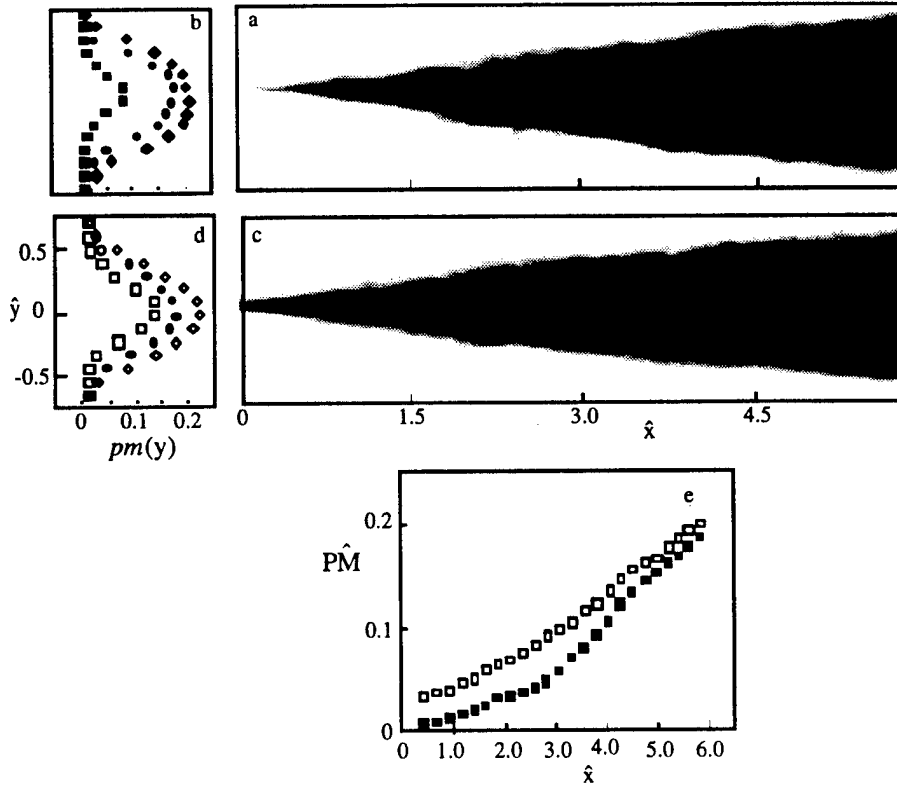


**Figure 48.** Average 2-D performance measure  $pm(x,y)$  and 1-D cross-stream distribution  $pm(y)$  [at  $x/\lambda_{K-H}=2.8$  ( ),  $3.7$  ( ), and  $4.6$  ( )] for the 42:14 shear layers for the unforced (a, b) and forced ( $f=225$  Hz) flow (c, d). The integral performance measure (e) for the unforced (closed symbols) and forced (open symbols) flow.

spreading angle of about  $15^\circ$  in the initial region and estimated the region where the shear layer undergoes a change in growth rate to lie in  $8000 \leq Re \leq 14000$ , with  $Re$  based on cross-stream extent of the shear layer and the velocity difference.

Figures 46c-d show the effect of direct small scale excitation on the time-averaged performance measure in the shear layer. The most striking feature of this composite is the very intense mixing near the shear layer centerline at all streamwise locations. The integral performance measure  $PM$  in the forced flow, shown in Figure 46e (open symbols), is equal to 0.04 and 0.11 at  $x/\lambda_{K-H}=1$  and 4.2, respectively, compared to 0.002 and 0.085 in the unforced flow (closed symbols). Furthermore, the peak values of the time-averaged  $pm(y)$  are always higher in the forced flow. In the forced 24:9 shear layer at  $x/\lambda_{K-H}=2.8$ , 3.7, and 4.6 (Figure 46d) the peak  $pm(y)$  values are 0.18, 0.2, and 0.23 (compared to 0.02, 0.12, and 0.18 in the unforced flow). In fact, the integral performance measure averaged over the full streamwise domain is increased with forcing to a level ( $PM_{av}=0.07$ ) which is almost double that of the unforced case ( $PM_{av}=0.038$ ). Also note that the high-frequency forcing results in a growth rate diminished by 15% for  $x/\lambda_{K-H} < 3.7$  (forcing initially suppresses growth of the spanwise vortices).

Figure 47a shows the time-averaged performance measure for the unforced 36:12 shear layer. These results indicate that the higher free-stream velocities strongly enhance mixing. The cross-stream extent of the shear layer is 3.3, 4.4, and 5.0 cm at  $x/\lambda_{K-H}=2.8$ , 3.7, and 4.6, and the corresponding Reynolds numbers are 8400, 11,200 and 12,700. The growth rate of the shear layer (assumed to be linear throughout the streamwise domain) is about  $15^\circ$ . The integral performance measure is always higher than in the 24:9 shear layer, but remains relatively small ( $PM < 0.04$ ) for  $x/\lambda_{K-H} < 2.4$ , beyond which point the flow undergoes mixing transition and  $PM$  increases sharply throughout the shear layer ( $PM > 0.13$ ). These  $PM$  values are somewhat higher

The local cross-stream extent for the 24:9 shear layer is  $\delta = 2.6$ , 3.1, and 3.8 cm at  $x/\lambda_{K-H} = 2.8$ , 3.7, and 4.6. The corresponding Reynolds numbers based on  $\delta$  and the velocity difference are 4100, 5020, and 6050, respectively. The growth rate of the shear layer is estimated from the average performance measure, and the spreading angle is about  $12^\circ$ . Karasso and Mungal's (1996) planar laser-induced fluorescence measurements of the concentration field in a 2-D liquid shear layer suggested two distinct regions of linear growth. They measured a

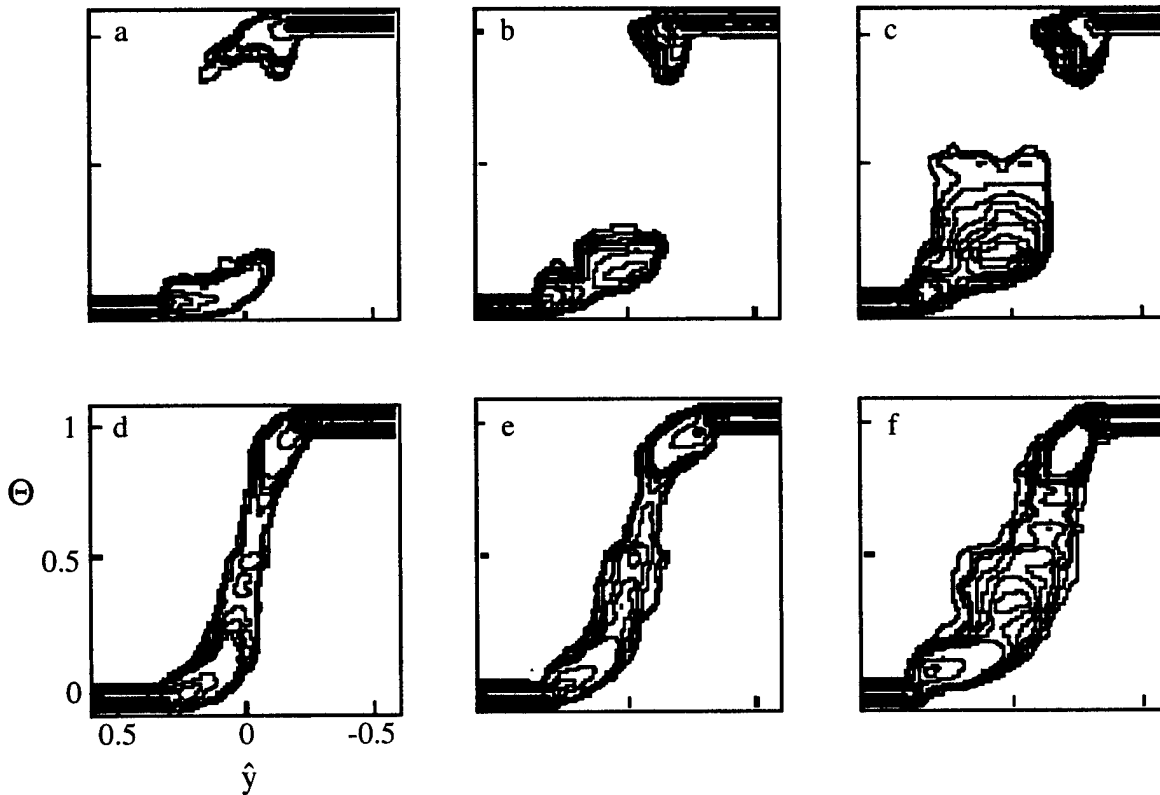
than the results of Wiltse (1993), who measured the temperature distribution in the same shear layer at the same velocity ratio facility using a rake of 31 cold wire sensors and found  $\hat{PM}(x) < 0.1$  for  $1 \leq x/\lambda_{K-H} \leq 5$ . These results also indicate that the integral performance measure can be significantly enhanced ( $\hat{PM}(x) > 0.13$ ) by spanwise excitation of streamwise and spanwise instability modes using an array of surface heating elements mounted at the flow partition. In the present experiments, the flow partition separating the two streams is equipped with an array of piezo-electric actuators whose spanwise nonuniformity leads to triggering of streamwise vortices and mixing enhancement. Thus, the results of Wiltse (1993) may be more comparable to those for the 24:9 shear layer than to the 36:12 results.

Figure 47c shows that the average performance measure for the forced 36:12 shear layer is somewhat similar to the forced 24:9 shear layer (Figure 46c), with a pronounced region of strong mixing around the centerline. Note that compared to the unforced flow, the cross-stream extent of the forced shear layer is slightly reduced for  $x/\lambda_{K-H} < 3$  due to suppression of the primary vortices in this region. The effect of the high-frequency excitation on mixing enhancement in the shear layer is greatest for  $x/\lambda_{K-H} < 4$ , where the integral performance measure is more than doubled at some spatial locations. Although mixing farther downstream is only slightly enhanced by forcing, the average integral performance measure is still increased by almost 40%.

The time-averaged  $\hat{PM}(x)$  and  $pm(y)$  for the unforced 42:14 shear layer are shown in Figures 48a-b. The growth rate for the 42:14 shear layer is about  $14^\circ$ , and slightly lower than for the 36:12 case ( $15^\circ$ ). The cross stream extent of the shear layer is  $\delta = 2.7, 3.7,$  and  $4.3$  cm at  $x/\lambda_{K-H} = 2.8, 3.7,$  and  $4.6$ , respectively, and the corresponding Reynolds numbers are 8000, 10,900 and 12,800. The integral performance measure is relatively unchanged ( $\hat{PM} \approx 0.05$ ) for  $x/\lambda_{K-H} < 2.8$ , but more than doubles downstream. For  $x/\lambda_{K-H} > 3.6$ , the flow is in transition and the integral performance measure at  $x/\lambda_{K-H} = 4.6$  increases to 0.18. The effect of high-frequency excitation on mixing in the 42:14 shear layer (Figures 48c-d) is similar to results presented for the 36:12 case (Figures 47c-d). Again, the integral performance measure is increased with forcing at all streamwise stations, especially for  $x/\lambda_{K-H} < 3.6$ . The growth of the shear layer is not significantly affected by forcing.

It is often advantageous in the representation of the scalar field in the shear layer to use the probability density function (pdf), defined as the probability density of finding fluid at some temperature at the specific location within the shear layer, Eq. (15). Koochesfahani and Dimotakis (1986) used laser induced fluorescence to examine the probability density function of species concentration in a liquid shear layer. They found that the pdf of the mixed fluid downstream of mixing transition ( $Re = 23,000$ ) is uniform across the entire cross-stream extent of the shear layer. Furthermore, the pdf was found asymmetric and biased toward the high speed side, suggesting that the shear layer does not entrain equal amounts of fluid from the two streams. Some issues related to the pdf were discussed in detail by Karasso and Mungal (1996) for scalar mixing in the liquid shear layer flow, and the typical pdf shapes were used to describe the mixing for different Reynolds numbers and initial boundary layer conditions. These authors assert that the pdf for the fully developed liquid shear layer evolves from a 'nonmarching' to a 'marching' type as the Reynolds number is increased from 14,000 to 35,000 at the same  $U_2/U_1$  ratio (0.25). The cross-stream distribution of the pdf is described as 'nonmarching' if the most probable value of the mixture fraction is invariant across the width of the shear layer (as observed by Koochesfahani and Dimotakis 1986 for  $Re = 23,000$ ). The pdf is described as 'marching' if the most probable mixture fraction is the average fraction at a given cross stream elevation.

The time average pdfs for the 24:9 shear layer at  $x/\lambda_{K-H} = 2.8, 3.7,$  and  $4.6$  for the unforced and forced flow are shown in Figures 49a-f. The probability of finding a fluid within a certain temperature range at some cross stream elevation was found for every time step and averaged over 150 cycles of the base flow. The minimum and maximum contour levels are  $0.1^\circ C^{-1}$  and  $5.1^\circ C^{-1}$ , respectively, and the increment is  $0.2^\circ C^{-1}$ . Figures 49a-c show that the pdf for the unforced flow



**Figure 49.** Averaged probability density function for the 24:9 shear layer for the unforced (a-c), and forced (d-f) flow ( $f=225$  Hz) at  $x/\lambda_{K-H}=2.8, 3.7$ , and  $4.6$ .

is nonmarching at all streamwise locations, with the most probable values of nondimensional temperature  $\Theta$  being 0.1, 0.18, and 0.2 at  $x/\lambda_{K-H} = 2.8, 3.7$ , and  $4.6$ , respectively. The fact that the peak values of the pdf are biased toward the high-speed (cooler) side of the shear layer suggests that an excess of the high-speed fluid is entrained in the primary vortex core. This is in agreement with findings of Koochesfahani and Dimotakis (1986), whose results indicate that in flows dominated by large vortical structures, a large excess of the high-speed fluid in the cores of the vortical structures is transported across the layer by the vortical motion but remains unmixed. The resulting pdf is nonmarching, as in Figures 49a-c. There is a small increase in mixing at the last streamwise position, as shown by the contours of the pdf, indicating a broader range of temperatures at each cross-stream elevation. It is noteworthy that the peak of the pdf migrates towards the center of the shear layer as one moves downstream, from  $\hat{y}=0.1$  and  $\Theta=0.15$  at  $x/\lambda_{K-H}=3.7$  to  $\hat{y}=0.05$  and  $\Theta=0.25$  at  $x/\lambda_{K-H}=4.6$ .

When the flow is forced at high frequency at the same velocity ratio (Figures 49d-f), the pdf becomes marching at the first streamwise location  $x/\lambda_{K-H}=2.8$  (Figure 49d), and the most probable temperature of the mixed fluid is the average temperature at a given cross-stream elevation. The fact that the pdf for the forced flow is marching with no unmixed fluid in the shear layer indicates that high-frequency excitation significantly increases mixing. Results of Karasso and Mungal (1996) suggest that the marching pdf occurs in the shear layer for Reynolds numbers ranging from 14,000 to 35,000 (based on the cross-stream extent of the shear layer and free-stream velocity difference), which is significantly higher than in the present experiments ( $4,000 \leq Re_\delta \leq 18,000$ ). Based on these observations, we conclude that high-frequency excitation results in mixing enhancement that would be observed if the Reynolds number of the base flow was significantly increased.



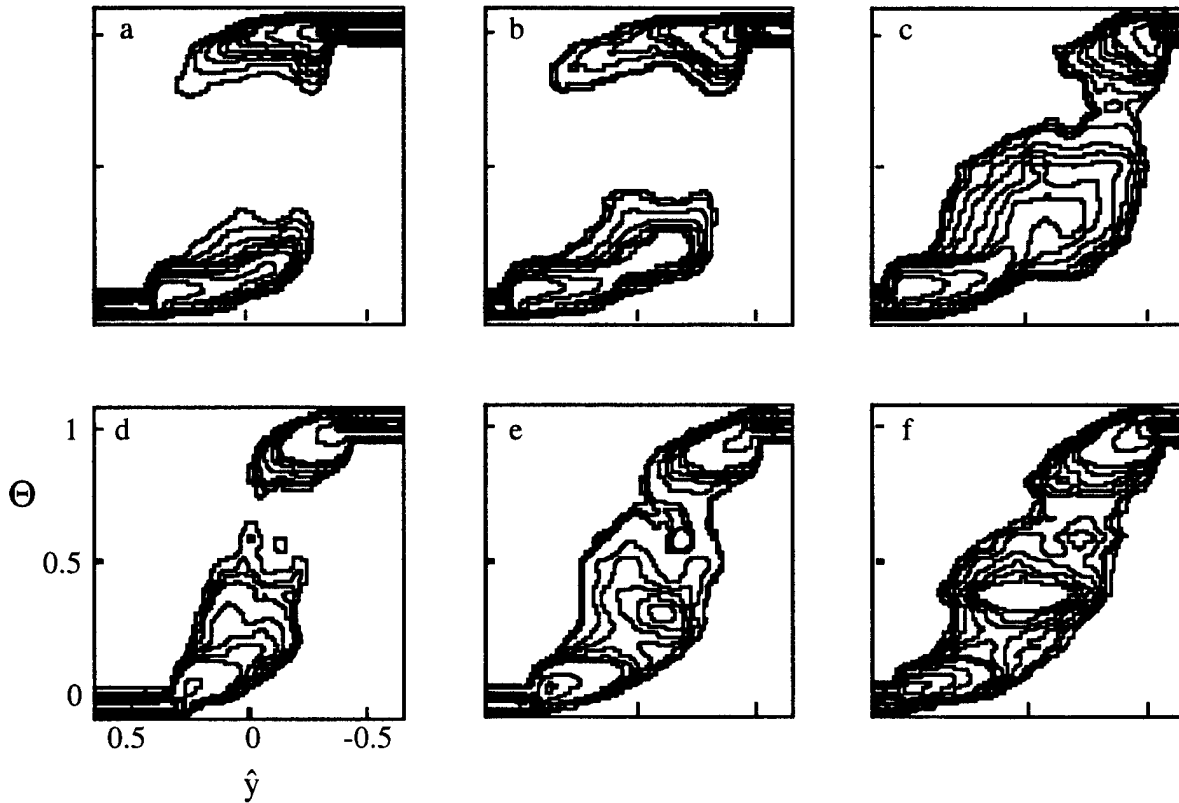


**Figure 50.** Averaged probability density function for the 36:12 shear layer for the unforced (a-c) and forced (d-f) flow ( $f=225$  Hz) at  $x/\lambda_{K-H}=2.8, 3.7$ , and  $4.6$ .

For the higher speed (36:12 and 42:14) cases (Figures 50a-c and 51a-c), the shape of the pdf for the unforced flow remains nonmarching for the first two streamwise stations. For the 36:12 shear layer (Figures 50a-c), the most probable values of  $\Theta$  are 0.17, 0.25, and 0.5 at  $x/\lambda_{K-H} = 2.8, 3.7$ , and  $4.6$ , respectively. The peak values of the pdf are still biased toward the high-speed side of the shear layer but the cross-stream extent over which the mixing occurs is wider than for the 24:9 shear layer. At the last streamwise location for the 36:12 shear layer ( $x/\lambda_{K-H} = 4.6$ ), the pdf is nonmarching for a large extent of the shear layer, but becomes marching towards the low-speed side. Karasso and Mungal (1996) also observed this "dual behavior" in the transition region between nonmarching and marching shapes. For the 42:14 shear layer (Figures 51a-c), the most probable values of  $\Theta$  are 0.2, 0.38, and 0.5 at  $x/\lambda_{K-H} = 2.8, 3.7$ , and  $4.6$ , respectively.

For the forced 36:12 and 42:14 shear layers (Figures 50d-f and 51d-f, respectively), the cross-stream extent of the pdf suggests that some mixing occurs over the entire width of the shear layer at all streamwise locations. The peak values of pdf are at  $\Theta=0.22, 0.29$ , and  $0.4$  for the 36:12 shear layer, and at  $\Theta=0.27, 0.31$ , and  $0.35$  for the 42:14 shear layer at  $x/\lambda_{K-H} = 2.8, 3.7$ , and  $4.6$ , respectively. Although high-frequency excitation partially suppresses the initial instability of the shear layer, vortical structures are still present in the flow and the cross-stream extent over which mixing occurs is much wider than in the 24:9 shear layer.

From the results presented so far, it is evident that the temperature field and mixing in the shear layer vary significantly with time, and that the most intense mixing occurs within the core of primary vortices. In order to obtain phase-averaged mixing information which can be related to averaged features of the large coherent structures, phase-locked measurements were performed by using time-harmonic forcing of the driving pump (described in Chapter II). This resulted in a

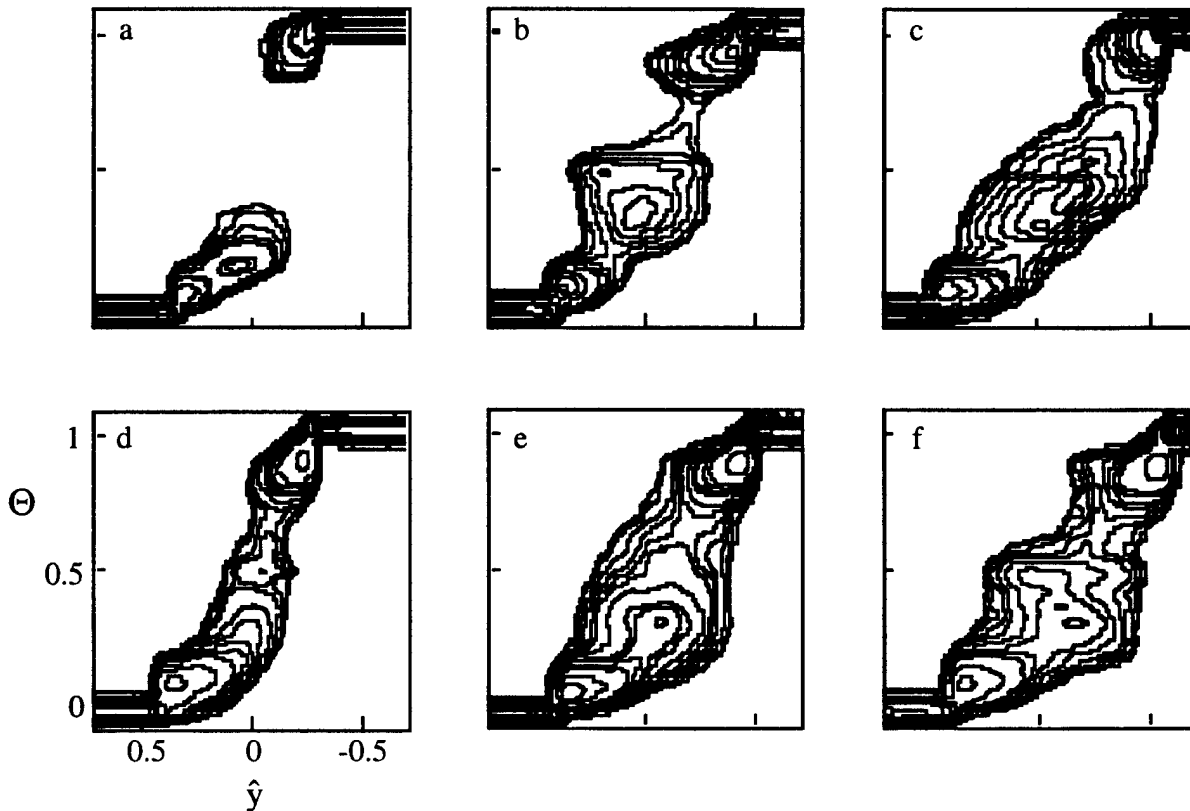


**Figure 51.** Averaged probability density function for the 42:14 shear layer for the unforced (a-c) and forced (d-f) flow ( $f=225$  Hz) at  $x/\lambda_{\kappa,H}=2.8, 3.7$ , and  $4.6$ .

streamwise domain where the flow is phase-locked to the forcing frequency (around the most unstable frequency of the shear layer).

Figures 52a-h show the phase-averaged r.m.s. temperature in the shear layer for the 36:12 shear layer, for the flow forced at low frequency ( $f_L=4.5$  Hz) (Figures 51a-d), and at low and high ( $f_H=225$  Hz) frequencies (Figure 51e-h). Four consecutive frames (phases) shown here represent one cycle of the forcing signal and are separated in time by 62.5 msec. In the low-frequency forcing configuration, mixing is localized to a narrow region around the primary vortices, and the phase-averaged temperature gradients between the streams are very sharp. Most fluid in the cores of the primary vortices is still unmixed and the fluctuating temperature field shows very little variation away from the thin interface that separates the two streams. When the flow is forced at both low and high frequencies, the phase-averaged primary vortex is still noticeable, but the temperature gradients at the interface are significantly diffused. The fluctuating temperature field suggests that small-scale motion is distributed across most of the cross-stream extent of the shear layer. Furthermore, the primary vortices are slightly larger in the forced flow, with cores containing fluid mixed much better than by low-frequency forcing. The increase in mixing in this case appears to be connected primarily to stretching of the material interface between the streams, which becomes highly convoluted due to introduction of small scales into the base flow. The temperature gradients are strongest in the braid region between the vortices, but are still significantly smaller than in the low-frequency forcing case.

Phase-averaged  $pm(x,y)$  and  $\hat{PM}(x)$  for the 36:12 shear layer forced at low frequency and combination of low and high frequencies are shown in Figures 53a-c. The temperature measurements were taken separately for partially overlapping regions, and phase-averaged performance measure was computed for one phase in the cycle by averaging over 150 cycles of the

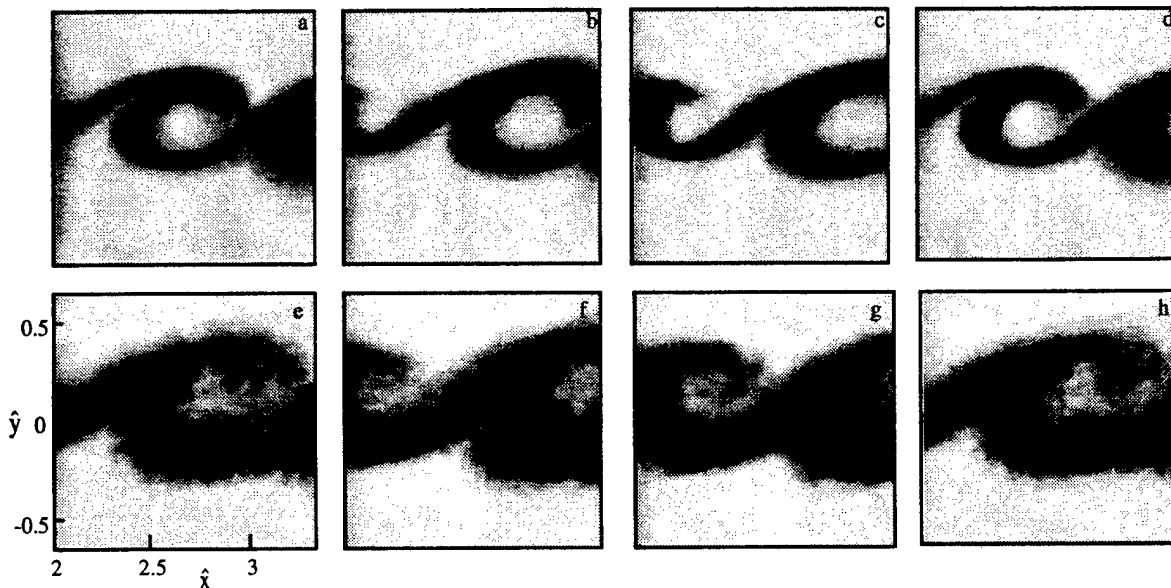


**Figure 52.** Phase averaged r.m.s. temperature for the 36:12 shear layer for flow forced at  $f=4.5$  Hz (a-d), and  $f=4.5+225$  Hz (e-h). Images are separated by 62.5 msec.

base flow. These results were then combined in a composite array over a spatial range greater than the field of view of the optical setup. The most prominent feature in Figure 53a (low frequency forcing) is that for  $x/\lambda_{K-H} < 3.5$  most of the mixing occurs in narrow bands near the edges of the primary vortices.

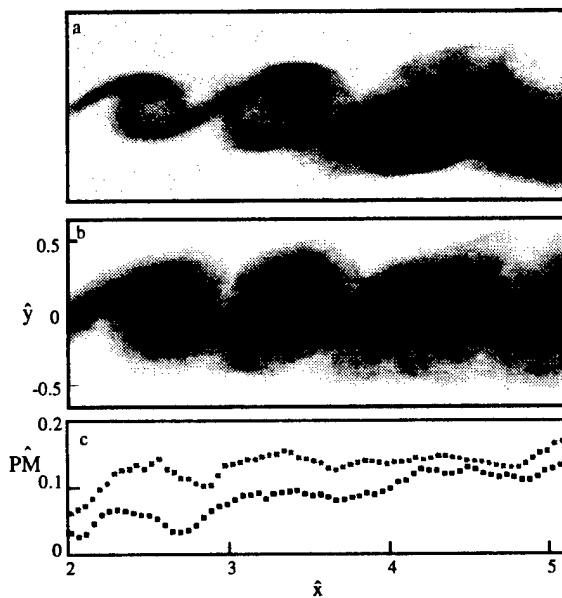


**Figure 53.** Phase-averaged  $pm(x,y)$  for the 36:12 shear layer for flow forced at  $f=4.5$  Hz (a), and  $f=4.5+225$  Hz (b). Phase-averaged PM for  $f=4.5$  Hz (black), and  $f=4.5+225$  Hz (gray) (c).

As the flow undergoes mixing transition ( $x/\lambda_{K-H} > 4$ ), patches of mixed fluid spread toward the core of the primary vortices. Nygaard and Glezer (1991) showed that the small-scale motions appear first near the high- and low-speed edges of the primary vortices, and then propagate towards the core leading to mixing transition. Figure 53b indicates that mixing occurs more rapidly when the flow is subjected to forcing at low and high frequencies. Notice that even at early streamwise locations, the entire vortex core consists of mixed fluid. The integral performance measure plot, shown in Figure 53c, shows that  $PM(x)$  for the flow forced at low and high frequencies (gray symbols) is always higher than  $PM(x)$  for the low-frequency forcing (black symbols). The average  $PM(x)$  (averaged over all streamwise locations) for the flow forced at low and high frequencies is increased by more than 40%, when compared to the low-frequency forcing.

## V. PROPER ORTHOGONAL DECOMPOSITION (POD)

The LIF measurements of optical distortions and temperature in the shear layer presented in Chapters III and IV are used to develop a reduced-order model of the temperature field dynamics based on a proper orthogonal decomposition technique. This chapter describes the development and robustness of the low-order representation.

### V.1. POD Technique and Applications

The main objective of optical phase correction schemes is to perform the correction in real time because in conventional optical detectors phase information is lost once the intensity is recorded. This procedure is further complicated by the absence of knowledge about evolution of the index of refraction field within the flow. Thus, a correction that is based on some past information has to be predicted sufficiently fast to be approximately correct when applied. The key to real-time computation of phase corrections is the availability of a low-order representation of the 2-D index field that will allow a predictor (e.g. neural network) to be trained using several orders of magnitude less data than if such representation is not available.

A low-order representation of the index of refraction field is developed using proper orthogonal decomposition, in which finite sets of eigenmodes optimally capture large and intermediate temperature scales, and thus the corresponding variations in index of refraction. The optimality (in the mean-square sense) of the proper orthogonal decomposition suggests this technique as a natural choice for use in the study of turbulent flows. Specifically, it provides the most efficient way of capturing the dominant components of a spatially and temporally complex process, in that it captures the most energy with a given number of modes (Holmes et al. 1996). In the present work, the selected eigenmodes form the basis set and are used to develop a system of ordinary differential equations that models the dynamics of the temperature field at the large scales. Because mixing in a plane shear layer is largely controlled by the large coherent structures, the capability of the proper orthogonal decomposition to capture the evolution of these structures with a low-order model provides a good tool for the study of mixing and the resulting optical distortions.

The temperature measurements are made at several streamwise locations ( $\hat{x}=1.5-5.1$ ) for the unforced and forced flow using the two-dimensional LIF technique described in Chapter II. The flow is forced at 225 Hz using an array of piezoelectric actuators mounted at the trailing edge of the splitter partition. In addition to that, time-harmonic forcing of the driving pump ( $f=3$  and 4.5 Hz) is used to induce a near-periodicity in the large-scale temperature variations, and thus reduce the phase variability in the turbulent flow. The proper orthogonal decomposition technique (method of snapshots) is used to identify the organized motions in the shear layer flow (Glezer et al. 1989). In most of the present experiments, 2400 consecutive instantaneous maps of the flow field, equivalent to 100 cycles of the fundamental instability, are used to compose a cross-correlation matrix.

The data consist of time series of a two-dimensional temperature field in an x-y plane of the shear layer. These data (with the mean removed) were assembled into a single matrix array  $A$

$$A = \begin{bmatrix} T(x_1, y_1, t_1) & T(x_1, y_2, t_1) & \dots & T(x_1, y_M, t_1) & \dots & T(x_M, y_M, t_1) \\ T(x_1, y_1, t_2) & T(x_1, y_2, t_2) & \dots & T(x_1, y_M, t_2) & \dots & T(x_M, y_M, t_2) \\ \vdots & \vdots & & \vdots & & \vdots \\ T(x_1, y_1, t_N) & T(x_1, y_2, t_N) & \dots & T(x_1, y_M, t_N) & \dots & T(x_M, y_M, t_N) \end{bmatrix} \quad (16)$$

where  $M=128$  was the number of pixels in the sensor array in the streamwise and cross-stream directions, and  $N$  was the number of time frames in each realization. The eigenvalues  $\lambda_j$  and

eigenmodes  $\mathbf{e}_j$  are normally computed from the eigenvalue problem  $\mathbf{A}^T \mathbf{A} \mathbf{e} = \lambda \mathbf{e}$ , where  $\mathbf{A}^T \mathbf{A}$  is an  $L \times L$  matrix and  $L = M \times M$  is the total number of pixels. These modes can also be computed from a singular value decomposition of the matrix  $\mathbf{A} = \mathbf{U} \mathbf{S} \mathbf{V}^T$ , where the diagonal matrix  $\mathbf{S}$  and matrix  $\mathbf{V}$  contain square roots of the eigenvalues and eigenmodes of  $\mathbf{A}^T \mathbf{A}$ , respectively. In the present work, the singular value decomposition, which is more efficient computationally, is used to determine eigensets of  $\mathbf{A}^T \mathbf{A}$ . The eigenmodes were normalized according to

$$\mathbf{e}_i \cdot \mathbf{e}_j = \delta_{ij} \quad (17)$$

where  $\delta_{ij}$  is the Kronecker delta. As discussed elsewhere (Aubry et al. 1988), the sum of all eigenvalues of  $\mathbf{A}^T \mathbf{A}$  is equal to the total energy in the flow. The action fraction ratio, defined as

$$\Lambda_j = \lambda_j / \sum \lambda_k$$

(Glezer et al. 1989), correspond to the fraction of the total energy contained in the  $j$ -th most energetic mode. The eigenmodes of  $\mathbf{A}^T \mathbf{A}$  depend on spatial coordinates only, and are used to expand the temperature field in a time series

$$T(x_i, y_j, t) = \sum_{k=1}^L a_k(t) \mathbf{e}_k(x_i, y_j) \quad (18)$$

where the temporal coefficients  $a_k(t)$  are uncorrelated in time, and  $\mathbf{e}_k(x_i, y_j)$  is the  $(i+jM)$ -th element of  $\mathbf{e}_k$ . Since the proper orthogonal decomposition applied to the full-field temperature data is optimal in the sense described above, the temporal coefficients  $a_i(t)$  can be directly obtained by projecting the temperature field along the direction of the corresponding eigenmodes (Sirovich et al. 1989):

$$a_i(t_j) = \sum_{k=1}^M \sum_{l=1}^M \mathbf{e}_i(x_k, y_l) T(x_k, y_l, t_j) \quad (19)$$

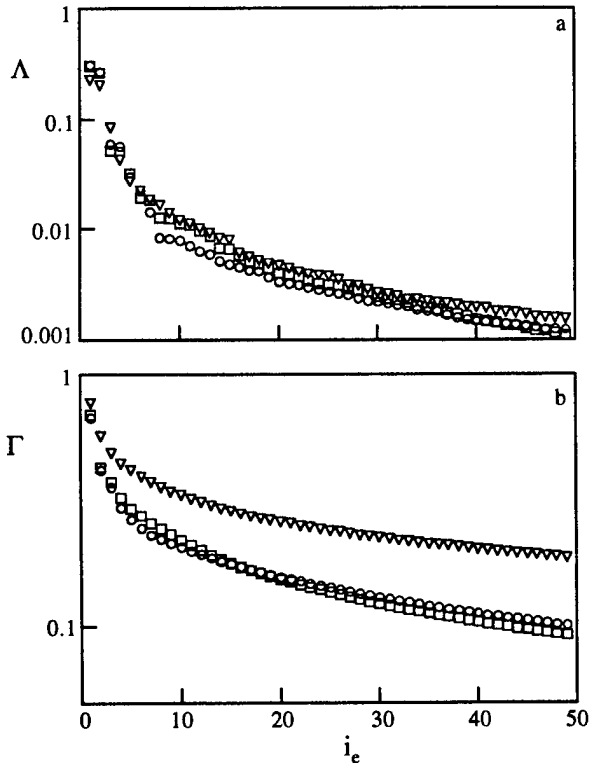


**Figure 54.** POD action fraction  $\Lambda$  (a) and energy fraction  $\Gamma$  (b) as a function of the number of eigenmodes ( $i_e$ ) for the 36:12 shear layer.

for fluid mechanics problems (turbulent jets, shear layers, etc.) the requirement is usually that  $N_a$

Figures 54a-b show the action fraction  $\Lambda_i$  and the energy fraction  $\Gamma_i = 1 - \sum_{j=1}^i \Lambda_j$  for the first 50 eigenvalues of the 36:12 shear layer for the unforced and forced flow ( $f=3$  Hz and  $f=225$  Hz). The action fraction in the five most energetic modes of the unforced flow is more than 70% within this streamwise domain. The first five modes of the flow forced at 3 Hz and 225 Hz contain more than 72% and 58% of the total energy, respectively. The first 10 modes capture more than 77% of the energy for the unforced and flow forced at 3 Hz, and more than 66% of the energy for the flow forced at 225 Hz. The next 10 modes of the unforced and low-frequency forced flow contain less than 7% of the total fluctuating energy, indicating that the large scales contain most of the energy. Figure 54b shows that for the high frequency forcing, the first mode is less dominant and the energy is distributed more evenly over the POD modes.

In many instances it is useful to determine the number of modes ( $N_a$ ) needed to achieve a required level of accuracy in the expansion (reconstruction) of the temperature field from Eq. (21). Sirovich et al. (1989) suggested that

modes must capture at least 90% of the energy and that the  $N_a$ -th mode contains less than 1% of the total energy. In the present experiments this requirement is met for  $N_a \approx 45$  for the unforced and low-frequency forced flow. Kirby et al. (1990) used the snapshot method to analyze a large eddy simulation of axisymmetric jet flow and showed that the velocity and pressure fields can be described accurately with fewer modes than the concentration field ( $N_a = 15$  and 31 for the velocity and concentration fields, respectively). These results indicate that the structure of the scalar (concentration or temperature) field is more complicated than that of the velocity field. From the previously defined ratio of the smallest momentum and scalar scales sustainable in the flow ( $\eta/\lambda_B = \text{Pr}^{3/4} \approx 4.3$ ), it follows that the temperature field is spread over a larger (but comparable) range of scales, and consequently more modes, capturing smaller scales, are needed to describe the temperature field with the same accuracy as the velocity field. The number of terms used in the truncated expansion is usually a trade-off between the required degree of accuracy and computational burden. It is useful to note that the action fraction in modes above  $N_a = 45$  is less than 0.2% for all three flow conditions (unforced, and forced at 3 and 225 Hz).

Figures 55a-j show the first ten two-dimensional POD modes of the unforced 36:12 shear layer for  $2 \leq \hat{x} \leq 3.4$ , along with the corresponding temporal coefficients (shown below each mode). The first two POD modes (Figures 55a and b) of the unforced flow are very similar and appear to be translated with respect to each other in the streamwise direction, i.e., mode 1 lags mode 2 by about

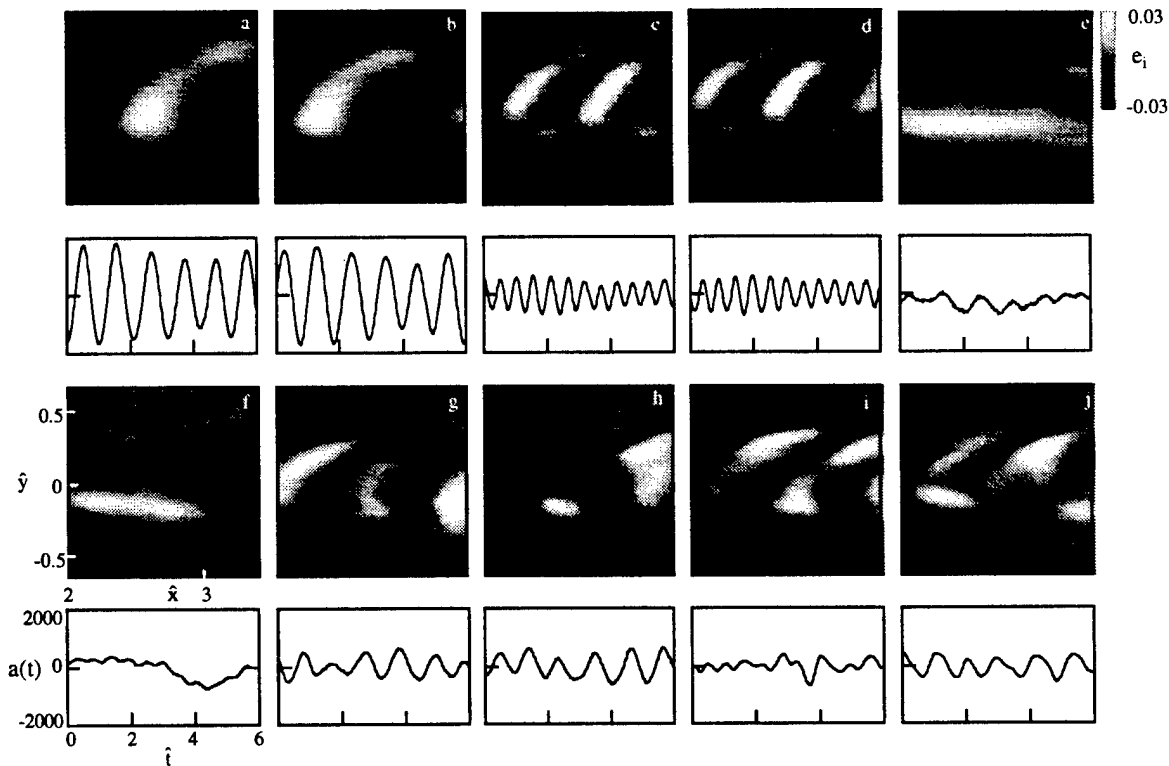


**Figure 55.** 2-D POD modes 1-10 (a-j) and temporal coefficients (shown below each mode) for the unforced 36:12 shear layer.

a quarter of wavelength in space ( $\lambda_{KH} = 4.5$  cm). These modes are associated with the large vortical structures propagating at the frequency of the fundamental instability wave, and the projection of the temperature field on these modes (shown below each mode) has a nearly periodic sinusoidal form. The corresponding temporal coefficients  $a(t)$  are  $90^\circ$  out of phase with respect to each other (with mode 1 leading). As noticed by Aubry et al. (1988), the phase shift observed in the POD

mode pairs is the expected outcome of the proper orthogonal decomposition for flows that are nearly translationally invariant in the streamwise direction.

Modes 3 and 4 (Figures 55c-d) are also similar in shape, and shifted out of phase with respect to each other. They are associated with the first harmonic of the fundamental frequency, i.e., the projection of the fluctuating temperature field on this pair results in a periodic wave with wavelength half the fundamental. Figures 55a-d also reveal that the maximum and minimum values (bright and dark regions) for modes 3 and 4 and modes 1 and 2 coincide in space. For example, a positive peak at  $\hat{x}=2.6$  and  $\hat{y}=0$  ( $\hat{y}=y/\lambda_{K-H}$ ) is evident both in Figure 55a for mode 1 and in Figure 55d for mode 4.

The spatial characteristics of some of the higher-order POD modes are influenced by the jitter of the coherent structures at the frequency of the fundamental instability wave and its higher harmonics. For example, the fifth mode (Figure 55e) shows a diffuse structure apparently unrelated to the structure of the lower order modes. However, spectral analysis of the temporal coefficients for the first 10 POD modes of the unforced flow (Figures 56a-j) reveals that the coefficient corresponding to the fifth mode (Figure 56e) has the dominant frequency of the fundamental instability wave in

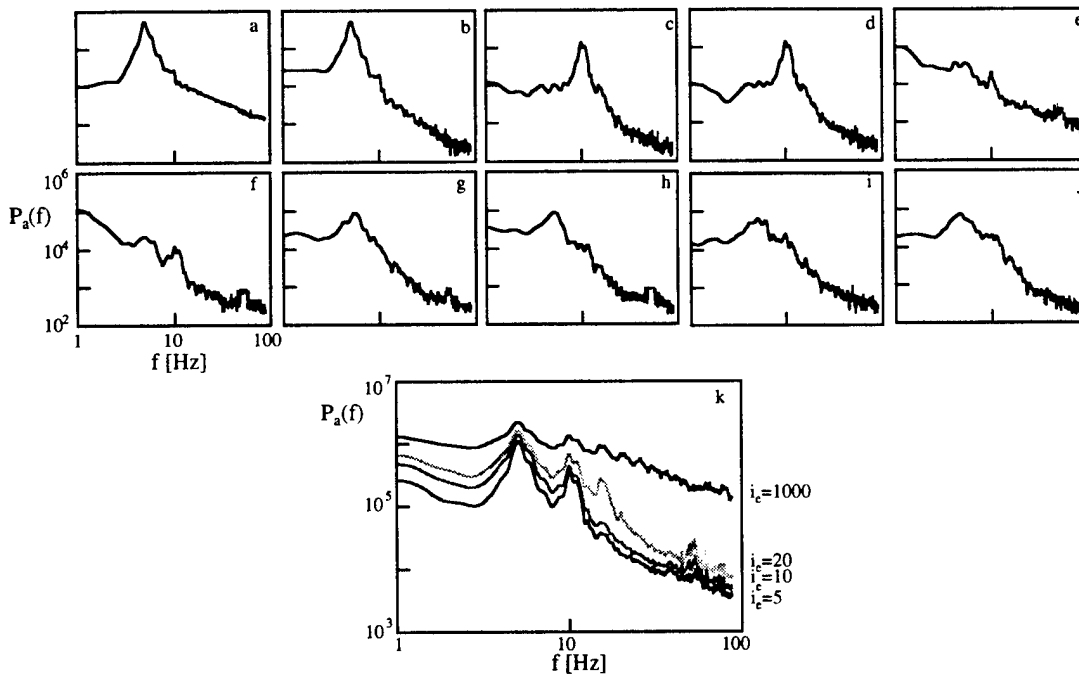


**Figure 56.** Spectra of temporal coefficients for POD modes 1-10 (a-j), and for the sum of first 5, 10, 20, and 1000 coefficients (k) for the unforced 36:12 shear layer.

addition to the peak at the first harmonic. This suggests that the structure of the fifth mode is influenced by the phase jitter of the instability wave occurring at the frequency of its first harmonic. Similarly, the spectrum of the temporal coefficient for mode 9 (Figure 56i) has a peak at the frequency of the second harmonic of the fundamental instability wave, along with peaks at the fundamental frequency and its first harmonic. This apparently shows the contribution of the jitter of the fundamental wave at a higher frequency that can not be represented by the lower order modes. Similar observations were made by Rajaei et al. (1994) who applied the POD technique (method of snapshots) to two-dimensional hot-wire velocity data from the forced shear layer that was formed between two air streams. Spectral analysis of the temporal coefficients of the velocity field revealed that the structure of some higher-order modes was influenced by the jitter of large structures (lower order modes) at the frequencies of the instability wave and its harmonics.

Although the higher order modes appear to have relatively insignificant energy content, they can not be completely ignored in the description of the flow dynamics, not only because they include disturbances at the higher frequencies, but also because of their contributions at the fundamental frequency.

Figure 56k shows the spectra (the amplitude of the Fourier Transform of temporal coefficients) determined from the sum of individual spectral amplitudes for the first 5, 10, 20, and 1000 temporal coefficients for the unforced 36:12 shear layer at  $2 \leq \hat{x} \leq 3.4$ . It is assumed that the sum of the individual spectral amplitudes for the first 1000 temporal coefficients corresponds to the spectrum determined from the complete set of temporal coefficients. It is noteworthy that the magnitude of spectral components at the fundamental frequency and its harmonics rapidly converges to the spectrum based on 1000 temporal coefficients as the number of temporal coefficients used in the summation is increased from 5 to 20 (the difference between the spectral amplitudes at the fundamental frequency and its first harmonic is reduced by more than 40% and 25%, respectively). The convergence is less rapid for the higher frequencies (smaller scales) that are associated with the higher order modes.

Figures 57a-j show the first 10 two-dimensional POD modes for the 36:12 shear layer at  $2 \leq \hat{x} \leq 3.4$  for the flow forced at  $f=3$  Hz, along with the corresponding temporal coefficients. Since the flow is forced at the frequency that is around the natural frequency of the shear layer instability, the POD modes are similar to those of the unforced flow. Furthermore, the external excitation promotes the rollup of the spanwise vortices closer to the flow partition, which increases the width

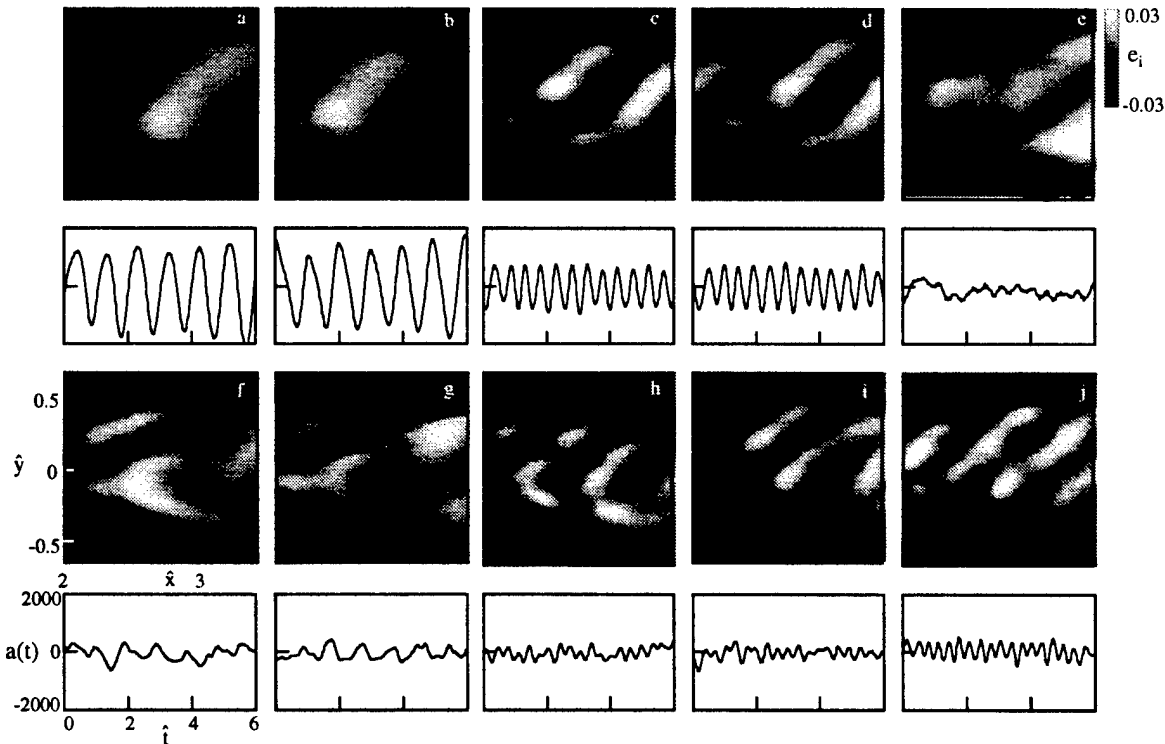


**Figure 57.** 2-D POD modes 1-10 (a-j) and temporal coefficients (shown below each mode) for the forced 36:12 shear layer ( $f=3$ Hz).

of the shear layer. Thus, the POD modes for the flow forced at 3 Hz are somewhat wider in the cross-stream direction than the unforced POD modes (by approximately 10%). The first four POD modes of the forced flow (Figures 57a-d) come in pairs, and correspond to large scale structures in the flow. The fifth POD mode of the forced flow (Figure 57e) shows, although somewhat



diffusely, structures similar to those of modes 1 and 2. As mentioned above, the fifth mode of the unforced flow is associated with the jitter of the fundamental instability wave at its first harmonic. Evidently, when the flow is forced at 3 Hz, the jitter of the forcing frequency at the frequency of its harmonics is reduced (but not completely eliminated). Furthermore, modes 9 and 10 of the unforced flow (Figures 55i-j), which show the contribution of the phase jitter at the second harmonic, are replaced by modes associated with the second harmonic of the forcing frequency. Their corresponding temporal coefficients (shown below each mode) are nearly periodic with a frequency three times the forcing frequency.

As mentioned in Chapter IV, high frequency excitation of the base flow results in significant mixing enhancement in the shear layer and initial suppression of the fundamental instability of the base flow. Consequently, the structure of the eigenmodes is substantially changed when high frequency forcing is applied. Figures 58a-j are composed of the first 10 POD modes for the forced 36:12 shear layer ( $f=225$  Hz) and the corresponding temporal coefficients (shown below each mode)

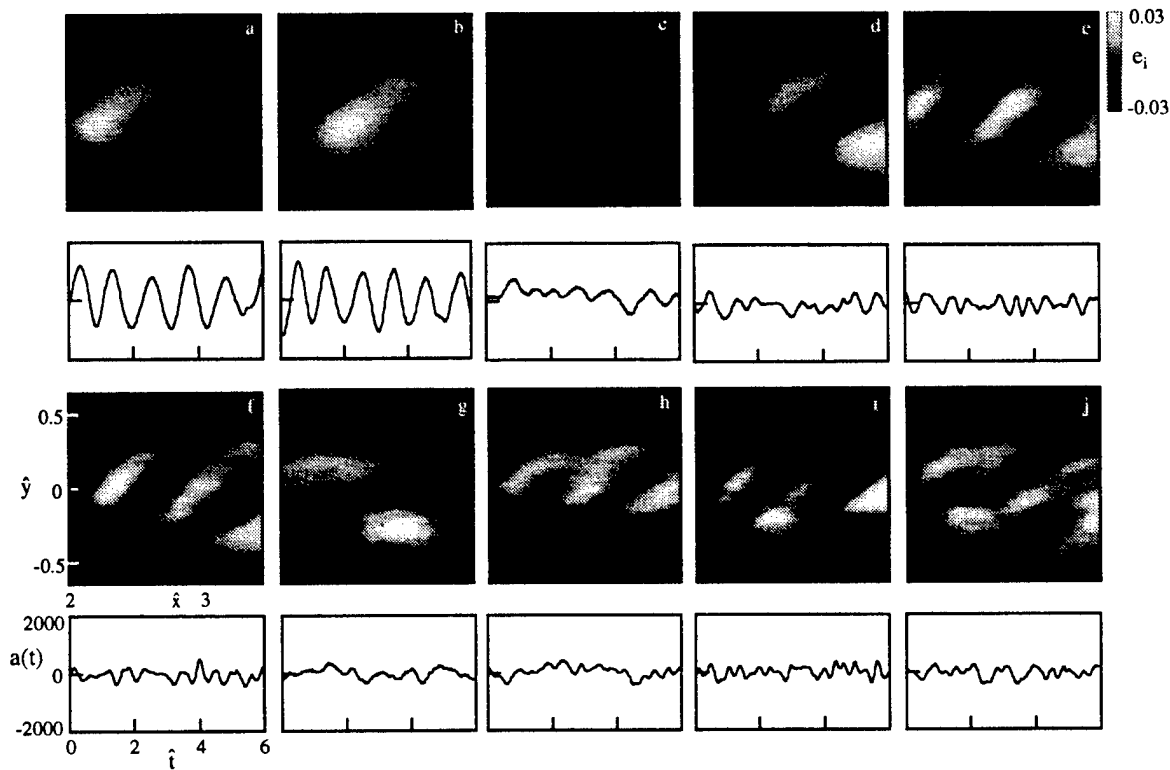


**Figure 58.** 2-D POD modes 1-10 (a-j) and temporal coefficients (shown below each mode) for the forced 36:12 shear layer ( $f=225$  Hz).

mode). The modes for the high frequency forced flow are narrower in the cross-stream direction than the unforced modes (reduction of about 10%). The first two POD modes (Figure 58a-b) have interchanging structures of opposite signs similar in shape to structures present in the unforced modes but tilted at a larger angle with respect to the cross-stream direction ( $40-50^\circ$ ). Clearly, the fundamental instability is not completely suppressed and some coherent motion is still present in the flow. The internal structure of the higher-order modes becomes more complicated as the energy content of the mode decreases. The large scale features that are characteristic even for the higher-order unforced modes (Figures 55g-j) are replaced by smaller structures (most noticeable in modes 9 and 10 in Figures 58i-j). The fine structure of the eigenmodes is continuously reduced in scale as the order of the mode is increased.

In the present work, the POD modes are generated over a spatial range limited by the field of view of the optical setup and the number of sensors (pixels) of the CCD array. In many flows, measurements are frequently made nonsimultaneously, by traversing a sensor through the flow (Glezer et al. 1989). In order to generate POD modes over a spatial range greater than the field of view of the optical setup, the POD modes corresponding to spatially overlapping regions are determined from the nonsimultaneous measurements and combined to generate composite POD modes. These modes resemble the modes that would be obtained from simultaneous data for a larger field of view.

The measurements were taken for the unforced 36:12 shear layer at three partially overlapping streamwise stations centered around  $\hat{x} = 2.2, 3.4$ , and  $4.6$ , with the field of view of 7 cm in both the streamwise and cross-stream directions. Each set of experimental data consisted of 2400 realizations of the temperature field, and was used to generate POD modes characteristic for that particular streamwise location. The value of the  $k$ -th eigenmode for the  $l$ -th overlapping region is denoted by  $e_{ij}^{kl}$ , where  $i$  and  $j$  denote individual pixels in the CCD array corresponding to the streamwise and cross-stream locations. In the present experiments, composite POD modes are generated from three partially overlapping streamwise regions, i.e.  $1 \leq l \leq 3$ . In the nonoverlapping part of each region, the composite POD modes are assumed to be equal to the modes generated from the measurements for that particular region. In the overlapping regions, the composite POD modes are determined using the approximation

$$\begin{aligned} e_{ij}^k &= w_1 e_{ij}^{k1} + w_2 e_{ij}^{k2} & c_1 \leq j \leq c_2 \\ &w_1 e_{ij}^{k2} + w_2 e_{ij}^{k3} & c_3 \leq j \leq c_4 \end{aligned} \quad (20)$$

where  $(c_1, c_2)$  and  $(c_3, c_4)$  denote the streamwise ranges where the temperature maps overlap, and  $w_1$  and  $w_2$  are the weights of the POD modes in the overlapping regions (i.e.,  $w_1 = (c_2 - j)/(c_2 - c_1)$  for  $c_1 < j < c_2$ ,  $w_1 = (c_4 - j)/(c_4 - c_3)$  for  $c_3 < j < c_4$ , and  $w_2 = 1 - w_1$ ).

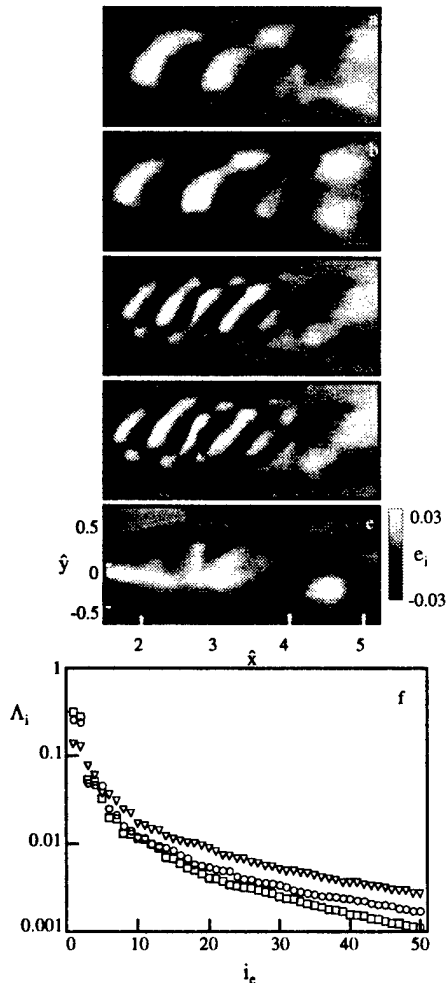


**Figure 59.** The five most energetic composite 2-D POD modes (a-e) and

Figures 59a-e show the five most energetic composite 2-D POD modes computed according to the scheme described above, together with the action fraction distributions for the three streamwise regions (Figure 59f). As mentioned above, the four most energetic modes are characterized by structures of high and low intensity. While the interface between the high- and low-intensity bands is sharply defined at early upstream locations ( $\hat{x} < 3.5$ ), it is more diffuse further downstream, especially in the transition region ( $\hat{x} > 4$ ). Notice that the interchanging bands are originally tilted at a fixed positive angle with respect to the streamwise direction. A similar observation was made by Rajaei et al. (1994) who analyzed the POD modes of a 2-D velocity field in the forced shear layer and noted that the tilted structures can either lose or gain energy from the mean flow, depending on their orientation. If they are tilted at a fixed angle with respect to the negative streamwise direction, the work of the Reynolds stress of the fluctuating velocity field against the rate of strain of the mean flow results in the transfer of energy from the mean flow to the disturbance (Mollo-Christensen 1971). If the structures are tilted at a

fixed angle with respect to the positive streamwise direction, which is the case in the present experiments for the temperature field, the energy is transferred back from the disturbance field to the mean flow.

As shown in Figures 59a-d, the high- and low-intensity bands in the composite POD modes are tilted with respect to the positive streamwise direction and lose energy until they split into two smaller structures located in the high- and low-speed streams. It is also clear from Figures 59a and b that the smaller structures have different convective velocities, so that the structure in the high-speed stream propagates faster than the one in the low-speed stream. Furthermore, the split into the smaller structures occurs in the transition region ( $\hat{x} > 4$ ) where mixing is significantly enhanced, as shown in Chapter IV. This phenomenon was originally observed by Rajaei et al. (1994) in the shear layer experiments, and referred to as "mode degeneration", which they suggested was associated with enhanced entrainment and mixing in the shear layer.

Another indication of the energy transfer from the large coherent structures is the steady decline of the energy content of the five most energetic modes with downstream distance, as shown in Figure 59f. The first five modes contain 72%, 63%, and 43% of the total energy in three overlapping regions centered at  $\hat{x} = 2.2, 3.4$ , and  $4.6$ , respectively. The decrease in the energy content of the low order modes with downstream distance is particularly evident for the first two modes, whose action fraction decreases by more than 50% at the last streamwise location compared to the first one. Furthermore, the energy content of the higher-order modes is steadily increased with downstream distance, indicating that some of the energy lost by larger structures is transferred to the smaller scale motions.

## V.2 Reconstruction and Approximations of the Temperature Data

Once the POD technique is applied to an ensemble of experimental data, the instantaneous temperature maps are expanded in terms of the POD modes using Eq. (18). The expansion of a temperature map would be exact if all modes were used in the expansion. Partial POD bases (e.g., containing fewer modes than the complete set) will incur larger errors when used to expand temperature distributions not in the ensemble used to construct the basis than in expanding distributions in that ensemble. In the present work, an expansion of a temperature map from the ensemble used to generate POD basis is called reconstruction, and an expansion of a temperature map not in that ensemble is called approximation. The distinction between the reconstruction and approximation is useful in evaluating the performance of the POD technique, since the quality of the approximation depends on the ability of the POD basis to capture the flow dynamics from a finite-size ensemble of temperature maps. This is particularly important in real-time applications, such as optical phase correction, where POD modes obtained off-line for well-defined flow conditions should be useful for different flow situations. The mean-square error of the approximation provides an upper bound on the error associated with the reconstruction of the original (measured) field, and decreases as the size of the ensemble increases (Sirovich et al. 1989).

In order to describe how well the modes computed from a finite-size ensemble represent the flow dynamics, it is useful to compare the POD modes and eigenvalues computed using different ensemble sizes. The similarity between the  $i$ -th POD mode obtained using different number of ensemble members is estimated from the inner product

$$\mu_i(R_1, R_2) = \sum_{k=1}^M \sum_{j=1}^M e_i^{R_1}(x_k, y_j) e_i^{R_2}(x_k, y_j) \quad (21)$$

where  $R_1$  and  $R_2$  denote the number of ensemble members used to generate the modes. Figures 60a-b show the similarity between the first 20 POD modes obtained using ensembles with 400 and 200, and 400 and 100 cycles of the 36:12 shear layer forced at  $f=4.5$  Hz. These results indicate that the structure of the first ten most energetic modes remains essentially unchanged as the ensemble size is decreased by a factor of two (Figure 60a). Even when the ensemble size is

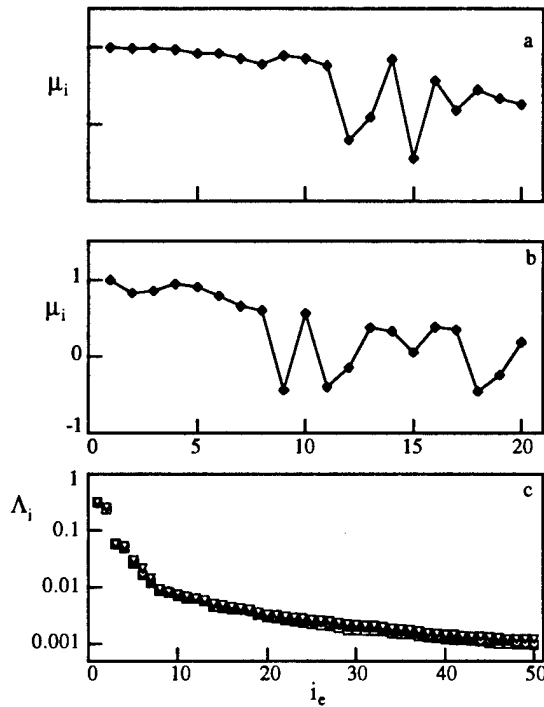


**Figure 60.** Similarity  $\mu_i$  between the POD modes obtained using different ensemble sizes for the forced 36:12 shear layer ( $f=4.5$  Hz): (a) 400 vs. 200 and (b) 400 vs. 100. (c) Action fraction  $\Lambda_i$  for 400 ( $\square$ ), 200 ( $\circ$ ) and 100 ( $\nabla$ ).

reduced by a factor of four (Figure 60b), the similarity measure  $\mu_i$  exceeds 0.8 for the first six most energetic modes. This suggests that the low-order modes can be determined from an ensemble with a small number of realizations. On the other hand, the higher-order modes depend significantly on ensemble size, and the similarity measure  $\mu_i$  can occasionally become negative (modes 9 and 11 in Figure 60b), suggesting a change in phase for that particular mode. This is in agreement with the observation that the higher-order modes are associated with the smaller scales in the flow, which can vary significantly with ensemble size.

Figure 60c, showing the action fraction for the first 50 POD modes determined from ensembles with different number of events (cycles of the base flow), reinforces that conclusion. Notice that the action fraction contained in first ten modes remains relatively unchanged as the ensemble size is reduced. The fraction of energy captured by the higher-order modes in Figure 60c decreases with increasing ensemble size, indicating that the lower-order modes are becoming more energetic as the ensemble size is increased.

Figures 61b-e show a typical example of the unforced flow reconstruction (36:12 shear layer) based on 10, 50, 100, and 200 modes, for a temperature map (shown in Figure 61a) from the

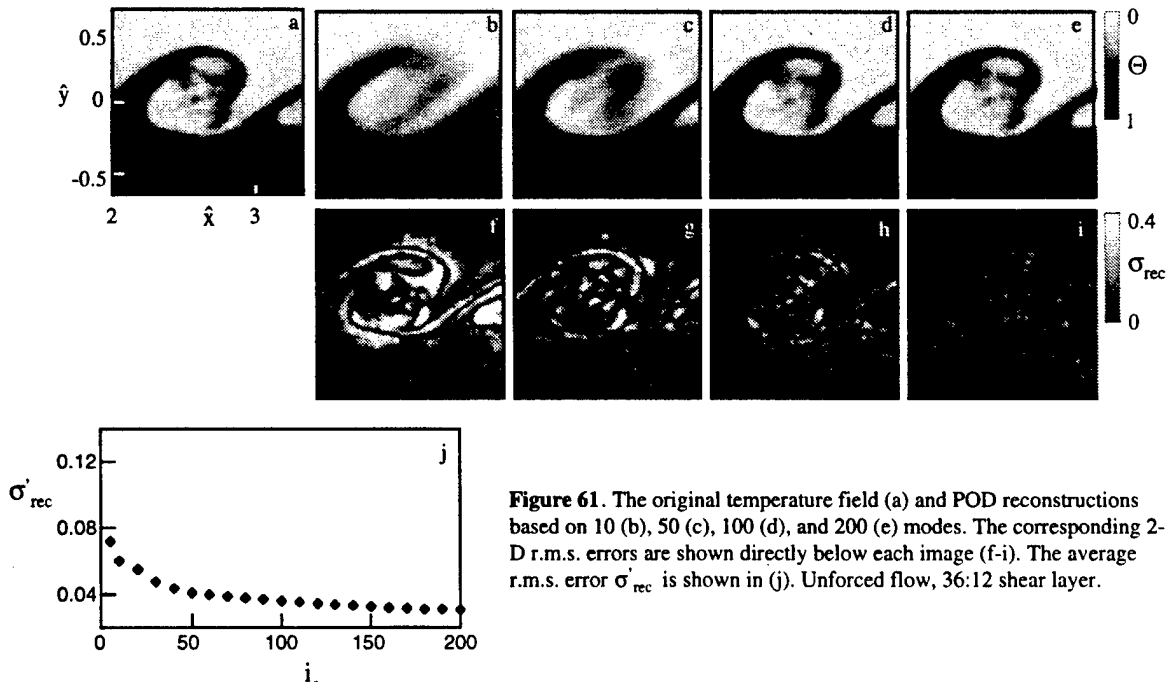


**Figure 61.** The original temperature field (a) and POD reconstructions based on 10 (b), 50 (c), 100 (d), and 200 (e) modes. The corresponding 2-D r.m.s. errors are shown directly below each image (f-i). The average r.m.s. error  $\sigma'_{rec}$  is shown in (j). Unforced flow, 36:12 shear layer.

ensemble used to generate POD modes. The corresponding 2-D root mean square errors of the reconstruction are shown in Figures 61 f-i. The root mean square error  $\sigma_{rec}$  is defined as

$$\sigma_{rec}(x, y, t) = \sqrt{\left[ \frac{T(x, y, t) - T_{rec}(x, y, t)}{\Delta T_m} \right]^2} \quad (22)$$

where  $T(x, y, t)$  is the instantaneous temperature field,  $T_{rec}(x, y, t)$  the reconstruction of the original field based on a selected number of POD modes, and  $\Delta T_m$  is the mean temperature difference between the free streams. The average root mean square error is determined from the spatial average (over the full image) and is used as a quantitative measure of the reconstruction,

$$\sigma'_{rec}(t) = \frac{1}{L} \sum_{i=1}^M \sum_{j=1}^M \sigma_{rec}(x_i, y_j, t).$$

It is evident from Figure 61 that a small number of modes (typically less than 50) is sufficient to capture the large-scale features from the original temperature field ( $\Theta = [T - T_L] / \Delta T_m$ ). The r.m.s. error images (Figures 61f-i), determined from the original and reconstructed maps, indicate that the largest error is localized in a thin region around the interface between the two streams. The quality of the reconstructed image and the relative error of the reconstruction are related to the number of modes used in the reconstruction. When 100 modes are used in the reconstruction, most of the small- and large-scale features from the original temperature map are reconstructed in the expansion, and further increase in the number of terms used in the expansion (to 200) results in only slightly better reconstruction (less than 1% improvement). As shown in Figure 61j,  $\sigma'_{rec}$  is equal to 6.0%, 4.1%, 3.6%, and 3.0% for 10, 50, 100, and 200 modes, respectively, and these numbers are typical of errors for different phases in one cycle of the base flow. The error

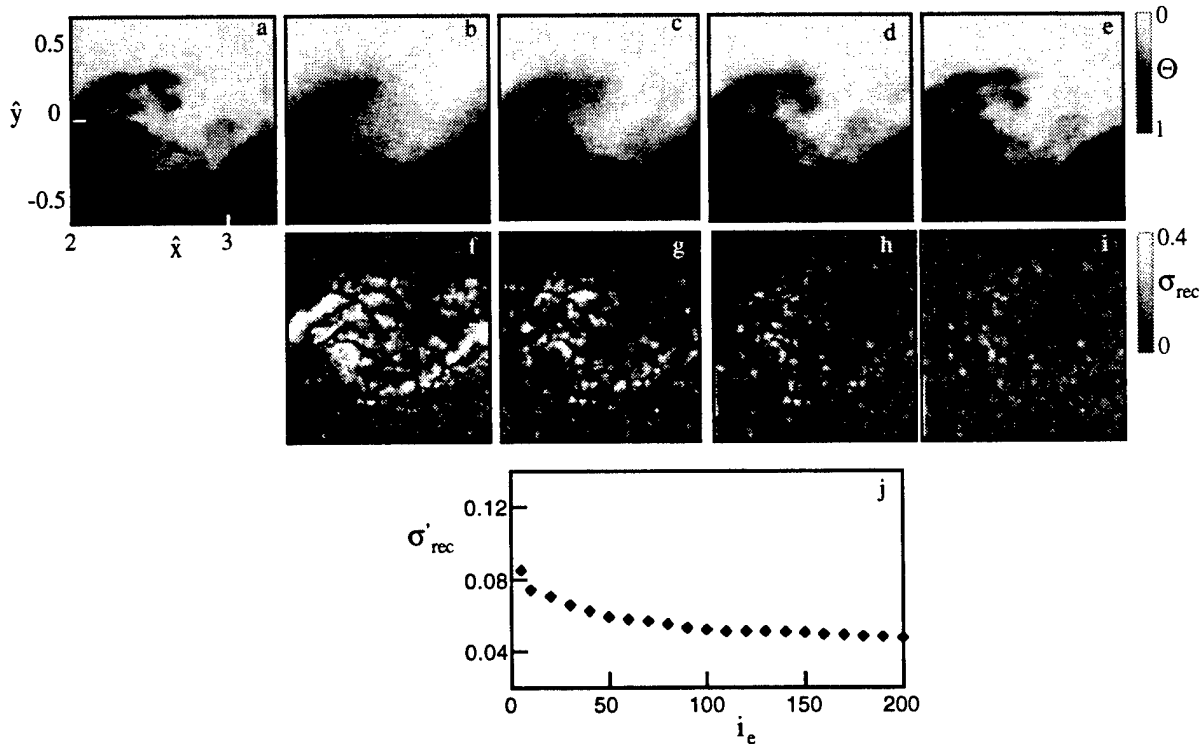


**Figure 62.** The original temperature field (a) and POD reconstructions based on 10 (b), 50 (c), 100 (d), and 200 (e) modes. The corresponding 2-D r.m.s. errors are shown directly below each image (f-i). The average r.m.s. error  $\sigma'_{rec}$  is shown in (j). Forced flow  $f=225$  Hz, 36:12 shear layer.

decreases sharply for the first ten modes after which the rate of decrease is considerably lower. Furthermore, because only 100-200 temporal coefficients are necessary to describe the flow once the POD modes are determined, the original space of  $O(10^4)$  in which the temperature field is represented (based on the number of pixels, i.e.  $128 \times 128$ ) is effectively reduced by a square root to a space of order  $O(10^2)$  (based on the number of modes used in the reconstruction).

The applicability of the proper orthogonal decomposition technique to the description of turbulent flows is further tested when the flow is forced at high frequency ( $f=225$  Hz) using a spanwise array of piezoelectric actuators, described in Chapter II. For the 36:12 shear layer, Figure 62 shows a typical instantaneous temperature map of the forced flow (a), and a sequence of four reconstructed maps based on 10, 50, 100, and 200 modes (b-e). The reconstructed images demonstrate that the POD procedure can effectively capture the small-scale features introduced by forcing when 100 modes are used in the reconstruction. The r.m.s. error of the reconstruction is more uniformly distributed throughout the flow field, and  $\sigma_{rec}$  is 7.4%, 5.9%, 5.2%, and 4.7% for 10, 50, 100, and 200 modes, respectively, which is only slightly higher than in the unforced flow.

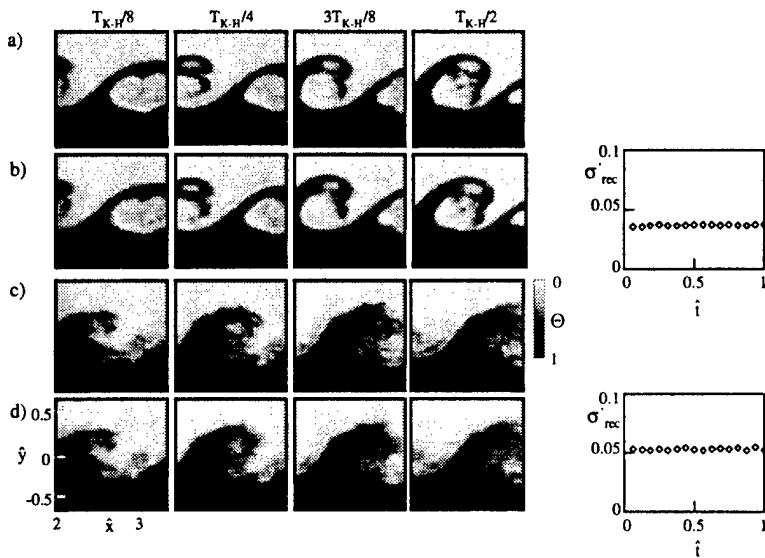


**Figure 63.** Sequence of 4 successive images separated by 25 msec for the 36:12 shear layer for the unforced (a) and forced (c) flows ( $f=225$  Hz). POD reconstructions based on 100 modes, or the unforced (b) and forced (d) flow. The average r.m.s. error  $\sigma_{rec}$  is shown to the right of each sequence.

(Figure 63d) flow fields for the flow forced at  $f=225$  Hz. It is evident that the average r.m.s. error of the POD reconstruction, shown to the right of each sequence, remains relatively unchanged throughout the cycle for both forcing conditions. The  $\sigma_{rec}$  during one cycle of the base (unforced) flow varies by  $\pm 0.06\%$  and  $\pm 0.1\%$  in the unforced and forced ( $f=225$  Hz) flow, respectively.

A more stringent test of the POD technique is the approximation of a temperature field measured for similar flow conditions but not included in the ensemble used to calculate the POD modes. An example of the approximation of a typical "nonensemble" temperature field is shown in Figures 64a-j for the unforced 36:12 shear layer. The error of the approximation of a "nonensemble" temperature field is defined as

$$\sigma_{app}(x, y, t) = \sqrt{\left[ \frac{T(x, y, t) - T_{app}(x, y, t)}{\Delta T_m} \right]^2} \quad (23)$$

where  $T_{app}(x,y,t)$  is the expansion of a nonensemble temperature field based on a selected number of POD modes. For the unforced 36:12 shear layer,  $\sigma'_{app}$  is only slightly higher than the error of the reconstruction of a typical temperature field from the ensemble. The  $\sigma'_{app}$  for the typical approximation is 6.8%, 5.0%, 4.6%, and 4.3% for 10, 50, 100, and 200 modes, respectively, as shown in Figure 64j where  $\sigma_{rec}$  for the typical reconstruction (closed symbols) is reproduced for comparison. It is perhaps more surprising that the approximation does a good job in capturing the features from the temperature field of the forced flow ( $f=225$  Hz), as shown in Figures 65a-j. Although more POD modes are necessary to capture all features from the original temperature field than in the unforced flow, it is clear that 50 modes can capture enough energy to reconstruct the large scales in the flow. When 200 modes are used in the approximation of the forced flow, much of the small-scale structures are captured and  $\sigma'_{app}$  is below 6%. The average r.m.s. error of the approximation  $\sigma'_{app}$  is 7.6%, 6.1%, 5.4%, and 4.8% for 10, 50, 100, and 200 modes respectively, and is shown in Figure 65j together with the reconstruction error for comparison.

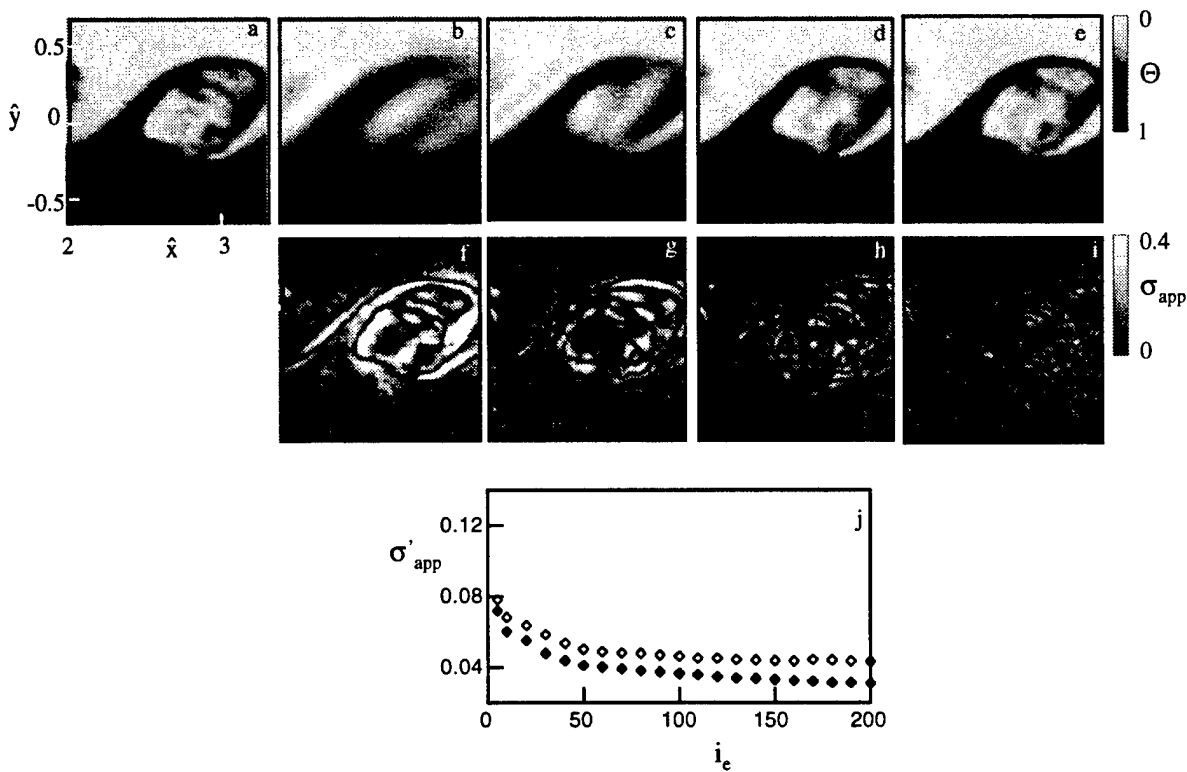


**Figure 64.** The original temperature field (a) and POD approximations based on 10 (b), 50 (c), 100 (d), and 200 (e) modes. The corresponding 2-D r.m.s. errors are shown directly below each image (f-i). The average r.m.s. error of the approximation (open symbols) is shown in (j), where the average r.m.s. error of the reconstruction (closed symbols) is reproduced for reference. Unforced flow, 36:12 shear layer.

The results presented in Figures 61-65 indicate that the quality of the reconstruction of the measured temperature field depends on number of POD modes used in the expansion in Eq. (21). It is also evident that the smaller scales in the flow (associated with the higher order modes) are filtered out in the reconstruction if the higher order modes are not used. Thus, it would be desirable to determine the length scales associated with certain groups of POD modes used in the reconstruction of the original flow field. To this end, a 2-D Fourier Transform of the reconstructed temperature field is computed when 10, 50, 100, and 200 POD modes are used in the expansion. We introduce spectral amplitudes defined by:

$$P_{\Sigma k_x}(k_y) = \sum_{i=1}^{M_x} P(k_{x_i}, k_y) \quad (24)$$

$$P_{\Sigma k_y}(k_x) = \sum_{i=1}^{M_y} P(k_x, k_{y_i})$$

where  $M_x=M_y=64$  denote the number of streamwise and cross-stream wavenumbers used in the summation,  $P(k_x, k_y)$  is the 2-D spectral amplitude, and  $k_x=1/\lambda_x$  and  $k_y=1/\lambda_y$  are wavenumbers in the streamwise and cross-stream directions. Figures 66a-d show spectral amplitudes for the reconstructions with 10, 50, 100, and 200 POD modes for the 36:12 shear layer for the unforced (Figures 66a-b) and forced (Figures 66c-d) flow ( $f=225$  Hz). The spatial frequency resolution is  $0.16 \text{ cm}^{-1}$  in both the streamwise and cross-stream directions. Results for the unforced flow suggest that modes 11-40 provide additional contribution (compared to modes 1-10) at spatial wavenumbers in the range  $0.5 \text{ cm}^{-1} < k_x < 1.5 \text{ cm}^{-1}$  and  $0.6 \text{ cm}^{-1} < k_y < 2.3 \text{ cm}^{-1}$ . When the number of modes is increased from 50 to 100, the amplitude of the spectral components within the range  $1.2 \text{ cm}^{-1} < k_x < 1.9 \text{ cm}^{-1}$  and  $1.0 \text{ cm}^{-1} < k_y < 2.6 \text{ cm}^{-1}$  is increased. Similarly, modes 101-200 mostly contribute in the range  $1.5 \text{ cm}^{-1} < k_x < 2.3 \text{ cm}^{-1}$  and  $1.7 \text{ cm}^{-1} < k_y < 3.3 \text{ cm}^{-1}$ . For the forced flow, modes 11-50 are associated with wavenumbers in the range  $0.2 \text{ cm}^{-1} < k_x < 1.2 \text{ cm}^{-1}$  and  $0.2 \text{ cm}^{-1} < k_y < 1.4 \text{ cm}^{-1}$ . It is also clear that modes 101-200 of the forced flow contribute in the range  $1.6 \text{ cm}^{-1} < k_x < 3.1 \text{ cm}^{-1}$  and  $1.5 \text{ cm}^{-1} < k_y < 3.6 \text{ cm}^{-1}$ .

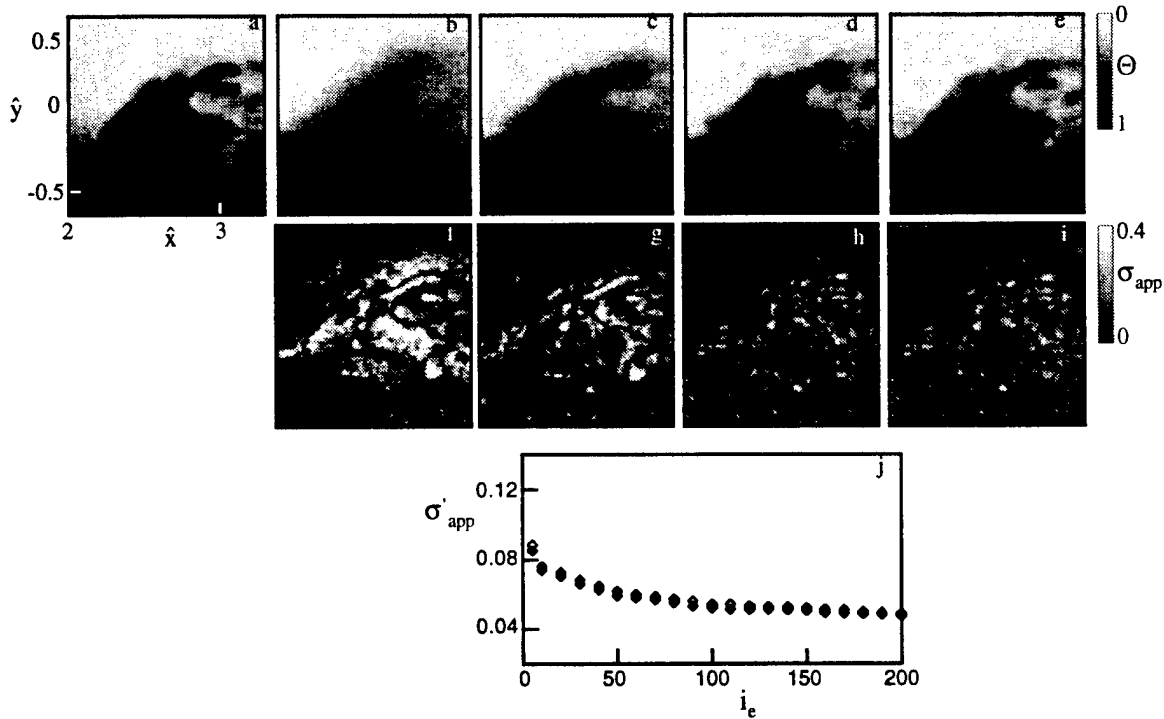


**Figure 65.** The original temperature field (a) and POD approximations based on 10 (b), 50 (c), 100 (d), and 200 (e) modes. The corresponding 2-D r.m.s. errors are shown directly below each image (f-i). The average r.m.s. error of the approximation (open symbols) is shown in (j), where the average r.m.s. error of the reconstruction (closed symbols) is reproduced for reference. Forced flow  $f=225$  Hz, 36:12 shear layer.

Figure 67 shows spectral amplitudes for the unforced (open symbols) and forced ( $f=225$  Hz) flow (closed symbols) for the reconstruction with 10 (a, b), and 200 (c, d) modes. A comparison of the unforced and forced flow spectra reveals two important differences: i) the amplitude of spectral



components at low wavenumbers (large length scales) in the forced flow is lower than in the unforced flow, and ii) the amplitude of spectral components at higher wavenumbers (smaller length scales) in the forced flow is higher than in the unforced flow. Figure 67a demonstrates that the first 10 POD modes of the forced flow provide less contribution than the corresponding unforced modes at all wavenumbers below the critical wavenumber  $k_y \approx 1 \text{ cm}^{-1}$  ( $\lambda_y \approx 1 \text{ cm}$ ). For the reconstruction with 200 modes (Figure 67c), the amplitude of spectral components for the forced flow is reduced (compared to the unforced flow) at all wavenumbers below  $k_y \approx 2 \text{ cm}^{-1}$ , and increased at all wavenumbers above that.

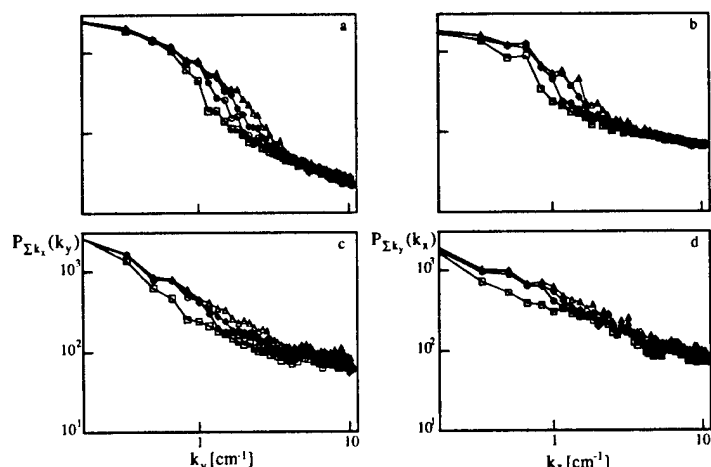


**Figure 66.** Spectral amplitudes of POD reconstructions using 10 ( $\square$ ), 50 ( $\circ$ ), 100 ( $\diamond$ ) and 200 ( $\triangle$ ) modes for the 36:12 shear layer for the unforced (a, b) and forced ( $f=225 \text{ Hz}$ ) flow (c, d) measured at  $2 \leq x/\lambda_K$ ,  $H \leq 3.4$ : (a and c), and (b and d).

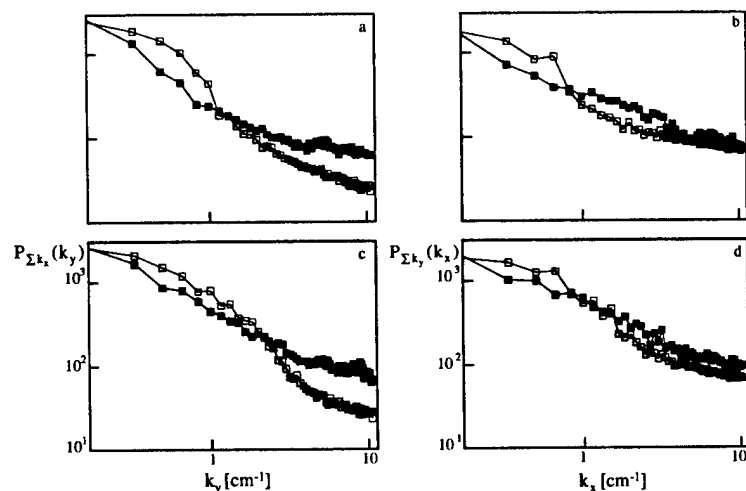


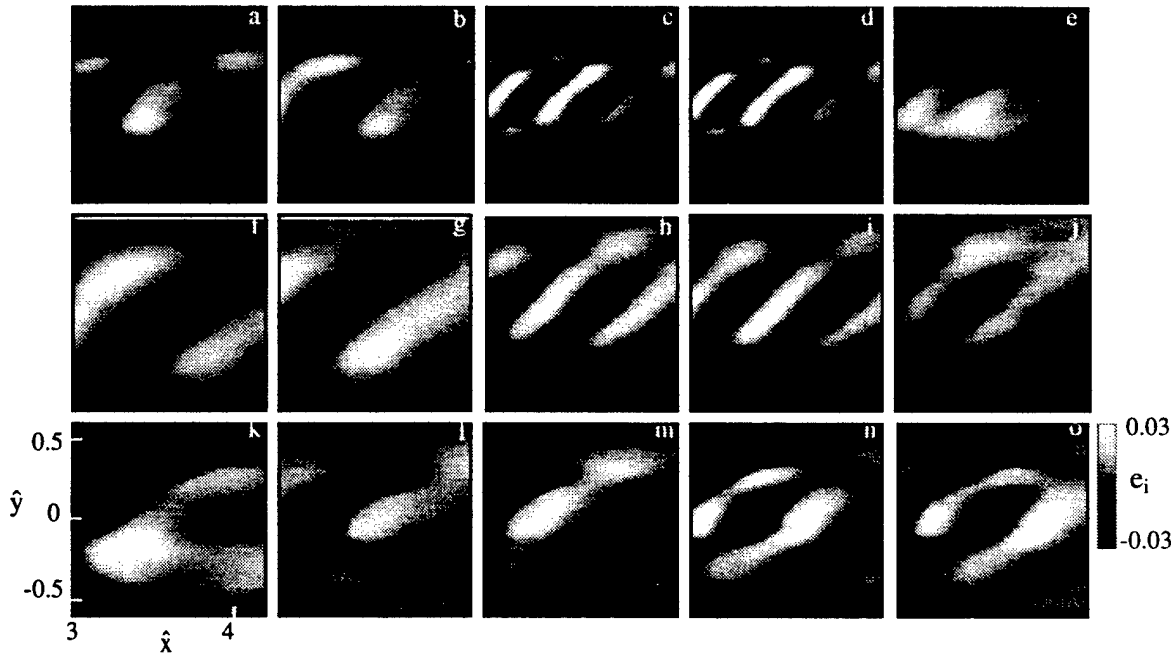
**Figure 67.** Spectral amplitudes of POD reconstructions using 10 (a, b) and 200 (c, d) modes for the 36:12 shear layer for the unforced (open symbols) and forced ( $f=225 \text{ Hz}$ ) flow (closed symbols) measured at  $2 \leq x/\lambda_K$ ,  $H \leq 3.4$ : (a and c), and (b and d).

In real-time applications it is often advantageous to have "global" POD modes that can be used to approximate the flow dynamics in different situations where the flow is either unforced, or subjected to forcing at different frequencies. This is of particular interest in active control of turbulence, for which the plant can potentially be modeled using a finite ODE system obtained from the projection of the governing equations onto the time invariant POD mode's basis determined off-line (Glezer et al. 1989). The implementation and effectiveness of control techniques that use low-order representations to identify the dominant structures in the flow largely depends on the robustness of the POD basis functions.

In order to test the robustness of the POD basis functions, we consider an example of a basis determined from the combined temperature data for two different forcing conditions. The measurements were taken at  $3 \leq \hat{x} \leq 4.2$  for the 36:12 shear layer, for two forcing frequencies (3 Hz and 4.5 Hz). Both the size of the spanwise vortices and frequency of the initial instability are influenced by the forcing conditions. Each set of data consists of approximately 100 cycles of the forcing frequency, and is used to separately generate "local" POD modes characteristic of the two forcing conditions (3 or 4.5 Hz). Furthermore, a total of 3000 temperature maps is assembled in a concatenated

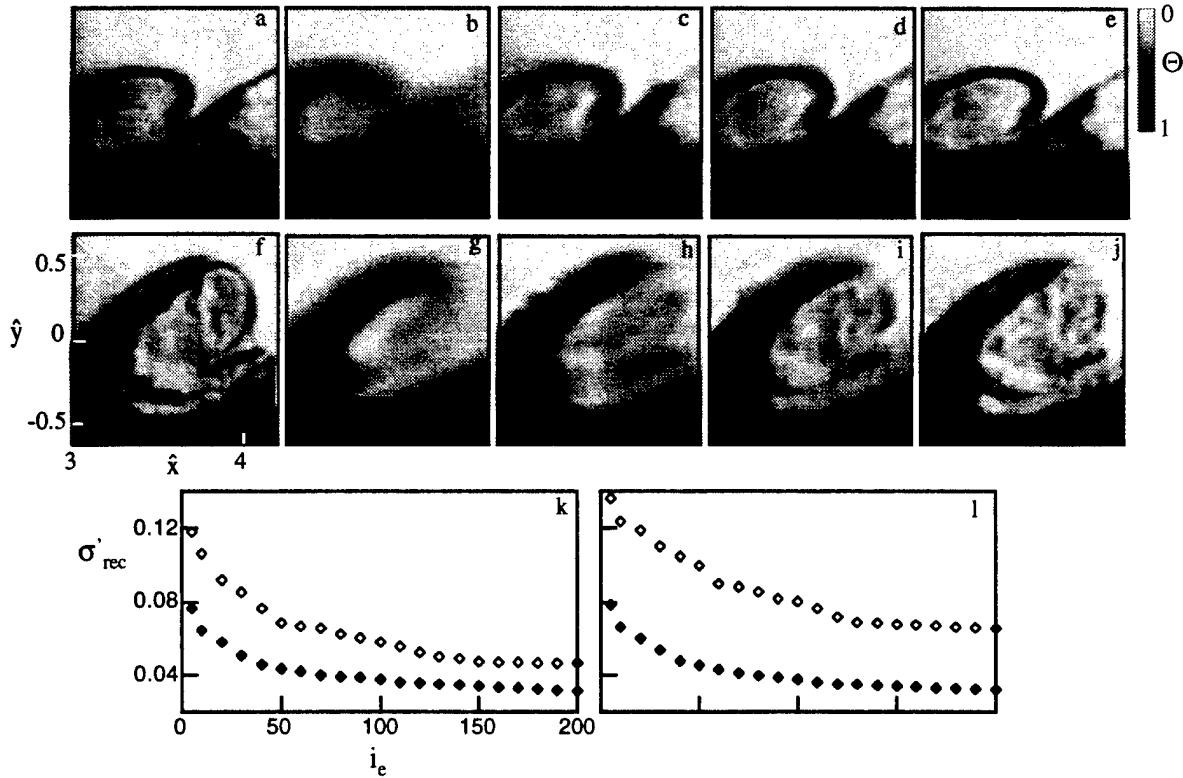
matrix  $\mathbf{A}$  defined in Eq. (16), where the first 1200 realizations correspond to approximately 100 cycles of the flow forced at 4.5 Hz, and the next 1800 realizations correspond to the same number of cycles of the flow forced at 3 Hz. The "global" POD modes computed from the eigenvalue problem  $\mathbf{A}^T \mathbf{A}$  are characteristic for both forcing conditions.

Figure 68 shows the five most energetic "local" modes of the temperature field for flows forced at 4.5 Hz (Figures 68a-e) and 3 Hz (Figures 68f-j), as well as the "global" modes determined from the composite flow matrix (Figures 68k-o). The "local" modes are POD modes computed for each forcing case separately, and are noticeably different in shape. Furthermore, the cross-stream extent of the "local" modes and the spatial features associated with the modes are different for the two forcing scenarios. This leads us to conjecture that the "global" modes, similar to those shown in Figures 68k-o, can be generated for other excitation regimes where the flow is forced at different frequencies. Note that "global" modes in Figures 68k-o combine the spatial features from the two sets of "local" modes in such a way that the spatial frequencies (number of high- and low-intensity bands) associated with them are changed (typically reduced). This indicates that the "global" modes are less optimal than the "local" modes, and that more modes will be needed in order to capture smaller spatial features (higher frequencies) from the original flow field.



**Figure 68.** The five most energetic "local" POD modes for the 36:12 shear layer for the flow forced  $f=4.5$  Hz (a-e) and  $f=3$  Hz (f-j), and "global" POD modes (k-o).

The temporal coefficients are obtained by projecting the instantaneous temperature fields for two different forcing conditions onto the "global" POD modes, and the robustness of the "global" modes is tested by comparing the original temperature field to one reconstructed by using a different number of modes. Figures 69a-e show the original temperature field for the flow forced at  $f=4.5$  Hz, and the reconstruction based on 10, 50, 100, and 200 "global" POD modes. Similarly, Figures 69f-j show the original temperature field and the reconstructions for the flow forced at  $f=3$  Hz. The average r.m.s. error  $\sigma_{rec}$  of the reconstruction based on "global" and "local" POD modes for  $f=4.5$  Hz and  $f=3$  Hz is shown in Figures 69k and l, respectively. It is clear from the original temperature maps that the size and the wavelength of the primary vortex are influenced by the forcing conditions and that the flow forced at 3 Hz contains more small-scale motions.



**Figure 69.** The original flow field (a and f) and POD reconstructions based on 10, 50, 100, and 200 "global" POD modes for the 36:12 shear layer for forced flow at  $f=4.5$  Hz (b-e) and  $f=3$  Hz (g-j). The average r.m.s. error  $\sigma_{rec}$  for reconstructions with "local" (closed symbols) and "global" modes (open symbols) for  $f=4.5$  Hz (k) and  $f=3$  Hz (l).

Notice that the spatial location and the spacing between vortices is captured with only 10 "global" modes (Figures 69b and g), and that the reconstruction captures most of the spatial features from the original maps when 200 modes are used. As is evident from the reconstructed images, as well as from the  $\sigma_{rec}$  (Figures 69k and l), the quality of the reconstruction is slightly worse (2-3%) for  $f=3$  Hz. The average  $\sigma_{rec}$  for the flow forced at 4.5 Hz is 10.6%, 6.8%, 5.8%, and 4.7% for the reconstruction based on 10, 50, 100, and 200 "global" POD modes, respectively, compared to 6.3%, 4.3%, 3.8%, and 3.0% for the same number of "local" POD modes. For the flow forced at  $f=3$  Hz,  $\sigma_{rec}$  is higher than for  $f=4.5$  Hz (12.3%, 9.9%, 8.0%, and 6.6% for the same number of "global" POD modes). However, these average errors are only 3-6% higher than the errors of the optimal reconstruction based on the "local" POD modes for  $f=3$  Hz. Apparently, the applicability of "global" modes in the particular application will be largely determined by the requirements placed on the reconstruction accuracy. In the situation where only the global behavior of the dynamical system needs to be controlled, a small number of "global" modes (up to 10) may be sufficient to capture the spatial location and the size of large structures in the flow, while in other situations where the small-scale motion is important, more modes (up to several hundred) may be needed.

#### V.4. Low-Dimensional Model of the Shear-Layer Flow

The Proper Orthogonal Decomposition technique, when applied to a turbulent flow field, yields an optimal functional basis that can be used to describe flow dynamics with a relatively small number of modes. It is not surprising that the idea of using the POD to generate a low-dimensional model of a turbulent flow developed shortly after this technique was successfully applied to extract large coherent structures from the channel and axisymmetric jet flows (Moin 1984 and Glauser and

George 1987). The approach owes much of its importance to the need to simplify the governing partial differential equations of fluid motion to a low-dimensional system (typically 10-200) of ordinary differential equations, that can be studied using well-known mathematical tools (Rajaei et al. 1993 and Aubry et al. 1988). The main goal of this approach is not to exactly reproduce small-scale details of the flow, but to understand meso- and large-scale turbulence dynamics in a typical flow, using the dynamical behavior of the ODE system that captures global characteristics of the governing equations.

Most applications of the POD technique to date have focused on developing models of the Navier-Stokes equations based on experimentally or numerically determined POD modes and the corresponding temporal coefficients. We use the POD technique to analyze the LIF temperature measurements in the shear layer in order to describe optical distortion of the propagating laser beam. Since the evolution of the temperature (and thus index of refraction) field is governed by the thermal energy equation:

$$\frac{\partial T}{\partial t} + \mathbf{U} \cdot \nabla T = \alpha \nabla^2 T \quad (25)$$

where  $\mathbf{U}$  is the velocity vector and  $\alpha$  is the thermal diffusivity, any low-dimensional model would have to account for the velocity field, which is not measured in the present experiments. The approach (Pearlstein and Cotrell 1997) is to expand the 2-D temperature field using a finite number of POD modes obtained from application of the POD technique to 2-D temperature measurements:

$$T(x, y, t) = \sum_{i=1}^{N_c} a_i(t) e_i(x, y) \quad (26)$$

where  $N_c$  is the number of terms in the expansion. Since the velocity field is not measured, it is assumed that a similar POD expansion based on the unknown velocity POD modes can be used to represent the velocity field

$$\mathbf{U}(x, y, t) = \sum_{i=1}^{M_c} g_i(t) \mathbf{u}_i(x, y) \quad (27)$$

where  $M_c$  is the number of terms in the expansion, and  $g_i(t)$  are the unknown temporal coefficients for the velocity field. The conversion of the partial differential equation (25) into a low-dimensional set of ordinary differential equations is heuristically based on the fact that the nonlinearities in both the Navier-Stokes ( $\mathbf{U} \cdot \nabla \mathbf{U}$ ) and thermal energy equation ( $\mathbf{U} \cdot \nabla T$ ) are quadratic. The resulting system of ordinary differential equations for the temperature temporal coefficients is of the form (Pearlstein and Cotrell 1997)

$$\dot{a}_i = c_i + \sum_{j=1}^{N_c} b_{ij} a_j + \sum_{j,k=1}^{N_c} d_{ijk} a_j a_k \quad (28)$$

where the coefficients  $c_i$ ,  $b_{ij}$  and  $d_{ijk}$  are unknown. The approach suggested by Pearlstein and Cotrell (1997) is to estimate the unknown coefficients  $c_i$ ,  $b_{ij}$ , and  $d_{ijk}$  using a least-squares fit of experimental data for the first  $N_c$  temporal coefficients of the temperature field. Figures 70a-e show the time traces for the derivatives of the first 5 temporal coefficients (black lines) and corresponding least-squares fits (gray lines) based on coefficients  $c_i$ ,  $b_{ij}$ , and  $d_{ijk}$ . The average r.m.s. error of the least-squares fit for the derivative of the  $i$ -th temporal coefficient is defined as

$$\sigma_i^{ls} = \frac{1}{N} \sum_{k=1}^N \sqrt{[\dot{a}_{ik}^{exp} - \dot{a}_{ik}^{ls}]^2} \quad (29)$$

$\Delta \dot{a}_i$

where  $N$  is the total number of time points, superscripts *exp* and *ls* denote the experimental and fitted derivatives of the temporal coefficients, and  $\Delta \dot{a}_i = \dot{a}_{ik}^{exp} - \dot{a}_{ik}^{ls}$ . For the first four temporal coefficients, the average r.m.s. error is less than 5%, while the error for the fifth coefficient is 10%.

Once the unknown coefficients  $c_i$ ,  $b_{ij}$  and  $d_{ijk}$  are determined from the least-squares fit of experimental data during a certain time interval (10 sec of the real flow), the ODE system Eq. (28)

is integrated to predict the temporal coefficients during a different time interval that was not used in the least-square fit. The resulting ODE system is integrated using experimental initial conditions for the temporal coefficients, and a second-order Runge-Kutta scheme. The time step used in the integration is equal to the time interval between the consecutive experimental realizations, so that the predicted results are directly comparable to the experimental data.

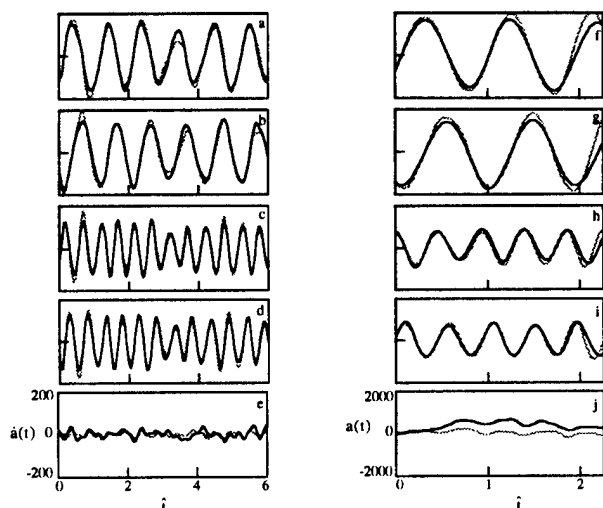


**Figure 75.** Low-dimensional model of the unforced 36:12 shear layer. Experimental (black lines) and least-square fitted (gray lines) derivatives of first 5 temporal coefficients (a-e). Experimental (black lines) and predicted (gray lines) values of first 5 temporal coefficients (f-j).

Figures 70f-j show the computed and experimental temporal coefficients for the first 5 modes of the unforced 36:12 shear layer at  $2 \leq \hat{x} \leq 3.4$ . These results indicate that the computed temporal coefficients (gray lines) compare reasonably well with the experimental data (black lines). The first four temporal coefficients track the experimentally observed time evolution remarkably accurately. The dominant frequency and the amplitude of the first four temporal coefficients are correctly reconstructed and their average r.m.s. error, defined as in Eq. (28), is less than 8%. The fifth coefficients is predicted less accurately (the average r.m.s. error is about 50%). As mention earlier in this chapter, this coefficient is associated with the POD mode that shows contribution of the phase jitter of the fundamental frequency. A time trace of the fifth coefficient shows aperiodic fluctuations not completely captured by the ODE system described in Eq. (28). Although the fifth coefficient is

underpredicted in amplitude, its general shape remains correct throughout the prediction interval.

It is important to note that the results presented in Figures 70f-j represent predictions of the temporal coefficients for a time interval not used in the least-square fit. This is particularly important if the ODE system described by Eq. (28) is to be used for the real-time prediction of the index of refraction field and the phase correction. One of the drawbacks of the fitted ODE system described here is that it can have solutions with finite-time singularities and/or bounded solutions that are unstable (Pearlstein and Cotrell 1997). This results in a need to update the ODE system frequently, especially when more than 5 temporal coefficients are used. Furthermore, the ODE system in Eq. (28) is truncated at 5 modes that contain more than 70% of the fluctuation energy. It has been pointed out by Rajaei et al. (1994) that the higher-order modes may be dynamically more active than their eigenvalues suggest, because they are associated with the higher frequencies in the flow. Work to account for the higher-order modes is currently in progress (Pearlstein and Cotrell 1997). In the work presented here, no attempt has been made to account for the lost energy of the higher-order modes (for discussion of different attempts to describe transfer of energy between small and large scales, see Holmes et al. 1996).

## VI. CONCLUSIONS

The optical distortion of a sheet of light transmitted through a planar shear layer between two uniform streams of unequal temperatures was investigated in a closed-return water facility. Instantaneous temperature distributions (from which the index of refraction can be directly determined) in planar cross-sections of the shear layer were obtained using measurements of the temperature dependent fluorescence of Rhodamine B which was uniformly mixed in both streams. The LIF measurements have demonstrated that pairs of high- and low-intensity streaks in the fluorescence image originate from the edges of large vortical structures where the angle between the direction of the light propagation and the local temperature (or index of refraction) gradient is large. It is also evident that the streaks are advected with the vortical structures and that they begin to form during the roll-up of the initial Kelvin-Helmholtz instability.

A novel correction scheme, based on simultaneous measurements of intensity of two fluorescent dyes with different temperature sensitivities, was used to remove optical effects from the fluorescence images and to obtain correct temperature distributions. The effectiveness of the temperature correction scheme was demonstrated for a variety of flow conditions, and corrected temperature maps were used to investigate mixing in the unforced and forced flow. The average r.m.s. bending angle, obtained using the ray-tracing equation and corrected temperature maps, was estimated to be between 50-100  $\mu$ rad for the unforced flow and 30-50  $\mu$ rad for the forced flow.

The effect of spanwise vortices on optical distortion of the laser sheet propagating through the shear layer was determined from the Strehl ratio time traces characterized by large positive and negative peaks. The fact that the largest index gradient was associated with the trailing edge near the low-speed side of the shear layer indicated that the index field was better mixed near the high-speed side of the shear layer.

The spatio-temporal distribution of optical distortions revealed a pair of spatially-periodic trajectories associated with the trailing and leading edges of the spanwise vortices. The ratio of the convective speeds associated with two trajectories is approximately equal to 1.4, indicating that the part of the shear layer close to the high-speed stream has a different speed than the part close to the low-speed stream.

The effect of the spanwise nonuniformities on distortion of the laser beam was determined from the LIF measurements in the y-z plane. The evidence suggested that the spanwise nonuniformities could have a large effect on optical distortion. The r.m.s. values of optical distortion in the y-z plane were higher than the distortions in the x-y plane. The maximum spanwise distortion could be as high as 40% of the mean intensity at some spanwise locations. These results also suggest that the average spanwise distortion strongly depends on phase during one cycle of the base flow.

High-frequency piezoelectric actuators were developed and used to reduce index of refraction gradient and the length scales that contributed to optical distortions. A flow visualization of the actuator flow revealed a well defined actuator jet synthesized from a train of vortex pairs formed at the edge of the actuator blade. The spectrum of the actuator temperature disturbance showed a sharp peak at the forcing frequency, along with a weaker peak at the first harmonic. Both spectral peaks were practically undetectable at a short distance away from the actuator, indicated rapid dissipation of small scales.

A time trace of the optical distortion in the forced flow suggested that optical effects could be mitigated using direct small-scale excitation. The maximum instantaneous distortion was reduced from almost 30% of the mean value in the unforced flow to less than 10% in the forced flow. The average optical distortion was reduced by more than 20% for all velocity ratios. The peak distortions in the spanwise direction were also significantly reduced when the flow was forced, and the r.m.s. distortion was practically constant throughout the cycle. This improvement in the

optical quality of the shear layer was explained by a drastic reduction of the index of refraction gradient and the length scales. It was found that the peak gradient was reduced by almost 40%, while the maximum length scales were reduced by more than 75%.

The relative importance of the diffusion zone thickness and shape of the interface on optical distortions was separately analyzed using an idealized model of the 24:9 shear layer. It was shown that the magnitude of the peak and r.m.s. distortions decreases as the diffusion zone thickness increases. It was also found that the shape of the interface that separates two streams in the shear layer strongly effects optical distortions. When the interface is perturbed with a periodic disturbance, the peak distortion is reduced by almost 50% when compared to distortions for the undisturbed interface.

The direct small-scale excitation resulted in a significant mixing enhancement in the shear layer and had a dramatic effect on spanwise vortical structures. This was particularly evident in the low Reynolds number flow where the fundamental instability of the shear layer was strongly suppressed. The average performance measure in the forced flow indicated intense mixing that extended across the entire width of the shear layer. The integral performance measure averaged over the full streamwise domain was almost double that of the unforced flow for all velocity ratios. While the pdf for the unforced 24:9 shear layer was nonmarching at all streamwise locations, it became marching when the flow was forced at high frequency.

A low-order description of a 2-D index of refraction field was developed using the proper orthogonal decomposition technique. It was found that the first 30 two-dimensional modes were capable of capturing as much as 80% of energy in both unforced and forced flows. The four most energetic POD modes of the unforced flow were associated with the large coherent structures, and their corresponding time-dependent coefficients exhibited nearly periodic behavior. The first mode in the high-frequency forced flow is less dominant and the energy is distributed more evenly over the POD modes.

The POD modes were used to reconstruct original temperature maps for the unforced and forced flows and the r.m.s. error of the reconstruction was found to be less than 10% for most of the cases. Furthermore, this technique was tested on a temperature field measured for similar flow conditions but not included in the ensemble used to calculate the POD modes. The resulting r.m.s. error was comparable to the error for the reconstruction. The length scales associated with certain groups of POD modes were determined using a 2-D Fourier Transform of the reconstructed temperature map computed for different number of POD modes. It was found that modes 10-50 mostly contribute in the range  $0.5 \text{ cm}^{-1} < k_x < 1.5 \text{ cm}^{-1}$  and  $0.6 \text{ cm}^{-1} < k_y < 2.3 \text{ cm}^{-1}$ . On the other hand, modes 51-100 contribute in the range  $1.2 \text{ cm}^{-1} < k_x < 1.9 \text{ cm}^{-1}$  and  $1.0 \text{ cm}^{-1} < k_y < 2.6 \text{ cm}^{-1}$ .

The POD technique was also used to develop a low-dimensional model of a shear layer flow that was based on a small number of POD modes. The unknown coefficients of the resulting system of ordinary differential equations were determined using a least-squares fit of experimental data for the temporal coefficients of the temperature field. The ODE system was then integrated to predict temporal coefficients during a different time interval that was not used in the least-square fit. Results indicate that the dominant frequency and amplitude of the computed temporal coefficients compare well with the experimental data.

## BIBLIOGRAPHY

- Aubry, N., Holmes, P., Lumley, J. L. and Stone, E. 1988 The dynamics of coherent structures in the wall region of a turbulent boundary layer. *Journal of Fluid Mechanics* **192**, 115-173.
- Bakewell, P. and Lumley, J. L. 1967 Viscous sublayer and adjacent wall region in turbulent pipe flow. *Physics of Fluids* **10**, 1880-1889.

- Ball, K. S., Sirovich, L. and Keefe, L. R. 1991 Dynamical eigenfunction decomposition of turbulent channel flow. *International Journal for Numerical Methods in Fluids* **12**, 585-604.
- Batchelor, G. K. 1959 Small-scale variations of convected quantities like temperature in turbulent fluid. *Journal of Fluid Mechanics* **5**, 113-133.
- Berkooz, G., Holmes, P. and Lumley, J. L. 1993 The proper orthogonal decomposition in the analysis of turbulent flows. *Annual Review of Fluid Mechanics* **25**, 539-575.
- Bernal, L. P. and Roshko, A. 1986 Streamwise vortex structure in plane mixing layers. *Journal of Fluid Mechanics* **170**, 499-525.
- Buch, K. A. and Dahm, W. J. A. 1996 Experimental study of the fine-scale structure of conserved scalar mixing in turbulent shear flows. Part 1.  $Sc \gg 1$ . *Journal of Fluid Mechanics* **317**, 21-71.
- Carpenter, B. N. and Pearlstein, A. J. 1996 Simulation of extraction of velocity from passive scalar data in a two-dimensional diverging channel flow. *Physics of Fluids* **8**, 2447-2459.
- Chew, L. and Christiansen, W. 1991 Coherent structure effects on the optical performance of plane shear layers. *AIAA Journal* **29**, 76-80.
- Crow, S. C. and Champagne, F. H. 1971 Orderly structure in jet turbulence. *Journal of Fluid Mechanics* **48**, 547-591.
- Dahm, W. J. A., Su, L. K. and Southerland, K. B. 1992 A scalar imaging velocimetry technique for fully resolved four-dimensional vector velocity field measurements in turbulent flows. *Physics of Fluids A* **4**, 2191-2206.
- Delville, J. *Characterization of the Organization in Shear Layers Via Proper Orthogonal Decomposition*. In *Eddy Structure Identification in Free Turbulent Shear Flows*, editors J.P. Bonnet and M.N. Glauser, Kluwer Academic Publishers, 1993.
- Delville, J., Bellin, S. and Bonnet, J. P. *Use of the Proper Orthogonal Decomposition in a Plane Turbulent Mixing Layer*. In *Turbulence and Coherent Structures*, editors O. Metais and M. Leseieur, Kluwer Academic Publishers, 1989.
- Dimotakis, P. E., Miake-Lye, R. C. and Papantoniou, D. A. 1982 Structure and dynamics of round turbulent jets. GALCIT Report FM82-01.
- Eckbreth, A. C. *Laser Diagnostics for Combustion Temperature and Species*. Gordon and Breach Publishers, Amsterdam, The Netherlands, 1996.
- Farina, D. J., Hacker, J. M., Moffat, R. J. and Eaton, J. K. 1994 Illuminant invariant calibration of thermochromic liquid crystals. *Experimental Thermal and Fluid Science* **9**, 1-12.
- Fourquette, D. C., Dimotakis, P. E. and Ching, W. K. 1995 Index-of-refraction imaging and aero-optics effects in a fully-developed axisymmetric turbulent jet. *AIAA Paper* 95-1980.
- Glezer, A., Kadioglu, Z. and Pearlstein, A. J. 1989 Development of an extended proper orthogonal decomposition and its applications to a time periodically forced plane mixing layer. *Physics of Fluids A* **1**, 1363-1373.
- Glauser, M. N. and George, W. K. An orthogonal decomposition of the axisymmetric jet mixing layer utilizing cross-wire measurements. *Proceeding Sixth Symposium Turbulent Shear Flows*, Toulouse, France, 1987.
- Hanson, R. K. 1988 Planar laser-induced fluorescence imaging. *Journal of Quant. Spectrosc. Radiat. Transfer* **40**, 343-362.
- Hinze, J. O. *Turbulence*. McGraw Hill, New York, 1975.
- Holmes, P., Lumley, J. L. and Berkooz, G. *Turbulence, Coherent Structures, Dynamical Systems and Symmetry*. Cambridge University Press, New York, 1996.
- Hugo, R. J. and Jumper E. J. 1995 Time-resolved, aero-optical measurements of a wavefront aberrated by a compressible free shear layer. *AIAA Paper* 95-1979.
- Jacobson, S. A. *An Experimental Investigation Towards the Active Control of Turbulent Boundary Layers*. Ph.D. Thesis, Stanford University, 1995.
- Jimenez, J., Cogollos, M. and Bernal, L. P. 1985 A perspective view of the plane mixing layer. *Journal of Fluid Mechanics* **152**, 125-143.
- Jumper, E. J., Hugo, R. J. 1992 Optical phase distortion due to turbulent-fluid density fields: quantification using the small-aperture beam technique. *AIAA Paper* 92-3020.



- Jumper, E. J., Hugo, R. J. and Cicchiello, J. M. 1994 Turbulent-fluid-induced optical wavefront dynamics: near and far field implications. *AIAA Paper* 94-2547.
- Jumper, E.J. 1997 Recent advances in the analysis of dynamic aero-optic interactions. *AIAA paper* 97-2350.
- Karasso, P. S. and Mungal, M. G. 1996 Scalar mixing and reaction in plane liquid shear layers. *Journal of Fluid Mechanics* **323**, 23-63.
- Koochesfahani, M. M. and Dimotakis, P. E. 1986 Mixing and chemical reactions in a turbulent liquid mixing layer. *Journal of Fluid Mechanics* **170**, 83-112.
- Koochesfahani, M. M. *Experiments on Turbulent Mixing and Chemical Reactions in a Liquid Mixing Layer*. Ph.D. Thesis, California Institute of Technology, 1984.
- Lumley, J. L. The structure of inhomogeneous turbulent flows. In *Atmospheric Turbulence and Radio Wave Propagation*, edited by A.M. Yaglom and V.I. Tatarskii, Nauka. Moscow, 1967.
- Lumley, J. L. Coherent structures in turbulence. In *Transition to Turbulence* edited by R.E. Meyer, Academic Press, New York, 215-242, 1982.
- Malley, M. M., Sutton, G. W. and Kincheloe, N. 1992 Beam-jitter measurements of turbulent aero-optical path differences. *Applied Optics* **31**, 4440-4443.
- McMackin, L., Masson, B., Clark, N., Bishop, K., Pierson, R., Chen, E. 1995 Hartmann wavefront sensor studies of dynamic organized structures in flow fields. *AIAA Journal* **33**, 2158-2164.
- McMackin, L., Wissler, J., Clark, N., Chen, E., Bishop, K., Pierson, R., and Staveley, B. 1994 Hartmann sensor and dynamic tomographical analysis of organized structure in flow field. *AIAA Paper* 94-2548.
- Moffat, R. J. 1988 Describing the uncertainties in experimental results. *Experimental Thermal and Fluid Science* **1**, 3-17.
- Moin, P. (1984) Probing turbulence via large eddy simulation. *AIAA paper* 84-0174.
- Moin, P. and Moser, R. D. 1989 Characteristic eddy decomposition of turbulence in a channel. *Journal of Fluid Mechanics* **200**, 471-509.
- Mollo-Christensen, E. 1971 Physics of turbulent flow. *AIAA Journal* **9**, 1217.
- Nygaard, K. J. and Glezer, A. 1991 Evolution of streamwise vortices and small-scale motion in a plane mixing layer. *Journal of Fluid Mechanics* **231**, 257-301.
- Nygaard, K. J. and Glezer, A. 1994 The effect of phase variations and cross-shear on vortical structures in a plane mixing layer. *Journal of Fluid Mechanics* **276**, 21-59.
- Oster, D. and Wygnanski, I. 1982 The forced mixing layer between parallel streams. *Journal of Fluid Mechanics* **123**, 91-130.
- Payne, F. R. *Large Eddy Structure of a Turbulent Wake*. Ph.D. Thesis, Pennsylvania State University, 1966.
- Pearlstein, A. J. and Cotrell, D. L. *Development of Low-Order Models for Aero-Optic Flows*. Cornell Workshop on POD-Galerkin Models, Cornell University, Ithaca, NY, October 13-14, 1997.
- Prenel, J. P., Porcar, R. and El Rhassouli, A. 1989 Three-dimensional flow analysis by means of sequential and volumic laser sheet illumination. *Experiments in Fluids* **7**, 133-137.
- Rajaei, M., Karlsson, S. K. F. and Sirovich, L. 1994 Low-dimensional description of free-shear-flow coherent structures and their dynamical behavior. *Journal of Fluid Mechanics* **258**, 1-29.
- Roberts, F. A. *Effects of Periodic Disturbances on Structure of Mixing in Turbulent Shear Layers and Wakes*. Ph.D. Thesis, California Institute of Technology, 1985.
- Sakakibara, J., Hishida, K., Maeda, M. 1993 Measurements of thermally stratified pipe flow using image-processing techniques. *Experiments in Fluids* **16**, 82-96.
- Sakakibara, J. and Adrian, R. J. 1997 Measurement of whole field temperature using two-color LIF. 34th National Heat Transfer Symposium of Japan, 421-422.
- Shack, R. V. 1971 Direct phase sensing interferometer. *JOSA* **61**, 655.
- Sirovich, L. 1987 Turbulence and the dynamics of coherent structures. *Q. Appl. Mathematics* **45**, 561.
- Sirovich, L., Ball, K. S. and Keefe, L. R. 1990 Plane waves and structures in turbulent channel flow. *Physics of Fluids A* **2**, 2217- 2226.

- Sirovich, L., Kirby, M. and Winter, M. 1990 An eigenfunction approach to large scale transitional structures in jet flow. *Physics of Fluids A* **2**, 127 - 136.
- Smith, S. H. and Mungal, M. G. 1998 Mixing, Structure and scaling of the jet in crossflow. *Journal of Fluid Mechanics* **357**, 83-122.
- Sutton, G. W. 1985 Aero-optical foundations and applications. *AIAA Journal* **23**, 1525-1537.
- Tatarskii, V. I. *The Effect of the Turbulent Atmosphere on Wave Propagation*. Israel Program for Scientific Translation, Jerusalem, 1971.
- Tennekes, H. and Lumley, J. L. *A First Course in Turbulence*. MIT Press., 1972
- Toda, M. and Osaka, S. 1979 Vibrational fan using the piezoelectric polymer PVF<sub>2</sub>. Proceedings of the IEEE, **67**, 1171-1173.
- Ukeiley, L. and Glauser, M. N. *Dynamics of Large Scale Structures in a Plane Turbulent Mixing Layer*. Report No. MAE-311, Clarkson University, 1995.
- Walker, D. A. 1987 A fluorescence technique for measurements of concentration in mixing layers. *Journal of physics E: Scientific instruments* **20**, 217-223.
- Weast, R.C. and Selby S.M. *Handbook of Chemistry and Physics*. The Chemical Rubber Co., 1966.
- Wiltse, J. M. and Glezer, A. 1993 Manipulation of free shear flows using piezoelectric actuators. *Journal of Fluid Mechanics* **249**, 261-285.
- Wiltse, J. M. and Glezer, A. 1998 Direct excitation of small-scale motions in free shear flows. Accepted for publication in *Physics of Fluids*.
- Wiltse, J. M. *Control of Mixing in a Nonreactive Shear Layer*. Ph.D. Thesis, University of Arizona, 1993.
- Wissler, J. B. and Roshko, A. 1992 Transmission of thin light beams through turbulent mixing layers. *AIAA paper* 92-0658.
- Zhou, X. and Sirovich, L. 1992 Coherence and chaos in a model of turbulent boundary layer. *Physics of Fluids A* **4**, 2855-2874.

## **B. A SMART, HIGH FRAME RATE CAMERA USING 3D SILICON CMOS VLSI CIRCUITS VERTICALLY OPTICALLY INTERCONNECTED FOR MASSIVELY PARALLEL IMAGE PROCESSING**

### **1. Introduction and Overview**

High speed imaging applications such as combustion, transMach fluid flow, and aerodynamic sensing require a high frame rate image acquisition system with frame rates in excess of 100 kfps (frames per second). Currently, imaging systems implemented using charge-coupled device (CCD) technology with off-chip analog to digital data converters are limited to continuous frame rates of approximately 1 kfps [1]. Analog data transfer bottlenecks, which are limited by signal to noise ratios and the requirement for fast ADCs, are the cause of this low frame rate limitation and the lack of scalability of these imaging systems. This report explores the detection and processing of real-time image sequences at high frame rates, which can be achieved with an optically interconnected massively parallel processor. Two layers of silicon (Si) CMOS circuitry, an imaging/preprocessing plane, and a processing plane, are vertically optically interconnected using through-Si three dimensional (3D) communication links. This creates a fully scalable system for massively parallel data transmission from image to processing plane. The top integrated optoelectronic circuit (OEIC) is a focal plane processing chip with an on-chip array of sigma delta analog to digital converter (ADC) front ends under each pixel. This Si CMOS chip is a scaleable high frame rate image capture building block, which uses the second layer of data processing to filter the sigma delta front end data to obtain images. The use of an array of vertically optically connected processors beneath the imaging array chip is an effective solution to this challenging data processing task.

To achieve image processing systems that operate, in real time, on large images with frame rates in the high kHz or MHz is beyond the capability of today's imaging systems. For example, a sigma delta analog to digital converter (ADC) generating a sequence of 256x256 8 bit images at a frame rate of 400 kHz must be clocked at more than 1.8 THz. Even when parallel ADCs are placed along the edge of the imaging array, the problem is only partially mitigated because the speed at which the ADCs must operate still increases with image size. To generate 256x256 8 bit images at a frame rate of 400 kHz, 256 ADCs need to be clocked at more than 7.3 GHz.

Herein, we describe a chip stack that implements, on the top chip, a fully parallel front end with one ADC per pixel. This provides a scaleable solution to the real time high frame rate image capture problem when it is coupled to a massively parallel optically interconnected processor. We show that to generate a sequence of 256x256, 8 bit images at a frame rate of 400 kHz, a 32x32 array of 230 MHz pipelined processors (each operating at 950 MIPS) is required. To keep the design scaleable the ADCs must reside

beneath the detector array, which is electrically interconnected on a per pixel basis for parallel connection to the detector plane. To connect to subsequent layers of processing, a through-substrate parallel optical data link is used.

## **2. Architecture of the Focal-Plane Readout System**

### **2.1 Parallel Readout System**

In conventional focal-plane readout systems, a single ADC performs data conversion for the entire array. In this case, noise can be introduced in the long analog shift register chains that cannot be removed and will cause a reduction of dynamic range. In addition, the analog circuits in a serial ADC are required to operate with the highest bandwidth of all focal-plane components, since the conversion rate is the same as the pixel data rate. For the sigma delta conversion of a 400 kHz frame rate, 256x256, 8 bit image sequence, if we assume an oversampling ratio of 72, then the sampling rate of the ADC front end must be more than 1.8 THz. Clearly a single ADC-based architecture is not a good choice for a high frame rate image readout system. To improve the signal-to-noise ratio (SNR), serial and semi-parallel on-focal-plane readout systems have also been proposed. Serial architectures remove pick-up and vibration sensitivity since no off-chip analog cabling is required. However, the data rate required is not improved, and noise can still be introduced in the analog shift registers between the focal plane and ADC. Semi-parallel architectures have been proposed [1] to overcome these problems. The ADC rate of these circuits is the much lower row read out rate. For our example of a 400 kHz frame rate, 256x256, 8 bit image sequence, if we assume all 256 rows have an ADC in parallel, then the clock rate of the ADC front end drops by 256, to slightly more than 7.3 GHz. This is at least a feasible clock speed, although only heterojunction bipolar transistor (HBT) technology has demonstrated the capability to realize near commercial ADCs at these speeds, and certainly not an array of 256.

To overcome the limitations of serial and semi-parallel readout, we have implemented a focal plane array (FPA) using a fully parallel readout architecture. Figure 1 shows this architecture, in which each pixel has its own ADC. To minimize the area of the ADC circuitry, only the front end of the sigma delta converter is implemented per pixel. Since sigma delta converters process only digital data after the front end, further noise cannot be introduced to the signal by shifting the now digital data. A processor is then needed to complete the ADC process. By grouping the pixels into subarrays, each can be served by one processing unit to perform the conversion. To provide the high data rate necessary between the imaging array/ADCs and processor, an integrated optoelectronic emitter on each subarray enables vertical optical through-silicon output of digital image data from the focal plane to the processor stacked below each subarray. This vertical coupling to the image plane allows the detector and processor arrays to be scaled while maintaining a fixed level of processing per pixel. The number of pixels included in the subarray is dependent on the bandwidth of the processor circuits. The SIMPil

processor [2] is being implemented for this program. If an  $8 \times 8$  subarray is used, the size of the processor and focal plane subarray match well, so by tiling an  $8 \times 8$  array of processor chips each containing 16 nodes, a  $256 \times 256$  pixel resolution focal plane can be achieved.

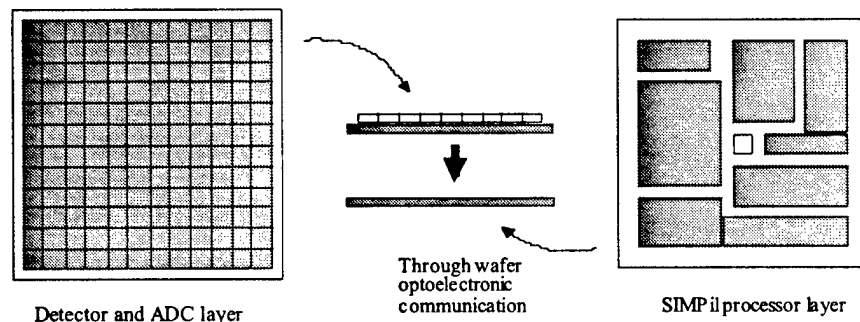


**Figure 1. Parallel on-focal-plane ADC with vertical optical link to SIMPil processor.**

To achieve a 400 kHz frame rate, each processor would need to process data at more than 1.8 Gbps (for an  $8 \times 8$  subimage image oversampled by 72 at 400 kHz). If we assume a fully pipelined 8 bit processor clocked at 230 MHz (achieving more than 900 MIPS), a frame rate of only about 50 kHz is possible. To achieve a 400 kHz frame rate, the first comb filter stage of the sigma delta converter must be under each pixel. If we assume that an 8 tap comb filter (which is no more than a 3 bit counter) is added to each pixel, then the 900 MIPS processors need only implement the remaining 9 tap low pass filter to produce the 8 bit image output. This filter can be implemented by the proposed processor to achieve the required 400 kHz frame rate.

To improve the signal-to-noise ratio (SNR), serial on-focal-plane readout systems have been proposed, as shown in Figure 2(a). This architecture removes pick-up and vibration sensitivity since no off-chip analog cabling is required [1]. However, the data rate required is unchanged, and noise can still be introduced in the analog shift registers between the focal plane and ADC. Semi-parallel architectures have been proposed [1], [3], [4] to overcome these problems, as shown in Figure 2(b). The ADC conversion rate of this circuit is the much lower row read out rate. For our example of the sigma-delta conversion of a 400 kHz frame rate  $256 \times 256$  8 bit image sequence, if we assume all 256 rows have an ADC attached in parallel as in Figure 2(b), then the clock rate of the ADC front end drops by 256 to slightly more than 6.6 GHz. This is at least a feasible clock speed, although only heterojunction bipolar transistor (HBT) technology has demonstrated the capability to realize near commercial ADCs at these speeds, although not an array of 256 of them. Thus this is not currently a feasible architecture and still does not solve the problem of noise being introduced through the long analog lines between the pixels and the ADCs.

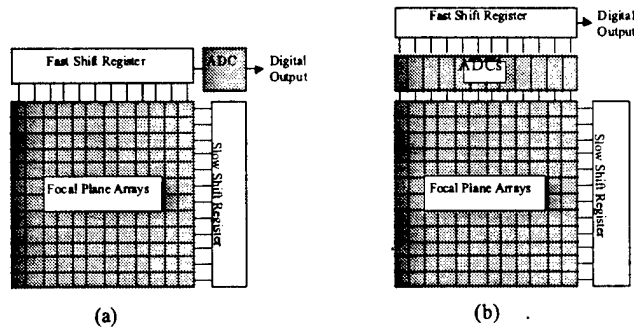


**Figure 2. Architecture of on-focal-plane readout system**

The pixels are grouped into subarrays, each served by one digital signal processing (DSP) unit to perform the conversion. An integrated optoelectronic emitter on each subarray allows through-silicon wafer output of digital image data from the focal plane to the processor stacked below each subarray. This vertical coupling to the image plane allows the detector and processor arrays to be scaled while maintaining a fixed level of processing per pixel. The number of pixels included in the subarray is depend on the bandwidth of DSP circuits.

An example of the type of processor proposed is the SIMPil processor. If an 8x8 subarray is used, the size of the processor and focal plane subarray seem to match reasonably well so that by tiling an 8x8 array of processor chips each containing 16 nodes, a 256x256 pixel resolution focal plane could be achieved. To achieve a 400 kHz frame rate, each processor would need to process data at more than 820 Mbps (for an 8x8 subimage image oversampled by 32 at 400 kHz). If we assume a fully pipelined 8 bit processor clocked at 102 MHz (achieving more than 410 MIPS) a frame rate of only about 50 kHz is possible. To achieve a 400 kHz frame rate we need to assume that the first comb filter stage of the sigma-delta converter is also under each pixel. For our example, if we assume that an 4 tap comb filter (which is no more than a 2 bit counter) is added to each pixel, then the 435 MIPS processors need only implement the remaining 4 tap low pass filter to produce the 8 bit image output. This filter can be implemented by the proposed processor to achieve the required 400 kHz frame rate.

## 2.2 Current input first order sigma-delta converter

To implement the parallel on-focal plane readout system, a new ADC is needed which can be fit into each pixel with reasonable speed and dynamic range. This section presents the current input first order sigma-delta converter that satisfies this requirement.

ADCs can be divided into two classes. One is the converters limited by component matching and the other is based on counting algorithms. Flash converters, pipeline converters, recursive converters and successive approximation converters are included in this first class. The accuracy of these converters is ultimately limited by the

component matching. A solution to overcome this limit is to use ADCs based on counting algorithms. One of these converters is the dual slope converter. This converter can be very accurate but the conversion rate is too slow. For instance, to obtain 8 bit accuracy, the converter needs a clock 256 times faster than the sample rate. This implies that the conversion rate is 256 times slower than the internal clock frequency. Sigma-delta converters are another data converter based on a counting algorithm [5], [6].

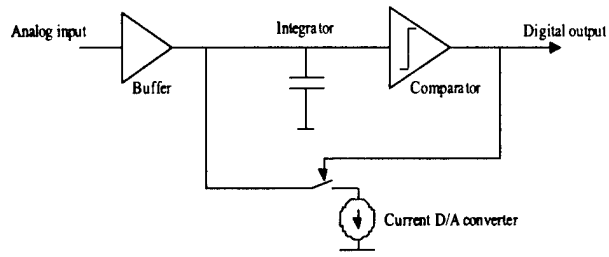
For a given accuracy, the internal clock frequency of a sigma-delta converter can be much smaller than that of a dual slope ADC. For example while a dual slope ADC requires an internal clock frequency of 256 times the sampling rate to obtain 8 bit accuracy, an oversampling ratio of 32 [5] or more is sufficient for a first order sigma-delta converter to achieve 8 bit accuracy. Because of its efficient counting algorithm, the trade-off between speed and accuracy is more advantageous for an sigma-delta converter.

In addition, the sigma-delta converter front end or modulator is small and low power. Only the modulator needs to be on the focal plane since its output is digital. Approximately 90% of the sigma-delta ADC circuitry is digital and can be located off the focal plane. This eases the problem of fitting the modulator into the allocated space under each pixel.

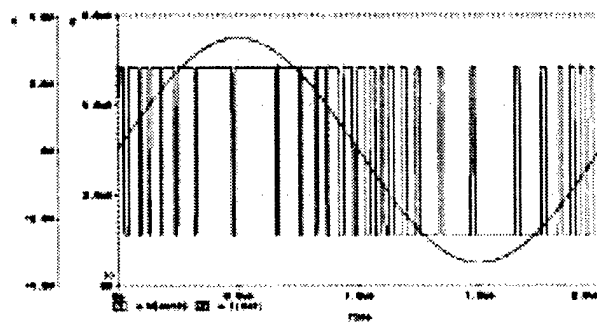
The current input sigma-delta ADC consists of a modulator and a digital filter section. The modulator samples the analog input and develops a corresponding digital bit stream, and the digital filter compresses the bit stream into the Nyquist rate multibit codes and performs noise filtering.

Figure 3 shows the current input sigma-delta modulator. It is composed of four parts. The first is a current buffer, which controls the bias voltage of the photodetector. The second is a current integrator, which is implemented with a capacitor. The capacitor size is as large as possible, for low  $1/f$  noise. The third is a current D/A converter, which provides a reference current to the input depending on the sign of output. The last stage is a comparator.

Figure 4 shows the PSPICE simulation of this converter with a sinusoidal input. The digital output contains the analog input and must be filtered digitally to get a digital representation of the signal.



**Figure 3. First order sigma-delta modulator**



**Figure 4. Simulation results of first order sigma-delta modulator**

There are three main building blocks used to realize this smart pixel image acquisition system. The first building block is the integrated photodetector array. Two implementations have been demonstrated herein: Si CMOS detectors and thin film hybrid integrated GaAs-based PiN detector arrays. This implementation realizes higher fill factor than the monomaterial Si detector array.

Figure 5 shows the layout of Si chip with integrated Si detectors, which has been fabricated and tested. This chip has an 8x8 array of detectors, an 8x8 array of ADCs, associated readout shift registers, and emitter driver. This chip sits above the DSP node that processes its data. The chip is functional and, with a DSP below, one tile of a scaleable high frame rate imaging system can be realized.



8 X 8 focal plane  
array: detectors and

Emitter

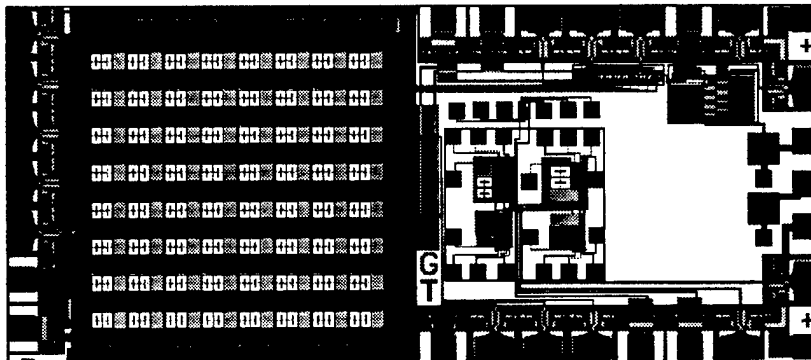


Figure 5. Si CMOS VLSI smart pixel imaging array.

Figure 6 shown the Si CMOS chip which has an 8x8 array of ADCs, associated readout shift registers, and emitter driver. This chip must be integrated with an array of detectors. This chip sits above the DSP node that processes its data. Figure 7 (a) and (b) show the test results of this chip when electrical DC inputs are provided. The chip is functional and with the addition of an array of detectors on top of each ADC and a DSP below, one tile of a scaleable high frame rate imaging system can be realized.

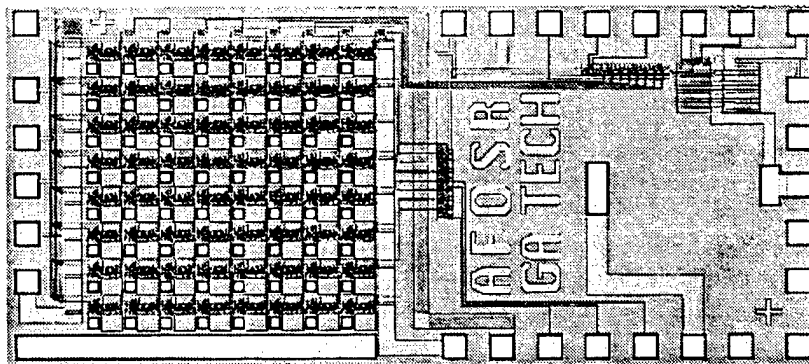
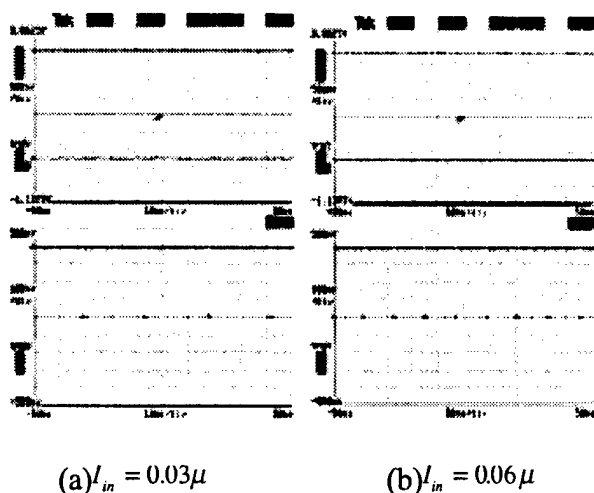
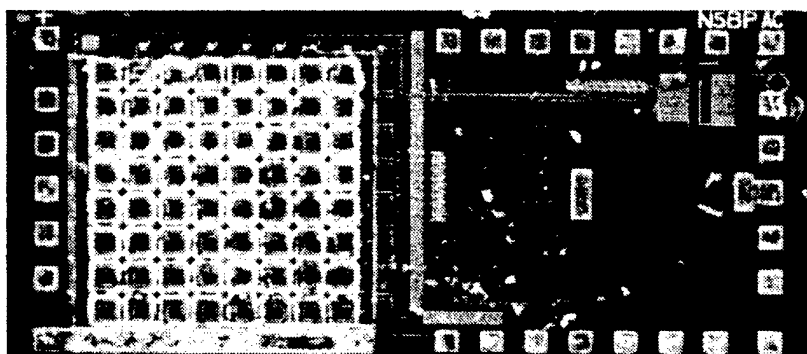


Figure 6. Chip with 8x8 ADCs, shift registers, and emitter driver.



**Figure 7. 8x8 ADC per pixel test results.**

Figure 8 is a photomicrograph of the the Si CMOS chip shown in Figure 6 which has been integrated with a thin film GaAs-based P-i-N detector array.

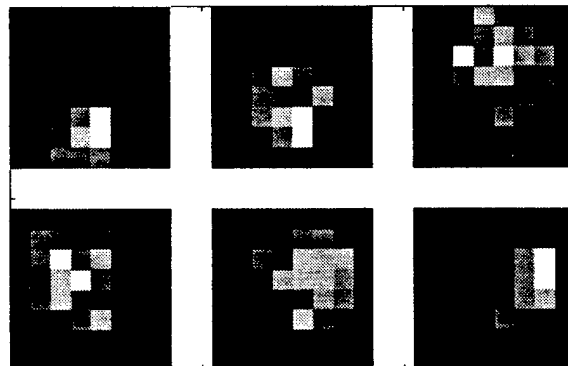


**Figure 8. Photomicrograph of hybrid integrated GaAs-based detectors directly on top of sigma delta ADCs to form integrated smart pixel imaging array.**

A test setup and test results from the Si circuit in Figure 5 are shown in Figure 9. A HeNe laser spot is imaged onto different portions of the detector array, and, as the laser spot moves as a function of time, the image shifts. This image capture scheme is operating at 970 bps.

The Si and GaAs-based imaging array smart pixel circuits have been fabricated and successfully tested, and the Si imaging array has been extensively tested. Each of the sigma delta ADCs is clocked at 15.6kHz, resulting in a frame rate of 976 fps. The output data is captured using a digital acquisition card in a Pentium-class computer. This test configuration, shown in Figure 9a, is the primary limitation of the measured frame rate.

Figure 9b shows the image data displayed on a video screen, which cannot display the measured frame rate. Simulated results indicate a frame rate capability in excess of 100 kfps. To measure this performance, a faster test facility is necessary. These imaging top chips are then stacked on top of the SIMPil digital signal processing chips in a 3D OEIC stack using a vertical optical through-Si communications link.



(a)

(b)

Figure 9. (a) Test setup; (b) test results.

### 3. The SIMD Pixel Processor (SIMPil)

#### 3.1 Processor Architecture

The digital component of the SIMD Pixel Processor (SIMPil) system designed at Georgia Tech consists of an array of SIMD (single instruction stream, multiple data streams) processors. Figure 10 illustrates a block diagram of one SIMPil node.

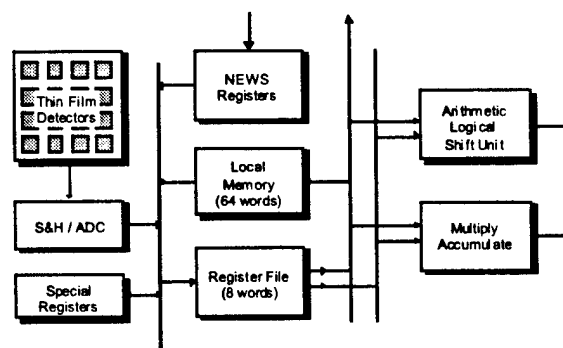
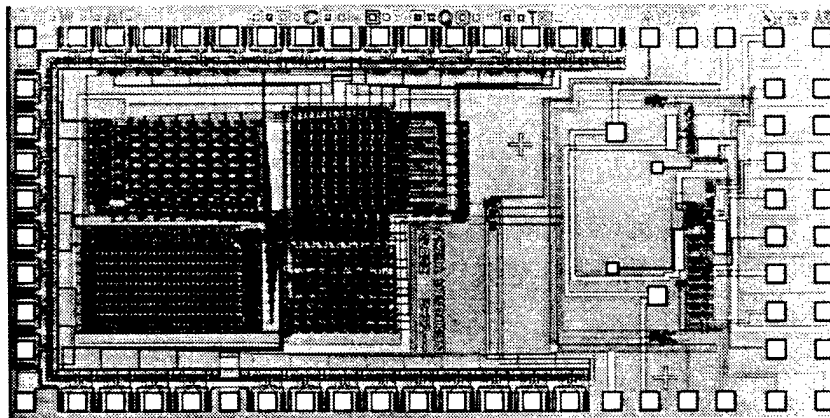


Figure 10: Block diagram of a SIMD Pixel Processor node

The node includes a traditional processor datapath plus additional units for interfacing with the thin film detector array. The first implementation of the node includes an 8 bit datapath with an arithmetical, logical, shift unit, and a 16 bit multiply-accumulator (MACC) used in many image processing applications. These functional units access an eight word register file. Each node has 64 words of local memory. (Up to 256 words can be addressed in the instruction set.) SIMPil nodes communicate through a nearest neighbor NEWS (north, east, west, and south) network using special registers in the datapath.

Each SIMPil node interfaces to a sub-array of thin film detectors in the focal plane array. In the current SIMPil implementation, a processor addresses 16 detectors. Future SIMPil node implementations can address up to 256 detectors. Each processor includes circuitry to convert light intensities at the detectors into digital values for processing. The instruction set architecture provides a SAMPLE instruction to synchronously capture light intensities at each detector of the focal plane array. The SIMD execution model allows the entire image to be sampled synchronously. Once the detector array data has been digitized, it can be processed on the SIMD nodes in a data parallel fashion. The first prototype of the SIMPil system consists of a single SIMPil node. This prototype node includes five main elements: register file, ALU, barrel shifter, multiply-accumulator, and local memory.

The Si chips shown in Figures 5 and 8 sit above the SIMPil processor chip, with a 3D vertical optical through-Si communications link connecting the two Si CMOS circuits. The bottom chip, which contains the SIMPil processor and the receiver is shown in Figure 11.



**Figure 11. Photomicrograph of the SIMPil node and receiver amplifier.**

## 3.2 Early Power Estimation Overview

Early consideration of processor power dissipation during the design process is becoming paramount with the prevalence of portable computing systems and increasing power densities [7]. Highly integrated systems based on SIMPil will be compact and lightweight while providing high resolutions and frame rates. This dense, high-performing system can dissipate large amounts of power resulting in a short battery life and high power densities requiring expensive packaging. However, low power opportunities which we explore now and in the future should allow continuous operation with low-cost heat removal techniques.

In the following section, the power dissipation of the prototype SIMPil node is estimated and divided among the major functional units. The area and energy efficiency of this special-purpose image processing architecture is evaluated and compared to general purpose processors targeting low power operation. Future systems using current and state-of-the-art technologies are evaluated. The opportunity of using massive parallelism for scaleable image processing applications is then investigated. The analysis concerns only the digital processing layer of the SIMPil node.

### 3.2.1 Power Estimation Method and SIMPil Results

The prototype SIMPil node was divided into components including the multiply accumulate unit, the barrel shifter, the ALU and register file, the on-chip memory, and the signal pads. Switched capacitance for each of these components was estimated using IRSIM-CAP, a switch level simulator with enhanced capacitance measurements. The total capacitance for each unit and the entire chip are presented in Table 1.

Component	Total capacitance
ALU	6.0 pF
Register File	23.1 pF
Barrel shifter <sup>1</sup>	27.9 pF
Memory <sup>1</sup>	37.1 pF
MACC <sup>1</sup>	45.9 pF
Pad frame	114.5 pF
Entire chip	230.9 pF

**Table 1: Total nodal capacitance of each component and the entire SIMPil prototype.**

To estimate the power for each individual unit, a Monte Carlo approach [8] was used to generate the input signals to each combinational logic unit. This probabilistic method allowed the average power of each unit to be known within 5% at a 99% confidence level with short simulation times. The memory power dissipation was more appropriately

<sup>1</sup> Each estimate redundantly includes the data buses shared by all functional units.

estimated using the circuit simulator H-SPICE. The average power of a processor is the important metric when considering battery lifetime and power density. Actual power estimates are based on a 5V power supply and a clock frequency of 50 MHz (Table 2). The global data and address busses are not gated to each functional unit. Therefore, the entire chip power is estimated as the sum of the components. This estimate is probably high because the internal bit lines of the local memory are isolated from switching when the memory is not enabled, and some functional unit estimates include switching of redundant buses. Additionally, the MACC and MUL instructions are multi-cycle which reduces power dissipation.

Functional Unit	Estimated Power Dissipation
MACC	20.5 mW
Barrel shifter	6.5 mW
Memory	~80.0 mW
ALU/ register file	12.2 mW
Total	~120.0 mW

**Table 2: Average power dissipation of each functional unit and a total chip power estimate.**

The above estimates are for a single SIMPil node. In a large system with multiple multi-node chips, the power for NEWS communication across chip boundaries must be estimated. We will assume that the global SIMD control is external to the system, but its amortized contribution to system power will be estimated in the future. The NEWS communication registers are the only signals to be driven "off-chip" during normal operation. H-SPICE was used to simulate the power to drive an 0.8  $\mu\text{m}$  output pad through a 64-pin PGA to a receiving pad on a second die. This power was found to be about 10.3 mW. If we assume that the nearest-neighbor communication is single cycle and that 10% of instructions are NEWS, the additional power of a boundary node transmitting an eight-bit NEWS register is 8.24mW. The additional power per system is:

$$\# \text{ Die} \leftrightarrow \sqrt{\text{NodesPerDie}} \leftarrow 8.24 \text{ mW}$$

Better estimates of total power could possibly be made by running a specific algorithm and considering the correlation between successive data samples of an image. These estimates will aid in future efforts to reduce node power. The total internal, digital chip power is about 120mW.

### 3.2.2 SIMPil Node Efficiency

SIMPil is evaluated in terms of area and energy efficiency by considering million operations per joule (Mop/Joule) and million operations per second per area (Mop/s·mm<sup>2</sup>). As a benchmark for comparison we have evaluated these metrics for two

32-bit low-power processors -- the PowerPC 603e [9] and DEC/ARM SA-1 [10] (Table 3). We consider fixed point performance only.

This comparison is of course not totally equivalent because the 603e devotes a large area to floating point operations and both are 32 bit machines containing large caches. However, these are requirements of such general purpose processors. SIMPil is a small, special-purpose processor for image processing applications and algorithms that map well to a SIMD architecture. The data path is only 8 bits for moderate intensity resolution. Therefore, we expect it to be very efficient for the set of applications it targets. Both of these commercial processors are fabricated in state-of-the-art 0.35  $\mu\text{m}$  processes. Using generalized scaling theory [11], we have projected the performance, area, and power of a SIMPil node fabricated with 0.35  $\mu\text{m}$  and 3.3 Volt technology. The power of a single node decreases to a value of 81.8 mW, mostly because of the reduction in supply voltage.

Process or	Power	Area	Clock freq.	Mop/ Joule	Mop/ s·m <sup>2</sup>
PPC 603e (0.35 $\mu\text{m}$ )	2.5 W	81 mm <sup>2</sup>	166 MHz	66	2.0
SA-1 (0.35 $\mu\text{m}$ )	120 mW	4.3 mm <sup>2</sup>	160 MHz	400	11.2
SIMPil (0.8 $\mu\text{m}$ )	120 mW	2.0 mm <sup>2</sup>	50 MHz	280	16.8
SIMPil (0.35 $\mu\text{m}$ )	81.8 mW	0.3 mm <sup>2</sup>	176 MHz	1442	310.

**Table 3: Power and area efficiency metrics for two low-power general purpose processors and SIMPil.**

These results assume an effective throughput of 0.67 instructions per cycle for SIMPil. These numbers express the efficiency of a simple architecture for a target set of applications. The energy efficiency of SIMPil would be even higher when voltage is scaled to 2.5 or 2.0 volts as in the PowerPC 603e and SA-1, respectively.

### 3.3 SIMPil Systems -- Current and Future

We envision SIMPil systems supporting high frame rates of 100 to 1000 frames/sec. Assuming that advanced image processing algorithms may require as much as 200 SIMPil operations per pixel per frame and that SIMPil has an effective throughput of about 0.67

instructions per cycle, we can find the maximum frame rate supported by current and future systems. The single node prototype currently being implemented includes a 8x8 detector array and a 50 MHz clock frequency can sustain a rate of 2616 frames/sec.

To evaluate the power dissipation and the system's suitability for mobile systems, we consider a 16x16 node 0.8  $\mu\text{m}$  system and a 64x64 node 0.35  $\mu\text{m}$  system (Table 4). These highly parallel systems are small enough to fit on four die, but the power dissipation, power density, and battery life are unacceptable. Battery life is projected based on a 27 W•h, one pound Ni-Cd battery [12].

SIMPil System	Size	Power	Power Density	Battery Life
16x16 (0.8 $\mu\text{m}$ )	512 mm <sup>2</sup> (4 chips 1.1 cm)	31 W	6.1 W/cm <sup>2</sup>	0.87 h
64x64 (0.35 $\mu\text{m}$ )	1556 mm <sup>2</sup> (4 chips 2.0 cm)	336 W	21.6 W/cm <sup>2</sup>	0.08 h

**Table 4: Possible future SIMPil systems**

Immediate savings in power can be realized through architectural driven voltage scaling [13]. SIMPil systems will run continuous applications that have a fixed throughput in terms of frames/seconds and in the number of operations per pixel, for the prescribed system resolution. Therefore, the clock frequency can be scaled down to match the fixed throughput. Furthermore, since the performance requirement of individual gates has been relaxed, the supply voltage can be reduced at the expense of speed.

We will take the upperbound on node performance for a certain resolution and 8x8 detectors per node to be 12.8 Mop/s. The 0.35  $\mu\text{m}$  node will exceed this rate by a factor of 9.2, allowing clock frequency reduction to 20 MHz. For a 0.35  $\mu\text{m}$  channel length, the voltage at which MOSFETs become velocity saturated is about 2.85V. The voltage can be scaled down to 1.2V and still maintain the 20 MHz clock frequency. The 64x64 node system would then dissipate only 5.1 W with a battery life of 5.3 hours and a power density of 0.33 W/cm<sup>2</sup>. Through this technique, power density can be significantly reduced but 24 hour operation is still a future goal. This extreme power reduction can be attributed to the scaling of image processing applications on this special purpose parallel machine. Further improvements in the energy efficiency of SIMPil and its communication should lead to reductions in power.

### 3.4 Massive Parallelism for Low Power

For a particular image resolution, there is a hard limit on the useful parallelism at one detector per node. More practical limits may happen earlier when node communication



dominates or area mismatch occurs between the nodes and detector array. Increasing the number of nodes will increase the number of chips increasing the number of boundary crossings. Timely distribution of instructions will also become harder, but this is somewhat mitigated by lower required clock frequencies. Having multiple pixels per node allows communication between pixels to occur through local memory and registers. If NEWS communication off-chip, which replaces memory loads, can occur in one cycle then the parallel overhead is negligible.

SIMPil nodes	Detectors per node	Number of Dies	Required performance per node
16x16	32x32	4	205.0 Mop/s
32x32	16x16	4	51.2 Mop/s
64x64	8x8	4	12.8 Mop/s
128x128 8	4x4	16	3.2 Mop/s
256x256 6	2x2	64	0.8 Mop/s

**Table 5: Performance requirement of node and system size as parallelism is increased for a fixed throughput application.**

Fixing the resolution at 512x512, the tradeoff of parallelism versus power dissipation can be investigated for a fixed throughput application. We must precisely define the overheads associated with increasing the number of processors. First, as the number of die increases there are more die crossings resulting in more power devoted to communication. However, this power also scales with frequency and supply voltage. Since this is a SIMD machine targeted towards specific applications, the overheads are not as high as a general purpose machine. The size of the first two systems presented in Table 5 are limited by the detector size as opposed to the SIMPil nodes.

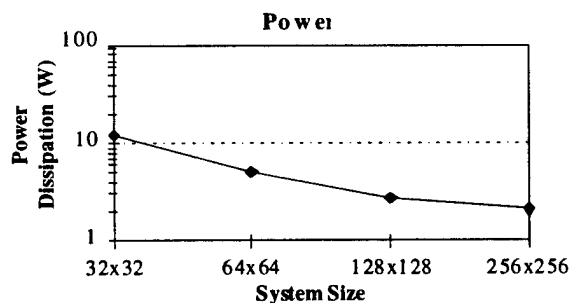


**Figure 12: Power dissipation as parallelism is increased for a fixed resolution and throughput.**

The first system cannot be realized at 0.35  $\mu\text{m}$  because the maximum performance of a node is only 118 Mop/s at 176 MHz. The power dissipation of the other four systems

after calculating the minimum clock frequency and supply voltage for the given performance is shown in Figure 12. From this figure and Table 5, it is clear that we are trading off system cost and size for power. We are sacrificing area efficiency (Mop/s-mm<sup>2</sup>) for gains in energy efficiency (Mop/J).

The power budget of a prototype SIMPil node has been estimated which will be valuable in future multi-node designs and implementations. This budget shows that an applications-dedicated smart camera system can be efficient in both area and power. For a fixed resolution, an upperbound on system throughput can be leveraged to save power through frequency and voltage scaling. Area efficiency can be sacrificed for lower power dissipation by increasing parallelism. Control overhead in a SIMD system grows slowly with this increase in number of nodes allowing lower and lower dissipation. The SIMPil system enabled by optoelectronic devices should be able to achieve high frame rates at reasonable resolution while maintaining lightweight and low power requirements.

#### **4. Thin Film Optoelectronic Device Integration**

To integrate the detector imaging array onto the silicon circuitry, and the emitter and detector for the through-Si vertical optical link, hybrid integration has been used. Hybrid integration, or the bonding of separately grown compound semiconductor devices on top of silicon circuitry, is an attractive option for the integration of the detector array and the through-substrate emitter and detector devices [14]. The optoelectronic materials are fabricated separately from the electronics, and multiple types of materials and devices can be integrated onto the same circuit.

##### **4.1 Thin Film Detector Array Integration**

To integrate the detector imaging array onto the silicon circuitry there are several options which can be explored. The detectors can be fabricated using monomaterial (single material) integration in the silicon CMOS, however, to achieve high fill factors and scaleable arrays the processing circuitry associated with each pixel must be minimized. An additional drawback to silicon detectors realized on a CMOS circuit process is the low absorption coefficient. The low absorption coefficient translates to low responsivity since the absorption length achievable in CMOS processes is small.

Hybrid integration, or the bonding of a separately grown detector array on top of the silicon circuitry, is an attractive option for the integration of the detector array. These integration techniques include the bump bonding of arrays of detectors onto pads on the silicon circuit, which is currently a commonly used technique for fabricating infrared focal plane arrays [15], and, alternatively, thin film integration can be utilized, which is similar to bump bonding, save that the detector devices and bonds are very thin in comparison to bump bonds [15].

Hybrid integration is an attractive alternative to monomaterial integration for two reasons. First, the material which comprises the detector array is fabricated separately from the electronics. Because of this fact, the detectors need not be the same material as the electronics (Si), which enables the use of higher responsivity materials such as direct gap compound semiconductors. This also implies that the detector materials do not have to be lattice matched to the circuitry materials (for example, direct growth onto the silicon circuitry). The second advantage of hybrid integration is that the detectors are integrated directly on top of the silicon circuitry, which enables scalability with high fill factors and the direct interconnection of every detector to circuitry which lies beneath it. One disadvantage of using flip chip bonding for hybrid integration of detector arrays is that the substrate must be transparent. Thin film bonded detector arrays do not suffer from this limitation since the substrate is removed from the devices.

There are two basic types of detectors which can be integrated with the silicon circuits: P-i-N and MSM (metal-semiconductor-metal) detectors. While MSM detectors are a viable option for integration since they are high speed, low capacitance detectors [16], they have a lower responsivity than the P-i-N detector and their geometry does not lend itself as well as the P-i-N to array integration. The MSM is a planar device which has two bonding pads in the same plane (the interdigitated fingers of the MSM). To achieve individually addressable pixels using MSMs, the spacing of the devices has to be large enough to allow space for the contact pads, thus decreasing the fill factor.

The integration method used with the P-i-N results in a higher fill factor than that of the MSM. This increased fill factor comes from exploiting the non-planarity of the P-i-N structure. The P-i-N device contacts are on the top and bottom of the structure; this is useful in terms of the integration because the pixels can be individually addressed through the device side bonded to the silicon circuit and share a common top contact, eliminating the pad space between detectors. For example, to electrically connect an  $N \times N$  array of P-i-N detectors only  $N^2 + 1$  dedicated pads on the silicon circuit are necessary, with  $N^2$  pads located underneath the detector array.

Examples of hybrid integration of compound semiconductor detectors onto silicon circuits include GaAs MSMs [16], which detect at 850nm, and InP/InGaAs/InAlAs MSMs [16], which detect at 1.3 and 1.55 micron wavelengths.

Thus, for the imaging array, GaAs-based detectors have been integrated onto the Si ADCs, and InP-based devices were bonded to the through-Si emitter and detector sites (these devices operate at wavelengths to which the Si is transparent). Figure 12a is a photomicrograph of an unbonded Si circuit as received from the MOSIS foundry. Figure 12b is a photomicrograph of the GaAs thin film detector array bonded onto the top of the circuitry, and Figure 12c shows the final integrated optoelectronic circuit, with the common top contact deposited onto the detector array, connecting the array to the silicon

circuit [17]. Each detector is individually interconnected to the silicon circuitry which lies beneath it through a metallized overglass cut on the circuit. Figure 8, shown previously, is a photomicrograph of a GaAs-based detector array bonded on top of sigma delta ADCs.

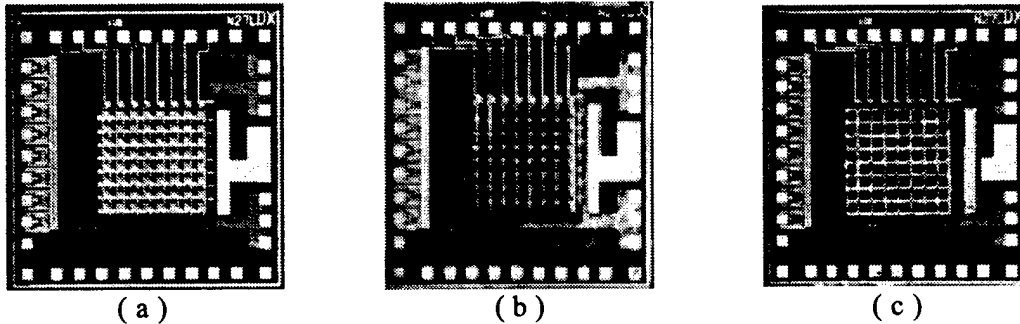


Figure 12. Photomicrographs: (a) the unintegrated Si circuit; (b) the Si circuit with a bonded thin-film array; (c) the integrated array with a common top contact.

## 4.2 Three Dimensional Through-Si Vertical Optical Interconnection

### 4.2.1 Optoelectronic Device Structures

The materials required for the through-Si vertical optical interconnection demonstration were comprised of light emitting diode (LED) and detector material operating at wavelengths longer than  $1.1 \mu\text{m}$  (corresponding to the bandgap of Si: Si is transparent to these wavelengths). The InGaAs/InAlAs detector material used was provided by the Army Research Labs (ARL, by Dr. Richard Leavitt) for inverted metal-semiconductor-metal detectors. A number of emitter materials were investigated, including InGaAsP low doped emission region material grown by EPI, Inc. and by Dr. A. Brown at Georgia Tech.

The ARL emitter structure with a highly doped emission region (ARL 602) is shown schematically in Figure 13.

In <sub>0.53</sub> Ga <sub>0.47</sub> As	p+= $1 \cdot 10^{19}$	100 Å
In <sub>0.52</sub> Al <sub>0.48</sub> As	p= $3 \cdot 10^{18}$	0.986 $\mu\text{m}$
In <sub>0.53</sub> Ga <sub>0.47</sub> As	p+= $1.2 \cdot 10^{19}$	0.45 $\mu\text{m}$
In <sub>0.52</sub> Al <sub>0.48</sub> As	n= $5 \cdot 10^{18}$	1.896 $\mu\text{m}$
In <sub>0.53</sub> Ga <sub>0.47</sub> As	n+= $1 \cdot 10^{19}$	1000 Å
n - InP substrate ARL602		

Figure 13. Layer Structure of ARL 602 Material.

The ARL602 emitter was designed for high speed by utilizing high doping in the active region. Based on information gathered from the published literature, a doping level of  $1.2 \times 10^{19} \text{ cm}^{-3}$  will produce 155 MHz operation. The resonant cavity enhancement effects were optimized by calculating the phase change throughout the device and optimizing for an integral number of wavelengths. To achieve enhancement of the spontaneous emission lifetime, it is desirable to align the active region with antinodes of the optical field intensity. This has been shown to provide up to a factor of 10 increase in the spontaneous emission lifetime. The index of refraction for the active region was found by linearly interpolating based on the binary indexes of refraction for the given design wavelength of  $1.3 \mu\text{m}$ .

A thorough investigation of the design tradeoffs for fabrication of high speed emitters revealed another avenue to explore. Our first design (ARL602) centered around a large device size for ease in alignment, a small injection current for low power consumption in the circuit and a highly doped active region for high speed operation of the LED's. However, high doping level in the active region causes a significant decrease in the optical conversion efficiency of these devices.

To achieve high speed operation with less doping in the active region (to achieve higher optical conversion efficiency for higher optical output power), we designed an LED that would be fabricated in a smaller size and that would have injection currents of up to 160 mA. By increasing the current density of the devices, the speed is also be increased with very little doping in the active region. The second device design was based on low doping in the active region. To obtain high output power we doped the active region to  $n = 2 \times 10^{17} \text{ cm}^{-3}$ . Literature reports that similar structures have been grown using liquid phase epitaxy (LPE) with no intentional doping to the active region. For LPE a background doping around  $n = 2 \times 10^{17} \text{ cm}^{-3}$  is typical for unintentionally doped InGaAsP. Finally, the active region was made  $1 \mu\text{m}$  thick to provide for a large volume of emissive material.

To achieve low resistivity contacts, gallium was included in the contact layers. To do this without causing absorption in these regions, we made contact layers at a wavelength shorter than the emission wavelength of  $\lambda = 1.3 \mu\text{m}$ . Since these regions were non absorbing they were not required to be extremely thin (in contrast to the InGaAs layers in the ARL602 material). The fact that these layers were thick made less impact on the substrate removal, which caused difficulty in the processing of the ARL 602 material. The final growth structure is shown below in Figure 14.

InGaAsP	$p+ = 3E+18 \text{ cm}^{-3}$	2000 Å $\lambda = 1.2 \mu m$
InP	$p = 2E+17 \text{ cm}^{-3}$	1.0 $\mu m$
InGaAsP	$n = 2E+17 \text{ cm}^{-3}$	1.0 $\mu m$ $\lambda = 1.3 \mu m$
InP	$n = 2E+17 \text{ cm}^{-3}$	1.0 $\mu m$
InGaAsP	$n+ = 1E+19 \text{ cm}^{-3}$	2000 Å $\lambda = 1.2 \mu m$
InP	$n = 3-8E+18 \text{ cm}^{-3}$	0.5 $\mu m$
N type ( $3-8e+18 \text{ cm}^{-3}$ ) InP Substrate		

Figure 14. Layer structure of EPI-132 material.

## 4.2.2 Thin Film Devices, Processing And Integration

### 4.2.2.1 Detectors

In order to match the specifications of the through-Si data link, a low capacitance per unit area, high responsivity, low noise photodetector was designed. A MSM meets all of these requirements save the responsivity, (which is poor, generally 0.2 to 0.4 A/W ) and the dark current, (which is relatively large in the InP material system [16]). The inverted metal-semiconductor-metal-semiconductor photodetector (I-MSM), with the electrodes defined on the bottom of the device, eliminates the shadowing effect of the electrodes, producing high responsivity. An InAlAs cladding layer minimizes the dark current thus yielding a low capacitance, large area detector for low noise, high speed, alignment tolerant integrated receiver operation. The cladding layer eliminates low frequency gain, and enhances the Schottky barrier height. The heterointerfaces were graded to ensure better carrier transport as well as improved dark current characteristics.

To create the I-MSMs, fingers of Ti/Pt/Au 2  $\mu m$  wide separated by 8  $\mu m$  were defined on the 250  $\mu m$  diameter MSMs, followed by a citric:H<sub>2</sub>O<sub>2</sub> (10:1) mesa etch (which included contact strips next to the square mesa) down to the InGaAs stop etch layer. To complete the fabrication of the I-MSMs, Au/In/Au (50/500/10 nm) was evaporated onto the contact strip to provide a high quality bond to the host substrate. The devices were then tested so that only operational MSMs were processed further. The I-MSM mesas were then covered with Apiezon W wax and were immersed in HCl, which selectively removed the InP growth substrate, stopping on the InGaAs stop etch layer. To avoid any defects within the epilayers of interest induced by the substrate removal, the whole structure was left in the HCl solution no more than 40 min. and was constantly monitored for InGaAs

surface defects. The InGaAs etch stop layer was subsequently removed using a citric:H<sub>2</sub>O<sub>2</sub> (1:1) selective etch. The I-MSMs were bonded to a Mylar transfer diaphragm [14], and the waxhandling layer was removed with TCE. At this point, the I-MSM fingers and the short contact strips on each side were facing away from the diaphragm. They were then aligned with respect to the Ti/Au pads defined onto silicon nitride coated silicon for single device characterization, or bonded onto circuits.

First, the I-MSMs were tested for dark current using a high sensitivity electrometer. The dark current plays an important role in the characteristics of the integrated receiver since only the low domain of the frequency spectrum will be used (1 MHz to 155 MHz) and the input signal will be in the order of 1  $\mu$ A. In order to minimize the dark current, different metal layer configurations (Ti(150 Å)//Au (2500 Å) and Ti(150 Å)//Pt(500 Å)//Au(2500 Å)) and heat treatments were studied to improve the photodetector reliability as a function of time. After metal deposition and integration the dark current was measured on the order of 1  $\mu$ A, with no difference found between the two metal layer configurations. A heat treatment was applied to the I-MSMs with various amounts of time for temperature ranging from 100 C to 300 C. The best results were obtained for a temperature of 240 C with Ti/Pt/Au electrodes, as shown in Figure 15. Higher temperatures would lower the Schottky barrier, resulting in higher dark current. The Pt layer within the contact acts as a barrier for Au diffusion toward the semiconductor that can occur with long annealing times (14 h), creating an alloy with the InAlAs material system. Similar tests with abrupt heterojunction MSMs produced higher dark currents than with the digitally graded structure.

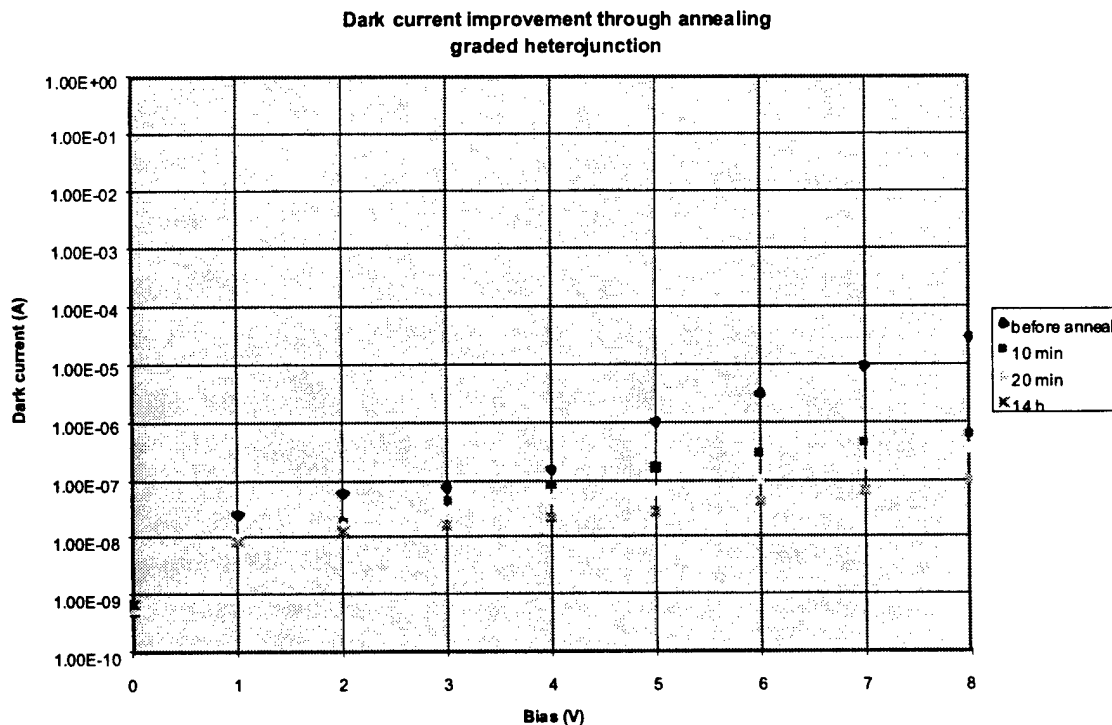


**Figure 15. Dark current as a function of bias for the I-MSM.**

The static capacitance was measured to be 200 fF for a  $250 \times 250 \mu\text{m}^2$  area with  $2 \mu\text{m}$  fingers width and  $8 \mu\text{m}$  fingers spacing, which match well with the theory and the circuit specifications. The measured responsivity was 0.6 A/W at 5 V and remained constant for higher applied bias. The responsivity was limited by the thickness of the absorbing layer ( $0.8 \mu\text{m}$ ) (this graded structure was previously designed for RF applications). Since the dark current was the characteristic of more concern we used the graded structure for its reduced dark current.

The I-MSM transient response was also measured. To examine the broad-band impulse response, the bias tee had a low frequency cut-off of 100 kHz, thus insuring that no slow response components were filtered from the output signal. In addition, the impulse response shape was highly dependent on the alignment of the single mode fiber onto the MSM. Long tails have been observed which are primarily due to RC time constant limitations. The typical transient response of the I-MSMs are shown in Figure 16. We measured a typical rise time of 45 ps, a fall time of 320 ps and a FWHM of 100 ps. In the frequency domain the deconvolution of the pulse for the system response gave a 3 dB frequency cut-off of about 1.1 GHz, which gave us sufficient speed for the system specification.

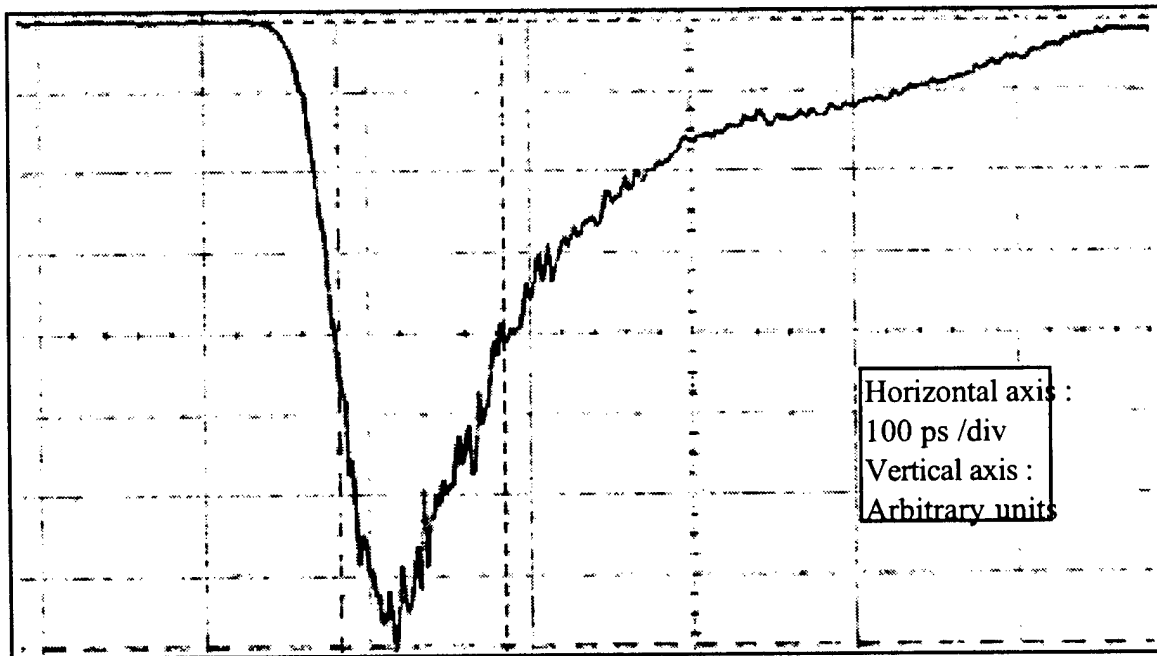


Figure 16. Typical transient response of I-MSM.



#### 4.2.2.2 Resonant Cavity Enhanced Thin Film Emitters

Processing of the InP/InGaAsP/InP-based EPI materials has been well established (historically better than that of the InGaAlAs-based ARL 602 materials), and the etches used for the substrate removal process are more selective than in the InGaAlAs materials system. The etches used included 3:1 HCl:H<sub>3</sub>PO<sub>4</sub> for etching of the InP regions, including the substrate, and 1:1:1 H<sub>2</sub>SO<sub>4</sub>:H<sub>2</sub>O<sub>2</sub>:H<sub>2</sub>O for the InGaAsP layers. These etches are very selective and will stop quickly as a function of composition. Etch rates were found to be approximately 3 μm/min. for InP etching using the 3:1 etch and 0.5 μm/min. for etching of the InGaAsP regions using the 1:1:1 etch.

The thin film LEDs were created using standard etching and microelectronics processing techniques. First, the material was metallized using a AuZn alloy for good contact properties to p-doped InGaAsP materials. The metal was then pixellated into an array of squares and the devices were annealed and then mesa etched through the bottom InGaAsP layer. The devices were then removed from the substrate by etching in the 3:1 HCl-based etch for approximately 45 minutes. The first 2000 Å thick InGaAsP contact layer was a good stop etch layer and exhibited very few defects. This enabled a one step etching process for removal of the substrate. After substrate removal, the processing was similar to all other thin film devices; the devices were encapsulated in black wax, adhered to a transparent transfer diaphragm and the black wax was removed.

Next, individual devices were transferred to Ti/Au bottom contact pads on SiO<sub>2</sub> coated silicon for individual device characterization or onto circuits for integrated characterization. The devices were then planarized and the top and bottom contacts isolated from each other using Dupont Polyimide 2611. This polyimide was then cured for 1 hour at 350°C. Next, aluminum masks were evaporated and patterned to allow oxygen plasma reactive ion etching to open a window in the top of the devices for deposition of the AuGe-based top contact metal, which also had a window subsequently opened to enable surface emission.

The thin film devices fabricated from the EPI material have excellent characteristics. A typical I-V curve has a turn-on voltage of 1.0 V and a series resistance of 15 Ω; these devices have vastly improved contacts compared to the ARL devices (easily explained given the n side contact material contains gallium). Another characteristic that is vastly improved for these devices is the light output. A calibrated L-I is shown in Figure 17. The output power available at injection currents which are consistent with the current transmitter circuit designs (80 mA) is over 8 times better than the ARL materials.

**LI Plot for EPI-132 100 $\mu$ m Devices as a  
Function of Injected Current**

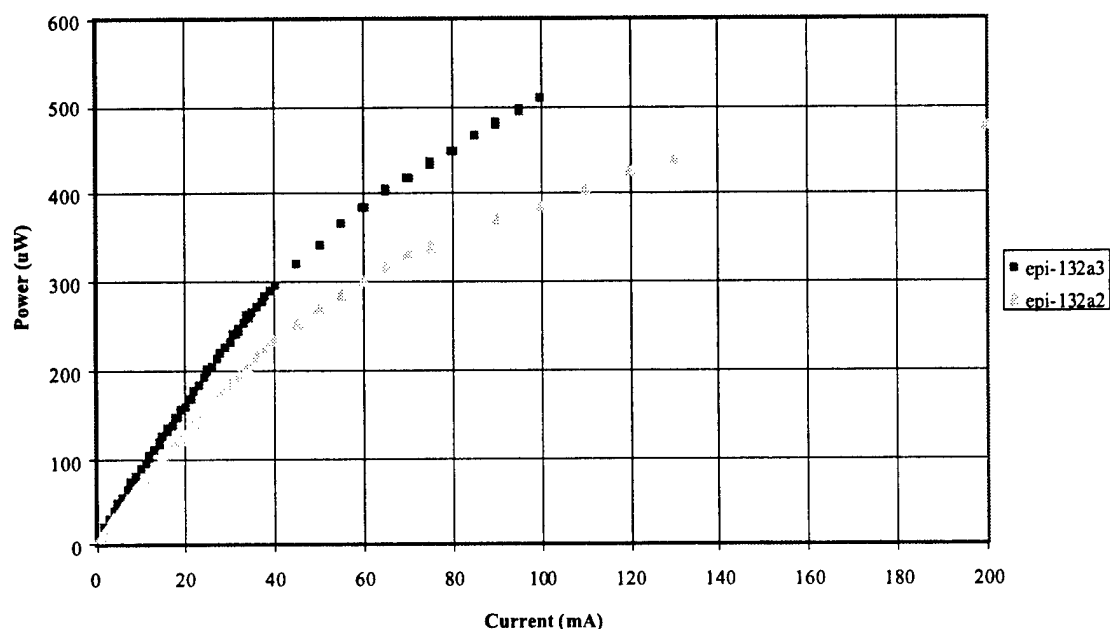


**Figure 17. Typical light output for EPI-132 100  $\mu$ m square devices.**

The other characteristic that is important to our through-Si demonstration is the spectrum of these devices. To take advantage of low loss in silicon, wavelengths greater than  $\lambda=1.1 \mu\text{m}$  must be used. These devices were designed to have an active region in the  $\lambda=1.3 \mu\text{m}$  wavelength region. As shown in Figure 18, these devices exhibit emission beyond  $\lambda=1.1 \mu\text{m}$ . It is interesting to see the two modes exhibited in the output spectrum of these devices. By using the resonant cavity model, it is possible to tune the cavity of these devices by adjusting the thickness of a top metal mirror that can be deposited after all other processing has been finished. The added top mirror would increase spectral purity, and, with an increase in mirror finesse, decrease the divergence angle, producing more directed output power. Although this would increase our need for good alignment, it could also decrease the required size of the detector (reducing the detector capacitance) and hence increase the speed of the receiver.

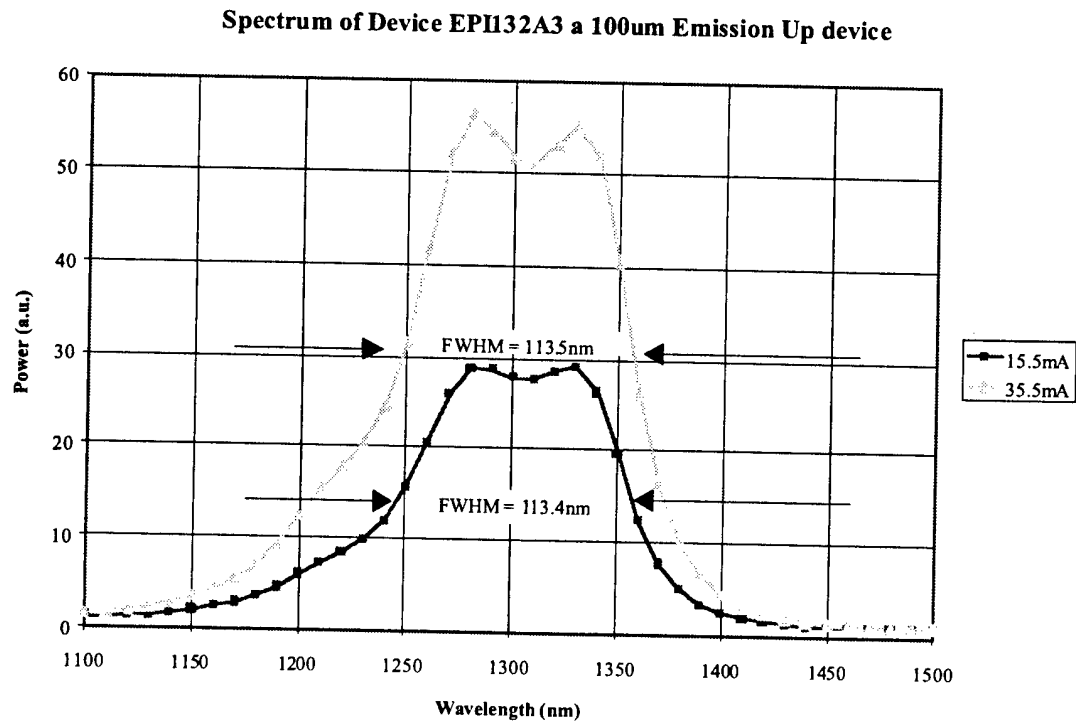


**Figure 18. Typical spectrum for a single EPI-132 device.**

For the smart camera to operate in a scalable fashion, through-Si optical link is critical. This has been an area of active research interest by a number of groups [18, 19, 20, 21, 22]. Related work by the authors has demonstrated numerous optical interconnection through stacked silicon foundry CMOS circuitry [23, 24], including one demonstration at a data rate of over 40 Mb/s with an open eye diagram. The system consists of a 0.8  $\mu$ m transmitter and receiver realized in foundry digital CMOS. Two layers of these circuits were integrated with thin film InP-based light emitting diodes and metal-semiconductor-metal photodetectors operating at 1.3  $\mu$ m (to which the silicon is transparent) to enable vertical optical through-Si communication between the stacked silicon circuits. Each silicon integrated circuit layer consisted of one optical transmitter and one optical receiver. These circuits were fabricated in 0.8  $\mu$ m standard silicon CMOS provided through the MOSIS foundry. The through-silicon wafer demonstration was performed using two of these chips, stacked to enable optical communication between the transmitter and receiver. These emitters, detectors, and interface circuits were the same that were integrated onto the smart camera Si CMOS circuits.

The smart camera optical receiver is comprised of a choice of two front-end amplifiers each directly connected to a on-chip comparator. One amplifier is a single ended, and the other a differential transimpedance amplifier. both designed so that the

output could drive an on-chip comparator to convert the analog amplifier output to a digital signal. Thus, the peak to peak output of the amplifiers must be 20 - 50 mV to drive the comparator, which converts to a 12 k $\Omega$  total transimpedance gain with a 50  $\Omega$  load, assuming an input power of -23 dBm (SONET OC3 specifications). For wide bandwidth, the single ended amplifier used a multi-stage, low-gain-per-stage configuration [25]. This amplifier was optimized for minimum power dissipation at a rate of 155 Mb/s with -23 dBm, leading to an open-loop, current-mode configuration. The thin film InP-based inverted metal-semiconductor-metal photodetectors (I-MSMs) were bonded onto the amplifier input pads. The fully integrated SIMPil bottom OEIC, with inverted MSM, is shown in Figure 19.

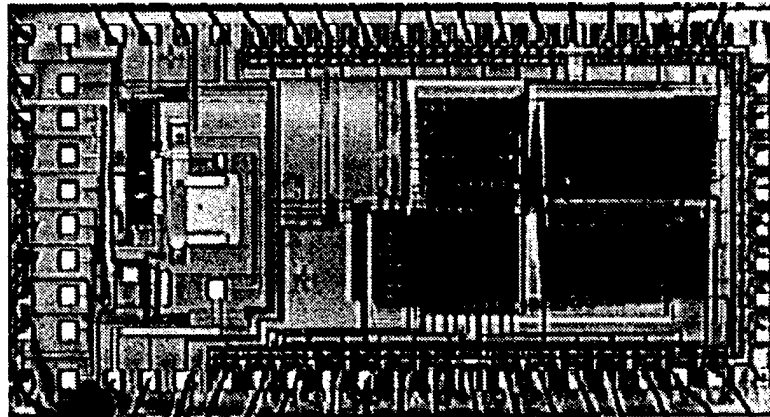


Figure 19. Fully integrated SIMPil microprocessor with InP-based inverted MSM.

The digital CMOS transmitter circuits were designed and optimized to provide up to 80 mA of output current to the light emitting diodes. Digital level input to this driver circuit was enabled by a 2-stage tapered buffer input designed to minimize power consumption at high speeds. The LED structures were pixellated (100  $\mu\text{m}$  on a side squares), the substrate was removed, and the devices were bonded onto the post-metallized circuit. Further post processing isolated and defined the top contact. The fully integrated bottom chip was then wire bonded into a 144 pin pin grid array package. The fully integrated top chip, which contains the InP-based emitter and the detector array, was then bonded onto the bottom SIMPil OEIC, as shown in Figure 20.

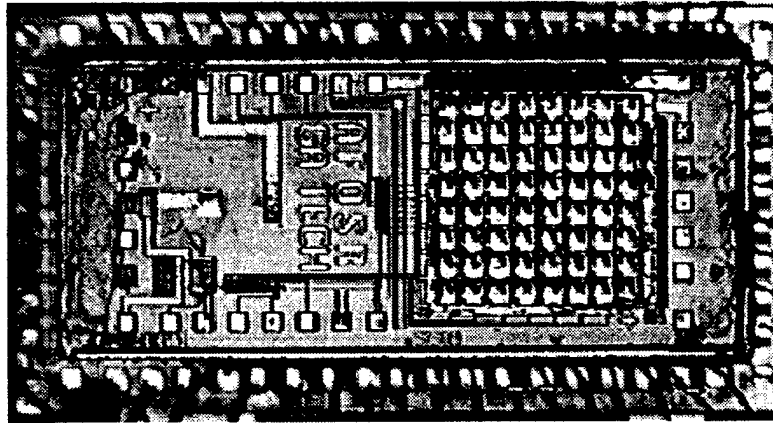


Figure 20. Stacked smart camera OEICs.

Currently, individual integrated top and bottom OEIC chips are under test, as is the stacked smart camera chip set. Preliminary results indicate that the optoelectronic portions of these chips are functional, and electrical tests indicate that the electrical portions are functional. However, noise in the receiver associated with the digital operation of the SIMPil circuitry must be addressed before full system operation can be achieved.

## 5. REFERENCES

- [1] B. Pain, E. Fossum, "Approaches and analysis for on-focal-plane analog-to-digital conversion," *Proceedings of SPIE*, v 2226, 1994, pp. 208-218.
- [2] H. Cat, J. Eble, D. Wills, V. De, M. Brooke, N. Jokerst, "Low Power Opportunities for a SIMD VLSI Architecture Incorporating Integrated Optoelectronic Devices," *GOMAC'96*, pp. 59-62, FL, Mar. 1996;  
S. D. Wills, S. W. Lacy, C. Camperi-Ginestet, B. Buchanan, H. Cat, S. Wilkinson, M. Lee, N. M. Jokerst, M. A. Brooke, "A three-dimensional high-throughput architecture using through-wafer optical interconnect" *IEEE Journ. of Light. Technol.*, no. 13 vol. 6, pp. 1085-1092, 1995;  
D. S. Wills "Smart pixel architectures for image processing", *Digest 1996 IEEE LEOS Summer Topical Meeting on Smart Pixels*, pp 93-94;  
Huy H. Cat, D. Scott Wills, Nan Marie Jokerst, Martin A. Brooke, April S. Brown, "Three-dimensional, massively parallel, optically interconnected silicon computational hardware and architectures for high-speed IR scene generation," *Proceedings of SPIE - The International Society for Optical Engineering*, v 2469, pp. 141-145, 1995;  
YoungJoong Joo, S., Fike, Kee Shik Chung, Martin A. , Brooke, Nan M. Jokerst, Scott Wills, " Application of Massively Parallel Processors to Real Time Processing of High Speed Images," *MPPOI*, pp.96-100, 1997;  
Huy H. Cat, Antonio Gentile, John C. EbleMyunghee Lee, Olivier Vendier, Young Joong Joo, Scott D. Wills, Martin Brooke, Nan Marie Jokerst, and April S. Brown, "SIMPil: An OE Integrated SIMD Architecture for Focal Plane Processing Applications," *MPPOI*, pp. 44-52, Oct. 1996.
- [3] Ulf Ringh, Christer Jansson, Kevin Liddiard, " Readout concept employing a novel on chip 16bit ADC for smart IR focal plane arrays," *Proceedings of SPIE - The International Society for Optical Engineering*, v 2745, pp.99-110, 1996.
- [4] Zhimin Zhou, Bedabrata Panigrahi, Barmak Nakamura Roger Mansoorian, Eric R. Junichi Fossum, "On-focal-plane ADC: recent progress at JPL," *Proceedings of SPIE - The International Society for Optical Engineering*, v 2745, pp. 111-122, 1996.

- 
- [5] J. C. Candy, G. C. Temes, "Oversampling methods for data conversion," *Proc 91 IEEE Pacific Rim Conf Commun Comput Signal Process*, pp. 498-502, 1991.
  - [6] J. C. Candy, G. C. Temes, "A tutorial discussion of the oversampling method for A/D and D/A conversion," *Proceedings - IEEE International Symposium on Circuits and Systems*, v 2, pp. 910-913, 1990.
  - [7] F. Najm (Dec. 1994). A survey of power estimation techniques in VLSI circuits. *IEEE Transactions on VLSI Systems*, 2, pp. 446-455.
  - [8] R. Burch, F. Najm, P. Yang, and T. Trick (Mar. 1993). A Monte Carlo approach for power estimation. *IEEE Transactions on VLSI Systems*, 1, pp. 63-71.
  - [9] T. Thompson (Dec. 1995). Two turbocharged PowerPCs. *Byte*, 20, pp. 209-210.
  - [10] 1995 Microprocessor Forum Presentation, DEC, <http://www.digital.com/info/semiconductor/strongarm>.
  - [11] G. Baccarini *et al.* (Apr. 1984). Generalized scaling theory. *IEEE Transactions on Electron Devices*, ED-31, pp. 452-462.
  - [12] M. Riezenman (May 1995). The search for better batteries. *IEEE Spectrum*, 32, pp. 51-56.
  - [13] A. P. Chandraksan, S. Sheng, and R. W. Brodersen (Apr. 1992). Low-power CMOS digital design. *IEEE Journal on Solid-State Circuits*, 27, pp. 473-484.
  - [14] C. Camperi-Ginstet, M. Hargis, N. Jokerst, and M. Allen (Dec. 1991). Alignable Epitaxial Lift-off of GaAs Material with Selective Deposition Using Polyimide Diaphragms. *IEEE Photonics Technology Letters*, 3, pp. 1123-1126.
  - [15] "Special issue on solid state image sensors," *IEEE Trans. on Elec. Dev.*, vol. 38, 1991.
  - [16] Olivier Vendier, Nan Marie Jokerst, Richard P. Leavitt, "Thin Film Inverted MSM Photodetectors," *IEEE Photonics Technology Letters*, vol. 8, no. 2, pp. 266-268, February 1996.
  - [17] S.M. Fike, B. Buchanan, N.M. Jokerst, M.A. Brooke, T.G. Morris, S.P. DeWeerth, "8x8 Array of Thin-Film Photodetectors Vertically Electrically Interconnected to Silicon Circuitry," *IEEE Photonics Technology Letters*, vol. 7, no. 10, pp. 1168-1170.
  - [18] A. Iwata, I. Hayashi, "Optical Interconnections as a new LSI technology," *IEICE Transactions on Electronics*, no. 1, vol. E76-C, 1992.
  - [19] S. Tang and R. Chen, "1-to-27 highly parallel three-dimensional intra and inter board optical interconnects," *IEEE Photon. Technol. Lett.*, vol. 6, no. 2, pp. 299-301, 1994.
  - [20] J. W. Goodman, F. J. Leonberger, "Optical interconnection for VLSI systems", S.-Y. Kung and R. A. Athale, *Proc. IEEE*, vol. 72, pp. 850-866, 1984.
  - [21] M. Koyanagi, H. Takata, H. Okano, S. Yokoyama, "Three-dimensional memory LSI with optical interconnections", *Electron. and Comm. in Jap.*, Part 2, vol. 76, no. 2, 1993.
  - [22] R. F. Carson, M. L. Lovejoy, K. L. Lear, M. E. Warren, P. K. Seigal, G. A. Patrizi, S. P. Kilcoyne, and D. C. Craft, "Low-power modular parallel photonic data links", *1996 IEEE ECTC proc.*, pp. 321-326.
  - [23] N. M. Jokerst, C. Camperi-Ginstet, B. Buchanan, S. Wilkinson and M. A. Brooke, "Communication through stacked silicon circuitry using integrated thin film InP-based emitters and detectors", *IEEE Photon. Technol. Lett.*, vol. 7, no. 9, 1995.
  - [24] Steven W. Bond, Sungyong Jung, Olivier Vendier, Martin A. Brooke, Nan M. Jokerst, "3D stacked Si CMOS VLSI smart pixels using through-Si Optoelectronic interconnections," *IEEE/LEOS summer tropical meetins*, 1998.
  - [25] M. Lee, O. Vendier, Martin A. Brooke and N. M. Jokerst, "A scalable CMOS current mode preamplifier design for an optical receiver", *Analog Integrated Circuits and Signal Processing*, vol. 12, no. 2, pp. 133-144, 1997.

### C. NEURAL NETWORKS PREDICTION OF MIXING LAYER FLOW STRUCTURE

A major goal of this research is to investigate the use of adaptive neural net hardware for 2-D and possibly 3-D plane mixing layer flow data prediction. Neural networks are nonlinear mapping functions and as such can learn to predict nonlinear dynamical systems. Several approaches have been investigated to predict the evolution of these systems [4,5,6,7,8]. We have built on this work with 4 new approaches, they are: Phase locked Direct prediction; Higher-Order Neural Networks with POD Modes; Higher-Order Sparse Neural Networks with POD Modes; and Higher-Order Sparse Neural Networks with Phase Locked POD Modes. We also attempted a direct approach similar to the previous work. For our work each approach utilizes the feedforward sigmoidal neural network trained with a gradient descending algorithm [10-27].

The phase locked prediction of POD modes with high order sparse neural networks has produced very good results. We have predicted the evolution of a previously unobserved 128 x 128 2-D flow data sequence approximately one quarter of a cycle of the forcing frequency into the future with an image accuracy of between 2% (best image) and 4% (worst image). Furthermore the sparse high order neural network used performs the predictions from just two prior flow images ( \_ and \_ a period in the past) using three matrix multiplies and two vector nonlinear mappings (which can be performed as fast table lookups). This makes real-time prediction practical if a fast parallel processor is used.

The neural nets do need to be trained on the flow they are expected to predict, and the training operations are considerably more CPU intensive than the prediction process, however, once a set of phase locked images is available from one cycle or period of the forcing function the network can train on that set of data images stand alone, so training on real-time flow data is possible with a parallel processor. We have used 500 phase locked flow images to train the networks (with better results generally obtained if more images are used) and our current training algorithm accesses the image data in 15 epochs of training, and so we would expect real time training to occur in about 7500 periods of the forcing frequency. For a forcing frequency of 5 Hz this is 25 minutes.

#### Direct Prediction

To see what an achievement the present results are let us consider the results of each of the other methods tried. The direct method is the most obvious method for training a neural network but the enormous amount of data being utilized for 2-D flow prediction was expected to make the direct method impractical. This was shown to be that case, with only poor results for predicting 1-D flow data obtained. However, the 1-D phased locked results obtained were promising, but they required lots of CPU time and the prospects of performing 2-D prediction looked poor.

In the direct prediction approach the predictor is presented with a time series of raw turbulence flow data and asked to predict future flow data. We have been applying this technique to data taken under a previous AFOSR grant by a member of our group (Glezer) and have shown that neural networks trained in this way out perform linear predictors trained on the same data. However, the large training sets (100 Mbytes) required to ensure that a good representation of the turbulent flow behavior is learned by the neural network make training slow

with currently available workstations. This is to be expected and is why the other methods described were investigated.

The first approach to predict the flow is a 1-D Data Direct Neural Networks Prediction. In this approach the predictor is presented with a time series of 1-D data turbulent flow and asked to predict the evolution of the flow. In this approach, the neural networks used 1 hidden layer and 8 hidden layer nodes. The network has been trained to predict 1-D turbulence flow 10 time steps into the future from data at the present time and 10 time steps in the past. The input is 31 samples at two time points, while the output is 31 samples at the future time point. There are 744 weights that need to be updated in training the network.

In Figure 1 below are a) a segment of the flow data we are using for this approach; b) the same segment as predicted by a neural network; c) the same segment as predicted by a linear predictor. All predictors are using data from 10 and 20 time steps in the past to predict the current time step. The neural network produces fewer artifacts in the unmixed areas of the flow and has a lower error than the linear predictor, however the linear predictor appears to be predicting the fine scale better than the neural network. The neural network used in this case uses half the number of weights that the linear predictor does and both networks were trained for the same number of iterations.

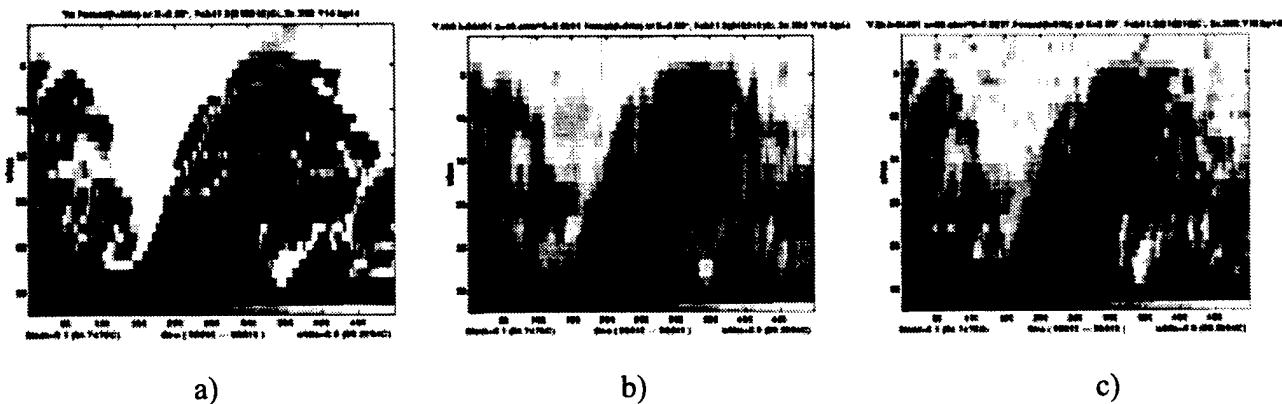


Figure 1 (a) is an Input Segment of 1-D Turbulent Flow. b) 1-D Data Direct Neural Networks Prediction. c) 1-D Data Linear LMS Prediction.

In quantitative terms, the average mean-square error can be calculated to evaluate the performance of the prediction. In processing 24,500 epochs, the average mean square value of the prediction error is 0.0231 using the Nonlinear Prediction Algorithm of Neural Networks Direct Prediction, and 0.0237 using the Linear LMS Prediction Algorithm. It took 21 hours to get this predicting result for 1-D Data Direct Neural Networks.

The workstation used for this simulation is a Sun SPARC Station 20 and the operating system is Solaris 2.4. With current workstations, the training requires large amounts of processor time that is necessary for the large training data in order to get a good representation of the flow behavior. This is to be expected and is why the following approaches have been investigated.



### Phased Locked Prediction

One way to reduce the amount of data required to train the predictors is to train them to predict forced turbulent flows in phase lock with the a forcing function. This means that the network is asked to predict what will happen at selected phases of the forcing function from data taken at earlier periods of the function. Since the training data is now provided only at selected phases of the periods of the forcing function, much less data can represent a long, well sampled, flow time period.

We have applied this technique to the data set used for direct prediction and have achieved promising results for prediction of a few selected phases. However, in order to get a representation of an entire period of the forcing function, the neural network must have one set of outputs for each phase selected. This leads to large networks which are also slow to train with currently available workstations.

The 1-D Data Phase-Locked Neural Networks has been applied to the 1-D data flow, already described. In this approach, the neural networks uses 1 hidden layer and 15 hidden layer nodes. The network has been trained to predict the 1-D data turbulence flow 128 time steps, which is the forced flow's period, into the future from data at the present time and 1, 2, 3, ..., 9 time steps in the past. The input is 31 samples at ten time points, while the output is 31 sample at the future time point. There are 5,115 weights need to be updated in training.

The results for this training in quantitative terms were that the average mean-square value of the prediction error was 0.0018, which is much better than the not phase locked prediction, Training took 52,820 epochs and 72 hours. Using the 1-D Data Phase-Locked Neural Networks, the training data is reduced and we could train a larger net and predict harder problems. However, the neural network is still too big to learn 2-D data flows on practical CPUs.

### ***2-D Data Plane Mixing Layer Prediction Using Higher-Order Neural Networks with POD Modes***

The activation level of an output node in a first-order neural network is determined by:

$$y_i = \Theta \left( \sum_j w_{ij} x_j \right)$$

Equation 1

where

$\Theta$  = a nonlinear threshold function

$x_j$  = the excitation values of the input nodes

$w_{ij}$  = the interconnection weight matrix elements

Note that the summation within the parenthesis in Equation 1 is a function of individual  $x_j$ 's. No advantage is taken of any known relationships between the  $x_j$ 's. Multi-layer, first-

order networks can learn invariance, but require a great deal of training, and produce solutions that are specific to particular training sets. A further disadvantage is that the mappings learned are opaque: it is not readily evident what features are being extracted or how classification is being performed. It is generally assumed that the output of intermediate-layer hidden nodes in the network correspond to specific feature, and in some applications it is possible to discern what these features are [1]. If a specific desirable feature set is chosen to make up the first layer of a neural network then this is called a higher order neural network. The output of nodes in a general higher order network is given by an equation of the form:

$$y_i = \Theta \left( \sum_j f(x_j) \right) \quad \text{Equation 2}$$

where the function  $f(x_j)$  are generally chosen to perform some desired task and to yield an intermediate-layer of known properties.

Previously some of us had shown that POD modes made a good choice for an internal representation of a periodically forced plane mixing layer [2]. We proposed to apply the POD representation as a first layer on a high order neural network. Figure 2 summaries the application of POD modes to 2-D Data Plane mixing layer prediction. Using this method the amount of training data needed is reduced dramatically. As has been shown in the earlier section of this report only a hundred modes will give an adequate reconstruction of a 2-D flow data set. In this approach, the neural network uses 1 hidden layer, 18 hidden layer nodes. Instead of training on 2-D image data, the network is essentially trained to predict the coefficients of the plane mixing layer flow.

In Figure 2 the results of predicting the coefficients from unforced flow data 10 frame-steps (about a quarter of the large roller frequency) into the future, from coefficients made at the present frame, and 10 frames-step in the past is presented. The network was trained for processing 28,400 epochs, the average mean square value of the coefficients' error is 0.0030 using the 2-D Data Plane mixing layer Prediction Using Higher-Order Neural Networks with POD Modes, and 0.0040 using the Linear LMS Method. It took two months of CPU time to get this result.

The input of neural network is 50 coefficient samples at two frame points, while the output is 50 coefficients at the future frame point. 1,500 ( $2 \times 50 \times 10 \times 50$ ) weights need to be updated. The number of weights for this neural networks' prediction is much fewer than if direct prediction, which needs 491,520 ( $2 \times 128 \times 128 \times 10 \times 10 \times 128 \times 128$ ). Generally, 2-D Plane mixing layer Prediction Using Higher-Order Neural Networks with POD Modes saves training time since the weights are fewer and it saves memory since the data set size is reduced.

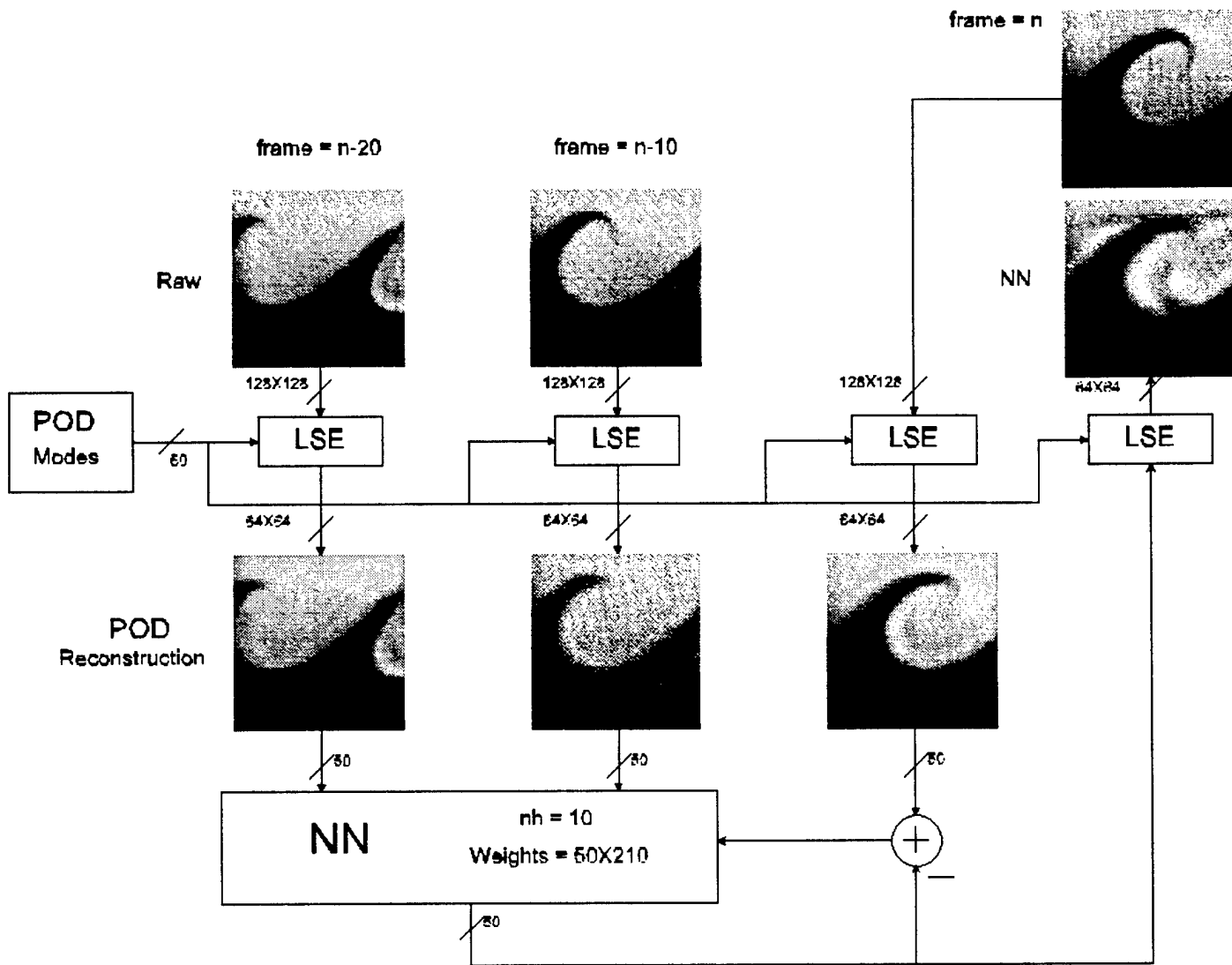


Figure 2. 2-D Data Plane mixing layer Prediction Using Higher-Order Neural Networks with POD Modes

### *Speed Up the Training Implemented in Different Programming Languages*

In this research, MATLAB has been used as a programming language to calculate the error and update the neural network parameters for predicting the plane mixing layer systems. MATLAB is a technical computing environment for numerical computation and visualization. It is an interactive system whose data elements are matrices [3]. This property makes itself be suited as a programming language for parallel calculation.

The testing function can be created and performed just like the intrinsic functions built into MATLAB. The graphical capabilities of MATLAB are quite powerful. All functions and plane mixing layer flow data can be plotted in two or three dimensions.

In order to speed up the training, a MATLAB Compatible C++ Matrix Library (MATCOM LIBRARY) has been tried to predict the same plane mixing layer system. MATCOM LIBRARY is a C++ matrix class based closely on the MATLAB language. It provides a great environment

for numerical computation. However, it has been shown that it does not help in speed for this application.

Another approach is that writing the entire code for calculating the error and updating the neural network parameters in C programming language [4]. C is a general-purpose programming language. It has been closely associated with the UNIX system, since it was developed on that system, and since UNIX and its software are written in C. C is a relatively "low level" language. The lack of parallel operation support makes the C programming language not help to speed up the neural network's training either.

According with the experimental results, it is clear that MATLAB is a well-suited programming language for predicting the time-series of plane mixing layer systems, since it has the ability for parallel calculation. The comparison of different programming language results is summarized in Table 1.

	Hand coded C	MATCOM LIBRARY	MATLAB
Small Matrices Multiplication (20 by 20)X(10 by 20)		0.0040 seconds	0.0036 seconds
Big Matrices Multiplication (300 by 900)X(900 by 400)	111 seconds	45 seconds	35.8 seconds
1-D Data Direct Neural Networks Prediction in Processing 100 Epochs	40 minutes	5.89 minutes	5.14 minutes

Table 1. The Comparison of Different Programming Languages' Results

### ***2-D Data Plane Mixing Layer Prediction Using Higher-Order Sparse Neural Networks with POD Modes***

To further speed up the training, Sparse Neural Networks were been investigated to predict the evolution of plane mixing layer flow. Assume the structure of the neural network contains a high proportion of near zero entries. To save memory and time these near zero-valued entries need not be stored and, not manipulated. This structure results in a saving of memory and CPU time. We do not have a good method of finding zero weights however we can make

intelligent guesses as to what weights to leave out to reduce the complexity of the networks. Because of our manual intervention, Sparse Neural Networks typically shows some reduction in ability to predict the plane mixing layer systems over a full net, however they are orders of magnitudes faster to train and use much less memory. In this approach several methods have been tried, such as Choosing a Subset of Inputs, which includes the first 10 samples of 50 coefficients, the first odd 10 samples of 50 coefficients, the first even 10 samples of 50 coefficients and the best 10 samples of 50 coefficients, and Partitioning Output.

The New approach, the 2-D Data Plane mixing layer Prediction Using Higher-Order Sparse Neural Networks with POD Modes, has been investigated to predict the evolution of 2-D plane mixing layer flow. In this approach, the neural networks use 1 hidden layer, and 500 hidden layer nodes. The network has been trained to predict the coefficients of the plane mixing layer flow 10 frame-step into the future from coefficients data at the present frame and 10 frame-step in the past. The differences between this approach and the 2-D Data Plane mixing layer Prediction Using Higher-Order Neural Networks with POD Modes are input and output of the network. Predicting errors are almost the same for choosing different subset of inputs, such as the first 10 samples of 50 coefficients, the first odd 10 samples of 50 coefficients, the first even 10 samples of 50 coefficients and the best 10 samples of 50 coefficients.

We chose to make our inputs is first 10 odd coefficients for the two historical data images, while the output is a partition of the hidden layer sample at the future frame point. With this scarcity, learning parameters needed to be updated are 10,500 ( $50 \leftarrow 2 \leftarrow 10 \leftarrow 10 + 10 \leftarrow 1$ ) weights in each training. The number of the weights used in this approach is more than in the 2-D Data Plane mixing layer Prediction Using Higher-Order Neural Networks with POD Modes, but sequential training is now possible with a separate network being trained for each of the 50 output coefficients. The architecture is shown in Figure 3 for the 2-D Data Plane mixing layer Prediction Using Higher-Order Sparse Neural Networks with POD Modes.

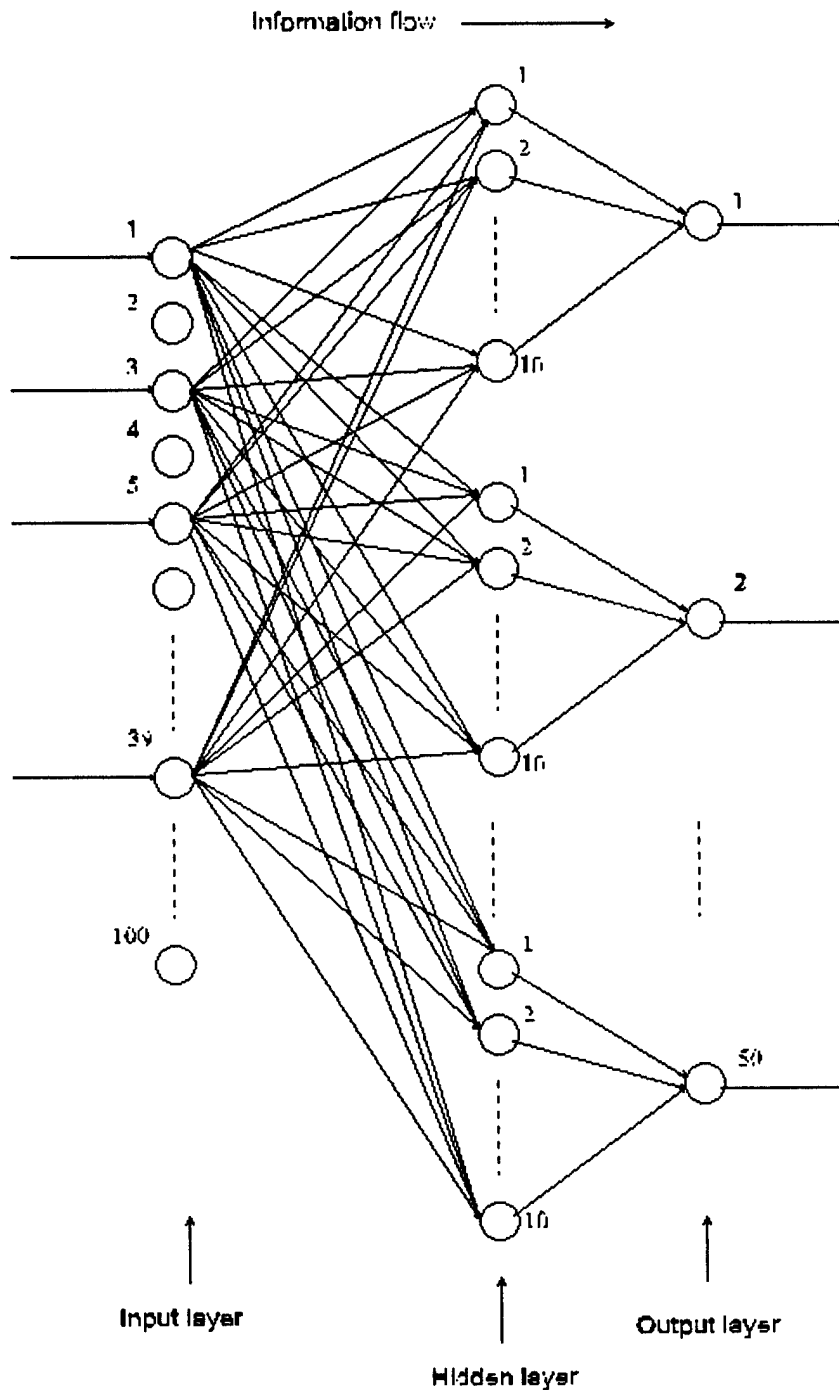


Figure 3 The architecture of 2-D data plane mixing layer prediction using higher-order sparse neural networks with POD modes

The predicting procedure of 2-D Data Plane mixing layer Prediction Using Higher-Order Sparse Neural Networks with POD Modes and its predicting result is presented in Figure 4. The average mean-square value of the predicted image Figure 4 c) error is 0.0060 in processing 5,000 epochs. In processing 20,000 epochs, the average mean square value of the coefficients' error is

0.0014 (4 times less error than without sparse networks) using this approach and it took 40 hours (30 times speed up over non-sparse network) for getting this predicting result.

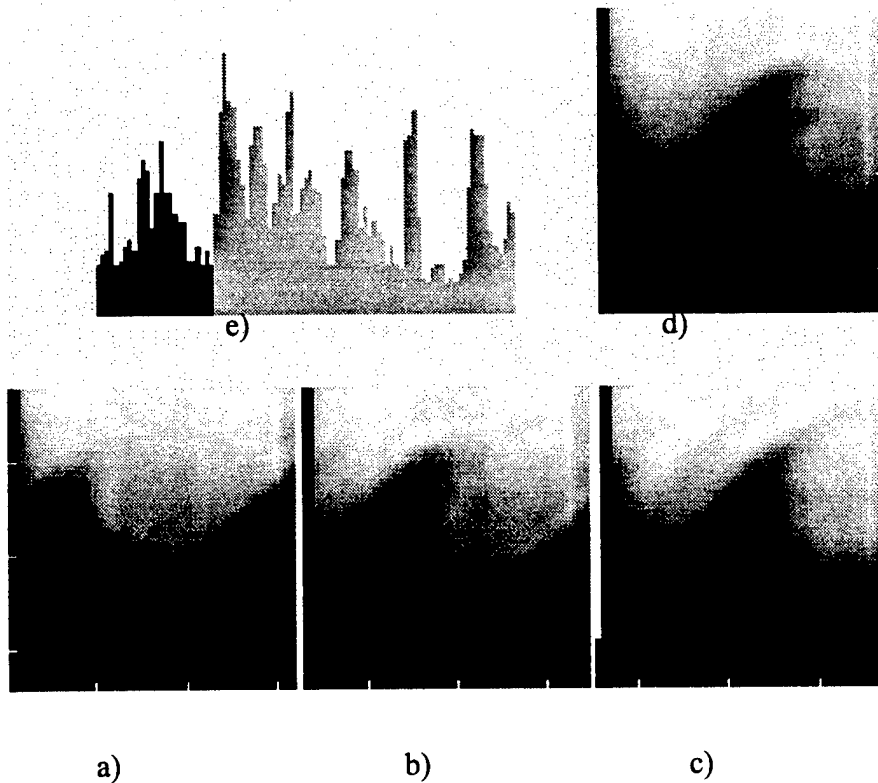


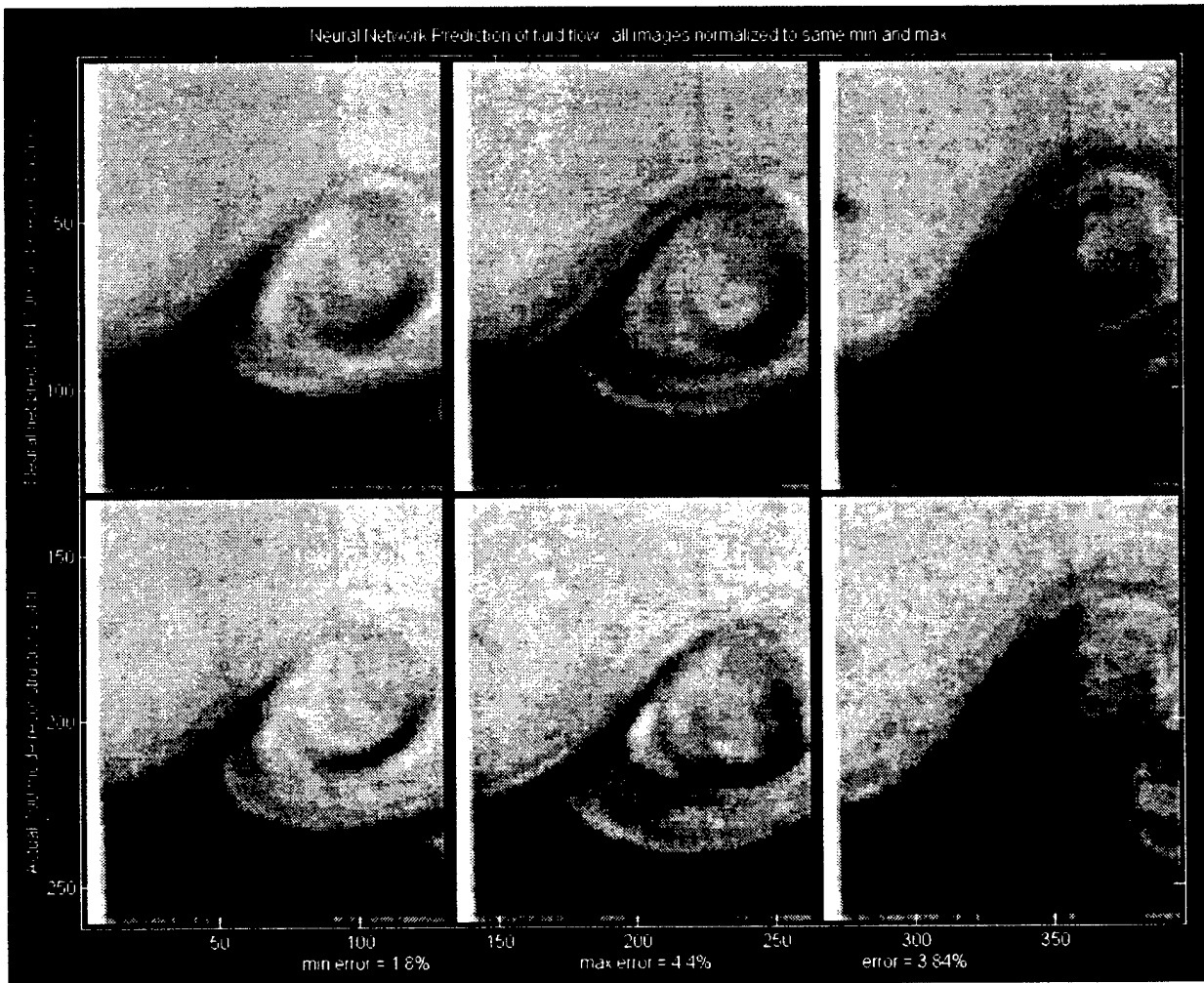
Figure 4. The results of 2-D plane mixing layer prediction using higher-order sparse neural networks with POD modes. Images a) and b) are the reconstructed from the POD coefficients input to the network. Image c) is the predicted flow cross section reconstructed from POD coefficients output by the network. Image d) is reconstructed from the actual POD coefficients of the flow image. Plot e) shows the neural network prediction error for the whole image sequence. The average error is 0.0014. The neural network was not trained on the image sequence of from which this example is taken.

### ***Neural Network Prediction of Phase Locked Flow Data Images***

The final approach tried in this work was to use phase locked 2-D data and to train networks to predict only one of the phases for a given period of the flow data. This greatly reduces the difficulty of the task performed by the neural network. It need only concern itself with events at one point in the period of the flow. The data input to the network for training looks similar to Figure 4 a) and b) while the output will be the coefficients at a later predicted time.

Neural networks were trained to predict 500 images of one phase, using 500 images each of two phases earlier (approx. 10 and 20 frames earlier). The networks were trained using the

first 50 POD mode coefficients of these images as inputs and the *first 100 modes* as outputs. The coefficients were computed for POD modes from a separate set of 567 images taken at the same phases but at a different (earlier) time. The results are presented in Figure 5. The figure shows the predicted images from a test set of 70 images that was not used for training. The images are the lowest and highest error images from the 70 image sequence and the image with the most difference from these first two. The error is the rms error of the two images normalized to the absolute maximum pixel magnitude in all 70 images. The images are all normalized to the same values..



a)

b)

c)

Figure 5. predicted (top) and actual (bottom) images from a test set of 70 images that was not used in training, a) is the lowest and b) the highest error images from the 70 image sequence. c) is the image with the most difference from the first two. The error is the rms error of the two images normalized to the absolute maximum pixel magnitude in all 70 images. The images are all normalized to the same values



## Conclusions

The predictive capabilities have been studied in detail for several approaches to time-series 2-D data plane mixing layer flow. In general, the more advanced networks allow more complex problems to be solved with reduced training time. The 2-D Data Plane mixing layer Prediction Using Higher-Order Sparse Neural Networks with POD Modes is superior to other approaches. The comparison of different approaches for predicting the 2-D data plane mixing layer flow is summarized in Table 2.

Table 2. Comparison of different approaches for predicting the 2-D data plane mixing layer flow

	Direct Neural Network Prediction of 1-D data	Linear LMS prediction with 2-D POD modes	Higher-Order Neural Network with 2-D POD Modes	Higher-Order Sparse Neural Network with 2-D POD Modes	Higher-Order Sparse Neural Network with Phase locked 2-D POD Modes
Training Time	21 hours	1.5 months	2 months	40 hours	24 hours
Mean square error	0.0231	0.0040	0.0030	0.0014	0.0004

Since a shorter training time allows us to train larger networks we generally saw much better results for each advance in the network architecture.

## Extension to 3-D flow prediction

Based on the results obtained here we believe that the sparse high order networks, could be trained on the POD modes of phase locked 3-D flow data and not exceed the capability of current state of the art work stations. The challenge of collecting 3-D flow data and training networks with this volumous record will be left to later work, however, it seems likely that it would take 1-2 months to train such networks on normal work stations. Perhaps some further improvements in neural network architecture will reduce this time. It is likely that, once trained, these networks would be capable of performing real time predictions of the 3-D flow field evolution when run on parallel processing computational systems.

## References

- [1] Gorman, R. P. and Sejnowski, T. J. 1988 "Analysis of Hidden Units in a Layered Network Trained to Classify Sonar Targets," *Neural Networks*, Vol. 1, pp75-89.
- [2] Glezer, A. et al. 1989 "Development of an extended proper orthogonal decomposition and its application to a time periodically forced plane mixing layer," *Phys. Fluids A1*(8), August.
- [3a] Kernighan, B. W. and Ritchie, D. M. 1978 "The C Programming Language," Bell Laboratories, Murray Hill, New Jersey.
- [3] The Math Works Inc. 1992
- [4] Casdagli, M. 1989 "Nonlinear Prediction of Chaotic Time Series," *Physica D* 35, pp.335-336, 1989.
- [5] Haykin, S. and Leung, H. 1992 "Model Reconstruction of Chaotic Dynamics: First Preliminary Radar Results," *Proc. IEEE ICASSP*.IV-125.
- [6] Nelson, D. E., Ensley, D. D. and Rogers, S. K. 1992 "Prediction of Chaotic Time Series Using Cascade Correlation," *SPIE vol.1709 Applications of Artificial Neural Networks III*.
- [7] Sidorowich, J. J. 1992 "Modeling of Chaotic Time Series for Prediction," *Interpolation, and Smoothing Proc. 1992 IEEE ICASSP*.IV-121.
- [8] Stright, J. 1988 "A Neural Network Implementation of Chaotic Time Series Predication," Air Force Institute of Technology, AFIT/GE/ENG/88D-50. December 1988.
- [9] Day, S. P. and Davenport, M. R. 1993 "Continuous-Time Temporal Back-Propagation with Adaptable Time Delays," *IEEE Transactions on Neural Networks*, Vol. 4, No.2, March 1993.
- [10] Werbos, P. 1974 "Beyond Regression: New Tools for Predication and Analysis in the Behavioral Sciences," PhD thesis, Harvard, Cambridge, MA, August 1974.
- [11] Freeman, J. A. and Skapura, D. M. 1991 "Neural Networks," by Addison-Wesley Publishing Company, Inc.
- [12] Hinton, G. E 1989 "Connectionist Learning Procedures," *Artificial Intelligence*, vol.40, No.1, pp.143-150.
- [13] Hinton, G. E. 1989 "Deterministic Boltzmann Learning Performs Steepest Descent in Weight-Space," *Neural Computation*, 1, 1989, pp.143-150.
- [14] Hinton, G. E. and T. J. Sejnowski, T. J. 1987 "Neural network architectures for AI," Tutorial No. MP2, AAAI87, Seattle, WA, July 1987.
- [15] Houk, J. C. 1992 "Learning in Modular Networks," *Proceeding of Adaptive and Learning Systems*. Yale University. pp.80-84, May,1992
- [16] Irie, B. 1988 "Capabilities of Three-Layered Perceptrons", *Proceedings of the IEEE International Conference on Neural Networks*, vol.1, pp.641.
- [17] Jones, R. D., Lee, Y. C. et al. 1990 "Nonlinear Adaptive Networks: a Little Theory, a Few Applications," Los Alamos National Laboratory Rpt. No. LA-UR-90-21.
- [18] Lapedes, A. and Farber, R. 1987 "Nonlinear signal processing using neural networks: Prediction and system modeling," *Tech. Rep. LA-UR-87-2662*, Los Alamos National Laboratory, NM, July 1987.

- [19] Li, L. and Haykin, S 1993 "A Cascaded Recurrent Neural Networks for Real-Time Nonlinear Adaptive Filtering," 1993 IEEE, pp.853-862.
- [20] Lippman, R.P. 1987 "An Introduction to Computing with Neural Nets," IEEE ASSP Magazine, April 1987, pp.4-22.
- [21] McClelland, J and Rumelhart, D. 1986 "Parallel Distributed Processing," vols. 1 and 2. MIT Press, Cambridge, MA.
- [22] Minsky, M. L. and Papert, S. 1969 "Perceptrons," Cambridge, MA: MIT Press.
- [23] Parker, D. B. 1985 "Learning Logic," Technical Report TR-47, Center for Computational Research in Economics and Management Science, MIT, Cambridge, MA, April 1985.
- [24] Rosenblatt, F. 1958 "The Perceptron: A Probabilistic Model for Information Storage and Organization," Psychological Review, vol.65, No.6, 1958.
- [25] Rosenblatt, F. 1962 "Principles of Neurodynamics," New York: Spartan, 1962.
- [26] Rumelhart, D. E., Hinton, G. E. and Williams, R. J. 1986 "Learning Internal Representations by Error Propagation," in Parallel Distributed Processing, vol.1, pp.318-362.
- [27] Weigend, A. S., Huberman, B. A. and D. E. Rumelhart, D. E. 1990 "Predicting the future: A connectionist approach," Int. J. Neural Syst., vol.1, no.3, pp.193-209.